

Synthesis of push-pull compounds for the sensitization of p-type semi-conducting oxides

Romain Brisse

▶ **To cite this version:**

Romain Brisse. Synthesis of push-pull compounds for the sensitization of p-type semi-conducting oxides. Material chemistry. Ecole Polytechnique (EDX), 2015. English. NNT : . tel-01870923

HAL Id: tel-01870923
https://theses.hal.science/tel-01870923

Submitted on 21 Sep 2018

HAL is a multi-disciplinary open access archive for the deposit and dissemination of scientific research documents, whether they are published or not. The documents may come from teaching and research institutions in France or abroad, or from public or private research centers.

L'archive ouverte pluridisciplinaire **HAL**, est destinée au dépôt et à la diffusion de documents scientifiques de niveau recherche, publiés ou non, émanant des établissements d'enseignement et de recherche français ou étrangers, des laboratoires publics ou privés.

Thèse de doctorat de l'Ecole Polytechnique

Spécialité : Chimie

Présentée par Romain Brisse le 21 Décembre 2015

Synthesis of push-pull compounds for the sensitization of p-type semi-conducting oxides

Synthèse de composés push-pull pour la photosensibilisation d'oxydes semi-conducteur de type p



Composition du jury :

Serge Palacin	CEA Saclay	Directeur de thèse
Bruno Jousselme	CEA Saclay	Co-directeur de thèse
Fabrice Odobel	CNRS – Université de Nantes	Rapporteur
Philippe Blanchard	CNRS – Université d'Angers	Rapporteur
Thomas Gustavsson	CNRS – CEA Saclay	Examinateur
Yvan Bonnassieux	Ecole Polytechnique	Examinateur

LICSEN - Laboratoire d'Innovation en Chimie des Surfaces et Nanosciences

CEA Saclay

Table of content

REMERCIEMENTS 11

INTRODUCTION 13

I. HOW TO BUILD THE BEST P-TYPE DSSC ? 17

I.A. General working principle of a p-type DSSC 19
I.A.1. Basics 19
I.A.2. The successive steps for photocurrent generation 21
I.A.3. Typical J-V characteristics for p-type DSSCs 21
I.A.4. Energetic requirements 22
I.A.5. The kinetic problems of p-type DSSCs 24
I.A.6. V_{OC} engeenering 25

I.B. How to build the best p-type DSSCs with NiO? 28
I.B.1. Introduction 28
I.B.2. Increasing the light harvesting properties of the film 28
I.B.2.a. Introduction, the dye/NiO light absorption competition 28
I.B.2.b. NiO engineering for enhanced light harvesting properties of the film 29
I.B.2.b.i. NiO parasitic light absorption 29
I.B.2.b.ii. Engineering NiO for more efficient light harvesting properties 31
I.B.2.c. Dye engineering for enhancing the light harvesting properties of the NiO film 31
I.B.2.c.i. The tool-box for light transitions 31
I.B.2.c.i.(i) “Localized” transition 32
I.B.2.c.i.(ii) Push-pull transition 32
I.B.2.c.ii. Mixing the transitions 32
I.B.2.c.iii. Enhancing dye light absorption 33
I.B.2.c.iii.(i) Resorting to highly absorbing dyes 33
I.B.2.c.iii.(ii) Resorting to dyes with wide absoprtion window 36
I.B.2.c.iv. Increasing the number of dyes grafted at the NiO surface 37
I.B.2.d. Reducing the electrolyte absorbance 39
I.B.3. Efficiently inject holes into NiO VB 39
I.B.3.a. Position of the NiO VB edge 39
I.B.3.b. An ultra-rapid and efficient hole injection 40
I.B.3.c. Is hole injection really so un-problematic ? 41
I.B.4. Fighting against charge recombination 43
I.B.4.a. What is known about charge recombination today 43
I.B.4.a.i. The EIS results by the goup of Wu 43
I.B.4.a.ii. Recent transient absorption spectroscopy results 44
I.B.4.a.iii. Possible reasons for the important charge recombination 45
I.B.4.a.iv. Is NiO a good conductor? 46
I.B.4.b. How to fight against geminate recombination? 47
I.B.4.b.i. Dye design strategies to prevent geminate charge recombination 47
I.B.4.b.i.(i) The case of dyes which pre-associate with I_3^- 47
I.B.4.b.i.(ii) Dye design to increase the charge-separated life time 47
I.B.4.b.ii. NiO surface engineering to reduce geminate recombination 51
I.B.4.c. Ensuring efficient hole transport to FTO 51

I.B.4.c.i. NiO surface engineering 51
I.B.4.c.ii. Electrolyte engineering 52
I.B.4.d. Ensuring Hole collection at the FTO contact 53

I.C. Conclusions and aim of this PhD 53

II. ORGANIC SYNTHESIS OF THE NEW DYES AND THEIR PHYSICAL PROPERTIES 61

II.A. Synthesis and physical properties of the bithiophen push-pull dyes 63
II.A.1. Choice of the molecules 63
II.A.1.a. Introduction 63
II.A.1.b. Evaluation of the strength of the different acceptors 64
II.A.1.b.i. Study of the chemical formulae of the different acceptors 65
II.A.1.b.ii. LUMO level calculation for the different acceptor groups 66
II.A.1.b.iii. Conclusions 67
II.A.2. Organic synthesis of the bithiophen dyes 67
II.A.2.a. Retro-synthetic scheme 67
II.A.2.b. Synthesis of the triphenylamine building block 68
II.A.2.b.i. Introduction 68
II.A.2.b.ii. State of the art for the synthesis of TPA (3) 68
II.A.2.b.iii. Synthesis of the boronic pinacol-ester triphenylamine (3) 70
II.A.2.c. Synthesis of the 5 acceptor groups (6), (9), (12), (15) and (19) 73
II.A.2.c.i. Synthesis of diisopropylphenyl-naphtalimide-bromobithiophen (6) 73
II.A.2.c.ii. Synthesis of the methylene-derivative acceptors (9), (12) and (15) 75
II.A.2.d. Microwave assisted Suzuki-Miyaura cross coupling of the various acceptors with TPA - Synthesis of (7), (10), (13), (16) and (19) 75
II.A.2.e. Deprotection with TFA - Synthesis of the final compounds (8), (11), (14), (17) 78
II.A.3. Toward DPP derivatives 78
II.A.3.a. Targeted synthetic pathway 78
II.A.3.b. Synthesis of the dyes with DPP skeleton 79
II.A.4. Conclusions 83

II.B. Physical properties of the synthesized dyes 84
II.B.1. Electrochemical studies 84
II.B.1.a. Electrochemical studies of the dyes in DMF 84
II.B.1.b. Electrochemical work on the tert-butyl ester protected version of the dyes 85
II.B.2. Steady state optical properties 89
II.B.2.a. Steady state UV/Visible absorption spectra 89
II.B.2.b. Steady state emission spectra 92
II.B.3. Summary and conclusion 94

III. NIO FORMATION THROUGH INK-JET PRINTING 99

III.A. The different NiO synthesis techniques 101
III.A.1. NiO prefabricated nanomaterial paste 101
III.A.1.a. General method for the paste preparation 101
III.A.1.b. NiO nanoparticles as the preformed object 102
III.A.1.c. Other prefabricated materials 103
III.A.1.d. Other pastes 104
III.A.2. NiO sol-gel route 105

III.A.2.a. The $Ni(OH)_2$ slurry way 105
III.A.2.b. The sol-gel templated way 106
III.A.2.b.i. Templating NiO films with pluronic tribloc copolymers 106
III.A.2.b.ii. Tuning the thickness of the F_{108} templated NiO films 109
III.A.2.c. Using other templates than pluronic block copolymers 111
III.A.3. Comparison of the different methods and conclusions 113
III.A.3.a. Comparison of the actual "two best NiO" 113
III.A.3.b. Conclusions 115

III.B. Doctor-blading NiO films with F_{127} as the copolymer block 115
III.B.1. Use of a "Classical" ink 115
III.B.1.a. Preparation of "classical" doctor-bladed NiO film with F_{127} as the templating agent 115
III.B.1.b. SEM analysis 117
III.B.1.b.i. Thick black zones 117
III.B.1.b.ii. Thin transparent zone 117
III.B.1.c. Possible mechanism for film morphology 120
III.B.1.d. Reproducibility issues 122
III.B.2. Increasing the viscosity of the ink 122
III.B.3. Conclusions 124

III.C. NiO films fabrication through ink-jet printing 124
III.C.1. Introduction 124
III.C.1.a. Generalities- Ink-jet printing for materials applications 124
III.C.1.a.i. An attractive technique 124
III.C.1.a.ii. Industrial challenges 125
III.C.1.b. IJP basic principles and requirement 126
III.C.1.b.i. Continuous IJP and Drop on demand IJP 126
III.C.1.b.ii. The successive steps of IJP 127
III.C.1.b.iii. Ink design and formulation for IJP 129
III.C.1.c. Ink-jet printing oxides via the sol-gel way 129
III.C.1.c.i. State of the art 129
III.C.1.c.ii. Combinatorial material synthesis 130
III.C.1.d. Conclusions 131
III.C.2. Fabrication of NiO films for DSSC through ink-jet printing 131
III.C.2.a. Ink preparation 131
III.C.2.a.i. Ink formulation for IJP 131
III.C.2.a.i.(i) First investigations 131
III.C.2.a.i.(ii) Decreasing the ink viscosity 132
III.C.2.a.i.(iii) Surface tension and contact angle 134
III.C.2.a.ii. Aging of the ink 134
III.C.2.b. Printer description 135
III.C.2.c. Printing parameters for NiO film preparation 135
III.C.2.c.i. First-step required: preparing the cartridge 135
III.C.2.c.ii. Common parameters for all films formation 136
III.C.2.c.iii. First set of parameters (« set-1 ») 136
III.C.2.c.iii.(i) Drop generation 136
III.C.2.c.iii.(ii) Film formation 137
III.C.2.c.iv. Second set of parameters (« set-2 ») 138
III.C.2.c.iv.(i) Drop generation 138
III.C.2.c.iv.(ii) Film formation 139
III.C.2.d. Role of humidity 139
III.C.2.e. Deposition of one layer of NiO substrates (NiO-1L samples) 139
III.C.2.e.i. Drying and sintering conditions 139

III.C.2.e.ii. Film morphology 139
III.C.2.f. Increasing the number of NiO layers 141
III.C.2.f.i. Interlayer drying of 30°C 141
III.C.2.f.ii. Interlayer drying of 100°C 144
III.C.2.f.iii. Interlayer sintering at 450°C 144
III.C.3. Study of NiO formation mechanism 147
III.C.3.a. TGA analysis 147
III.C.3.b. NiO formation mechanism study with XPS 149
III.C.4. Conclusions 153

IV. BUILDING EFFICIENT DSSCS WITH THE NEW DYES AND IJP NIO 161

IV.A. Introduction 163

IV.B. p-Type DSSCs with NiO-1L films, sensitized with dye (8) 163
IV.B.1. Sensitizing the NiO-1L electrodes with dye (8) 163
IV.B.1.a. Solvent choice 163
IV.B.1.b. Dying bath duration 164
IV.B.1.c. Solid state UV/Vis spectra of the sensitized NiO film 165
IV.B.2. p-Type DSSCs tests methodology 167
IV.B.2.a. Fabrication of the DSSC 167
IV.B.2.b. Parameters for the solar cell tests 168
IV.B.3. Results 169
IV.B.4. Conclusion 170

IV.C. p-Type DSSCs performances with thicker NiO films 171
IV.C.1. Solar cell fabrication and test parameters 171
IV.C.2. Dual pore, nanofiber like morphology 171
IV.C.3. Compact nanoparticle morphology: 173
IV.C.3.a. Optical properties 173
IV.C.3.b. Photovoltaic performance 175

IV.D. Introducing a NiO_x contact layer between FTO and NiO 177
IV.D.1. NiO_x thin layer deposition 177
IV.D.2. Influence of the NiOx sub layer on the p-type DSSC performance 180

IV.E. Performance of the IJP NiO electrodes with other bithiophen dyes 182
IV.E.1. Sensitization of the NiO electrode 182
IV.E.1.a. Solutions preparation 182
IV.E.1.a.i. Dye (14) 182
IV.E.1.a.ii. Dye (11) and (17) 183
IV.E.1.b. Sensitization of NiO 183
IV.E.1.c. Device tests on NiO-4L electrode 185
IV.E.2. Conclusion 188

IV.F. Conclusions 189

CONLUSION OF THE THESIS 193

EXPERIMENTAL PART 195

I. ORGANIC SYNTHESIS (CHAPTER 2, PART I) 197

I.A. General conditions 197

I.B. Synthesis of the different intermediates and final molecules 198

II. PHYSICAL PROPERTIES (CHAPTER 2, PART 2) 226

II.A. Generalities 226

II.B. Electrochemistry 226

II.C. UV-Visible spectra in solution 227

II.D. DFT/TDDFT calculations 228

III. DSSC FABRICATION THROUGH IJP. SOLAR CELL TESTS. (CHAPTER 3 AND CHAPTER 4) 229

III.A. Generalities 229

III.B. DSSC fabrication 229
III.B.1. Cleaning the FTO substrates 229
III.B.2. Preparing the NiO_x precursor solution 230
III.B.3. Deposing the NiO_x layer 230
III.B.4. Preparation of the $NiCl_2$ diluted ink for printing 230
III.B.5. Preparation of the printer 231
III.B.6. Preparation of the substrates 231
III.B.7. Mesoporous NiO Film deposition 232
III.B.8. Sensitization of the photocathode 233
III.B.8.a. Sensitization solution preparation 233
III.B.8.b. Substrate sensitization 233
III.B.9. Preparation of the Electrolyte 233
III.B.10. Solar cell fabrication 233
III.B.11. Photovoltaic measurements 234

IV. MISCELLANEOUS INFORMATION 235

IV.A. Doctor-bladed films Ink-0 morphology 235

IV.B. Rheological properties 235

IV.C. NiO film thickness measurements 235

IV.D. NiOx thickness measurements 235

IV.E. NiO sensitized film solid-state absorption measurements 235

IV.F. NiO formation mechanism study with IJP film (Ink-1) 236

ANNEXES 239

I. ANNEX 1 - ANOTHER PHOTOCATHODE MATERIAL THAN NIO ? 241

I.A. A $Cu^{(II)}$ material, CuO: 241

I.B. Delafossite $Cu^{(I)}$ materials : 241
I.B.1. $CuAlO_2$ 242
I.B.2. $CuGaO_2$ 243
I.B.3. $CuCrO_2$ 243

I.C. ITO material 244

I.D. Other materials 244

I.E. Conclusions 245

II. ANNEX 2 - CHOICE OF THE CATALYTIC SYSTEM FOR SM COUPLING 247

III. ANNEX 3 - DFT/TDDFT RESULTS 250

III.A. Introduction 250

III.B. Results 251
III.B.1. Dye (8) 251
III.B.2. Dye (11) 253
III.B.3. Dye (14) 255
III.B.4. Dye (17) 257

III.C. Various remarks 258

III.D. Modular analysis of the push-pull interaction 259
III.D.1. Modular gap tuning 259
III.D.2. Frontier orbitals coupling 260

III.E. Dipolar moments of the dyes and orientation 264
III.E.1. Dye (8) 264
III.E.2. Dye (11) 264
III.E.3. Dye (14) 265
III.E.4. Dye (17) 265

IV. ANNEX 4 – RED ABSORBING DYES REVIEW 267

V. ANNEX 5 – LIGHT SOAKING EFFECT 269

ABSTRACT 271

Remerciements

Je remercie toutes les personnes qui ont, de près ou de loin, participé à l'aboutissement de ce projet de thèse, tout particulièrement Tiphaine, « ma cothésarde » pour sa gentillesse et sa grande aide sur tous les aspects. Après deux stages et une thèse au même endroit, nos chemins professionnels se séparent maintenant et je ne doute pas qu'ils se recroiseront.

Je remercie également tout particulièrement Rita Faddoul, Thomas Berthelot et Alexandre Causier pour leur précieuse aide avec l'imprimante jet d'encre, ainsi que Jean-Mauel Raimundo et Praveen Chandrasekar pour avoir synthétisé et fourni de nombreux composés clefs pour ce travail de thèse. Un grand merci à Guillaume Deau (contrat d'apprentissage) pour son aide précieuse en synthèse également et à Laure Pantaleo (stagiaire M2) pour ses manips sur CuSCN. Une pensée particulière va à Stéphane Campidelli pour les clichés MEB magnifiques qu'il a réalisés. Un grand merci à Thomas Gustavsson et Valentin Mafféis pour m'avoir fait découvrir le merveilleux monde de la spectroscopie optique stationnaire et ultrarapide, ces connaissances me seront très utiles pour la suite j'en suis sûr. Merci également à Jocelyne Leroy pour les analyses XPS, sa gentillesse et son aide pour l'interprétation des spectres. Merci à Claire et Cédric pour leurs conseils en chimie organique et pour leur aide sur le banc également. Merci à Renaud pour les quelques relectures et autres avis toujours pertinents. Merci à Vincent Artero et Nicolas Kaeffer pour les quelques échanges que nous avons eus. Merci à Bernard Geffroy et Denis Tondelier pour leur aide à Orgatech et la confiance qu'ils m'ont donnée dans l'utilisation du simulateur solaire. Je remercie vivement Valentina Ivanova pour les nombreux conseils également ainsi que Catherine Jullien, Brigitte Mouanda et Nabila Debou, pour toutes les petites choses de la vie de tous les jours au labo. Merci à Serge Palacin de m'avoir accueilli.

Enfin, je ne remercierai jamais assez Bruno, ce fut un honneur d'être dans ton équipe, très à l'écoute, toujours l'idée qu'il faut pour résoudre un problème, merci de m'avoir fait confiance et donné autant d'autonomie et de liberté, toujours avec le sourire. Sans tout cela, je ne pense pas

que j'aurais pris autant de plaisir à travailler. La liste des collègues que je souhaite par ailleurs remercier pour les conseils et surtout la bonne humeur au cours de ces trois années au LICSEN est longue … Mais ils se reconnaitront j'en suis sûr. Je leur dis à bientôt ! Mes amis d'ici ou d'ailleurs (un grand Merci à Amandine et Elise) et ma famille ont également grandement contribué à ce travail, merci à eux. Je dédis cette thèse à mes grands-parents.

«Alors il est où le cookie aux rillettes ». F.S.



Introduction

Dye-Sensitized Solar cells (DSSCs), initially developed by the work of Grätzel and O'Regean[1] in the early 90's offer competitive performance. Recently, a high value of 14% photo-conversion yield was obtained for DSSCs, making them really promising as a cost effective alternative to the market-dominating Si-based technology [5]. DSSCs are part of the third generation solar cells (comprising organic solar cells [2], perovskite solar cells [3] and quantum dots solar cells [4]) which display low cost of fabrication, though effort toward enhanced scalability must be done. DSSCs are generally composed of a photoanode and a cathode, sandwiching an electrolyte. The working principle resembles the one of natural-photosynthesis: a dye molecule absorbs light in the visible range [6], but the solar energy is not stored in chemical bonds and is rather directly converted to electricity.

This thesis focuses on p-type, photocathodic DSSCs. The development of this type of cells is very recent [7] and actually their performance remains far below the one of the "classical", photoanodic DSSCs, due to several constitutive hurdles. However, such solar-cells are precious to study, regarding the possibilities offered by the Tandem-Dye Densitized Solar Cell (T-DSSC) configuration [8]. T-DSSCs actually possess theoretical photo-conversion efficiency that are superior to the "one photo electrode" configuration that is: 40% (T-DSSC) *vs* 30% (one electrode classical DSSC) [9]. Another aspect is the possibility offered by the p-type photocathodes for hydrogen production, when the dye of the photocathode is associated to HER (Hydrogen Evolution Reaction) catalyst, allowing for direct storage of the Sun Energy into chemical bonds, and allowing thus carbon free hydrogen. Tandem photoelectrochemical cells for water splitting represent a paradigm in that purpose [10].

Fabricating efficient p-type DSSCs is a first step toward efficient tandem devices. In that goal, the present work focuses on the synthesis of new sensitizers for NiO based photocathodes and on a new method for NiO fabrication, ink-jet printing.

The first chapter is centered on the working principle of p-type DSSCs, and the issues inherent to this type of solar cell. The actual solutions that were found to increase their performance were reviewed.

The second chapter is dedicated to new push-pull organic dye synthesis and characterization (optical and electrochemical properties).

The third chapter ponders upon, NiO photocathode fabrication, through ink-jet printing. A state of the art, presenting the best NiO preparation method was firstly done. Ink-jet printing technique was described and finally, the NiO photoelectrode preparation with this method was presented.

This thesis finishes by the photovoltaic performance of the ink-jet printed films, with the various synthesized dye. The sensitization conditions are discussed, as well as the effect of a new NiO_x sub-layer over the solar cell performances.

1. O'Regan, B. & Grätzel, M. A low-cost, high-efficiency solar cell based on dye-sensitized colloidal TiO2 films. *Nature* **353,** 737–740 (1991).
2. Roncali, J., Leriche, P. & Blanchard, P. Molecular Materials for Organic Photovoltaics: Small is Beautiful. *Adv. Mater.* **26,** 3821–3838 (2014).
3. Li, X. *et al.* Improved performance and stability of perovskite solar cells by crystal crosslinking with alkylphosphonic acid ω-ammonium chlorides. *Nat. Chem.* **7,** 703–711 (2015).
4. Chuang, C.-H. M., Brown, P. R., Bulović, V. & Bawendi, M. G. Improved performance and stability in quantum dot solar cells through band alignment engineering. *Nat. Mater.* **13,** 796–801 (2014).
5. Kakiage, K. *et al.* Highly-efficient dye-sensitized solar cells with collaborative sensitization by silyl-anchor and carboxy-anchor dyes. *Chem Commun* **51,** 15894–15897 (2015).
6. Grätzel, M. The advent of mesoscopic injection solar cells. *Prog. Photovolt. Res. Appl.* **14,** 429–442 (2006).

7. He, J., Lindström, H., Hagfeldt, A. & Lindquist, S.-E. Dye-Sensitized Nanostructured p-Type Nickel Oxide Film as a Photocathode for a Solar Cell. *J. Phys. Chem. B* **103,** 8940–8943 (1999).
8. Nattestad, A. *et al.* Highly efficient photocathodes for dye-sensitized tandem solar cells. *Nat. Mater.* **9,** 31–35 (2010).
9. Odobel, F. *et al.* Recent advances and future directions to optimize the performances of p-type dye-sensitized solar cells. *Coord. Chem. Rev.* **256,** 2414–2423 (2012).
10. Li, F. *et al.* Organic Dye-Sensitized Tandem Photoelectrochemical Cell for Light Driven Total Water Splitting. *J. Am. Chem. Soc.* **137,** 9153–9159 (2015).

I. How to build the best p-type DSSC ?

I.A. General working principle of a p-type DSSC

I.A.1. Basics

For p-type DSSCs the photo-electrode is the cathode. With such a device, the dye's light absorption induces a photo-generated electron flux corresponding to a photo-reduction of the electrolyte redox-shuttle. Under irradiation, electrons flow from the photocathode/dye composite material, to the electrolyte. This is the reverse process as for n-type DSSCs.

Except some rare examples, a p-type semi-conductor is employed as the photocathode material and ensures, through hole conduction inside its VB, the desired electron flux toward the electrolyte. In the majority of the case, NiO has often been the p-type material employed and actually, despite several shortcomings, permitted to obtain the best results for p-type DSSCs [1]. Some research groups have been trying to replace NiO, essentially with delafossite material [2]. However, up to now, no real breakthrough was obtained (this aspect is tackled in Annexe 1). The most employed redox shuttle is still the I_3^-/I^- redox couple, like for n-type DSSCs. As described later in this thesis, research to replace this redox couple is of paramount importance in the field of p-type DSSCs and leads to some recent breakthroughs by the group of Udo Bach who used cobalt[3] and iron[1] based electrolytes (see Fig. 1). On the other hand, an important amount of research was dedicated to dye design for NiO based photo-cathodes. A selection of the today's most efficient dyes have been represented in Figure 2, even if the best one is by far PMI-6T-TPA, developed by Bauërle and Bach [4].

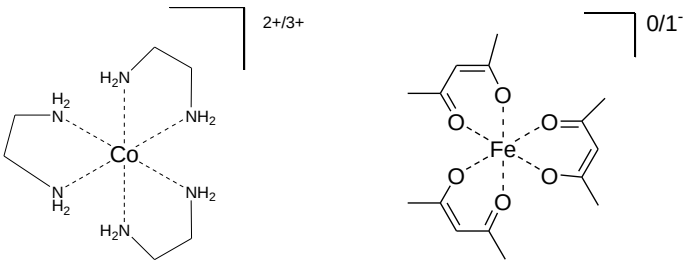
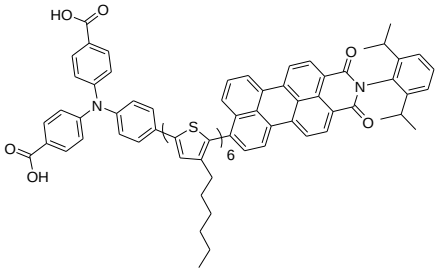


Fig. 1- The actual two best performing redox shuttle for p-type DSSCs, giving records V_{OC} values.

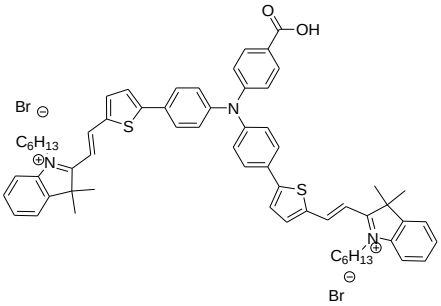
PMI-6T-TPA.

PCE = 2.5% (2015, Bach et al., Fe electrolyte).

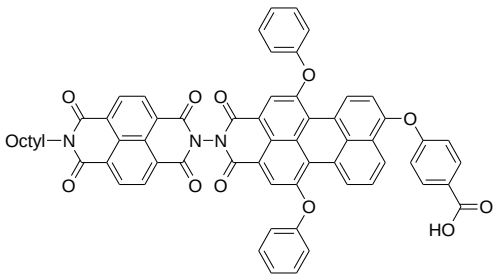
PCE = 0.61% (2012, Bach et al. Iodine based electrolyte)



CAD3, PCE = 0.25% (2015, Gibson et al. Iodine based electrolyte)



PMI-NDI, PCE = 0.20 % (2009, Odobel et al., Co based electrolyte)



QT-1

PCE = 0.33% (2015, Zhang et al., Iodine based electrolyte)

PCE = 0.50% (2015, Zhang et al, Co based electrolyte)

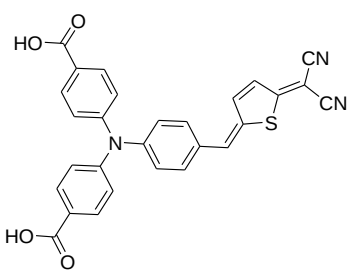


Fig. 2- A selection of today's best dyes employed for NiO sensitization alongside with their efficiency under 1 Sun irradiation (AM 1.5).

I.A.2. The successive steps for photocurrent generation

A simplified and summarizing working principle scheme of a NiO based p-type DSSC is depicted on Fig. 3. The first step is the dye excitation with sunlight, which comes from the cathode side **(1)**. Hole injection **(2)** is the second phenomenon to happen, rather than redox-shuttle reduction, a charged separated state is thus formed (**NiO$^{(+)}$-Dye$^{(-)}$**) [5]. The role of the redox shuttle is to oxidize the as-formed reduced dye, this is called the dye regeneration process **(3)**. The injected hole is transported to FTO, via the mesoporous network of the p-type semi-conducting oxide **(4)**. Finally, the external circuit permits to regenerate the redox shuttle at the counter electrode by electron transfer from the redox shuttle (which ensured charge transport by diffusion) to the counter electrode, which is generally made of platinum.

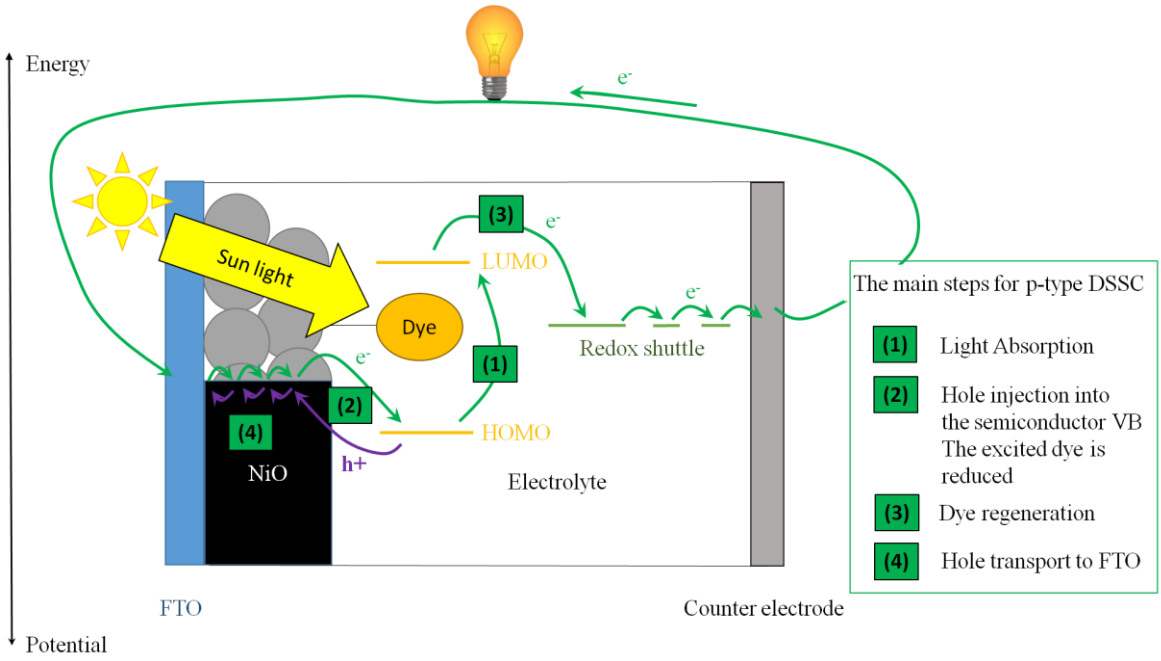


Fig. 3- Simplified working principle of a NiO based p-type DSSC

I.A.3. Typical J-V characteristics for p-type DSSCs

A typical J-V curve for p-type DSSCs is shown on Fig. 4. The important parameters for such a curve are indicated: short-circuit current (J_{SC}), open-circuit potential (V_{OC}) and Fill-Factor (FF). The PCE yield is the power generated at the maximum power point of the curve, divided by the light power input used to irradiate the solar cell ($P_{incident}$).

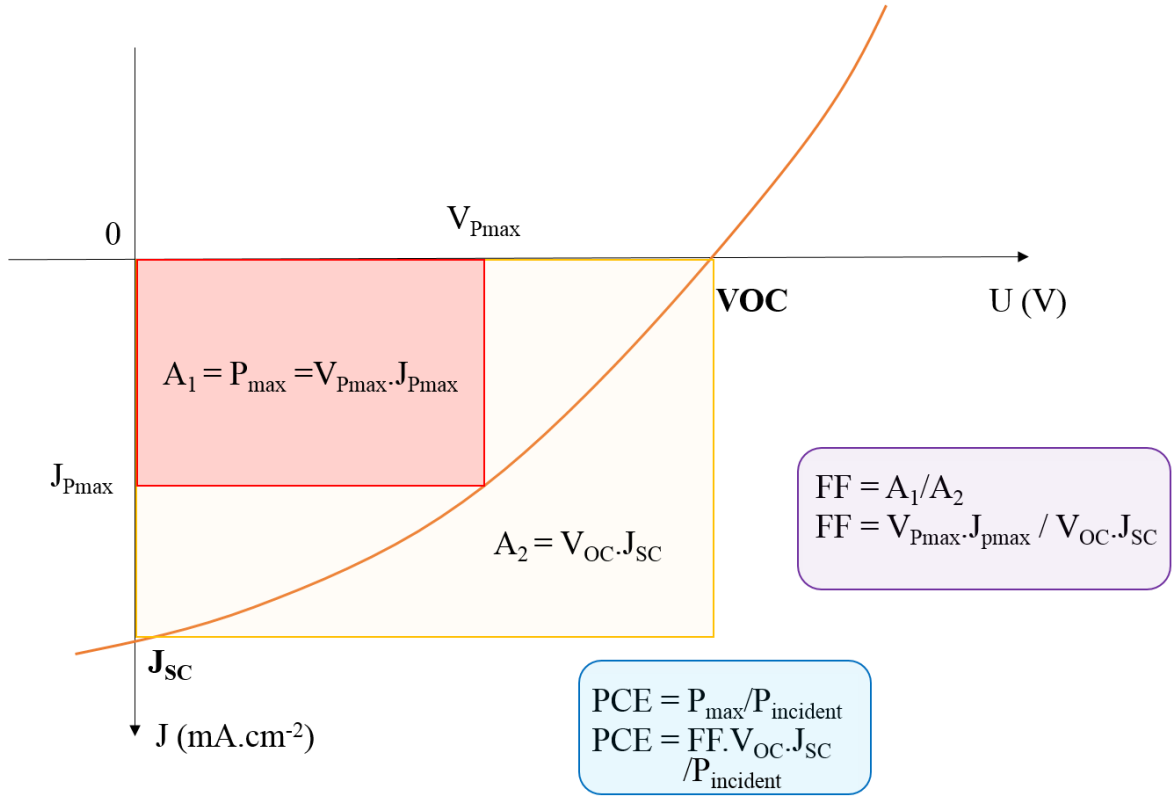


Fig. 4- Typical J-V characteristics for a p-type DSSC. P_{max} is the maximum power that can be generated by the solar cell under illumination and corresponds to A_1, the area of the red rectangle (defined by a voltage:V_{Pmax} and a current density: J_{Pmax}). A_2, the area of the orange rectangle, defines the theoretical maximum power that could be delivered if there were no loss.

For p-type DSSCs, the J_{SC} values now reach 8 mA.cm^{-2} for some few examples [6,7]. However, in general, the values for what are considered to be efficient photocathodes are between 2 and 5 mA.cm^{-2} [8,9]. V_{OC} values with iodine-based electrolyte are generally low and around 100 mV [10,11,12] with few examples displaying values around 120/150 mV [9,13,14,15,16] and one example displaying a high V_{OC} of 294 mV [17] (with PMI-6T-TPA as dye). As represented on Fig. 4, a low FF value (at best 40%) is the main issue for p-type DSSCs, as detailed further. This all turns that the performance of p-type DSSCs are still low and their PCE are far below the ones for n-type DSSCs.

I.A.4. Energetic requirements

In order to ensure the photovoltaic effect to happen, there are some energetic requirements to be satisfied for the components of a p-type DSSC. First of all: the dye's HOMO must be below the semi-conductor's valence band (VB) edge, in order to provide enough driving force for hole

injection. Secondly, the dye's LUMO must lie above the Nernstian redox potential of the redox couple implied in the regeneration reaction, in order to provide sufficient driving force for dye regeneration. The VB edge value used for NiO is generally + 0.53 V *vs* NHE (or - 5.13 eV *vs* vacuum, NHE was taken at -4. 6V with respect to the vacuum level [18]) and the redox potential of the couple implicated in dye regeneration for iodine based electrolyte, $\{I_3^-/I_2^{\bullet-}, I^-\}$ is -0.18 V *vs* NHE [19].

The question of the limit value for hole injection driving force is tackled later in this chapter (see I.B.3.c), but recent works anyway suggest that hole injection driving force should be substantial, if one wants the device to work properly at positive bias [20].

For dye regeneration driving force, one can think of the very efficient dye, CDA3 (see Fig. 2). This dye, with only a 170 mV driving force for dye regeneration [8], generated a J_{SC} of 8.21 $mA.cm^{-2}$. On the other hand the dye PMI-NDI, developed by the group of Fabrice Odobel, shows limited photocurrent values with iodine based electrolytes (1.76 $mA.cm^{-2}$) attributed to a weak regeneration driving force (~80 mV).

Importantly, another way to consider energetic issues in a p-type DSSC, as detailed on Fig. 5, is to take in consideration that the first step following dye excitation is the hole injection into NiO valence band [21]. Then, for hole injection driving force calculation, one should consider the excited dye reduction potential. This potential is "$E°(Dye^*/Dye^-)$" on Fig. 5 and is used to be calculated by adding to the ground state dye's reduction potential "$E°(Dye/Dye^-)$", the energy stored during dye excitation[22]:"$E_{0\text{-}0}$". This formula is in acquaintance with the fact that when excited a dye molecule is more easily reduced compared to ground state. Based on this, the driving force for hole injection (ΔG_{inj}) is then calculated as the difference of the dye's excited reduction potential and the semi-conductor VB edge. On the other hand, the driving force for dye regeneration (ΔG_{reg}) is the difference between the ground-state oxidation potential of the reduced form of the dye, that is the ground state reduction potential of the dye (see Fig. 5).

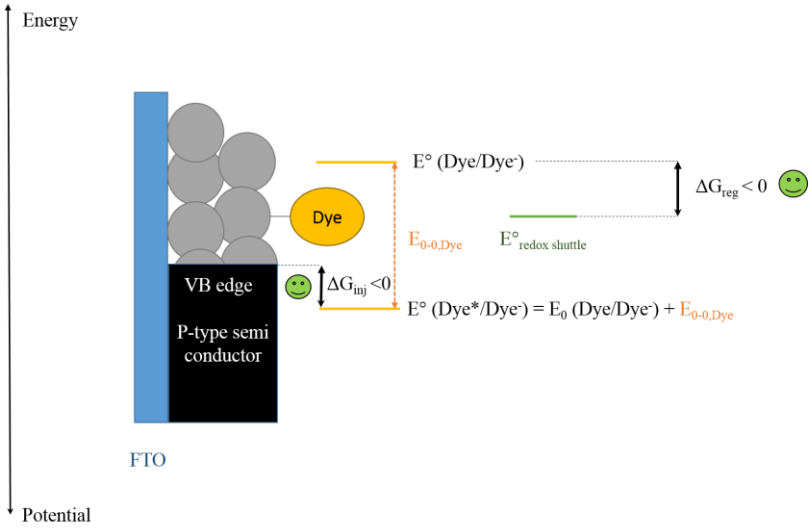


Fig. 5- Energetics of a p-type DSSC (simplified scheme).

I.A.5. The kinetic problems of p-type DSSCs

On paper, suitable energetic design should permit to have efficient devices, like for TiO_2 based DSSCs. However, one of the main issues for p-type DSSCs is the unfavourable recombination reactions. As one can see on Fig. 6, there are three reactions preventing electrons to flow in the desired way, which then represent three different recombination pathways.

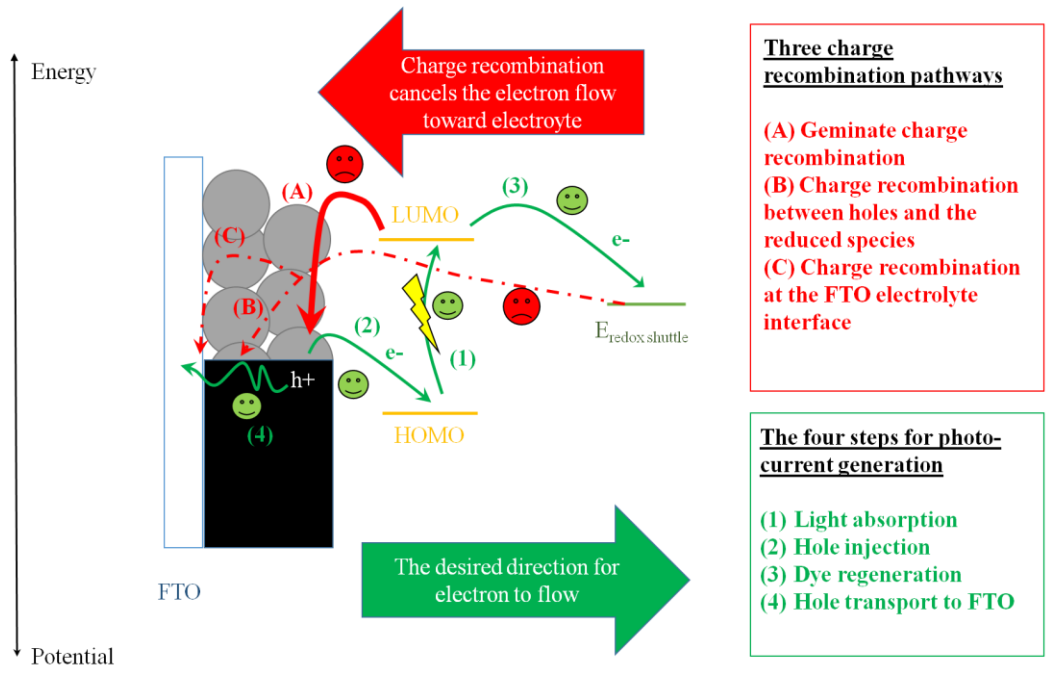


Fig. 6- The different charge recombination pathways for p-type DSSCs

The first one is called the geminate pathway, and represents recombination between the reduced dye and the injected holes in NiO. The second one relates to the recombination between injected holes in the NiO and the reducing species in the electrolyte. This recombination pathway can happen everywhere in the NiO film, especially for NiO thick film, it is possible that this recombination pathway prevents the hole to reach efficiently the FTO electrode (or I^- ions to get out of the NiO film, as the diffusion current of that species should also be taken into account). The third recombination path, maybe less described for p-type DSSCs, but recently pointed out to have dramatic influence on the cell performance when using an iron complex as a redox shuttle[1], is the recombination at the FTO/electrolyte interface. Fighting against those 3 recombination pathways is very important if one wants to increase the fill factor of these cells, as recombination arises at low bias for NiO based p-type DSSCs.

I.A.6. V_{OC} engeenering

An important issue for p-type DSSCs is the maximum photo-voltage that can be generated by the solar cell, in test conditions (generally, 1 Sun irradiation, with the AM 1.5 standard). This maximum photo-voltage is generated when the current is equal to zero on the J-V curve, i.e. in open-circuit conditions. This voltage is the V_{OC}. As said above, V_{OC} of p-type DSSCs are still low despite recent breakthroughs.

In order to better understand V_{OC}, a "thought" experiment corresponding to V_{OC} generation is depicted in Fig. 7. For sake of simplicity, a p-type DSSC for which the counter electrode is connected to mass reference electrode was considered. This allows considering the Fermi level of the counter electrode and the electrolyte as fixed. In order to signify the open-circuit condition, an open switch was placed between the two electrodes.

Prior to irradiation, the Fermi-level of the electrolyte and the one of the photo-cathode are aligned (since the equilibrium is supposed to be reached), the hypothesis of band bending inside the particle [23] was not taken into account on this scheme. After light irradiation, hole injection occurs into NiO. This is why the Fermi level in NiO goes down in energy, close to the VB edge. This creates a positive photo-voltage. However, this situation corresponds to an "ideal" situation. In

fact, some of the holes injected into NiO recombine (see I.A.5 for the different types of recombination). Then, as the hole concentration in NiO is reduced, the NiO Fermi level "goes up" in energy, the "ideal" photo-voltage is reduced.

As shown on Fig. 7, when iodine electrolyte is employed with NiO, the ideal V_{OC} is low, due to the small energy difference between NiO VB edge and the Fermi level of the iodine electrolyte (approximately 200 mV). So, to increase $V_{OC,}$ one can first consider to decrease NiO VB edge. This strategy has been adopted by doping NiO with other transition metals and permitted to slightly increase V_{OC} (by less than 60 mV) [24,25,23]. Another strategy is to employ redox couples with a redox potential more negative than for I_3^-/I^-, which results in moving up-ward the Fermi level of the electrolyte. Based on these ideas, Udo Bach and Leone Spiccia actually implemented two new efficient redox shuttles, with dramatically more negative redox potentials than iodine electrolytes. The first one, $[Co^{II/III}(en^a)_3]$ (see Fig. 1), E_{Fermi} = -0.05 V *vs* NHE, in ACN) permitted to reach V_{OC} values as high as 709 mV [3] and the second one, $[Fe^{II/III}(acac)_3]$ (see Fig. 1, E_{Fermi} = -0.2 V *vs* NHE, in ACN) permitted to reach V_{OC} = 645 mV.

The second strategy to increase V_{OC} is to fight against charge recombination, in order to keep the Fermi level under open circuit conditions as close as possible to the VB edge of NiO and to permit that V_{OC} is close to its "ideal" value, as described in Fig. 7. An important example on this topic is the cobalt$^{II/III}$ electrolyte employed by Gibson et al.[26]. Any phenomenon that can slow down charge recombination may actually increase V_{OC}.

[a] en = ethylene diamine

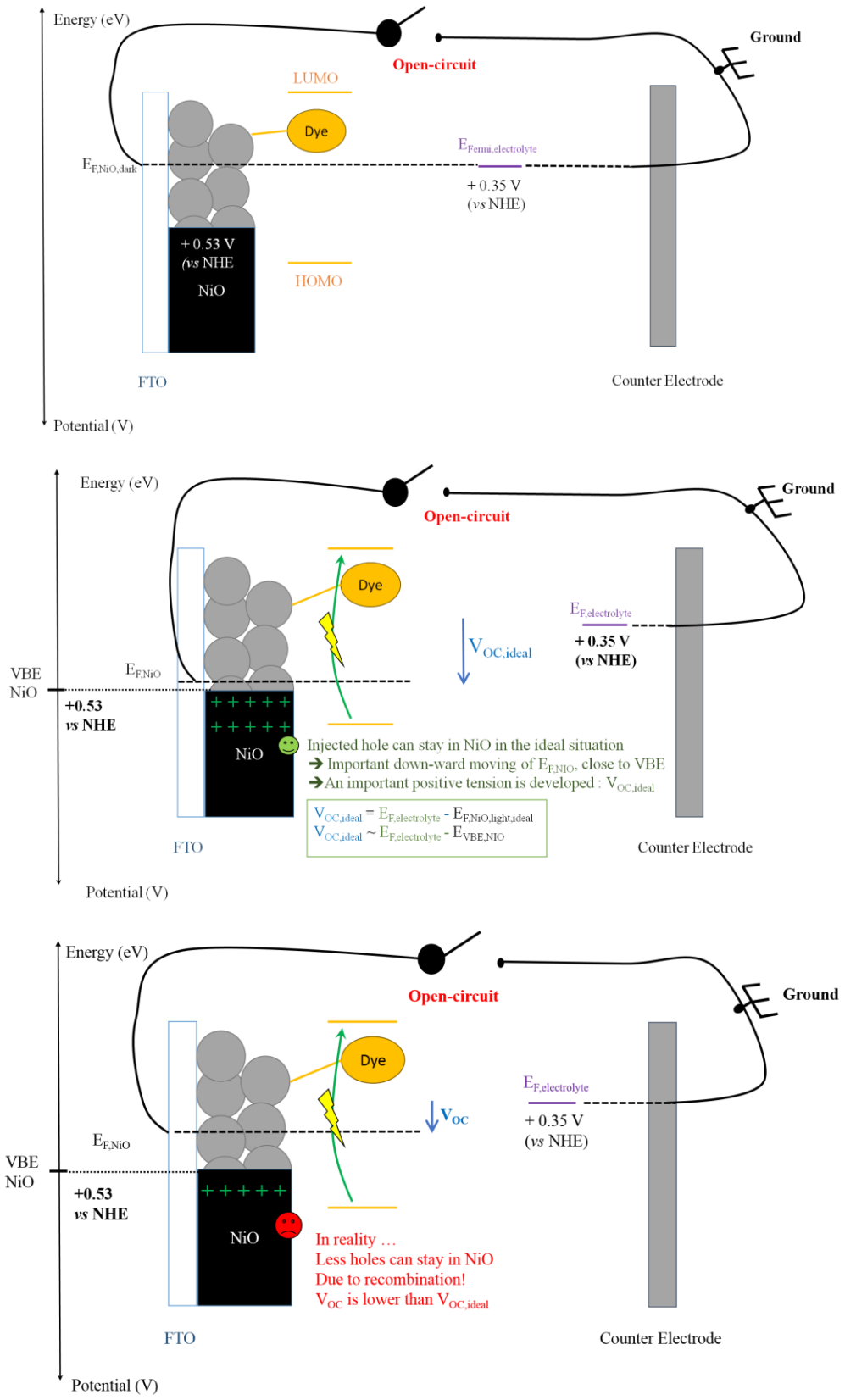


Fig. 7- "Thought" experiment for the generation of a photovoltage under illumination for p-type DSSCs. The situation in the dark is taken as a starting point (top). An ideal situation, under illumination is depicted in the middle. The real situation is depicted at the bottom. The electrolyte considered here is the "classical" iodine electrolyte: 0,1M I_2 / 1M LiI in acetonitrile.

I.B. How to build the best p-type DSSCs with NiO?

I.B.1. Introduction

Thanks to an increasing number of publications dealing with p-type DSSCs, it is possible to draw a cartography on how to improve each step, in the working principle of a NiO based p-type DSSC. This chapter is divided into sections, which actually describe how each of these steps was improved up to now.

I.B.2. Increasing the light harvesting properties of the film

I.B.2.a. Introduction, the dye/NiO light absorption competition

Increasing the light harvesting properties of the {NiO / dye} film can be summarized by improving the following aspects:

➔ Dye molar extinction coefficient

➔ Dye absorption spectral window width

➔ Dye loading at the NiO surface

➔ The specific surface area of NiO per volume unit of film and its accessibility by the dye molecule, during the sensitization step (suitable pore size)

➔ The thickness of the NiO film

However, one also has to take into account an issue for NiO use as a photocathode material: its important self-absorption. For instance a 1µm-thick, undyed NiO film, as described by the group of Bach, already absorbs 30% to 40% of the incident light [4]. That means that a 4µm-thick bare NiO film would absorb 85% of light. This issue is a major one and makes the use of thick NiO films simply impossible, contrary to TiO_2, which is more transparent. The NiO self-absorption is not known to allow high photocurrent generation, as naked NiO mesoporous electrode have very poor performance [27]. This is why NiO self-absorption is detrimental for device performance. In order to reduce this effect, one can consider the following possibilities:

➔Increasing the porosity of the film (meaning that less NiO is present in a given film volume)

➔Decreasing the number of defects of the NiO material (as NiO parasitic absorption comes from the presence of defects in the material, as said below)

➔Decreasing the NiO thickness

So as to give a clear picture of the competition between dye light absorption and NiO light absorption, one can resort to the ratio between dye absorbance and NiO absorbance, as described by the group of Bach [28] (eq. 1). This absorption ratio should be maximal for better light harvesting properties of the photocathode. Another aspect that should also be mentioned is the parasitic absorption of the electrolyte employed, since for instance the classical iodine based electrolyte absorbs at low wavelengths a substantial amount of light [27].

$$\textbf{Absorbance ratio (Dye:NiO)}\ (\lambda) = A_{dye}(\lambda) / A_{NiO(}\lambda)$$

(eq. 1)

I.B.2.b. NiO engineering for enhanced light harvesting properties of the film

I.B.2.b.i. NiO parasitic light absorption

NiO is a wide band-gap p-type semi-conductor (3.4 to 4.6 eV [29]), which should then provide good transparency in the visible region and be very suitable for p-type DSSC application. Then, where does the self-absorption of NiO come from?

In order to understand the reasons for NiO coloration, one should think of the origin of the p-type conductivity of this material. For NiO, p-type conductivity comes from the fact that it is a non-stoichiometric material, with oxygen excess [30]. To compensate for the oxygen richness, defect species as Ni^{3+} species (which could be Ni_2O_3 or NiOOH [31]), or even Ni^{4+} species [32] exist in NiO material. In a way, hydrogen atom may also compensate the oxygen excess, through the creation of species such as $Ni^{II}(OH)_2$. One can understand that the creation of Ni^{3+} species correspond to the creation of holes in the VB of NiO and then corresponds to a doping process. This actually stands for an explanation for NiO p-type conductivity. However, if the p-type conductivity is ensured by the defect species, Boschloo and Hagfeldt stated that Ni^{3+} species have a strong black coloration compared to Ni^{2+}, due to enhanced d-d transitions (Ni^{2+} has the d^8 configuration). This mechanism for NiO self-absorption is the one most often presented [33] and actually meets well with the electrochromic behavior of NiO, which is described below. Interestingly, one should notice that another self-absorption mechanism, coming from the possible presence of Ni metal defects in the film has also been accurately reported [34].

As a matter of fact, depending on the potential that is applied to NiO, its color is different: as said above, NiO is an electrochromic material. When its Fermi level lies far in NiO band-gap, there is almost no hole in the VB, this is the bleaching situation. When the Fermi level is pushed toward more positive potentials the number of holes increases and the coloration of NiO as well. The holes that are present display brown coloration first and then black coloration. As suggested by Hagfeldt and Boschloo, two different absorbing species may be formed when increasing the Fermi level to positive potentials. The first one is supposed to be Ni^{3+} species. The second one seems to be less understood, though a recent study by Dini and coworkers speaks for the presence of Ni^{4+} species [32]. For both species, the absorption peaks ranges between 350 nm and 550 nm and also extends to the NIR region (see Fig. 8 for the overall feature of NiO absorbance). At rest, that is, when not in contact with electrolyte, nor biased, the Fermi level of NiO is close to its VB edge and then NiO displays a substantial coloration.

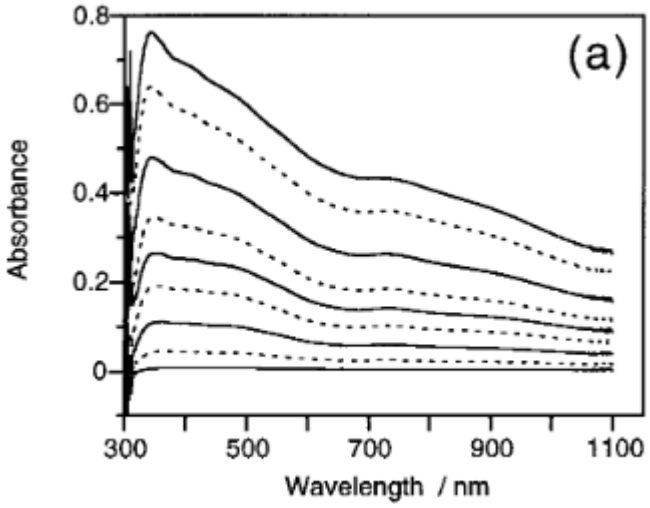


Fig. 8- Taken from the ref. by Hagfeldt and Boschloo. Potential-dependent optical spectra of nanostructure NiO, in presence of an aqueous electrolyte, from 0.310 to 1.110 V *vs* NHE, by step of 0.10 V. The bleach state at 0.01V *vs* NHE has been subtracted. The spectral features were described to be independent of the NiO environment. 0 (electrolyte etc.). The value of + 0.210 was used for converting the value *vs* {AgAgCl, 3M} to NHE reference.

This electrochromic behaviour, induces competition between NiO and dye absorption and is then a limit for NiO use at positive bias, as pointed out and proven by the group of Bach, who estimated the efficiency loss to be about 5% for a device with a $Co^{II/III}(en)_3$ based electrolyte [20].

I.B.2.b.ii. Engineering NiO for more efficient light harvesting properties

There are actually a few examples dedicated to enhancing NiO optical properties. The important point, as said above, is to increase the dye/NiO absorbance ratio. Bach et al. increased the NiO crystallinity of the NiO nanoparticles (see chapter 3 for more details) without decreasing dye up-take, and a better NiO transparency was invoked [17]. The same group also reported an original NiO microball morphology. The films made out of these microballs presented an increased Dye/NiO absorption ratio and this permitted to reach high J_{SC} value (*i.e.* 7 $mA.cm^{-2}$, for a 6 µm substrate). The increase was attributed to a better crystallinity of NiO or a more important specific surface. The group of Li also suggested that the morphology of NiO could induce a more important dye loading in some cases [16] (see chapter 3 for more details). Another point, also exemplified by the group of Bach showed that a more crystalline NiO material also induced more light diffusion inside the NiO film and then increased the light pathway, and this was reported to be beneficial for the solar cell performance [17].

I.B.2.c. Dye engineering for enhancing the light harvesting properties of the NiO film

I.B.2.c.i. The tool-box for light transitions

This paragraph is the occasion to detail two types of light absorption transitions that have been exploited for dye design for p-type DSSCs up to now. We chose to separate these transitions considering the electron movement following light absorption, once the dye is grafted onto the NiO surface. Electron movement at the NiO surface may be important to understand in p-type DSSCs in order to better understand recombination / hole injection kinetics.

The first type of transition can be called a “localized transition”, light absorption does not induce particular electron movement regarding the NiO surface (we include MLCT transitions for Ru-based dyes for instance, here). The second one is the push-pull transition, it is a specific transition, which corresponds the mixing of the orbitals of different chromophores in the molecule, a donor and an acceptor. It gives rise to a new transition and then an electron movement from the donor-part to the acceptor part following light absorption (details are given in Annex. 3).

I.B.2.c.i.(i) "Localized" transition

Some chromophores, corresponding to a "localized" light absorption transition have been known by the chemists for a long time and have thus been employed as sensitizers for p-type DSSCs. Among them, one can refer to two categories: the purely organic dyes, and the metal-organic dyes. The first one being preferable in order to avoid resorting to expensive and sometimes scarce metals. Among purely organic dyes, one can consider the following: coumarin[35], squaraine [36,37], perylene monoimide derivatives [4,14,15], perylene di-imide [38], sexithiophen [4], diketopyrrolopyrole [13], cyanine derivatives [35], « fast-green » dye [35] or bodipy [39]. For the metal-organic counterpart, one can refer to the use of: zinc porphyrins [40,41], metaloporphycenes [42] and finally ruthenium dyes [11,43,44,45,46].

I.B.2.c.i.(ii) Push-pull transition

Another way to generate light transition for conjugated molecules is to resort to "push-pull" type transitions. This type of light transition is different compared to the one described above since it induces a direct spatial movement of electrons from a donor (electron-rich) to an acceptor (electron poor) site, upon absorption. It requires an at least non-zero degree of mixing between the two Pi-conjugated entities so as to permit the movement of electrons from one entity to another. For NiO based photocathodes, up to now, the vast majority of push-pull dyes that were used are triphenyl-amine based, for the electron donor group. Several different acceptors have been employed in association with the triphenylamine donor group: malonitrile groups (and the famous P1) [10, 7,13,47,48], tricyano group [10], bodipy [6], indolium [6,8], (N,N)diethyl-thiobarbituric acid [10, 49,47] , DCANQ [50], TCF [50], PMI [9], iso-indigo[51], and Ru derivatives [12].

I.B.2.c.ii. Mixing the transitions

Some dyes light absorption is only based on "localized" transitions, by the use of distinct chromophores (such as PMI-NDI, see on Fig. 9), other display a major transition which is a push-pull transition (like P1, see Fig. 9). Finally, other dyes mix the push-pull and the "localized" transitions, like for instance the Ru dyes of Wu et al. [11] (dye O18 was exemplified on Fig. 9). The working mechanism of a dye depends on the degree of coupling between the different parts of the

dye. For light absorption (especially the push-pull transitions), the working mechanism can be clarified by simulating the absorption spectrum of the dye with TD-DFT calculation.

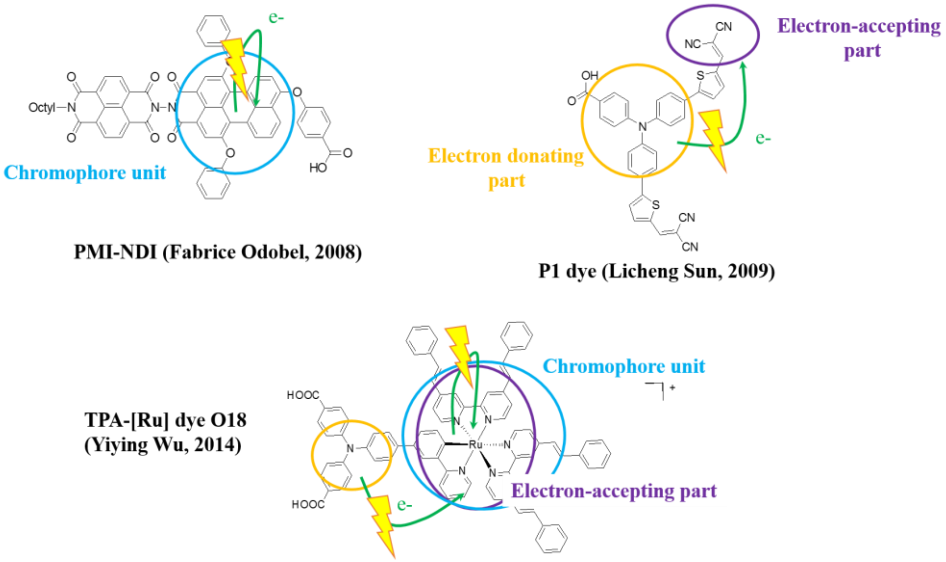


Fig. 9- An example of "localized" transition dye: PMI-NDI, an example of a push-pull type dye (the first one to be used for p-type DSSCs: P1) and an example of a dye combining both types of transitions

I.B.2.c.iii. Enhancing dye light absorption

I.B.2.c.iii.(i) Resorting to highly absorbing dyes

A recent example of dye engineering, for enhanced optical properties of the NiO film, has been shown by Gibson et al [6]. They presented a series of dyes belonging to the same family (the "push-pull, double acceptor" family, see above) with increasing molar absorption coefficient (see Tab. 1). The increase in the dye molar exctinction coefficient was directly linked to the generation of high J_{SC}, stressing the importance of strongly absorbing dyes for highly efficient devices.

Tab. 1- The dyes series described by Gibson et coll [5], increasing molar extinction coefficient for a dye family so as to increase J_{SC}.

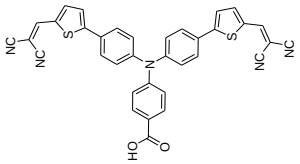
Dye	**$\varepsilon_{\lambda max}$ ($mol^{-1}.L.cm^{-1}$)**	**J_{SC} ($mA.cm^{-2}$)**
P1	57 900	5.37
GS1	65 700	5.87
CAD3	94 580	8.21

What is then the best strategy to enhance the dye molar extinction coefficient ? If one considers using localized transition dyes, the strategy resides in employing strongly absorbing entities. This

strategy was succesfull for squaraine dyes for instance, synthesized by the taiwanese Lin et al.[37], and successfully implemented into efficient p-type DSSC.

If one considers push-pull type dyes, one can first of all say that the push-pull transitions are generally allowed ones and then exhibit high molar extinction coefficients [5]. However, for push-pull dyes in p-type DSSCs, structure-property relationship for dye's molar extinction coefficients are scarcely established. However, a possibility that showed very efficient is the "double acceptor strategy" so as to increase dye molar extinction coefficient. It is for instance striking to remark that the double acceptor dye CAD3 dye absorbs 4 times more light than CAD1, its monosubsituted version and reaches an impressive value close to 100 000 $mol^{-1}.cm^{-1}.L$ for ε (see Fig. 10). On Fig. 9, P1 dye [52] (sometimes called "dye S" [47]) and its monoacceptor analogous, "dye 4" were also represented and for the sake of comparison, the described performance were all taken from the same reference (ref [47]). The performance of the double acceptor dye P1 are again better than the one of the mono acceptor compound, owing to an almost doubled molar extinction coefficient. If the double acceptor strategy permits to enhance dye light absorption, one can also mention than there exists mono acceptor compounds that are also strongly absorbing, as examplified by Yen et al. and their "dye 6" [47]. The performance of these dyes in p-type DSSC are good too (see Fig. 9).

Fig. 10- The double acceptor strategy and the mono-acceptor strategy for push-pull dye design. The NiO used for CAD dyes is different from the one for the other dyes, which explains the performance difference between the dyes and the different dye loadings.



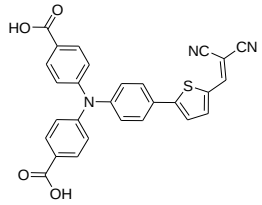
Dye S » or P1

$\varepsilon_{\lambda max}$ = 67 500 $mol^{-1}L.cm^{-1}$.

PCE = 0.101%

J_{SC} = 2.31 $mA.cm^{-2}$

Dye loading = 129 $nmol.cm^{-2}$

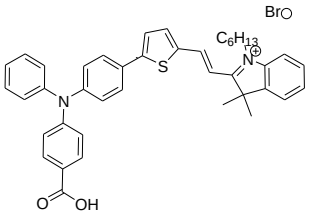


« Dye 4 » $\varepsilon_{\lambda max}$ = 34 500 $mol^{-1}L.cm^{-1}$

PCE = 0.093%

J_{SC} = 2.25 $mA.cm^{-2}$

Dye loading = 130 $nmol.cm^{-2}$



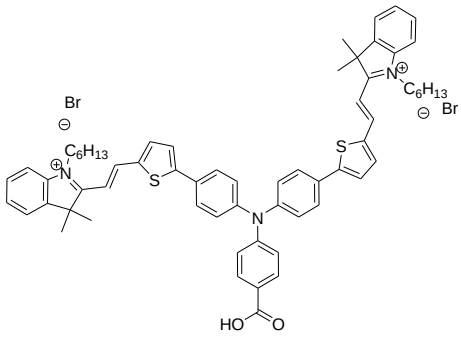
« CAD1 »

$\varepsilon_{\lambda max}$ = 22 900 $mol^{-1}L.cm^{-1}$

PCE = 0.09%

J_{SC} = 3.32 $mA.cm^{-2}$

Dye loading = 6.7µmol.cm^{-2}



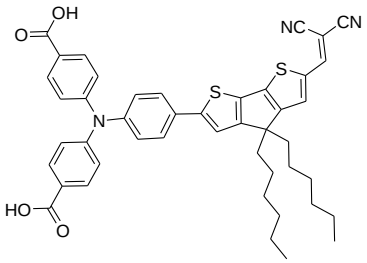
« CAD3 »

$\varepsilon_{\lambda max}$ = 94 580 $mol^{-1}L.cm^{-1}$

PCE = 0.25%

J_{SC} = 8.21 $mA.cm^{-2}$

Dye loading = 7.36 µmol.cm^{-2}



« dye 6 »

$\varepsilon_{\lambda max}$ = 67 600 $mol^{-1}L.cm^{-1}$

PCE = 0.087%

J_{SC} = 2.05 $mA.cm^{-2}$

Dye loading = 108 $nmol.cm^{-2}$

I.B.2.c.iii.(ii) Resorting to dyes with wide absoprtion window

Some compounds naturally possess a large absorption window, such as Ru derivatives (these compounds bear the advantage of possessing several transitions). For instance, the "simple" Ru derivative so called "O12" and developed by the group of Wu, possess an absorption window between 300 nm and about 580 nm, with a reasonable molar extinction coefficient value around 15000 $mol^{-1}L.cm^{-1}$ [45], quite constant over this range,. The same group interestingly enhanced their Ru based compound light harvesting properties by using modified ligands, which lead to the formation a "panchromatic dye" O18 (see Fig. 9) [11]. The absorption window of this dye was comprised between 650 nm and 350 nm, with a constant ε value around 30 000 $mol^{-1}.L.cm^{-1}$). Another example illustrating how to increase the width of the spectral absorption could be the example of the two bodipy dyes employed by Gibson et al. The first bodipy dye exhibits a narrow spectral absorption window, due to the conjugation break between the bodipy entity and the triphenylamine group [39]. When permitting the conjugation between the two entities, the spectral width was increased as in dye GS1[6].

So as to even more increase the amount of light absorbed per molecule, and to cover a wide range of absorption wavelengths, combination of such chromophores can be employed, in a so called « multichromophoric » approach, such as the one described by Odobel et al. with squaraine-perylene monoimide (perylene mono-imide, PMI) derivatives [36]. In this case, the shape of the absorption spectrum is very close to the sum of each chromophore. Due to the increase in the absorption window, the dye is quite efficient (J_{SC} = 2.73 $mA.cm^{-2}$), though there is a competition between internal de-excitation and hole injection with NiO, possibly because the squaraine and the PMI units are not totally decoupled. Interestingly, the energy transfer phenomenon from the high energy chromophore unit (PMI) to the low energy chromophore unit (squaraine) was not observed.

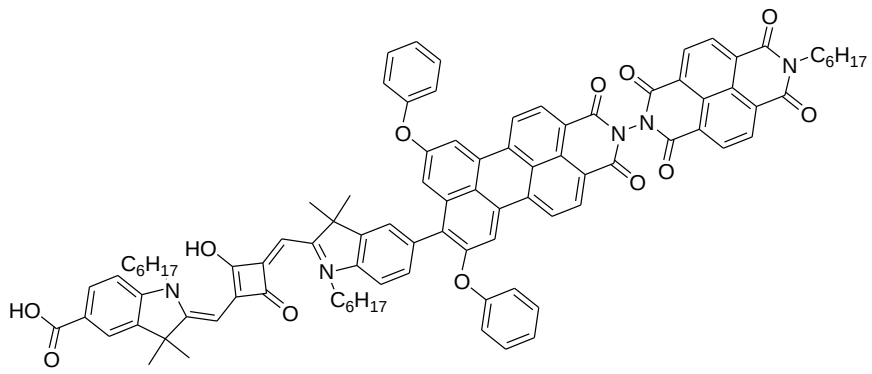


Fig. 11- SQ-PMI-NDI dye

The famous triphenylamine-sexithiophen-perylenemonoimide (PMI-6T-TPA), synthesized by the group of Peter Bauërle [4] is a two distinct chromophore dye. Though this dye is often presented as a "push-pull" sensitizer, it looks more as double chromophore, "dyad", for which the first chromophore is the (triphenylamine)-sexythiophen group and the perylene-monoimide plays the double role of second chromophore and secondary electron acceptor, judging by its HOMO/LUMO orbitals that are decoupled [4]. This molecule is a strong absorber over a wide region of the spectrum (from 300 to 550 nm), due to the association of the two strongly absorbing entities: sexithiophen (ε =50 000 mol-1.L.cm-1 at about 475 nm [53]) and PMI (ε = 45 000 mol-1.L.cm-1 at about 550 nm [53]). However, the exact "working principle" of PMI-6T-TPA, like for PMI-SQ-NDI dye is actually not published. Eventually, an interesting example which permitted to extend the window absorbed with one photo-electrode has been sensitize NiO with two complementary dyes in terms of absorption, by Chang et al [37]. Unfortunately, this strategy did not bring real improvements.

I.B.2.c.iv. Increasing the number of dyes grafted at the NiO surface

A possible strategy to graft more dyes at the surface of NiO can be to place two anchoring groups on the sensitizer. This strategy was actually adopted by Lin et al., with a study of the squaraine dyes, p-SQ1 and p-SQ2 [37]. The dye p-SQ2 possessed two anchoring carboxylic acid groups and its dye loading was actually multiplied by two compared to p-SQ1 which only possessed one carboxylic acid anchoring group. However, the "two anchoring group strategy for better dye loading" is actually not always valid, as for the two dyes "3" and "5" synthesized by the same

group [47], the two anchoring groups induced a less important dye loading. However, in both cases, it was noted that the compounds with two anchoring groups performed better once implemented into the p-type DSSC.

Similarly, in the same paper, the double acceptor dye P1 (or "dye S"), with only one anchoring group, was compared to its mono-acceptor, two anchoring group, version, so called "dye 4". Actually, similar levels of dye grafting were obtained for both dyes (see Fig. 10).

As a conclusion, one can say that when it is possible to have two anchoring groups on the molecule, this strategy permits to obtain better performances, but not necessarily a better dye loading (then the better performance may come from a better hole injection process). On the other hand, for the dyes for which only one anchoring group is possible, like for the triphenylamine double acceptor dyes, good performance in p-type DSSCs are obtained too, certainly owing to an increased molar extinction coefficient.

For dye loading, another important point seems to be the overall size of the dye. As shown by a recent paper by Wu et al. when the size of the dye is too important, like for their double PMI-6T-TPA dye, dye loading is reduced, due to steric issues for dye grafting at the NiO surface [15].

Interestingly also, in order to increase dye loading at the NiO surface, it seems that the strategy to employ flat and small dyes is an interesting option. This is suggested by the recent work of Zhou et al., who employed QT1 as a very flat, very small and very efficient dye [7].

One can finally add that it should be possible to play trigger the dye loading by palying with the time and the solvent during the sensitization step, as suggested by the very recent work by Zhu et al. [49,b]. However, drawing general conclusions about the dye loading is not easy since the thickness of NiO is not always mentioned in the papers and only the geometric dye concentration (obtained by the help of dye desorption experiment) is mentioned . The amount of dye per volume unit of NiO film should be more suitable for comparison between publications. Also, if a high dye loading is important so as to increase the optical properties of the photo-electrode, one should

[b] Besides, this aspect seems to be a key point in a parallel field of research, when co-grafting species at the NiO surface is required in photocatalytic devices [54].

mention that dye aggregation, has to be avoided and is sometimes presented to be detrimental for the photocathode efficiency [13].

I.B.2.d. Reducing the electrolyte absorbance

It is known that the currently most used electrolytes, with iodine, highly absorb light between 350 and 450 nm and then can compete at short wavelengths with dye light absorption (a spectrum is displayed in the SI of ref [4]). Even if the NiO films employed up to now have been quite thin (1 to 2 µm), this effect must be taken into account if one considers the tandem DSSCs application. In this case, for one photo-electrode, light has to cross at least 25µm of electrolyte. Here dye design is important if one wants to consider this issue. Changing the electrolyte, to a more transparent one is another, more simple option, as shown by Powar et al.[3], when comparing iodine based electrolyte and the famous $[Co^{2+/3+}(en)_3]$ based electrolyte, which absorbance is dramatically reduced.

I.B.3. **Efficiently inject holes into NiO VB**

I.B.3.a. Position of the NiO VB edge

For hole injection from the dye to NiO, the position of NiO VB edge is of paramount importance. Actually, the VB edge position of NiO has been estimated by spectro-electrochemistry, in absence of redox species in the electrolyte. Such studies rely on the optical signature of the holes in NiO VB. When the Fermi level gets close enough to the NiO VB edge, hole absorption is detected and this permits to determine NiO VB edge. In presence of an aqueous electrolyte at pH 6.8, NiO VB was estimated to be ca. 0.2 *vs* {Ag/AgCl/3M in KCl}, that is 0.410 *vs* NHE [55]. Similar studies were performed in the most used organic solvent: acetonitrile [26,19]. Also, the studies were performed in presence of a $LiClO_4$ salt, probably to take into account the possible VB edge positive shift induced by Li^+ cations [26], which are almost always present in p-type DSSCs' electrolyte [c]. In this latter case, the VB edge was found to be at -0.12 V *vs* Fc^+/Fc, i.e.

[c] This effect of the Li^+ cations to shift the NiO VB was proven to occur, in a recent publication by the group of Hammarström et al.[24]. Besides, another possible effect going in this direction could be the one of the additives employed in the iodine based electrolyte by the group of Udo Bach [4] (use of *tert*-butyl pyridine and guanidinium thiocyanate). For the famous $[Co^{2+/3+}(en)_3]$ electrolyte, the large amount of ethylene diamine present in the electrolyte is also thought to play a role of NiO band shifting to positive potentials, due to the acidity of the protons it bears [3].

approximately 0.53 V *vs* NHE [d,e]. The group of Bach also reported the value of 0.7 V *vs* NHE for NiO ionization potential [56]. The value of 0.53 V *vs* NHE for NiO VB edge is the value used through all this PhD thesis, because it is the most used value in literature.

I.B.3.b. An ultra-rapid and efficient hole injection

As exemplified in early works on phosphorus porphyrins by Odobel et al.[57], and confirmed by an important number of publications by the groups of Wu [45,11,58] Hammarström[59,14,60] Dietzek [61] and Sun [10], hole injection into NiO VB is the next step after dye excitation, is extremely rapid and then can efficiently compete with the dye return to the ground state. For this reason, hole injection is generally presented as being "not an issue" for p-type DSSCs.

In a primary approach it is interesting to remark that it seems that hole injection driving force does not need to be too important to permit an efficient hole injection process. As an example, one can consider the ruthenium dyes developed by the Wu group [45], for which the excited state reduction potential lies very close to the NiO VBE (hole injection driving force close to zero). Despite that, extremely rapid hole injection was noticed with these compounds. For the other dyes, for which transient absorption studies permitted to conclude that hole injection was efficient, the values for hole injection driving force vary. Values around 300 eV were reported for the simple squaraine dye ("SQ") developed by Odobel [36]. For push-pull triphenylamine based dyes, hole injection driving force values are generally higher and above 600 mV, due to the interaction between the acceptor and the triphenylamine dye. These interactions slightly depopulate the triphenylamine, which is then harder to oxidize. Finally, for perylene-imide dyes, values around 700 to 800 mV can be calculated [14].

An exception is the multi-chromophoric dye implemented by Odobel et al. in 2013. Indeed, the working principle of this dye is very different than for other dyes. In this case, hole injection was found to compete with hole/electron recombination internal to the dye [36]. Recently also,

[d] See chapter 2 for the potential values conversion.

[e] Interestingly, another photo-electrochemical study, by the group of Bach suggests a VB edge at about 0.25 vs the "electrolyte" potential. The electrolyte is composed of cobalt species in ACN, with Li^+ cations in the form of LiTFSI. The Fermi level of this electrolyte has been estimated to be at -0.025 V *vs* NHE. This turns out the VB edge at about 0.25/0.30 V *vs* NHE, which is different from the value found by Gibson et all. in ref [19]. However, here, the electrolyte contains redox species and also the "additives" are different, then the values are not really comparable.

Bräutigam et al. showed that for a Ru dye, it was important to have withdrawing groups on the ligand for efficient hole injection[61]. Another exception is the bodipy dye described by Gibson et al.[39], for which hole injection was not efficient and as the injection rate was estimated to be around 50%. This was certainly due to the decoupling of the absorbing bodipy entity with NiO, due to the conjugation break and the too important tunneling distance between the light absorption center and NiO.

On this point one should remark that a tunneling mechanism for hole injection between the dye HOMO and NiO is a possible efficient mechanism. The very efficient dye PMI-6T-TPA[4] and the efficient SQ1[37] also appear to function with a tunneling mechanism for hole injection, judging by the shape of their simulated HOMO orbitals. On this aspect, it is obvious that "Non-tunneling" mechanisms also permit extremely rapid hole injection, like for the push-pull dye P3 [10]. The Ru based dye by the group of Wu, O_{12}, is one of the dyes for which hole injection occurs by tunneling. This dye displayed an extremely rapid hole injection constant, faster than 180 fs [f].

I.B.3.c. Is hole injection really so un-problematic ?

Recent studies with the dye PMI-6T-TPA, which has relatively small hole injection driving force (400mV) and for which tunneling is the mechanism for hole transfer from the dye to NiO, showed that hole injection could actually be a real issue for the actual best performing dye. Transient absorption studies were performed on NiO films dyed with PMI-6T-TPA, with the nanosecond time scale for a limit. Contrary to previous studies, the key point was that this time, the potential of the studied sensitized electrodes was also varied during the transient absorption studies.

[f] Which was the resolution of the apparatus (femtosecond transient absorption apparatus).

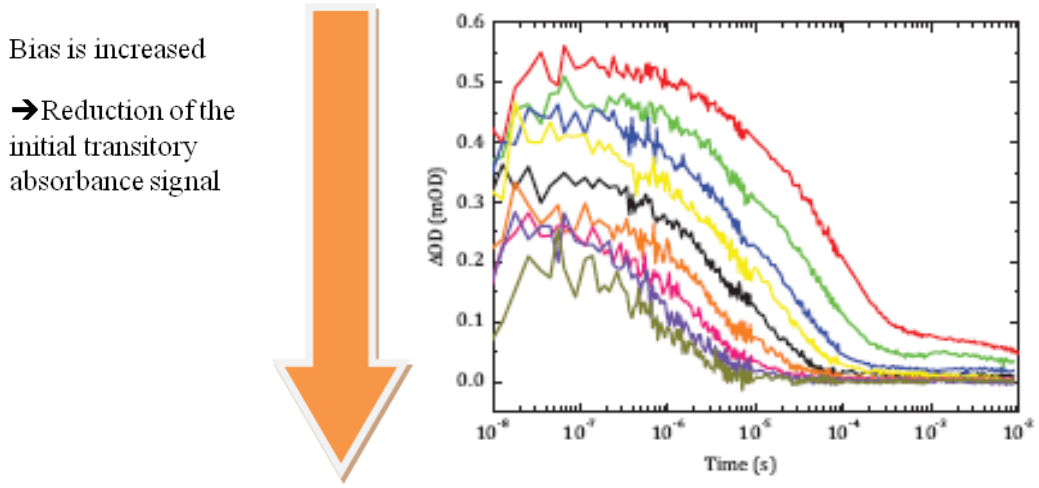


Fig. 12- Reproduced from the publication by Bach and coworkers. Bias dependent transient absorption decay, measured at 850 nm (signal of the charge separated state), using an inert electrolyte. From 0mV (red) to 750 mV (dark green), voltage is reported *vs* the electrolyte Fermi level ($Co(en)_3$ electrolyte). One can see that the red trace initial amplitude is more important at 0V than at 750 mV, indicating a less efficient hole injection when increasing the bias of the cell.

It was observed that when the Fermi level of the NiO/dye electrode was moved to positive values of potential, the initial amplitude of the Transient Absorption Signal of the charge separated state of the dye on NiO signal was reduced (see Fig. 12). This was attributed to a less efficient hole injection process, itself attributed to the lower driving force for hole injection for PMI-6T-TPA, which HOMO lies quite close to NiO VB, and the low degree of coupling between this dye HOMO and the electronic states of NiO. For this, the authors indicated that compounds with higher driving force for hole injection should be employed for the next generation of dyes for p-type DSSCs. If one considers the assumptions by the group of Udo Bach, high holes injection driving force, though representing an important energy loss, might be necessary for the solar cell to work at higher positive potentials. This could be an advantage of the push-pull, triphenyl-amine based dyes, compared with PMI-6T-TPA for instance.

Another aspect concerning the efficiency of hole injection and especially the coupling between dye HOMO and NiO is the dye's anchoring group used in p-type DSSCs. Indeed, the vast majority of the dyes for p-type DSSCs resort to carboxylic acid groups. As they are electro-poor substituents, better anchoring groups could be employed, so as not to represent a barrier for hole

injection. Few investigations have actually been performed concerning other anchoring groups, such as acac groups [74], or pyridine rings [63],[64],[g].

I.B.4. Fighting against charge recombination

Once the hole has been injected into NiO VB, the main issue is to fight against charge recombination, in order that photocurrent / photo-voltage generation happens.

I.B.4.a. What is known about charge recombination today

I.B.4.a.i. The EIS results by the goup of Wu

In 2012, the group of Wu performed an Electrochemical Impedance Study on a 1.5µm NiO substrate, sensitized with the push-pull dye O_2 (see Fig. 13), in presence of an iodine electrolyte [65]. They studied the recombination resistance in two situations: in the dark and under one Sun illumination. The recombination resistance is the resistance that is used in the equivalent circuit used in EIS, to represent the recombination phenomenon in the DSSC. Then if the recombination resistance is small, recombination is high.

Wu and coworkers found that with their dye O2, when the cell was irradiated, the recombination resistance was dramatically reduced at low bias (see Fig. 14). This means that in their conditions, even at low bias, recombination are important and that these recombination were due to the irradiation of the cell. They attributed this photo-induced drop in recombination resistance, (so called “photo-shunt”) to the high rate of geminate recombination between the reduced dyes and the injected holes in NiO. This light induced current leakage was presented to be largely responsible for the low FF of NiO base p-type DSSCs. At higher, positive, bias potential, the recombination resistance under illumination was close to the one in the dark. It was associated to the recombination between the injected holes and the reduced electrolyte species (I^-). This pathway corresponds to the dark current of the cell. With iodine electrolyte, dark current is very

[g] The latter one may be interesting for preventing a suspected positive band shifting of NiO due to its protonation by the –H atom liberated by the carboxylic acid of the dye, during the grafting process.

important on NiO, due to its catalytic activity for the oxidation of I^-, as underlined by some results obtained by Wu et al. [65,h].

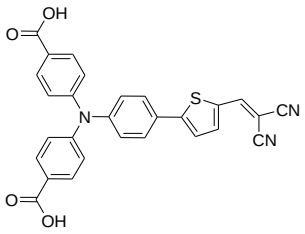


Fig. 13- Dye O_2

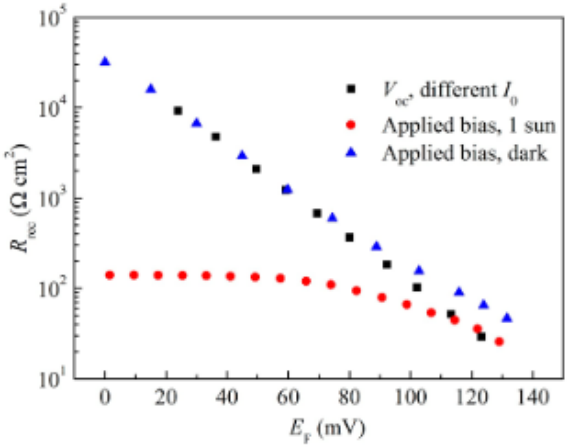


Figure 4. R_{rec} measured by EIS using two experimental configurations: (i) under different illumination at V_{oc}, (ii) under 1 sun illumination applying different dc bias, and (iii) in the dark applying different bias. The voltages were corrected to Fermi level E_F.

Fig. 14- Reproduced from the work of Wu et coll.

I.B.4.a.ii. Recent transient absorption spectroscopy results

In another study, by the group of Udo Bach, with a 1.5 µm NiO film, dyed with PMI-6T-TPA and a $[Co^{II/III}(en)_3]$ electrolyte, a time-resolved transient absorption study at varying potentials was performed (actually the same as described in the hole injection section, see I.B.3.c). It was observed that the dye regeneration yield was gradually decreased when coming from short-circuit conditions, to open-circuit conditions. Interestingly, contrary to the work carried out by the group of Wu, Bach et al. did not found that at relatively high potentials recombination between the injected holes and the cobalt reduced species was an important loss mechanism (with the help of

[h] Actually, in the supporting information of ref. [65], figure S4, the J-V curve of a compact NiO film is shown and compared to FTO and shows the catalytic behaviour of NiO for I^- oxidation.

front-back IPCE experiments). It is possible that the cobalt electrolyte employed there, which is a slow redox couple, or the dense dye packing of TPA-2T-NI at the surface of NiO blocks such recombination. One should mention that the film studied was 1.5 µm thick, which prevents to draw conclusions for longer distance hole transport efficiency.

Hammarström and coworkers also performed a similar study in absence of redox species in the electrolyte, with a Ru dye (Ru-NMI) [66]. They found that the recombination kinetics with their dye was governed by two process: one rapid and one slow. The slow process is more important at negative potential and the rapid at positive potential. This was presented as a reason for the poor fill factor of the solar cell.

I.B.4.a.iii. Possible reasons for the important charge recombination

The reason(s) for the high rate and the rapidity of geminate recombination with NiO are not clearly identified. It is thought to arise from the high number of traps, intra-band gap states of NiO and their wide distribution which was recently shown by Hammarström et al.[24] and also suggested in another parallel study by Peiris et al.[67]. For NiO, the trap state distribution above the VB edge has a different shape that the one for TiO_2 for instance, which shows an exponential shape. This difference could be a key point.

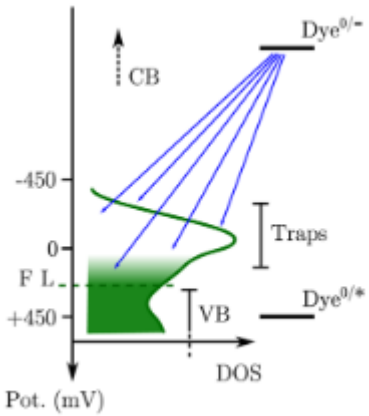


Fig. 15- NiO Density of states, especially, trap state distribution above the Valence Band Edge. The potential scale is vs Ag+/Ag and this picture was reproduced from the work of D'Amario et al.[66] The dye mentioned is Ru-NMI.

Some researchers [5,65] also stressed that NiO has low relative permittivity compared to TiO_2 (11.9 for NiO, 30-170 for TiO_2 [33]). This indeed induces that holes and electrons coulombic interactions

are less screened in the case of NiO. Besides, this low permittivity may also induce a strong band-bending inside NiO particles, contrary to TiO_2, as suggested by Wu et al [23]. Following that hypothesis, a high electric field (which would be favorable for hole extraction however) should be present inside NiO particles. It is also noteworthy that NiO is a highly capacitive material [20], and the influence of this factor over the efficiency of the cell has not been seriously investigated…Speculations are important !

I.B.4.a.iv. Is NiO a good conductor?

NiO is often presented as a material with unfavorable conductivity and with low hole mobility (10^{-8} to 10^{-7} cm^2/S) [68]. Though the conduction mechanism of NiO is still under debate, a recent study by Hammarström et al. clearly suggested that mesoporous NiO is very conductive: an undyed NiO electrode could sustain current values as high as 20 $mA.cm^{-2}$ at 1V, in a two electrode set-up, with an iodine based electrolyte[24]. It is true that the film employed there was thin (700 nm), and that NiO conductivity at higher thickness, suitable for more efficient solar cells, has not yet been proved. That high conductivity value is in agreement with the recently described high J_{SC} value for NiO [6,7], (above 8 $mA.cm^{-2}$), which could not be possible if the material were insulating.

The hole conduction mechanism for NiO in p-type DSSCs is not clearly elucidated, and its low electric properties could explain the important charge recombination that occur in p-type DSSCs. There are actually two main theories. The first one relates to surface transport of the holes by hoping between the surface states of NiO and this could explain the important charge recombination [68]. A hole transport mechanism which is predominantly internal to the nanoparticle network was recently proposed by Hammarström et al.[24], for an un-sensitized, thin (700 nm) electrode. In their paper, by resorting to EIS studies, they found that the Warburg resistance (which is the resistance related to the transport of the hole through the NiO film) did not change in presence or in absence of a saturated quantity of Li^+ cations in the electrolyte. If conduction happened through the surface of the NiO nanoparticle, the Warburg resistance should be sensitive to the presence of Li^+ ions in the electrolyte.

I.B.4.b. How to fight against geminate recombination?

I.B.4.b.i. Dye design strategies to prevent geminate charge recombination

Geminate recombination is the annihilation of the charge separated state. What is called a charge separated state is recalled on Fig. 16. For these recombination to be overcome, dye design must be performed so that the reduced dye has enough time to transfer its electron to the redox mediator in the electrolyte. Depending on the redox mediator, the time necessary to operate the electron transfer from the reduced dye to the redox mediator varies. All these aspects are explained in the following paragraphs.

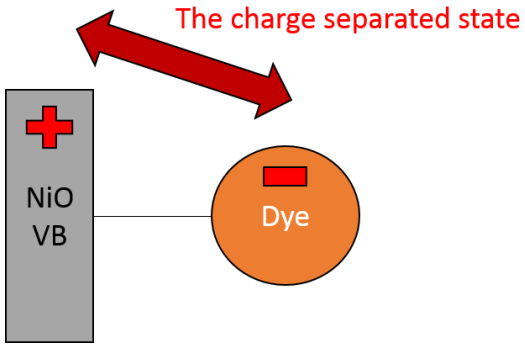


Fig. 16- Schematic representation of the dye-NiO charge separated state.

I.B.4.b.i.(i) The case of dyes which pre-associate with I_3^-

When iodine-based electrolyte is employed, some dyes are assumed to pre-associate with I_3^-, ensuring an extremely efficient dye regeneration mechanism. Then the charge separated state actually does not need to be very long to avoid geminate recombinations. This is was observed with the very efficient dye P1 for instance, for which the charge separated lifetime does not exceed 10 ps in absence of electrolyte [10]. However, the mechanism for dye pre-association is not very well understood, although it is suspected to occur for numerous dyes such as coumarin[69] , perylene imide dyes [14] and other push-pull dyes [8].

I.B.4.b.i.(ii) Dye design to increase the charge-separated life time

For dyes which do not pre-associate, or when the electrolyte is not an iodine-based one, strategies were adopted to reduce geminate recombination and to give time to the reduced dye to be regenerated. This issue is of paramount importance for electrolytes without iodine, so as to reach

high V_{OC}. The electrolyte used for this purpose contains Cobalt complexes for instance[3], which exhibit slower recombination rates than iodine and require then longer life time for the charge separated state.

The general idea is to decouple the LUMO of the dye from the NiO surface. An efficient means can be to resort to anchoring groups which decouple the dye from the NiO surface. Odobel and coworkers observed an extremely long charge separated state for a simple Iridium complex dye, for which the anchoring group (which was phosphonate) was decoupled from the dye by a methylene group [70].

Another developed strategy was to increase the distance between the dye LUMO and the surface of NiO. In 2012, the Wu group [45] showed that for a series of simple Ru dyes for which the Ru center was gradually moved away from the NiO surface by introduction of phenyl groups between the Ru center and the anchoring group, the charge separated life-time was also increased (from 0.14 ps for O8 dye to 52.87 ps for O12 dye). As expected, the cell performance was dramatically increased when the distance between the surface of NiO and the Ru center was increased (from 0.009% for O_8 dye, to 0.051% for O_{12} dye).

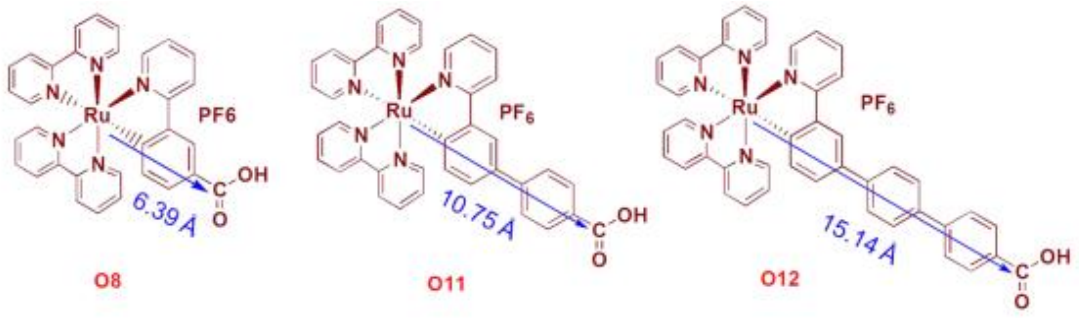


Fig. 17- The structure of the elongated Ruthenium derivatives

In 2008, Odobel et al. implemented, for p-type DSSCs the strategy of the secondary acceptor for fighting against geminate charge recombination, with the PMI-NDI dyad [60]. For this dye, light absorption is performed at the level of an enriched PMI entity (see Fig. 9). Hole injection occurs very quickly into NiO (0.5 ps). Very rapidly too (1ps), the electron promoted to PMI LUMO is shifted to the NDI moiety. Once transferred, due to the decoupling between the two entities, the electron is trapped in the NDI entity, far from the NiO surface, preventing its recombination with

the hole in the NiO VB. Hence the charge separated state as formed is very long lived. It was measured to be in the range of 5 to 50 µs for its second exponential component, which is five orders of magnitude higher when compared to the simple PMI dye [40].

If this strategy revealed to be efficient for obtaining a long-lived charged separate state, the current generated was not high. With the iodine electrolyte, the driving force for dye regeneration (~ 80 mV) was too low [14]. For a 2µm thick film, the J_{SC} was 1.76 mA.cm^{-2}, the V_{OC} was 120 mV and PCE was 0.073%. With another electrolyte and a cobalt(II/III) redox mediator, the driving force for hole injection dye regeneration was more important. However, since the cobalt couple is a slow redox couple, high J_{SC} could not be reached, though a higher value of V_{OC} was obtained due to less charge recombination across the NiO film, compared with iodine. It was certainly not possible to use an even less easily reduced secondary acceptor because sufficient driving force for electron transfer from the PMI to the NDI group must remain (PMI LUMO is approximately at - 0.65 V *vs* NHE and NDI is as - 0.26 V *vs* NHE).

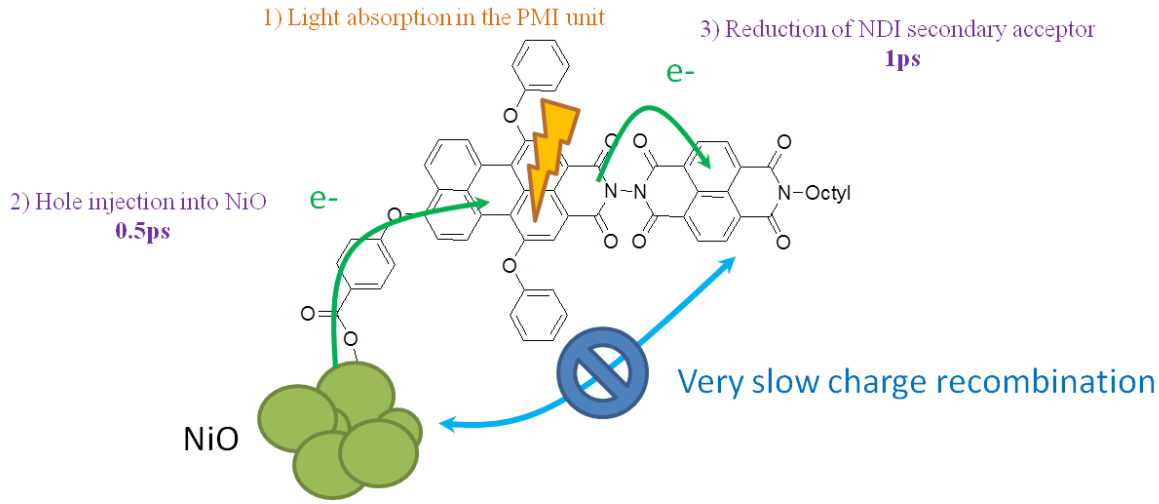


Fig. 18- The working mechanism of PMI-NDI on NiO

The group of Udo Bach reported another dyad, PMI-6T-TPA. This dye is composed of two decoupled absorbers[i], a triphenylamine-sexithiophen and a PMI (depleted in electrons, compared to the one used by the group of Odobel). The PMI unit plays also the role of the secondary electron acceptor. Very long-lived charge separated states were reached with this dye (more than

[i] The decoupling is enhanced by a cleverly placed hexyl chain at the link between the two chromophores.

13µs for the long-lived exponential decay second component). This time, the dye regeneration driving force did not appear to be an issue and high J_{SC} could be reached (more than 5 $mA.cm^{-2}$ [,4] and 7 $mA.cm^{-2}$, with the NiO microballs [28]), as well as the highest reported performance for p-type DSSCs. In the reference paper for PMI-6T-TPA, the location of the LUMO of the dye far from the NiO surface was also shown crucial by comparison of the efficiency of PMI-6T-TPA with its shorter equivalent PMI-4T-TPA and PMI-2T-TPA[4].

In the aim of generating a long-lived charge separated state, the group of Licheng Sun implemented push-pull dyes for NiO DSSCs in 2008 [71]. Since then, several push-pull dyes were implemented and gave good results. Push-pull dyes are often presented are charge transfer compounds, because the optical HOMO/LUMO transition corresponds to a spatial movement of the electron from HOMO to LUMO. By positioning the LUMO far from the anchoring group, this type of compound should allow long lived charges separated states. However, that was not the case: as for P1, (as said above) the life time of the charge separated state did not exceed 10 ps. Today, the quite efficient push-pull dye CAD2 has been reported to display 100 ps charge separated life-time. This life-time is higher than for P1, but no clear reason was given in the publication. In the same publication, another dye CAD1 was reported to have a 300 ps charge separated lifetime. This was attributed to the fact that this dye lied straighter on the NiO surface, preventing charge recombination [8]. Interestingly, other recent push-pull sensitizers (double acceptor), for which thiophen rings were introduced between the triphenylamine and the NiO surface so as to delay charge recombination, revealed to be powerful dyes [72,73] (but the life time of their charge separated state on NiO is not yet known).

The photo-physic results of the recent very efficient dyes CAD3 and QT1 (see Fig. 2) have not been published. For QT1, the author showed that this dye was compatible with the cobalt based electrolyte. This phenomenon stands against all the theories presented above: QT1 is a very small dye, for which geminate recombination should be important due to the proximity with NiO. Then QT1 was not expected to be compatible with the Cobalt electrolyte. The author mentioned a possible long life of the reduced thieno-quinoid form. It is also possible that being small, the dye packs very well at the NiO surface and then in a way, geminate recombination becomes

impossible. Another iso-indigo dye ("ISO-Br"), also quite small and with no secondary acceptor unit was shown to be compatible with the cobalt electrolyte. The mechanisms for dye design so as to obtain long-lived charge separated state have still not fully revealed all their mysteries …

I.B.4.b.ii. NiO surface engineering to reduce geminate recombination

Two papers actually referred to the idea of isolating NiO with Al_2O_3 thin layer so as to decrease charge recombination (upon which geminate recombination). The first one was published in 2010 by Uehara et al. [74]. In this paper, the aluminate layer was deposited by plunging the NiO films into aluminum-tri-*sec*-butoxide and sintering. This led to V_{OC} and J_{SC} improvements. Wu et al. increased the degree of control of aluminate deposition method by using ALD [69]. One ALD cycle was optimal and also permitted to increase the DSSC efficiency (V_{OC} increasing from 110 mV to 150 mV and J_{SC} increasing from 0.83 $mA.cm^{-2}$ to 0.95 $mA.cm^{-2}$, the FF was also increased from 34% to 38%, in agreement with the reduced geminate charge recombination). When the number of ALD cycles was increased, higher V_{OC} were obtained, however due to the insulating character of the coated aluminate film, J_{SC} dropped. The aluminate film decreased geminate recombination and induced passivation of the FTO electrolyte interface. In this case, the V_{OC} increase was due to less important photo-generated holes recombination.

I.B.4.c. Ensuring efficient hole transport to FTO

The question of hole transport to the FTO electrode resides in the diminution of the hole / redox species recombination. The importance of hole / electrolyte recombination can be studied by dark-current measurements. Enhancing the electrical properties by doping NiO may permit to get rid of this problem. However, very little research permitted to draw conclusions.

I.B.4.c.i. NiO surface engineering

Several surface engineering methods permit to prevent NiO / electrolyte charge recombination. First of all, one can say that the Al_2O_3 layer described above also plays this role. Dye design, with surface blocking substituents also revealed to be an efficient strategy, like for the CAD2 dye developed by Gibson (though the presence of the blocking substituents projected the acceptor closer to the NiO surface and then enhanced geminate charge recombination). In the recent paper

by Perera et al. it was shown that for the $Fe(acac)_3$ electrolyte they developed, (see I.A) introducing CDCA as a supplementary adsorbant species in the electrolyte permitted to dramatically decrease hole/electrolyte recombination (from 2.03%, PCE reached the record value of 2.51%)[1]. CDCA is a well known molecule that is generally used in the sensitization step, so as to reduce dye aggregation at the NiO surface by co-grafting. Perera and coworkers used CDCA directly in the electrolyte. Then, their strategy is slightly different. CDCA was used here in the aim of forming supra-molecular entities on NiO surface, as described for TiO_2[76], this being favorable to reduce charge recombination[76]. Another NiO surface engineering example is the reducing of the surface defects of NiO nanoparticles, performed by Zhang et al, by performing an additional post treatment of the NiO electrode at high temperature (550°C) during a short time. This permitted to increase the V_{OC} by almost 100 mV ! Another point is that the dye packing at the NiO surface also allows to decrease the hole / electrolyte recombination, as exemplified with the use of NiO hollow spheres, which for an unclear reason induces a more important dye packing at the NiO surface [16] (see chapter 3 for more details). Finally another strategy can be to lower the position of the NiO VB edge, so that dark-current starts at more positive potential. This has been performed by doping NiO with small amount of other transition metals as Co[23], Li[24], Mg [77,25].

I.B.4.c.ii. Electrolyte engineering

In the aim of changing of the iodine-based electrolyte, transition metal complexes were used as the redox shuttle. One of the advantage of metal complexes is the bulkiness of their ligands, which permits to reduce the approach of the complex to the NiO surface and then reduce charge recombination with the hole in NiO. Also one should underline that for the cobalt electrolyte employed up to now, the $Co^{II/III}$ redox transition was implied. This transition implies a low-spin / high-spin transition for the complex, which is energy demanding (reorganization energy). Once the complex is on its reduced form (*ie* after dye regeneration), it takes more energy to be reoxidized by the hole in the NiO network [3,26]. One should remark that if the last phenomenon delays charge recombination, it is however known to limit the overall photocurrent generation, since the slowness of the complex is also detrimental for the dye regeneration step. In the case of the $Fe(acac)_3$ electrolyte, no spin configuration change is involved in the redox process [1]. Then,

charge recombination are more important … But the rapidity of the complex to perform redox reaction permits to reach important photocurrent, with the pre-requisite of fighting against hole / electrolyte recombination by the use of CDCA in the electrolyte and the use of a blocking layer (*vide infra*), ensuring overall record performance for p-type DSSCs.

I.B.4.d. Ensuring Hole collection at the FTO contact

Even if the use of a compact TiO_2 layer is common for n-type DSSCs, this technique is not so widespread in the field of p-type DSSCs. However, the usefulness of such a BL in the case of a iodine based electrolyte was clearly shown in the work of Zhang et al [78] with an impressive current enhancement: from 40µA.cm^{-2} without the BL to 1.32 mA.cm^{-2} with the BL (which was approximately 50 nm thick, judging from the SEM pictures of that publication). This enhancement was attributed to a better contact between NiO material and the FTO electrode. Wu et al. emphasized that a NiO_x thin layer, due the fact that NiO catalysis the oxidation of I^- may only have a role of contact improvement between the NiO network and FTO [65]. Then the role of the NiO_x layer may only be a contact layer, not a blocking layer, as for n-type DSSCs.

I.C. Conclusions and aim of this PhD

P-type DSSCs suffer from several problems, inherent to their photocathode material, which found no better equivalent up to now however, NiO. In a nutshell, a combination of factors induces that when the bias of the NiO based solar cell is increased, the photo-current is dramatically decreased: the low fill-factor of p-type DSSCs is a real bottleneck. Charge recombination is the most important hurdle to be overcome for a breakthrough to be done in this field.

A solution to increase the performance of p-type DSSCs is then to understand better NiO and to find innovative ways to modify this material for future enhanced performance of p-type DSSCs. On this aspect, it is important to develop new methods that could for example permit better control of the NiO film formation. Ink-jet printing could be one of these methods. It is one of the scopes of this PhD thesis to study the viability of ink-jet printing for NiO photo-cathodes for p-type DSSCs.

Two of the main issues for p-type DSSCs are the geminate charge recombination and the parasitic NiO light absorption. Push-pull design appears to be an efficient strategy for sensitizer, so as to face these two issues. In the past, and very recently, this class of dyes gave excellent performances, especially very high photocurrent generation, with iodine electrolyte. The exact rationale for the efficiency of push-pull sensitizers for p-type DSSCs is yet to be found. Especially, despite a charge transfer character, push-pull compounds do not generate particularly long-lived charge separated states. Probably, for an unclear reason, these dyes induce pre-association with I_3^- and this is could be a reason for their high efficiency. In this thesis, the synthesis and device implementation of new push-pull sensitizers (see Fig. 19) is presented, in the aim of obtaining highly absorbing dyes, which can compete with NiO parasitic absorption. Some efforts on the dye design were also done in the aim of decreasing geminate charge recombination. The synthesized dyes' physical properties were deeply assessed. Eventually, the new dyes were all tested as sensitizers for the NiO photocathode, in a p-type DSSC configuration, with ink-jet printed NiO films.

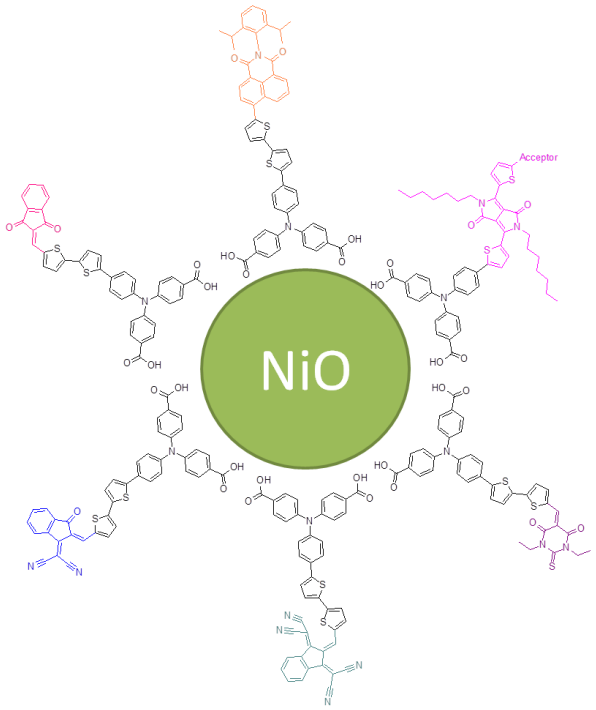


Fig. 19- The targeted dyes of this thesis

References

1. Perera, I. R. *et al.* Application of the Tris(acetylacetonato)iron(III)/(II) Redox Couple in p-Type Dye-Sensitized Solar Cells. *Angew. Chem. Int. Ed*, **54**, 3758-3762 (2015).
2. Yu, M., Draskovic, T. I. & Wu, Y. Cu(I)-based delafossite compounds as photocathodes in p-type dye-sensitized solar cells. *Phys. Chem. Chem. Phys.* **16,** 5026–5033 (2014).
3. Powar, S. *et al.* Highly Efficient p-Type Dye-Sensitized Solar Cells based on Tris(1,2-diaminoethane)Cobalt(II)/(III) Electrolytes. *Angew. Chem. Int. Ed.* **52,** 602–605 (2013).
4. Nattestad, A. *et al.* Highly efficient photocathodes for dye-sensitized tandem solar cells. *Nat. Mater.* **9,** 31–35 (2010).
5. Odobel, F. *et al.* Recent advances and future directions to optimize the performances of p-type dye-sensitized solar cells. *Coord. Chem. Rev.* **256,** 2414–2423 (2012).
6. Wood, C. J., Summers, G. H. & Gibson, E. Increased photocurrent in a tandem dye-sensitized solar cell by modifications in push-pull dye-design. *Chem. Commun.* **51**, 3915-3918 (2015).
7. Zhang, Q.-Q. *et al.* A push–pull thienoquinoidal chromophore for highly efficient p-type dye-sensitized solar cells. *J. Mater. Chem. A* **3,** 7695–7698 (2015).
8. Wood, C. J. *et al.* Red-Absorbing Cationic Acceptor Dyes for Photocathodes in Tandem Solar Cells. *J. Phys. Chem. C* **118,** 16536–16546 (2014).
9. Weidelener, M. *et al.* Synthesis and characterization of perylene–bithiophen–triphenylamine triads: studies on the effect of alkyl-substitution in p-type NiO based photocathodes. *J. Mater. Chem.* **22,** 7366–7379 (2012).
10. Qin, P. *et al.* Synthesis and Mechanistic Studies of Organic Chromophores with Different Energy Levels for p-Type Dye-Sensitized Solar Cells. *J. Phys. Chem. C* **114,** 4738–4748 (2010).
11. He, M., Ji, Z., Huang, Z. & Wu, Y. Molecular Orbital Engineering of a Panchromatic Cyclometalated Ru(II) Dye for p-Type Dye-Sensitized Solar Cells. *J. Phys. Chem. C* **118,** 16518–16525 (2014).
12. Wood, C. J., Robson, K. C. D., Elliott, P. I. P., Berlinguette, C. P. & Gibson, E. A. Novel triphenylamine-modified ruthenium(II) terpyridine complexes for nickel oxide-based cathodic dye-sensitized solar cells. *RSC Adv.* **4,** 5782–5791 (2014).
13. Favereau, L. *et al.* Diketopyrrolopyrrole derivatives for efficient NiO-based dye-sensitized solar cells. *Chem. Commun.* **49,** 8018–8020 (2013).

14. Pleux, L. L. *et al.* Synthesis, photophysical and photovoltaic investigations of acceptor-functionalized perylene monoimide dyes for nickel oxide p-type dye-sensitized solar cells. *Energy Environ. Sci.* **4,** 2075–2084 (2011).
15. Click, K. A. *et al.* A double-acceptor as a superior organic dye design for p-type DSSCs: high photocurrents and the observed light soaking effect. *Phys. Chem. Chem. Phys.* **16,** 26103–26111 (2014).
16. Yang, H. B. *et al.* One-Step Fabrication of Unique Mesoporous NiO Hollow Sphere Film on FTO for High-Performance P-Type Dye-Sensitized Solar Cells. *Adv. Mater. Interfaces* **1,** 1300110 (2014).
17. Zhang, X. L. *et al.* Sensitization of nickel oxide: improved carrier lifetime and charge collection by tuning nanoscale crystallinity. *Chem. Commun.* **48,** 9885–9887 (2012).
18. Bockris, J. O., Reddy, A. K. N. & Gamboa-Aldeco, M. E. *Modern Electrochemistry 2A: Fundamentals of Electrodics*. (Springer Science & Business Media, 2001).
19. Gibson, E. A. *et al.* Role of the Triiodide/Iodide Redox Couple in Dye Regeneration in p-Type Dye-Sensitized Solar Cells. *Langmuir* **28,** 6485–6493 (2012).
20. Daeneke, T. *et al.* Dominating Energy Losses in NiO p-Type Dye-Sensitized Solar Cells. *Adv. Energy Mater.* **5,** 1401387 (2015).
21. Odobel, F., Le Pleux, L., Pellegrin, Y. & Blart, E. New Photovoltaic Devices Based on the Sensitization of p-type Semiconductors: Challenges and Opportunities. *Acc. Chem. Res.* **43,** 1063–1071 (2010).
22. Hagfeldt, A., Boschloo, G., Sun, L., Kloo, L. & Pettersson, H. Dye-Sensitized Solar Cells. *Chem. Rev.* **110,** 6595–6663 (2010).
23. Natu, G. *et al.* Valence Band-Edge Engineering of Nickel Oxide Nanoparticles via Cobalt Doping for Application in p-Type Dye-Sensitized Solar Cells. *ACS Appl. Mater. Interfaces* **4**, 5922–5929 (2012).
24. D'Amario, L., Boschloo, G., Hagfeldt, A. & Hammarström, L. Tuning of Conductivity and Density of States of NiO Mesoporous Films Used in p-Type DSSCs. *J. Phys. Chem. C* (2014).
25. Zannotti, M. *et al.* Ni Mg mixed metal oxides for p-type dye-sensitized solar cells. *ACS Appl. Mater. Interfaces* **7**, 24556–24565 (2015).
26. Gibson, E. A. *et al.* Cobalt Polypyridyl-Based Electrolytes for p-Type Dye-Sensitized Solar Cells. *J. Phys. Chem. C* **115,** 9772–9779 (2011).
27. Zhu, H., Hagfeldt, A. & Boschloo, G. Photoelectrochemistry of Mesoporous NiO Electrodes in Iodide/Triiodide Electrolytes. *J. Phys. Chem. C* **111,** 17455–17458 (2007).

28. Powar, S. *et al.* Improved photocurrents for p-type dye-sensitized solar cells using nano-structured nickel(II) oxide microballs. *Energy Environ. Sci.* **5,** 8896–8900 (2012).
29. Alidoust, N., Toroker, M. C. & Carter, E. A. Revisiting Photoemission and Inverse Photoemission Spectra of Nickel Oxide from First Principles: Implications for Solar Energy Conversion. *J. Phys. Chem. B* **118,** 7963–7971 (2014).
30. Adler, D. & Feinleib, J. Electrical and Optical Properties of Narrow-Band Materials. *Phys. Rev. B* **2,** 3112–3134 (1970).
31. Flynn, C. J. *et al.* Hierarchically-Structured NiO Nanoplatelets as Mesoscale p-Type Photocathodes for Dye-Sensitized Solar Cells. *J. Phys. Chem. C* **118,** 14177–14184 (2014).
32. Marrani, A. G., Novelli, V., Sheehan, S., Dowling, D. P. & Dini, D. Probing the Redox States at the Surface of Electroactive Nanoporous NiO Thin Films. *ACS Appl. Mater. Interfaces* **6,** 143–152 (2014).
33. Dini, D., Halpin, Y., Vos, J. G. & Gibson, E. A. The influence of the preparation method of NiOx photocathodes on the efficiency of p-type dye-sensitized solar cells. *Coord. Chem. Rev.* **304–305,** 179–201 (2015).
34. Renaud, A. *et al.* Origin of the Black Color of NiO Used as Photocathode in p-Type Dye-Sensitized Solar Cells. *J. Phys. Chem. C* **117,** 22478–22483 (2013).
35. Mori, S. *et al.* Charge-Transfer Processes in Dye-Sensitized NiO Solar Cells. *J. Phys. Chem. C* **112,** 16134–16139 (2008).
36. Warnan, J. *et al.* Multichromophoric Sensitizers Based on Squaraine for NiO Based Dye-Sensitized Solar Cells. *J. Phys. Chem. C* **118,** 103–113 (2014).
37. Chang, C.-H., Chen, Y.-C., Hsu, C.-Y., Chou, H.-H. & Lin, J. T. Squaraine-Arylamine Sensitizers for Highly Efficient p-Type Dye-Sensitized Solar Cells. *Org. Lett.* **14,** 4726–4729 (2012).
38. Feihl, S. *et al.* Nickel oxide nanostructured electrodes towards perylenediimide-based dye-sensitized solar cells. *RSC Adv.* **2,** 11495–11503 (2012).
39. Lefebvre, J.-F., Sun, X.-Z., Calladine, J. A., George, M. W. & Gibson, E. A. Promoting charge-separation in p-type dye-sensitized solar cells using bodipy. *Chem. Commun.* **50,** 5258–5260 (2014).
40. Maufroy, A. *et al.* Synthesis and properties of push–pull porphyrins as sensitizers for NiO based dye-sensitized solar cells. *J. Mater. Chem. A* **3,** 3908–3917 (2015).
41. Tian, H. *et al.* Enhancement of p-Type Dye-Sensitized Solar Cell Performance by Supramolecular Assembly of Electron Donor and Acceptor. *Sci. Rep.* **4,** (2014).

42. Feihl, S. *et al.* Integrating metalloporphycenes into p-type NiO-based dye-sensitized solar cells. *Chem. Commun.* **50,** 11339–11342 (2014).
43. Pellegrin, Y. *et al.* Ruthenium polypyridine complexes as sensitizers in NiO based p-type dye-sensitized solar cells: Effects of the anchoring groups. *J. Photochem. Photobiol. Chem.* **219,** 235–242 (2011).
44. Freys, J. C., Gardner, J. M., D'Amario, L., Brown, A. M. & Hammarström, L. Ru-based donor–acceptor photosensitizer that retards charge recombination in a p-type dye-sensitized solar cell. *Dalton Trans.* **41,** 13105–13111 (2012).
45. Ji, Z. *et al.* Synthesis, Photophysics, and Photovoltaic Studies of Ruthenium Cyclometalated Complexes as Sensitizers for p-Type NiO Dye-Sensitized Solar Cells. *J. Phys. Chem. C* **116,** 16854–16863 (2012).
46. Ji, Z., Natu, G. & Wu, Y. Cyclometalated Ruthenium Sensitizers Bearing a Triphenylamino Group for p-Type NiO Dye-Sensitized Solar Cells. *ACS Appl. Mater. Interfaces* **5,** 8641–8648 (2013).
47. Yen, Y.-S. *et al.* Arylamine-Based Dyes for p-Type Dye-Sensitized Solar Cells. *Org. Lett.* **13,** 4930–4933 (2011).
48. Ji, Z., Natu, G., Huang, Z. & Wu, Y. Linker effect in organic donor–acceptor dyes for p-type NiO dye sensitized solar cells. *Energy Environ. Sci.* **4,** 2818–2821 (2011).
49. Wu, F., Zhu, L., Zhao, S., Song, Q. & Yang, C. Engineering of organic dyes for highly efficient p-type dye-sensitized solar cells. *Dyes Pigments* **124,** 93–100 (2016).
50. Weidelener, M. *et al.* Synthesis and Characterization of Organic Dyes with Various Electron-Accepting Substituents for p-Type Dye-Sensitized Solar Cells. *Chem. – Asian J.* **9,** 3251–3263 (2014).
51. Ameline, D. *et al.* Isoindigo derivatives for application in p-type dye sensitized solar cells. *RSC Adv.* **5,** 85530–85539 (2015).
52. Li, L. *et al.* Double-Layered NiO Photocathodes for p-Type DSSCs with Record IPCE. *Adv. Mater.* **22,** 1759–1762 (2010).
53. Cremer, J. Novel head-to-tail coupled oligo(3-hexylthiophen) derivatives for photovoltaic applications. (2005).
54. Yu, Z., Li, F. & Sun, L. Recent advances in dye-sensitized photoelectrochemical cells for solar hydrogen production based on molecular components. *Energy Environ. Sci.* (2015).
55. Boschloo, G. & Hagfeldt, A. Spectroelectrochemistry of Nanostructured NiO. *J. Phys. Chem. B* **105,** 3039–3044 (2001).

56. Powar, S. *et al.* Improved Photovoltages for p-Type Dye-Sensitized Solar Cells Using CuCrO2 Nanoparticles. *J. Phys. Chem. C* **118,** 16375–16379 (2014).
57. Borgström, M. *et al.* Sensitized Hole Injection of Phosphorus Porphyrin into NiO: Toward New Photovoltaic Devices. *J. Phys. Chem. B* **109,** 22928–22934 (2005).
58. Ji, Z. & Wu, Y. Photoinduced Electron Transfer Dynamics of Cyclometalated Ruthenium (II)–Naphthalenediimide Dyad at NiO Photocathode. *J. Phys. Chem. C* **117,** 18315–18324 (2013).
59. Morandeira, A., Boschloo, G., Hagfeldt, A. & Hammarström, L. Photoinduced Ultrafast Dynamics of Coumarin 343 Sensitized p-Type-Nanostructured NiO Films. *J. Phys. Chem. B* **109,** 19403–19410 (2005).
60. Morandeira, A. *et al.* Improved Photon-to-Current Conversion Efficiency with a Nanoporous p-Type NiO Electrode by the Use of a Sensitizer-Acceptor Dyad. *J. Phys. Chem. C* **112,** 1721–1728 (2008).
61. Bräutigam, M., Kübel, J., Schulz, M., Vos, J. G. & Dietzek, B. Hole injection dynamics from two structurally related Ru–bipyridine complexes into NiOx is determined by the substitution pattern of the ligands. *Phys. Chem. Chem. Phys.* **17,** 7823–7830 (2015).
62. Warnan, J. *et al.* Acetylacetone anchoring group for NiO-based dye-sensitized solar cell. *Dyes Pigments* **105,** 174–179 (2014).
63. Jin, B. *et al.* New Pyridine Anchoring Dyes for P-type Dye-Sensitized Solar Cells. *Chem. Lett.* (2013).
64. Cui, J. *et al.* Organic Sensitizers with Pyridine Ring Anchoring Group for p-Type Dye-Sensitized Solar Cells. *J. Phys. Chem. C* **118,** 16433–16440 (2014).
65. Huang, Z. *et al.* Probing the Low Fill Factor of NiO p-Type Dye-Sensitized Solar Cells. *J. Phys. Chem. C* **116,** 26239–26246 (2012).
66. D'Amario, L., Antila, L. J., Pettersson Rimgard, B., Boschloo, G. & Hammarström, L. Kinetic Evidence of Two Pathways for Charge Recombination in NiO-Based Dye-Sensitized Solar Cells. *J. Phys. Chem. Lett.* **6,** 779–783 (2015).
67. Peiris, T. A. N., Sagu, J. S., Wijayantha, K. G. U. & García-Cañadas, J. Electrochemical Determination of the Density of States of Nanostructured NiO Films. *ACS Appl. Mater. Interfaces* **6,** 14988–14993 (2014).
68. Odobel, F. & Pellegrin, Y. Recent Advances in the Sensitization of Wide-Band-Gap Nanostructured p-Type Semiconductors. Photovoltaic and Photocatalytic Applications. *J. Phys. Chem. Lett.* **4,** 2551–2564 (2013).

69. Morandeira, A., Boschloo, G., Hagfeldt, A. & Hammarström, L. Coumarin 343−NiO Films as Nanostructured Photocathodes in Dye-Sensitized Solar Cells: Ultrafast Electron Transfer, Effect of the I3−/I− Redox Couple and Mechanism of Photocurrent Generation. *J. Phys. Chem. C* **112,** 9530–9537 (2008).
70. Gennari, M. *et al.* Long-Lived Charge Separated State in NiO-Based p-Type Dye-Sensitized Solar Cells with Simple Cyclometalated Iridium Complexes. *J. Phys. Chem. Lett.* **5,** 2254–2258 (2014).
71. Qin, P. *et al.* Design of an Organic Chromophore for P-Type Dye-Sensitized Solar Cells. *J. Am. Chem. Soc.* **130,** 8570–8571 (2008).
72. Zhu, L., Yang, H. B., Zhong, C. & Li, C. M. Rational design of triphenylamine dyes for highly efficient p-type dye sensitized solar cells. *Dyes Pigments* **105,** 97–104 (2014).
73. Zhu, L., Yang, H., Zhong, C. & Li, C. M. Modified Triphenylamine-Dicyanovinyl-Based Donor–Acceptor Dyes with Enhanced Power Conversion Efficiency of p-Type Dye-Sensitized Solar Cells. *Chem. – Asian J.* **7,** 2791–2795 (2012).
74. Uehara, S., Sumikura, S., Suzuki, E. & Mori, S. Retardation of electron injection at NiO/dye/electrolyte interface by aluminium alkoxide treatment. *Energy Environ. Sci.* **3,** 641–644 (2010).
75. Natu, G., Huang, Z., Ji, Z. & Wu, Y. The Effect of an Atomically Deposited Layer of Alumina on NiO in P-type Dye-Sensitized Solar Cells. *Langmuir* **28,** 950–956 (2012).
76. Salvatori, P. *et al.* Supramolecular Interactions of Chenodeoxycholic Acid Increase the Efficiency of Dye-Sensitized Solar Cells Based on a Cobalt Electrolyte. *J. Phys. Chem. C* **117,** 3874–3887 (2013).
77. Huang, Z. *et al.* Enhanced performance of p-type dye sensitized solar cells based on mesoporous Ni1−xMgxO ternary oxide films. *RSC Adv.* **4,** 60670–60674 (2014).
78. Zhang, X. L. *et al.* Enhanced open-circuit voltage of p-type DSC with highly crystalline NiO nanoparticles. *Chem. Commun.* **47,** 4808–4810 (2011).

II. Organic synthesis of the new dyes and their physical properties

II.A. Synthesis and physical properties of the bithiophen push-pull dyes

II.A.1. Choice of the molecules

II.A.1.a. Introduction

As said in the first chapter, push-pull molecules present some key advantages for implementation into p-type DSSCs. In the aim of tuning the absorption range of the p-type DSSC photocathode, early works (2010) by Sun and coworkers reported on the synthesis of various double-acceptor psuh-pull molecules with triphenylamine as the donor group and various acceptors of different strength [1]. In this trend, we wanted to synthesis new push-pull molecules, with new accepting groups, so as to tune the absorption range of the photocathode. The different molecules that were targeted are represented below (see Fig. 20). As one can see, they are made of three different building blocks.

The first one is the triphenylamine entity. It is actually the only donor entity that has been employed for push-pull design for p-type DSSCs up to now, due to an adapted HOMO level for hole injection [j]. The strategy we adopted was the mono-acceptor strategy, with two carboxylic acids as the anchoring groups. As said in chapter 1, two anchoring units, up-to-now, always permitted to obtain better device performance. The second building block is the link between the triphenylamine part and the acceptor part of the molecule. We selected a simple bithiophen bridge, which was, to the best of our knowledge, never investigated for mono-acceptor push-pull dyes, for p-type DSSCs. This bridge is expected to permit good communication between triphenylamine and the acceptors. In the present work, the synthetic trials, to change the bithiophen entity to a dipyrrolopyrrole entity, in the purpose of enhancing the dye absorption toward the red part of the spectrum are also tackled.

For the acceptor building block, five chemical entities were targeted. The first one is the naphtalimide entity, the second one is a diethyl-thiobarbituric derivative and finally, three different indane derivatives. Expect the thiobarbituric acceptors, which is then revisited in this thesis, all the other ones are new in the field of p-type DSSCs.

[j] Though it was recently questioned, see chapter 1.

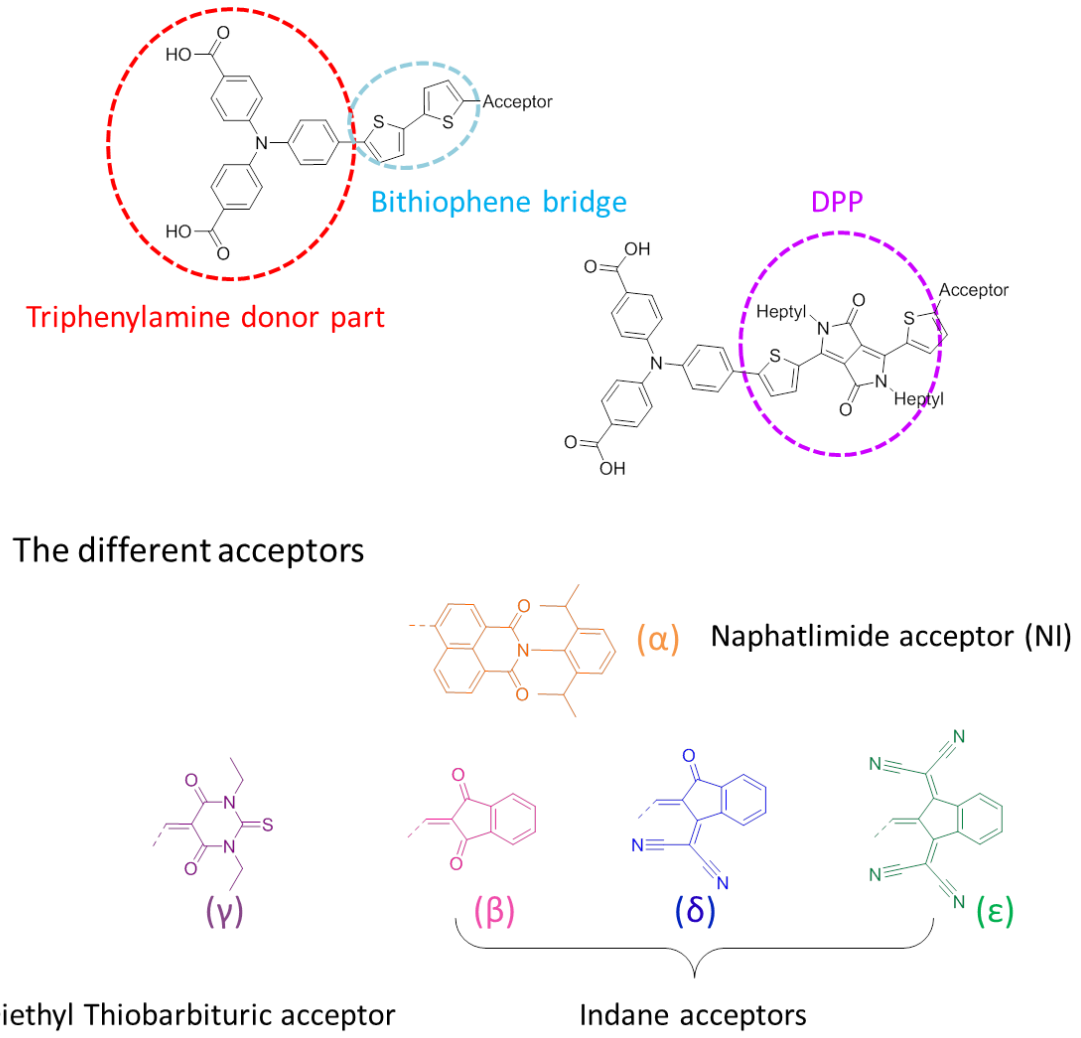


Fig. 20- The targeted dyes dyes in this chapter- A triphenylamine-bithiophen common donor part and five different accepting groups (here, named as α to ε). The bithiophen link was also purposed to be replaced by a DPP entity.

II.A.1.b. Evaluation of the strength of the different acceptors

The aim of this paragraph is to clarify the notion of acceptor strength and then to justify the choice of the different targeted dyes in this thesis, in terms of absorption range.

The electron accepting capability of a compound is evaluated through its electron affinity (EA). Compounds with high EA are strong electron acceptors. In terms of chemistry, there are two main strategies which influence the EA of a compound:

- The electron deficiency of the Pi-system at the ground state. Pi-systems can be rendered electron deficient by decorating them with electron withdrawing groups (strong "-M" or "-I" effect), among which, C=O, CN, NO_2 (from the less strong to the strongest electron withdrawing group).
- The stability of the system after electron injection. Sometimes, systems can be rendered very stable after electron injection, through aromatization for instance or through large delocalization of the injected electron.

Based on this, the evaluation of the strength of the different acceptors is presented in the following paragraphs.

II.A.1.b.i. Study of the chemical formulae of the different acceptors

For **(α)**, the -M effect of the two "C=O" is supported by the large stabilization of positive charge permitted by the naphthalene cycle. Then a partial and diffuse positive charge is present on **(α)**. Also, the fact that once injected into **(α)** the electron is delocalized (and then stabilized) over the naphthalene ring participates into the electron accepting character of **(α)**. However, the +M effect of the central nitrogen atom reduces the efficiency of the "C=O"–M effect. Then one can understand that **(α)** is the weaker acceptor of the series studied here.

For **(β)**, the –M effect of the two "C=O" is also present and supported by the presence of the charge stabilizing phenyl ring. The effect of the two "C=O" is stronger than for **(α)** because of the absence of nitrogen atom. Then **(β)** is a stronger acceptor than **(α)**.

The **(δ)** form has the same Pi-system as **(β)** (a phenyl ring), but one of the two C=O has been replaced by two strongly electron withdrawing cyano groups. Then **(δ)** is a stronger acceptor than **(β)**. The same remark is valid for **(ε)**, which is expected to be the strongest acceptor among the targeted indane derivatives.

For **(γ)**, the high EA certainly stems from a different mechanism than for the other acceptors. The Pi system is less extended in this case (there is no naphthalene nor phenyl ring). Then, the three electron withdrawing groups (two C=O and one C=S) generate partial positive charges which are, contrary to other acceptors, not diffuse. This partial positive charge is counterbalanced by the donor effect of the nitrogen (+M effect) which is itself supported by the electronically donating

ethyl groups (+I effect). At first sight, all this would suggest that **(γ)** is not an exceptionally strong acceptor.

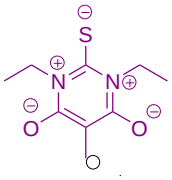


Fig. 21- A possible mesomer form for the reduced (γ) acceptor

However, Fig. 21 highlights that upon reduction, **(γ)** acceptor can be drawn under a mesomeric form which shows an aromatic stabilization. This formula suggest that upon reduction, **(γ)** is a very stable acceptor entity and is then prone to reduction and then a strong acceptor.

II.A.1.b.ii. LUMO level calculation for the different acceptor groups

The LUMO levels of the different acceptors in vacuum were calculated. LUMO levels calculated by DFT are close to EA of the components [2]. The results, as well as the associated isodensity plots are summarized in Fig. 22. The order predicted by analyzing the chemical formulae of the indane derivatives is confirmed: from the weakest to the strongest, **(α)** < **(β)** < **(δ)** < **(ε)**. Calculation also permitted to confirm that **(γ)** is a very strong acceptor. Eventually, the acceptors can be classified from the weakest to the strongest: **(α)** < **(β)** < **(γ)** < **(δ)** < **(ε)**.

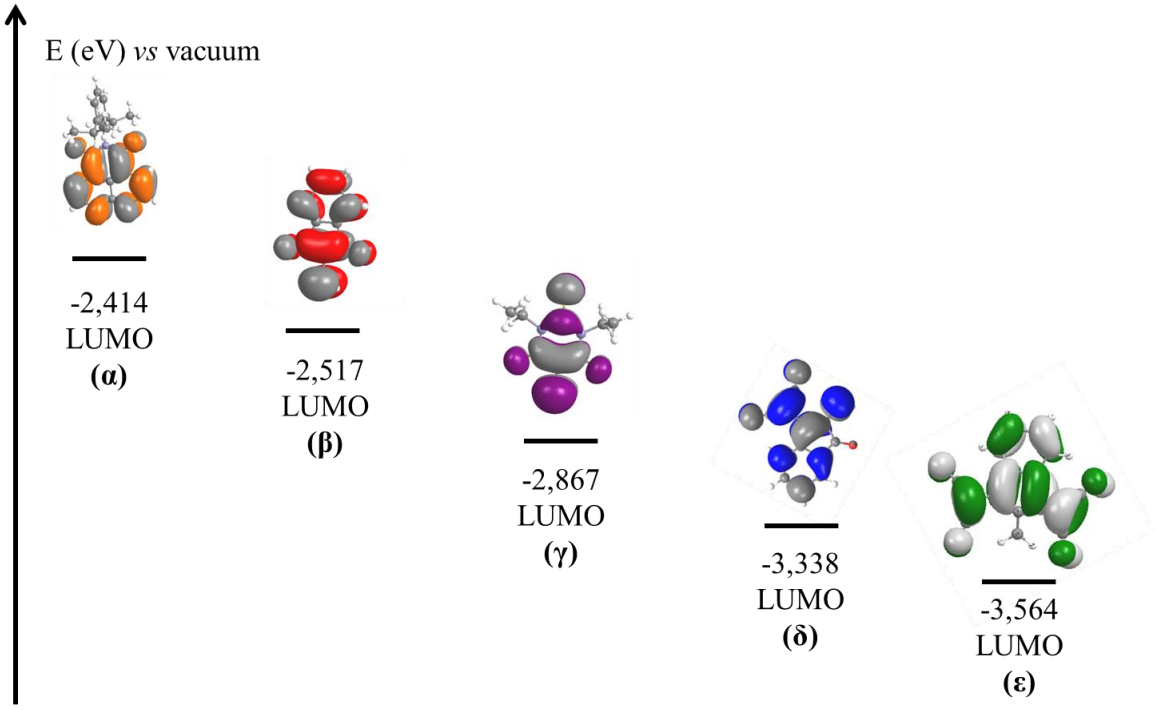


Fig. 22- Calculated LUMO levels for the different acceptors, in vacuum and the associated isodensity plots (isovalue was set at 0.02). From the left to the right, respectively (α) to (ε).

II.A.1.b.iii. Conclusions

The different targeted molecules possess different accepting groups, for which there is a gradual increase in the accepting strength. Due to the fact that all the molecules share the same triphenylamine bithiophen donor part, the targeted dyes are expected to exhibit absorption ranges consistent with the above ranking [k]. In this purpose, after the organic synthesis work operated for the different dyes, their steady state optical properties are presented.

II.A.2. **Organic synthesis of the bithiophen dyes**

II.A.2.a. Retro-synthetic scheme

A retrosynthetic scheme is presented in Fig. 23. The strategy chosen is to synthesize the different building blocks separately and to resort to coupling reactions so as to obtain the final molecules. The bithiophen was first coupled with the different accepting groups. Afterwards, coupling was performed with the triphenylamine to obtain the desired compounds. Importantly, the

[k] A discussion about this aspect is presented in annexes 3, where the HOMO / LUMO orbital of the donor and the acceptor part, coupling in the final push-pull molecule is discussed. Typically, it is shown that the coupling between the acceptor and the donor part is essentially HOMO/HOMO and LUMO/LUMO. This explains that the LUMO strength of the acceptor is conserved in the final molecules.

triphenylamine was used under a *tert*-butyl ester protected version during the whole synthesis and was only deprotected at the last step, so as to obtain the final di-carboxylic acid bithiophen push-pull derivatives. This permitted to enhance the solubility of the different synthetic intermediates and to facilitate the synthetic work.

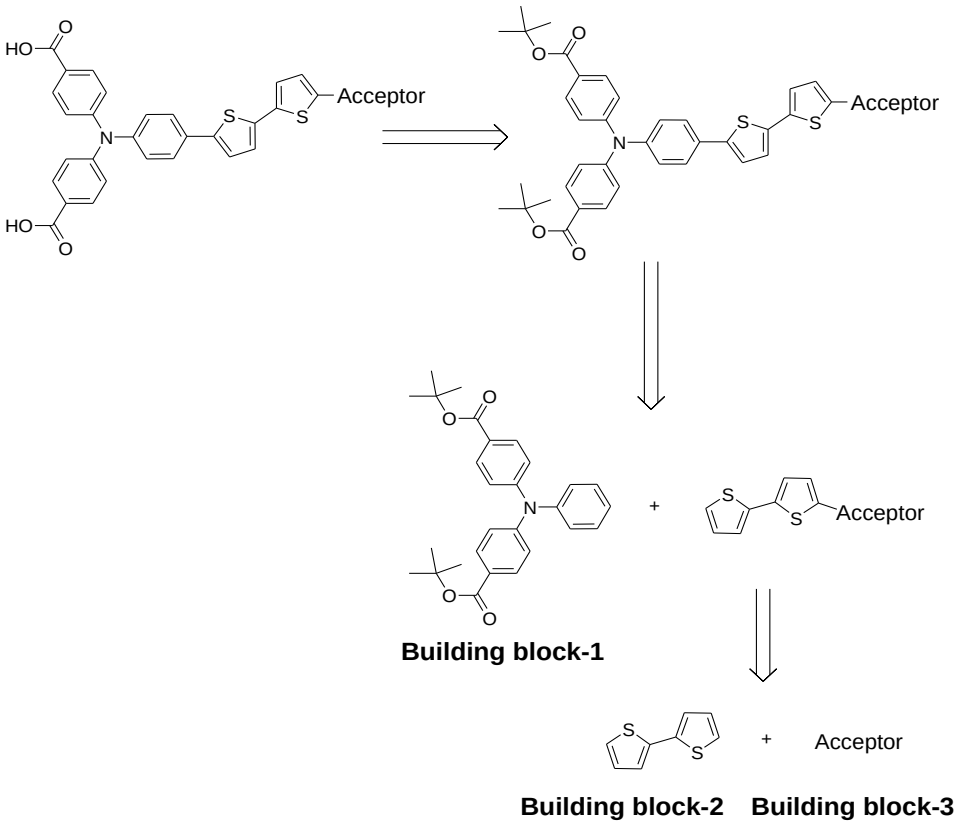


Fig. 23- Retrosynthetic scheme for the synthesis of the different bithiophen compounds

II.A.2.b. Synthesis of the triphenylamine building block

II.A.2.b.i. Introduction

The triphenyl-amine (TPA) was chosen to be synthesized in the final form of boronic acid pinacol ester **(3)**. The purpose was to permit a Suzuki-Miyaura cross-coupling (SM) with brominated bithiophen derivatives. SM cross-coupling conditions resort to boron derivatives, which are generally environmental benign[3]. They were preferred to Stille conditions in order to avoid toxic Stanyl derivatives.

II.A.2.b.ii. State of the art for the synthesis of TPA (3)

In the past, the synthesis of TPA **(3)** was already described by the work of Bauërle [4,5] and Lin[6]. Both groups resorted to Buchwald-Hartwig conditions, so as to couple two *tert*-butyl ester

benzoates groups to an aniline ring, to obtain the triphenylamine derivative **(1)**, in one or two steps (for more details, *vide infra*). Halogenation, of the nucleophilic position of **(1)** permitted to obtain derivative **(2)**. Bäuerle described iodination and Lin bromination. Finally, Miyaura borylation was performed in order to obtain the desired product **(3)**. The reaction yield was higher in the case of iodine starting derivative (this was probably due to the increased polarizability of the C-I bound compared to the C-Br bound).

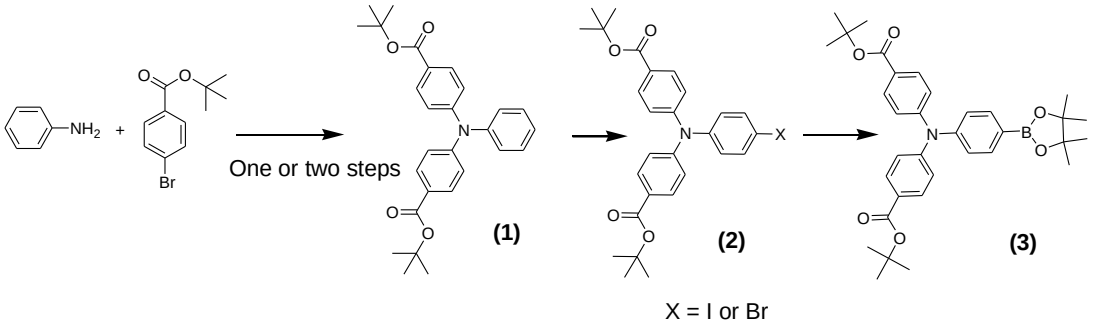


Fig. 24- Synthetic route employed by Bäuerle, Cremer and Lin for the synthesis of (3)

Concerning the first step, it should be noted that Bäuerle could not to obtain **(1)** in one step, although various conditions (number of equivalents, temperature, base employed) were tested in this purpose [5,4]. Besides, it was mentioned that heating was not possible because it induced ester cleavage of the starting material. Hence, they proposed a room temperature synthesis of **(1)** in two steps (see Fig. 25), the first step involving 1.5 equivalent of aniline, probably to increase the selectivity of the reaction toward the monoarylated product (DPA).

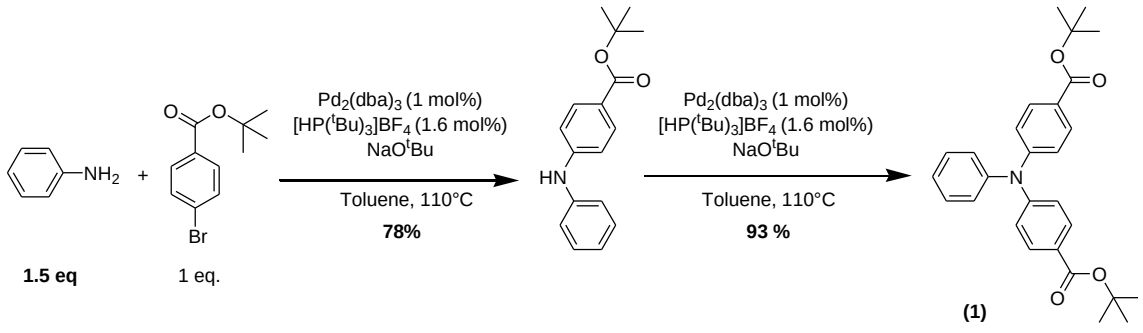


Fig. 25 – Two steps synthesis of (1) proposed by Bauërle et al.

In 2012, Lin et al. described a one-pot, direct, synthesis of pure **(1)** [6]. The starting reagents employed were the same as those used by Bäuerle et al. However, NaO^tBu was employed as the

base, rather than KO^{t}Bu and the catalyst was also changed (tetrakis ligand). The mixture was also heated (8 hours at 80°C and 1 hour at 110°C) and no ester cleavage was reported. The yield of the reaction was moderate (40%). The reasons for the one-pot synthesis to be successful were not discussed in Lin publication. Interestingly however, as far as a 2014 publication, by Cai et al., is concerned [7], the choice of the base is very important for the diarylation of aniline derivatives under Buchwald-Hartwig conditions. In this publication, the influence of various bases over the selectivity and the efficiency of the reaction was investigated, through a methodology study. The high efficiency and selectivity of NaO^{t}Bu compared to KO^{t}Bu or other strong bases such as NaH or KOH, for the diarylation of aniline was pointed out. However, the reason for the effect for the base counter ion to have such a strong influence remained elusive. When weaker bases were employed (K_3PO_4, Cs_2CO_3, K_2CO_3, Na_2CO_3), the selectivity was oriented toward the monorarylated product, and Cs_2CO_3 enabled the best conversion efficiency.

It is worth mentioning that another approach was recently described by Gibson et al.[8], on the basis of the works of Ghosh [9] and also probably Liu [10]. A very similar product, with methyl esters, rather than *tert*-butyl esters, was obtained (see Fig. 26). However, one should notice that this approach is less "atom economical" than the one presented above and also resorts to toxic $POCl_3$. This is why the Bäuerle / Lin, route was chosen in the present work.

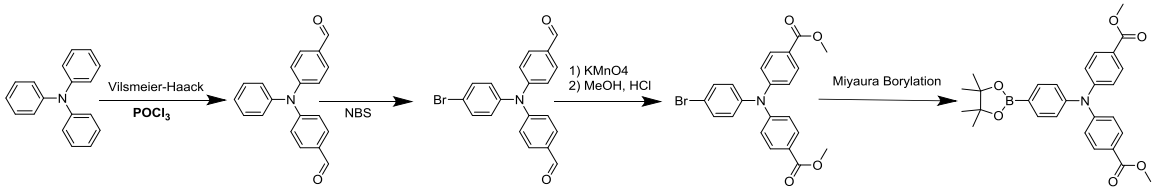


Fig. 26 – Alternative synthetic route described by Gibson et al. for the synthesis of the methylester version of TPA

II.A.2.b.iii. Synthesis of the boronic pinacol-ester triphenylamine (3)

In this thesis, the synthesis of **(1)** was performed in one step, in optimized conditions compared with the one of Lin et al. According to Bäuerle's route, iodination was performed with monochloride, followed by the Miyaura borylation reaction. We do not detail the last two steps,

because the experimental conditions were kept almost identical to literature, the conditions were reported in the experimental part [1].

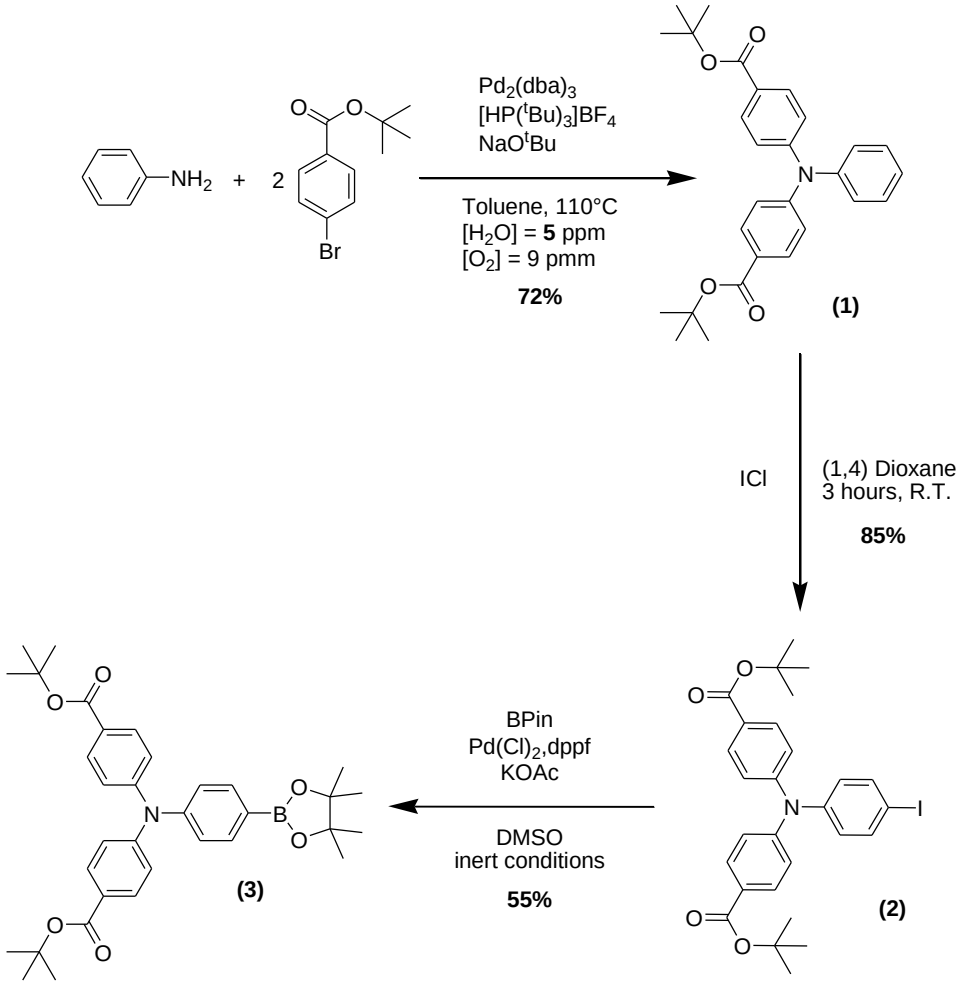


Fig. 27- Synthetic route for the obtention of (3)

The first trials for the reaction according to Lin's way were not successful in our conditions. Our first attempts in order that the reaction occurs were to change the catalyst and to use the one used by Bauerle's: $Pd_2(dba)_3$ (see Fig. 25). This trial was unsuccessful. Then it was tried to increase the catalyst yield to 6 mol %, rather than 2 mol %, but a variation of this sole parameter did not permit the one-pot synthesis of **(1)** in high yields. Since Lin described that the solvent used for the reaction was dry, the water content of the toluene that we had used for all our trials was measured by a Karl-Fisher apparatus. It was found to be 70 ppm, which is a low value, corresponding to

[1] It is noteworthy that the borylation reaction should be performed in very dry conditions and also in order to reduce the homocoupling reaction (see II.A.2.c.i chances to happen, the initial mixture was stirred at room temperature for one hour after all the reagents had been introduced into the reaction flask.

usual value of the commercial “dry” solvents. However, it was tried to operate the reaction, with a highly dry toluene, for which an additional drying step, on molecular sieves (4A) was performed. The value measured for this as dried toluene for the water content was 5 ppm this time. When the reaction was performed, the desired product could be isolated, by recrystallization from methanol, in good yield (72%).

It appears that strict exclusion of water is necessary to get **(1)** in one step and in good yield. Interestingly, it was remarked that only when strict anhydrous conditions were applied, a slight exothermic process was noticed to happen just after the last reagent was introduced … and, hopefully, the reaction was successful! The reason for the high sensitivity of the reaction to water remains unclear. We suggest that the nature of the targeted product (bulky and electron rich TPA) is not the origin of this sensitivity, as for instance the group of Uozumi reported an efficient direct synthesis of TPA, from aniline, in water [11]. They used a resin-supported Pd catalytic system, different from the more classic system which was used for the synthesis of **(1)**. We propose that the nature of the interaction between the catalytic system used for the direct synthesis of **(1)** and water, is a key parameter for the reaction efficiency.

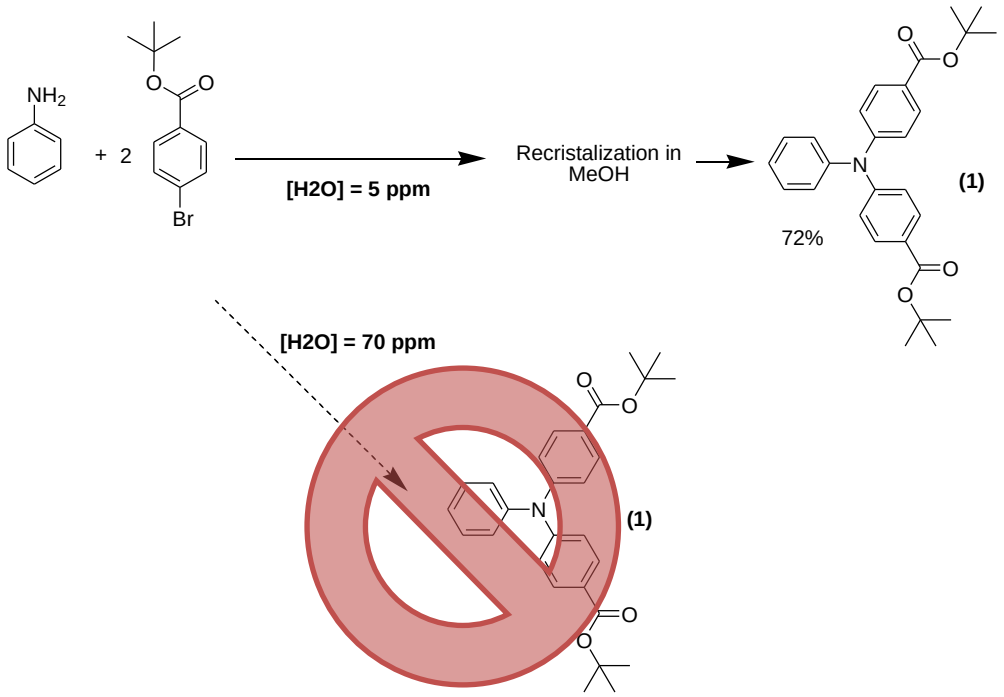


Fig. 28 – Water content influence for the synthesis of (1)

II.A.2.c. Synthesis of the 5 acceptor groups (6), (9), (12), (15) and (19)

II.A.2.c.i. Synthesis of diisopropylphenyl-naphtalimide-bromobithiophen (6)

The synthetic strategy the bromo-bithiophen-naphtalimide derivative was to first functionalize a starting naphtalic anhydride **(A)** with (2,6)-di-isopropyl aniline (see Fig. 29). This synthesis was inspired from literature [12,13] and enabled the formation of the compound **(4).** The presence of *isopropyl* groups on **(4)** permitted that the next synthesis steps were performed with compounds that are soluble in common organic solvents.

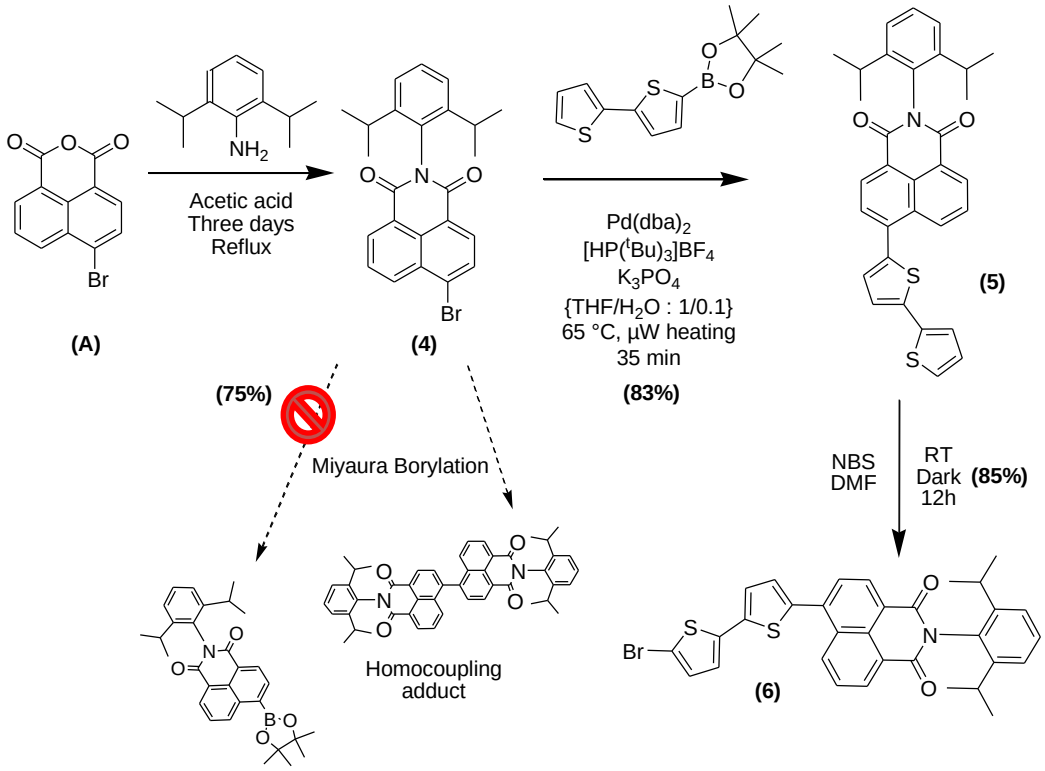


Fig. 29- Synthetic pathway for the obtention of naphtalene accepotr (6)

In order to covalently graft the bithiophen group to the naphtalimide acceptor **(4)**, two options were considered. The first option was to form the pinacol-boronic ester of the naphtalimide derivative **(4)**. The traditional use of BuLi for boronic acid formation was not possible here, since it would induce hydrolysis of the imide function. This is why the Miyara borylation conditions were chosen, since they are known to be very mild and group tolerant [3]. For this, the same reaction conditions as for the borylation of **(2)** were employed. However, with this set of

conditions, it was not possible to isolate the desired product. The parasitic adduct, so called "homocoupling product" which comes from the consecutive reaction between the boronic ester formed and the starting brominated product was predominantly obtained (see Fig. 29). For this, a second strategy was operated. It was intended to use the commercially available bithiophen boronic pinacol-ester, as the boron reagent in the SM cross coupling reaction. This strategy was successful and permitted to obtain **(5)** in good yields (83%). It is worth mentioning that the reaction was performed under microwave heating. The reaction conditions were very similar to those used for the coupling of the various synthesized acceptors with triphenylamine, described in the next part, which gives further synthetic details. Finally, the bromination of **(5)** was performed with NBS. This electrophilic addition permitted the synthesis of the desired brominated bithiophen naphtalimide acceptor group in good yield (85%) **(6)**.

II.A.2.c.ii. Synthesis of the methylene-derivative acceptors (9), (12) and (15)

The three methylene derivatives were synthesized in association with Dr. J.M. Raimundo (CEISAM, Marseille). Acid-catalysed Knoevanagel condensation was used in order to condensate the different acceptors onto bromo-bithiophen-aldehyde (see Fig. 30).

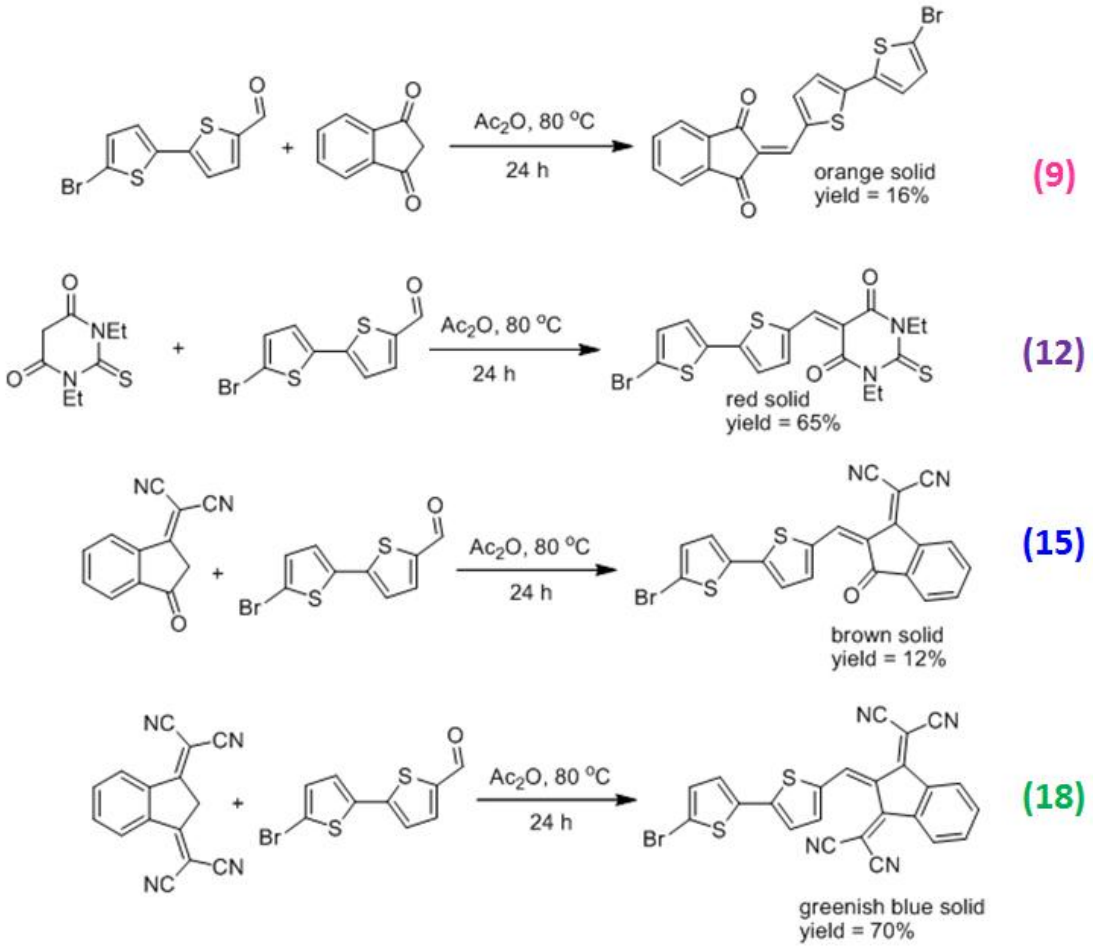


Fig. 30- Synthetic pathaway summary for the three bithiophen brominated acceptors (9), (12), (15) and (18). The synthesis was performed by Praveen Chandrasekar (CINAM, J.M. Raimundo's group).

II.A.2.d. Microwave assisted Suzuki-Miyaura cross coupling of the various acceptors with TPA - Synthesis of (7), (10), (13), (16) and (19)

The various brominated acceptors synthesized (*vide supra*) were coupled with the boronic-acid pinacol ester triphenylamine **(3).** SM cross coupling conditions were employed, with microwave irradiation assistance (see Fig. 31). The catalytic system employed here was $\{Pd(dba)_2/[HP^tBu_3]BF_4\}$. It is a classical system for efficient Suzuki coupling and is known for its

high activity [14]. On this aspect, further details were gathered in annexe 2. Moreover, the microwave irradiation permitted to shorten the time of reaction and undoubtedly enhanced the yield of the synthesis. The base used K_3PO_4 is also classical [4,15,14]. One should remark it was necessary to grind the base so that the reaction is successful. The solvent mixture used: {THF / H_2O}: {1/0.1}, is classical too. The 10% water content is thought to enhance the base solubility in the reaction mixture. With these experimental parameters, good yields were obtained for compound **(7)**, **(10)**, **(16)**.The synthesis of the thiobarbituric-acid derivative **(13)** permitted to isolate the product (15% yield). However, the tetracyano compound **(19)** could not be synthesized in these conditions.

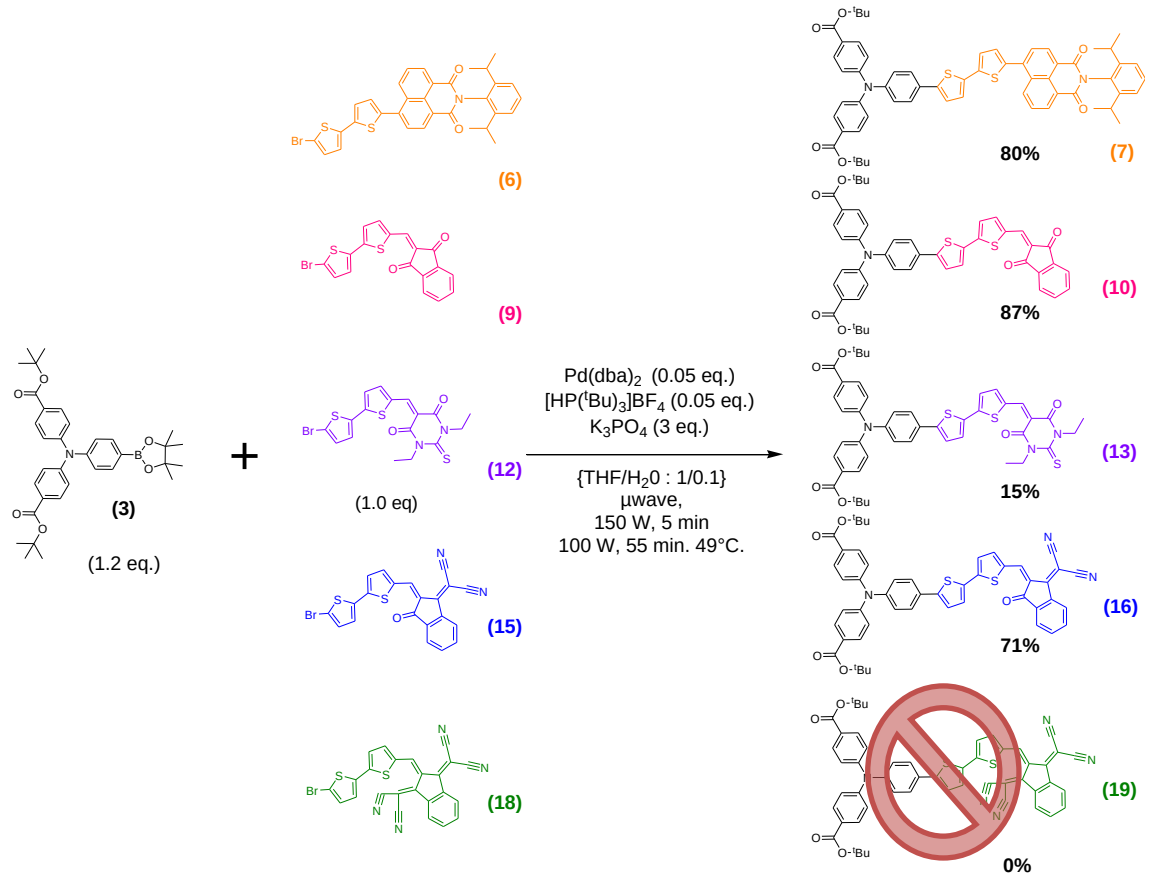


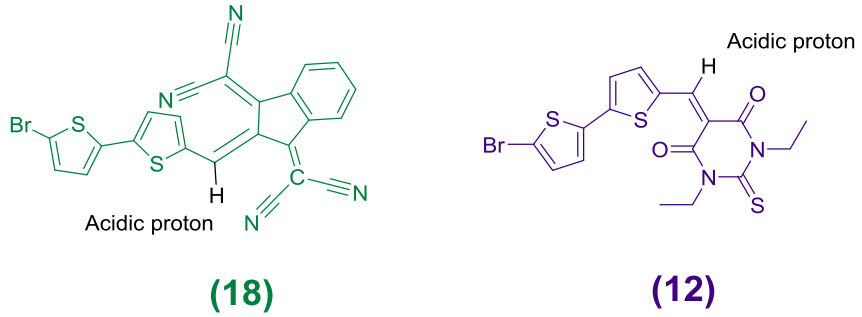
Fig. 31- SM coupling of the different brominated acceptors with TPA (3), under microwave assisted heating.

We think that the reaction was not successful for the last two compounds **(13)** and **(19)**, due to their sensitivity to basic conditions. In fact, as shown on Fig. 32 and Tab. 2, for these compounds, the proton that is close to the accepting group may display an acidic character (so called

"$H_{ethylenic}$"). NMR analysis confirms this idea since the chemical shifts of these protons indicate that they are strongly deshielded.

Tab. 2- ^{1}H NMR chemical shift (ppm) of $H_{ethylenic}$ for the different bithiophen compound (9), (12) and (15), in $CDCl_3$

Compound	(9)	(12)	(15)	(18)
Chemical shift (in ppm) for $H_{ethylenic}$,	8.07	8.67	8.82	9.91



(18) **(12)**

Fig. 32- Very acidic proton may be responsible for tbe low efficiency of the reaction.

Microwave heating, applied to Suzuki cross coupling is quite a recent technique. Actually, the first reported example goes back to 1996 [16].This method generally provides high synthetic yields and dramatically reduces reaction time, compared to conventional heating methods. The reasons for such efficiency are briefly reminded and explained in this paragraph. Provided the medium is polar, the energy is somehow focused into the system: microwaves penetrate the whole reaction flask, from the edges, to its heart and heating can be generated just next to any reaction center, through dipole-dipole frictions. Then, a ready to use and important quantity of thermal energy is available for the desired chemical reaction to happen and is not limited by the thermal conductivity of the medium. Also, as the quantity of energy generated by dipoles friction is important and quickly generated, it sometimes can not be easily evacuated, then superheating phenomena can happen (for instance the solvent boiling point can be overstep !) and this can even generate hot spots [16]. These local high temperatures can be responsible for enhancement of the reaction yield and reduction of completion time. As a consequence of this more efficient heating process, microwave heating applied in organic chemistry has also been proven to save a huge

amount of energy, compared to traditional heating methods[17]. For all this, this technique is sometimes depicted as being part of green chemistry [18].

II.A.2.e. Deprotection with TFA - Synthesis of the final compounds (8), (11), (14), (17)

The protected ester compounds **(7)**, **(10)**, **(13)** and **(16)** were finally and successfully deprotected with 25 equivalents of TFA per ester functions, in DCM (see Fig. 33). This method is a very common method for the deprotection of triphenyl-amine terbutyl ester protected dyes [15,6,19].

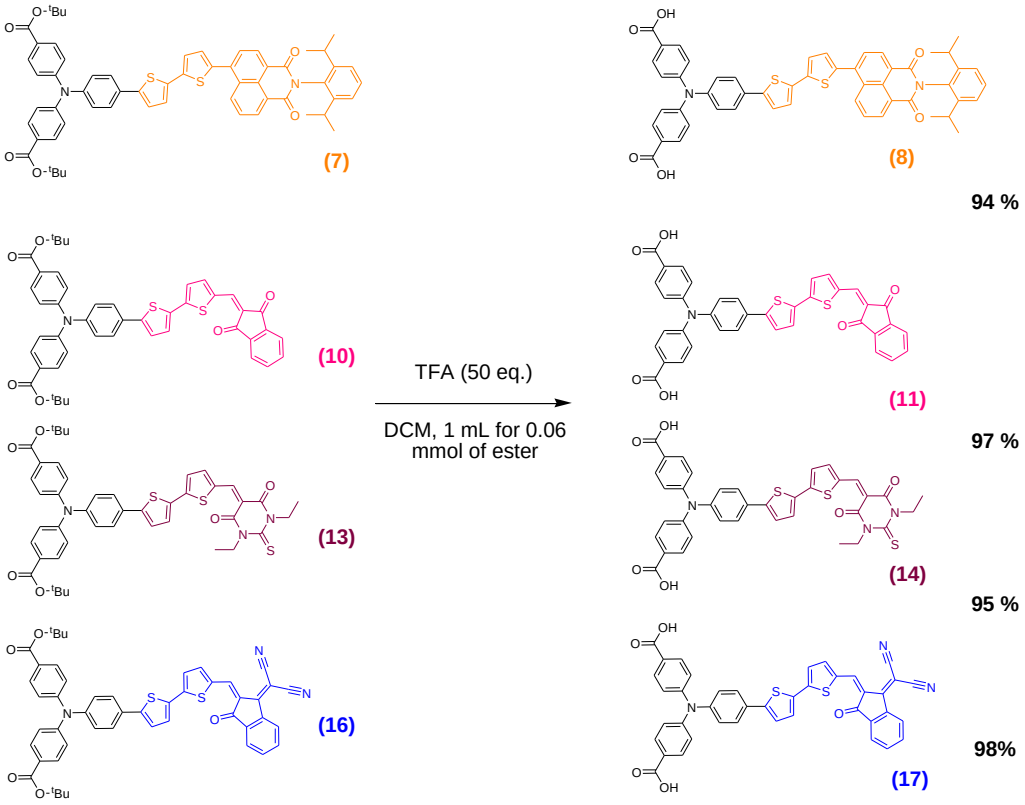


Fig. 33- Deprotection of the tertbutyl est compounds with TFA.

II.A.3. **Toward DPP derivatives**

With the aim of increasing the absorption range toward the red part of the spectrum, it was intended to introduce the DPP motif in lieu of the bithiophen bridge (see Fig. 20 for the general formula).

II.A.3.a. Targeted synthetic pathway

The retro-synthetic pathway that was purposed for the synthesis of compound is shown on. This pathway actually was inspired from the reaction tools described above. The thiophen-DPP **(20)**

core was first functionalized with alkyl chains (heptyl), so as to enhance its solubility. The mono-bromination of **(20)** out of NBS was expected to be possible according a publication by Lambert el al.[20], using very short reaction time. And then, with similar coupling reactions as for the bithiophen dyes described above, the desired TPA-DPP-Acceptor derivatives were targeted.

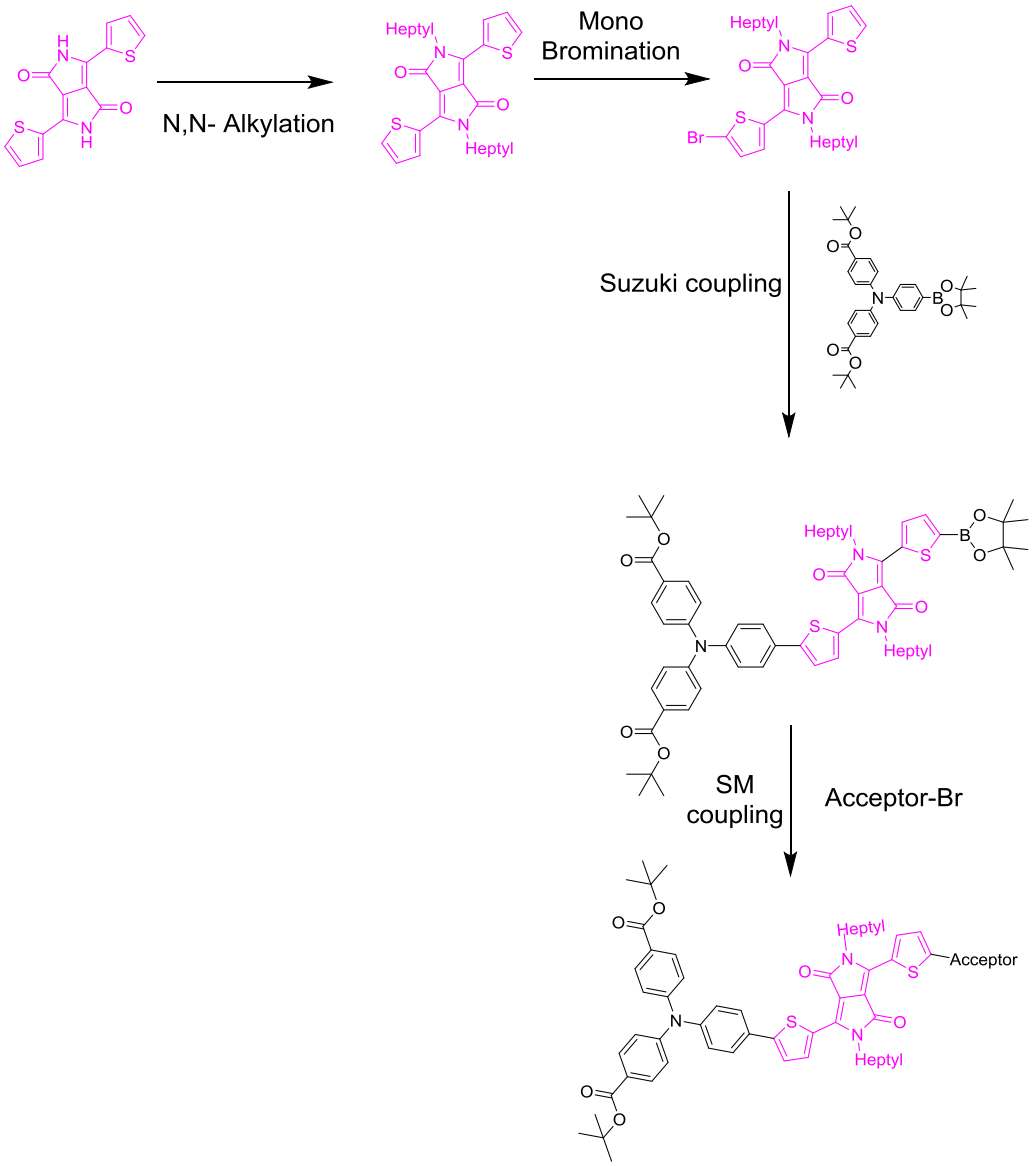


Fig. 34- The strategy to obtain thiophen-DPP derivatives

II.A.3.b. Synthesis of the dyes with DPP skeleton

The first step concerns the synthesis of the diheptyl derivative **(20)** according the literature. The reaction of N-alkylation was performed with 1-bromooctane with 55% yield [20].

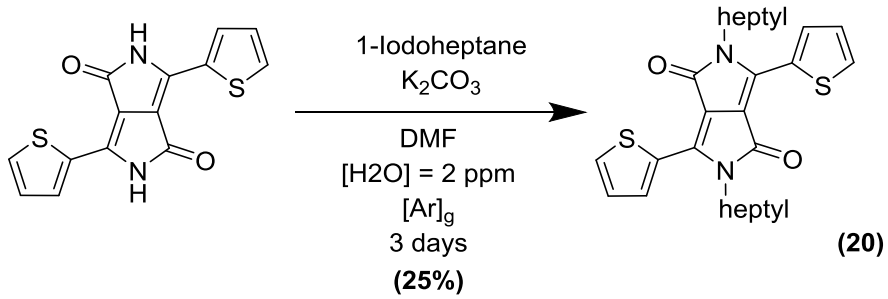


Fig. 35- Reaction conditions for the synthesis of (20)

As a matter of fact, in the present work, an iodinated chain was preferred. Indeed, due to the higher polarisabilty of the C-I bound, compared to a C-Br bound, the reaction was expected to have an increased yield. Despite that, it was moderate (25%). The heptyl, different but close to the octyl chain; is not thought to be the reason for this discrepancy.

An explanation could be that side reactions of the heptyl-iodide are in this case important, because of the five equivalents employed (like in the Lafleur-Lambert publication [20]). In order to increase the yield, it should be tried to use less equivalents of 1-iodoheptane. Two equivalents [21,22] or 2,5 equivalents[23] may actually induce a better yield as reported. The duration of the synthesis might also be an important parameter for the success of the reaction and should be shortened to 24 hours or one night, like it is done in the majority of the publications [21,23].

The reaction was also found to be highly water sensitive. Indeed, the first synthetic trials were not strictly anhydrous and the reaction appeared to be quenched with water traces (0% yield). Operating in strictly anhydrous conditions (2 ppm of water determined by Karl-Fischer) made it possible to get quantitative amounts of the desired. Interestingly, a piece of explanation could be found in Stas et al. publication[22]. They isolated a side product (in the case of DPP alkylation with branched brominated chain) which they attributed to the hydrolysis, with water traces, of the halogenated derivative (see Fig. 36). In addition, other side products, such as the mono-alkylated DPP derivative[22], or some O-alkylated product, which were actually isolated by Frebort et al.[24] could explain the moderate yield of the reaction.

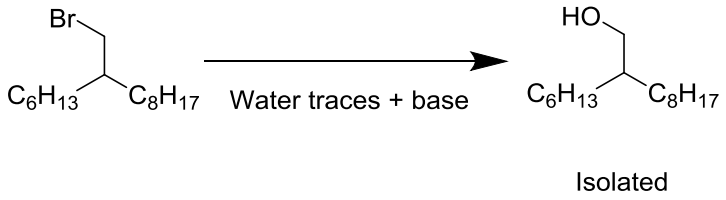


Fig. 36 - Hydrolysis of the halogen derivative in the presence of water, during the N-double alkylation of a DPP-dithiophencore

After **(20)** isolation, it was intended to perform the mono-bromination of one of the two nucleophilic positions of **(20)**. This step corresponds to a disymetrisation of the compound. In our conditions however, this reaction was unsuccessful, mainly leading toward the dibrominated product. This is why, is was chosen to keep going with this dibrominated derivatives, and to perform the disymetrisation at the next step, during the purification step by separation of the di-triphenylamine adduct with the mono-triphenylamine desired product..

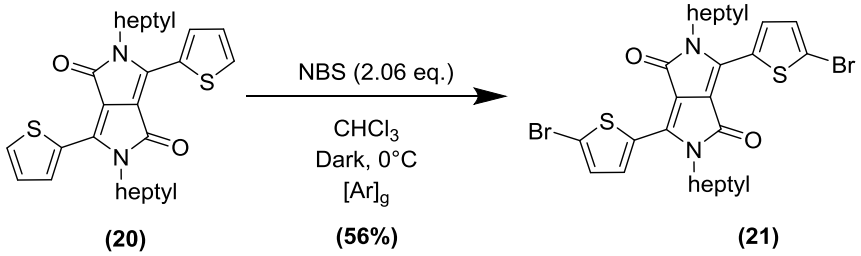


Fig. 37 - Reaction conditions for the synthesis of (19)

Then, di-bromination of compound **(20)** was successfully carried out with NBS in the dark and at 0°C. (Fig. 37). Considering that NBS is equivalent to "Br^+", in terms of reactivity, the moderate yield of the reaction (56%) could be explained by the competition between the various nucleophilic sites of the DPP core as described by Wallquist [25] (cf. Fig. 38).

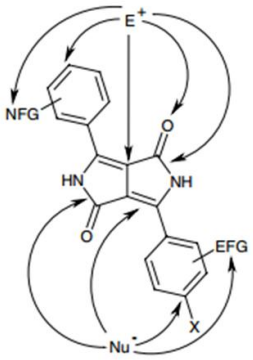


Fig. 38 – Electrophilic and nucleophilic positions of a DPP core (reproduced from Wallquist, O, High Performance pigments, Wiley-VCH, 2001; pp 170) .

The brominated DPP skeleton was coupled with TPA in the same conditions as for the four bithiophen acceptors described above (II.A.2.e). Unfortunately, only the product resulting from the consecutive double coupling of the two triphenyl amine on the DPP core could be isolated (Fig. 39. This was attributed to the low solubility of the initial DPP derivative in the reaction mixture (as a reminder, the solvent system that was used was {THF/H_2O : 1/0.1}). We think the association of this low solubility and the microwave heating is responsible for the mono-coupling desired product not to be formed quantitatively. Several attempts were performed in order obtain the targeted mono coupled product. Conditions similar to literature for symmetric phenyl-DPP di-brominated compounds were un-successful [26, 27, 28] as well as a tentative to add the TPA derivative was dropwise, at a very slow rate. However the solubility issue of the initial derivatives could not be addressed. It could be tried to operate the reaction with a large excess of DPP compound, rather than the one equivalent employed here. Another strategy could be to form the boronic ester species of the DPP core and to perform the coupling reaction with the iodine derivative of the TPA **(2)**. Eventually, the targeted thiophen DPP dye could not be isolated unfortunately.

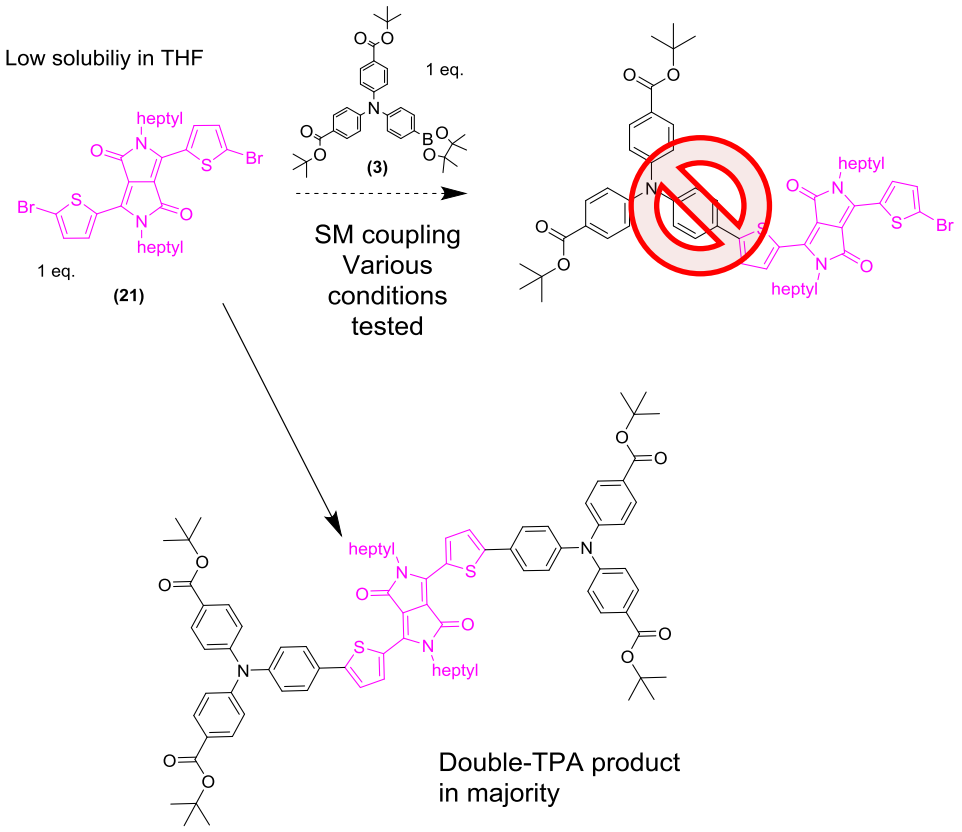


Fig. 39- The double TPA product, obtained as a majority product when SM coupling was performed between (21) and the TPA-boronic ester (3).

II.A.4. Conclusions

In this part, four new bithiophen push-pull dyes were synthesized, all bearing a TPA electron rich entity, a bithiophen as the Pi-linker, and various new acceptors [m], of gradually increased strength. One naphtalimide derivatives was obtained, alongside with two indanes and one thiobarbituric derivative.

The key steps for their synthesis being an efficient SM cross-coupling reaction, assisted by microwave irradiation and the synthesis of the donor entity, in drastically inert conditions. Further synthetic efforts should however be performed in order to synthesize the indane-tetracyano acceptor and the targeted DPP derivatives, which are expected to display suitable features for NiO based photocathodes.

[m] For push-pull dyes for p-type DSSCs.

II.B. Physical properties of the synthesized dyes

The optical and electrochemical properties of the four bithiophen dyes synthesized are assessed in this paragraph. Experimental work was corroborated with quantum calculation, in order to better read into the dyes' physical properties. For practical issues, the results of these calculations are gathered in annexes 3.

II.B.1. Electrochemical studies

The redox properties of the different bithiophen dyes were assessed in solution, by the mean of cyclic voltammetry. In a first attempt, it was purposed to find a common solvent for all the compounds, so as to be able to make relevant comparisons. However, for compounds with indane group, due to the flatness of the Pi-conjugated skeleton (Pi-staking) and to the presence of two carboxylic acids, solubility in common organic solvents was reduced. Actually, only DMF was found suitable to solubilize all the dyes. Thus the electrochemical work was firstly performed in DMF.

II.B.1.a. Electrochemical studies of the dyes in DMF

The cyclic voltammograms of the bithiophen dyes in DMF are displayed on Fig. 40 and the redox potentials are summarized in Tab. 3. All the dyes display oxidation waves that are not well defined and not reversible, at approximately +1.30 V *vs* NHE. An irreversible reduction wave is also observed for all dyes except dye **(8)**. The most puzzling observation is that in DMF all the dyes possess similar reduction potentials. This fact does not match with the properties of the different accepting groups present on the molecules. Moreover, the reduction potentials are not in agreement with the theoretical LUMO levels of the dyes, which were found very different from one another (see Fig. 42).The reason for the discrepancy is unclear, but it can be proposed that in presence of DMF, the acceptor based on indane motifs exists in another form (aggregate, zwitterionic form …[29]). For this reason, the redox properties of the dyes were studied on their *tert*-butyl ester version, in dichloromethane (DCM).

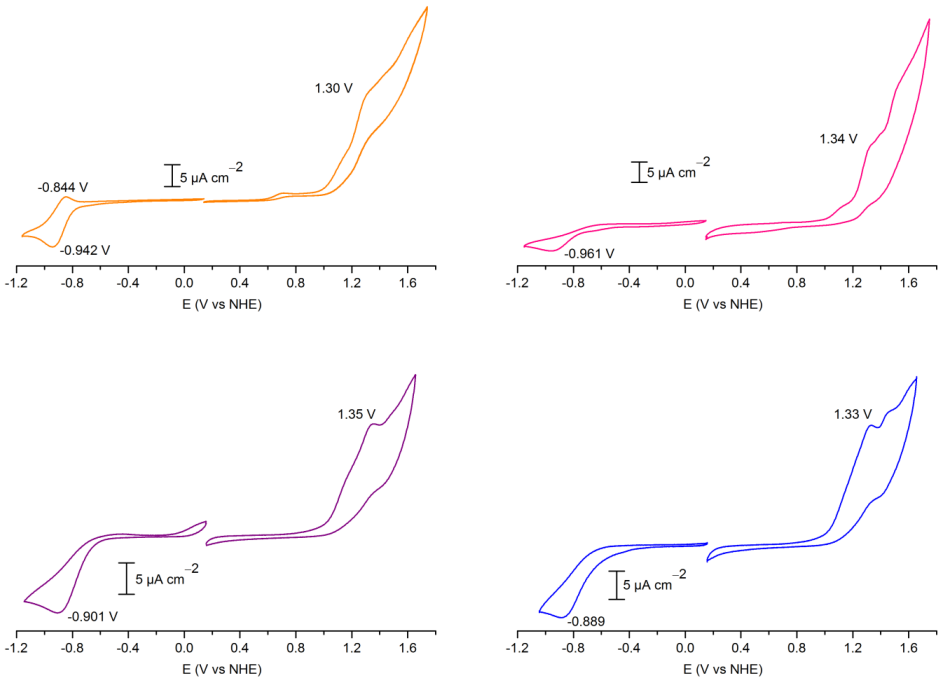


Fig. 40- The cyclic voltammetry of (8), (11), (14) and (17) in DMF respectively from top left corner to down right corner.

Tab. 3- Electrochemical data of the four bithiophen dyes in DMF. The potentials are referred to NHE reference electrode.

Compound	E_{red} (V)	E_{ox} (V)
(8)	-0.89	1.30
(11)	-0.96	1.34
(14)	-0.90	1.35
(17)	-0.89	1.33

II.B.1.b. Electrochemical work on the tert-butyl ester protected version of the dyes

The cyclic voltammograms of the dyes, in DCM, on their *tert*-butyl ester protected version are displayed on Fig. 41. The results are summarized in Tab. 4.

Tab. 4- Redox potentials of the bithiophen dyes in DCM. The redox potentials are reported *vs* NHE reference electrode.

Compound	E_{ox} (V)	E_{red} (V)
(7)	1.20 / 1.44	-0.98
(10)	1.27	-0.75
(13)	1.28	-0.58
(16)	1.27	-0.41 / -0.86

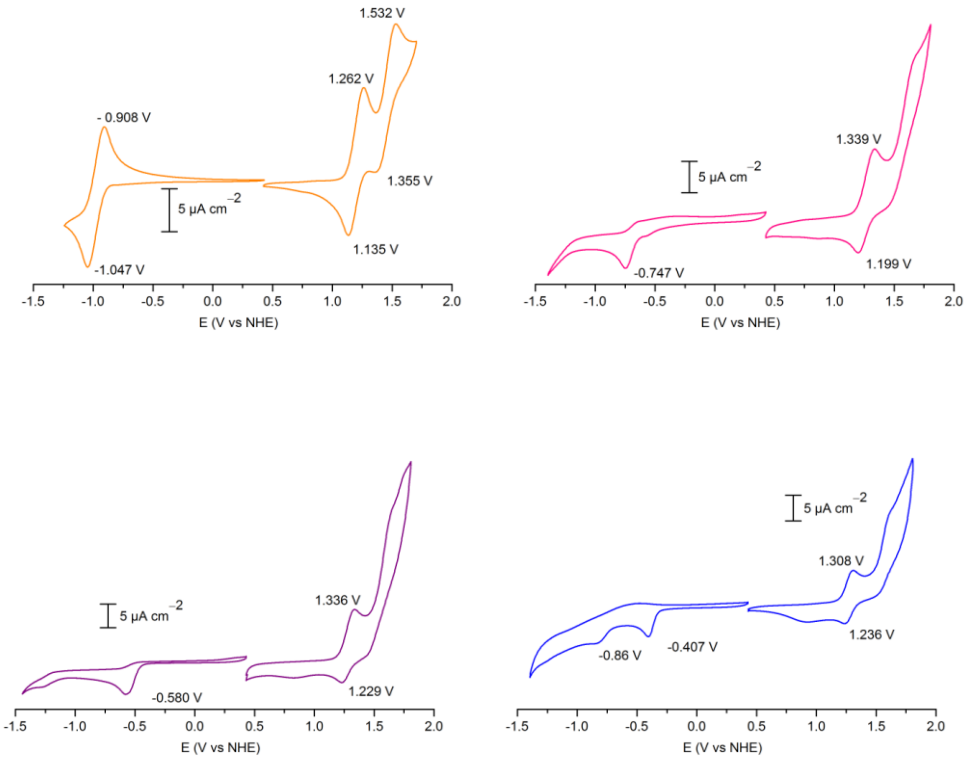


Fig. 41- Cyclic voltammetry of (7), (10), (13) and (16) in DCM, respectively form upper left corner to down right corner.

This time, the dyes display reduction potentials which dramatically differ from one another. This experimental result is more in agreement with the theoretical calculations and the different structure of the molecules. The dyes' reduction potentials follow this trend: stronger is the acceptor, more positive is the reduction potential of the donor-acceptor molecule. This observed trend is in good agreement with the trend observed with the theoretical calculations, for the evolution of the LUMO levels as one can see on Fig. 42. One can remark that for dye **(16)**, a

second reduction wave is noticed at -0.86 V *vs* NHE. This value is close to the one obtained for the reduction potential found for the deprotected compound in DMF. It is possible that in DCM, part of dye **(16)** molecules exists in the same form as **(17)**.

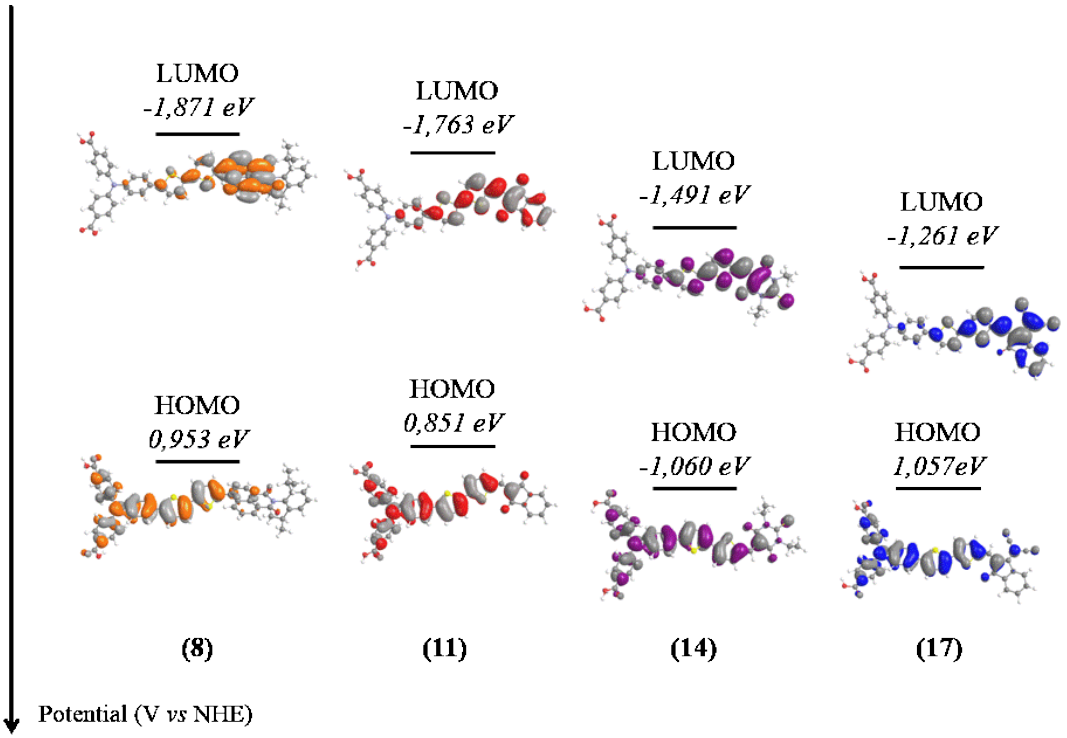


Fig. 42- Theoretical HOMO / LUMO levels, for the different bithiophen dyes (under their protected *tert*-butyl version)

The reduction process is governed by a reversible reduction wave for dye **(7)**. This reversibility is due to the great chemical stability of the radical-anion generated after electron injection. This stability may be permitted by the large electron delocalization into the naphthalene system. For the other dyes reduction are irreversible. This is probably due to their ethylenic function, which is situated in the electron accepting part. As suggested in the work by Oliva et al.[1] it is possible that after reduction of the colorant, the obtained radical anion dimerizes due to the reactivity of the double bond induced by the ethylenic hydrogen atom.

All the dyes possess very similar first oxidation potentials (see Tab. 4), between 1.20 V and 1.28 V, *vs* NHE. These values are in the same range as for the values in DMF. It was however not possible to precisely compare the values regarding the influence of the electron withdrawing carboxylic acid groups over the oxidation potential of the dyes, due to the poor resolution of the CV in DMF.

The fact that the dyes possess similar oxidation potential is in agreement with their common electron rich combined TPA-bithiophen moiety, which manages the oxidation process. One can remark that for **(7)**, the first oxidation potential is slightly more positive than for the other dyes (70 mV of difference). This result emphasizes that for **(7),** the electron donor part feels less the electron withdrawing influence of the acceptor. Dye **(7)** possesses a large dihedral angle (43.7°, see annexe 3) at the level of the link between the bithiophen and the NI unit, this represents a conjugation break. In the case of the dyes with indane motifs, the Pi-skeleton is very flat and facilitates interactions between the donor part and the acceptor part of the molecule. The shape of the HOMO orbitals of the dyes also supports this result. For dye **(7)**, the HOMO does not reach the accepting moiety of the dye contrary to the indane derivatives for which the HOMO is conjugated over the entire molecule.

For all the dyes, the oxidation process is governed by a first oxidation wave which is quasi-reversible. This may illustrate the stability of the radical cation created after oxidation, due to the partial delocalization of the radical electron through the thiophen bridge which is largely involved in the HOMO orbital.

A second oxidation wave also occurs. This wave is quasi-reversible for **(7)** but hardly distinguishable or quasi irreversible for compounds **(10)**, **(13)** and **(16)**. In a study of different push-pull compounds bearing amino-derivative donor groups Oliva et al. [30] suggested that the irreversibility of the second oxidation in such compounds is due to the spreading of the positive charge to the electron acceptor moiety, which leads to great instability of the molecule and then degradation. In the case of the flat compound **(10)**, **(13)** and **(16)**, we propose that the enhanced Pi-communication between the donor part and the acceptor part, due to the flat structure of the molecule may also promote easier decomposition. In the case of **(7)** the dihedral angle evoked above may help preventing the spreading of the positive charge after the second charge injection to the electron poor part and then renders the second oxidation wave quasi-reversible.

II.B.2. Steady state optical properties

The steady state optical characterization of the four bithiophen compounds is presented here. In order to be in agreement with the electrochemical work, the analyses were performed on the *tert*-butyl ester protected version of the dyes in DCM. Also, the presence of the *tert*-butyl protecting groups is thought to be important so as to avoid unwanted aggregate formation.



Fig. 43- The four *tert*-butyl ester protected dyes in DCM. From the left to the right: (7), (10), (13), (16).

II.B.2.a. Steady state UV/Visible absorption spectra

The UV visible absorption spectra of the four bithiophen dyes are presented on Fig. 44. The relevant optical properties of these dyes are all displayed in Tab. 5. All the dyes display two main and intense absorption bands. The highest energy band is centered at approximately 360 nm, and its intensity vary between 30 000 and 50 000 $mol^{-1}.L.cm^{-1}$.

The low energy band's features vary from one dye to another. The main observation is that when the strength of the acceptor is increased, this band shifts toward higher wavelengths: 442 nm for **(7)**, 519 nm for dye **(10)**, 542 nm for dye **(13)** to 590 nm for **(16)**. This result explains the distinct colors of the dye molecules in solution (see Fig. 43). As expected, the theoretical calculation results reveal the HOMO / LUMO push-pull nature of the transition associated to this band (see annexes for the simulated spectrum). An important charge transfer happens from the donor site to the acceptor site, upon irradiation. In agreement with the electrochemical work, the increase of the

acceptor strength is responsible for the lowering of the LUMO and the shift of the peak absorption wavelength toward high wavelengths.

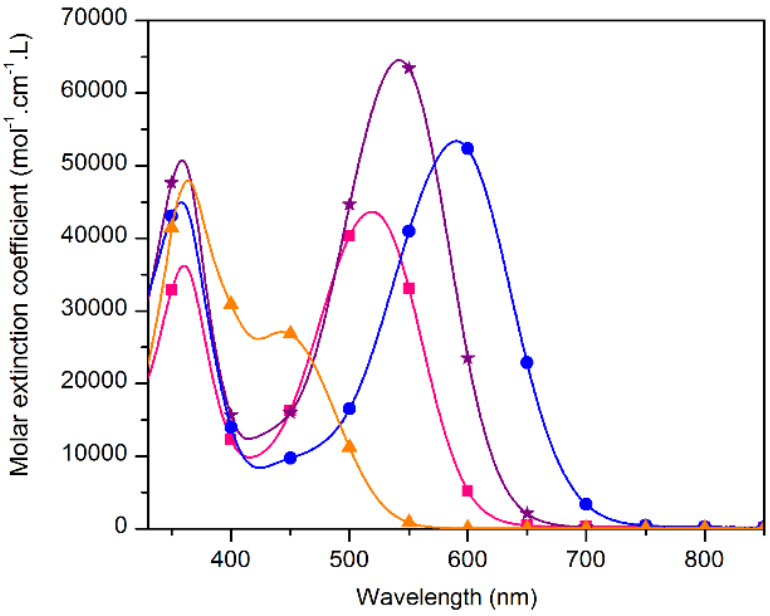


Fig. 44- Absorption spectrum in DCM of the *tert*-butyl ester protected version of the dyes.

Dye 7 = Orange (triangles), Dye 10 = pink (squares), Dye 13 = purple (stars), Dye 16 = (circles).

A second important feature for the low energy band is its important width and also its high to very high intensity. Dye **(7)** displays the less intense transition, with a peak molar extinction coefficient of 27 100 $mol^{-1}.cm^{-1}.L$. This result is to be linked with a less important HOMO / LUMO overlapping than for the other dyes (see Fig. 42), the shape of the HOMO/LUMO orbitals was displayed), due to the conjugation break between donor and acceptor entities. The indane derivatives display more intense transitions, ranging from 43 700 $mol^{-1}.cm^{-1}.L$ for dye **(10)** to 53 400 $mol^{-1}.cm^{-1}.L$ for dye **(16)** and finally reaching 64 500 $mol^{-1}.cm^{-1}.L$ for dye **(13)**. This high values reflects an excellent HOMO / LUMO orbital overlapping, which facilitates the light induced electronic transitions. This excellent overlapping is itself due to the flat geometry of the indane derivatives. Dye **(13)** is actually almost perfectly flat[n]. It is worth stressing the very high

[n] Another point which could be stressed here is the evolution of the epsilon value as a function of the interthiophen dihedral angle. These dihedral angles are described in annex 3 for each compound. The following correlation can be made: the more important the dihedral angle, the smaller the epsilon value. If one sees the push-pull transition as a movement of electrons from the donor site to the acceptor site, this correlation could make sense. The angle between the two thiophens could act as a “brake force” for the

molar extinction value for **(13)** at the peak wavelength (64 500 $mol^{-1}.L.cm^{-1}$). This value is not far from the actual best performing double-acceptor push-pull dyes [31,19] (which display molar extinction coefficients in the range of 90 000 $mol^{-1}.L.cm^{-1}$). If one considers the mono-acceptor design of these dyes, the value obtained almost equalizes the performance of the strongest absorbing dye in this category, synthesized by Lin et al. (so called "dye 6", 67 600 $mol^{-1}.L.cm^{-1}$, see Fig. 10 in the chapter 1 for the chemical formula) [6].

Finally, for dyes **(13)**, and **(16)**, it is worth mentioning an additional intermediate transition at approximately 430 nm and 440 nm respectively, with average molar extinction coefficients around (*ie.* between 10 000 and 15 000 $L.mol^{-1}.cm^{-1}$). Quantum chemistry calculations permitted to attribute this band to a push-pull transition. The calculations also permitted to establish that this intermediate band was also present for **(10)**. This band could not be experimentally discerned. This is certainly due to the overlapping between the low and high energy bands which are closer in the case of dye **(10)** than for the other indane dyes.

Tab. 5- Absorption energies and intensity of the different absorption bands for the four bithiophen dyes.

Compound	**Low energy band** λ_{max} (nm), $\varepsilon_{\lambda max}$ ($L.mol^{-1}.cm^{-1}$) **CT band**	**Intermediate band** λ_{max} (nm), $\varepsilon_{\lambda max}$ ($L.mol^{-1}.cm^{-1}$) **CT band**	**High energy band** λ_{max} (nm), $\varepsilon_{\lambda max}$ ($L.mol^{-1}.cm^{-1}$) **Donor centered**
(7)	442 (27 100)	X	364 (47 970)
(10)	519 (43 700)	Not experimentaly distinguishable	361 (36 221)
(13)	542 (64 500)	430 (13 000) [(a)]	359 (50 674)
(16)	590 (53 400)	440 (9 000) [(a)]	358 (44 924)

(a) The maximum absorption wavelength as well as the molar extinction coefficients were largely approximated.

electron periodic movement upon light irradiation. The extremely flat geometry of dye **(13)** could represent an "ideal" situation for obtaining high epsilon value.

II.B.2.b. Steady state emission spectra

This work was performed by Valentin Maffeis (collaboration with Thomas Gustavsson, CEA Saclay)

The steady state fluorescence behavior of the four bithiophen dyes was assessed. The low energy band as well as the high energy band were excited. All the dyes were found to be emissive for both bands. The fluorescence spectra are displayed in Fig. 45. For clarity, the low energy band is called $S_0 \rightarrow S_1$ and the high energy band is called $S_0 \rightarrow S_2$, in regard of the respective excited states that are generated.

The $S_0 \rightarrow S_1$ transition generates a fluorescence band which structure is complex (presence of shoulders) and differs from one dye to another.

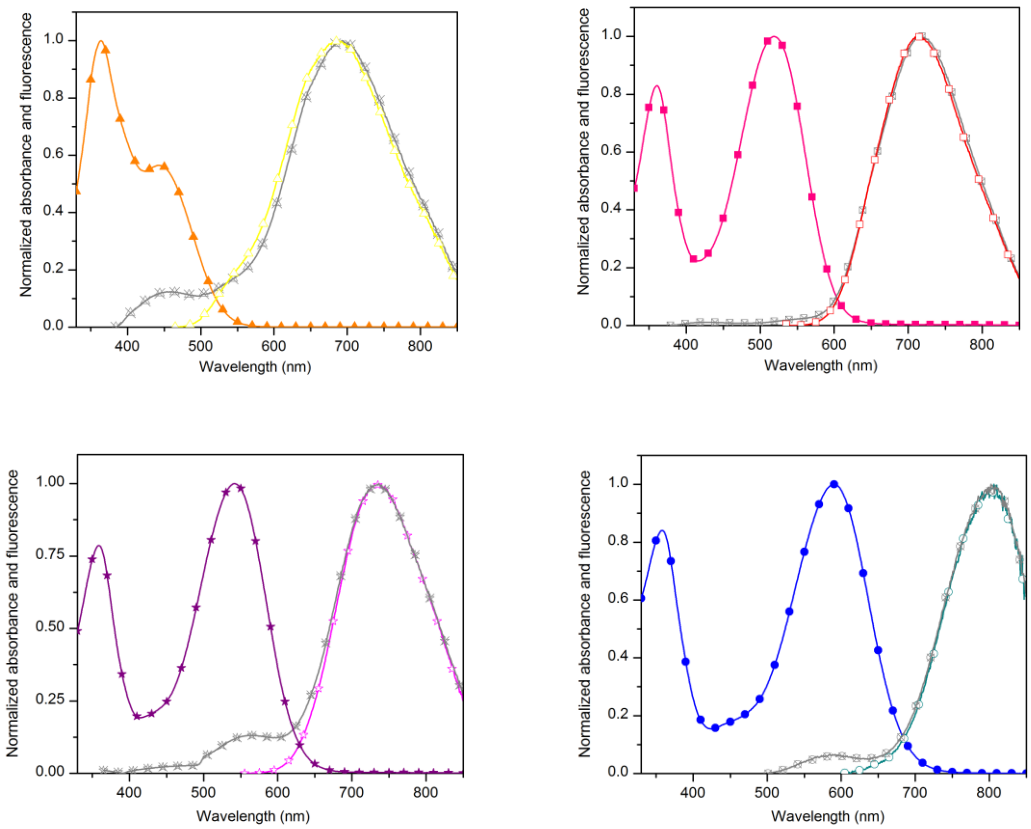


Fig. 45- Absorption-fluorescence spectrum of the *tert*-butyl-ester protected version of the bithiophen dyes in DCM.In color and filled shapes, absorption spectrum of the protected dye in DCM, same legend as in Fig. 44.In grey (crossed shapes), the emission spectrum after $S_0 \rightarrow S_2$ transition (excitation at 350 nm). In light color (empty shapes), the emission spectrum resulting from the $S_0 \rightarrow S_1$ transition. Dye (7) (excitation at 450 nm) = Yellow trace, empty triangles. Dye (10) (excitation at 520 nm) = red trace, empty squares. Dye (13) (excitation at 540 nm) = pink trace (empty stars). Dye (16) (excitation at 590 nm) = empty circles.

Large Stoke shifts (see Tab. 6) were observed for the dyes (246 nm for dye **(7)** and values around 200 nm for the indane derivatives). This large Stoke shift signifies different structure for the ground state S_0 and the excited state S_1. Considering the large Stoke shift, the charge transfer (CT) nature of the $S_0 \rightarrow S_1$ transition and the relative polarity of the solvent employed (DCM), which helps stabilizing a CT stat, we suggest that the main emission band corresponds to the steady state fluorescence of a long-lived CT state (see Fig. 46).

The $S_0 \rightarrow S_2$, donor centered transition, generates two emission bands. The first one, high energy band, has a relative intensity which is low compared to the second one. The absence of this band for **(10)** is noted. This band could corresponds to the fluorescence of a so called S' state which nature is unknown. The low fluorescence of this state could correspond either to its inherent low population, or, to important quenching. Further investigations should be performed in order to understand better S'. The second emission band coincides with the emission induced by the main $S_0 \rightarrow S_1$ transition for all the dyes. This results suggests that the high energy, $S_0 \rightarrow S_2$ absorption band eventually induces a transfer to the CT state. Considering that the $S_0 \rightarrow S_2$ transition is donor-centered, it is assumed that an electron shift from the donor to the acceptor follows the $S_0 \rightarrow S_2$ transition. It could be seen as a reduction of the acceptor group by the excited donor entity.

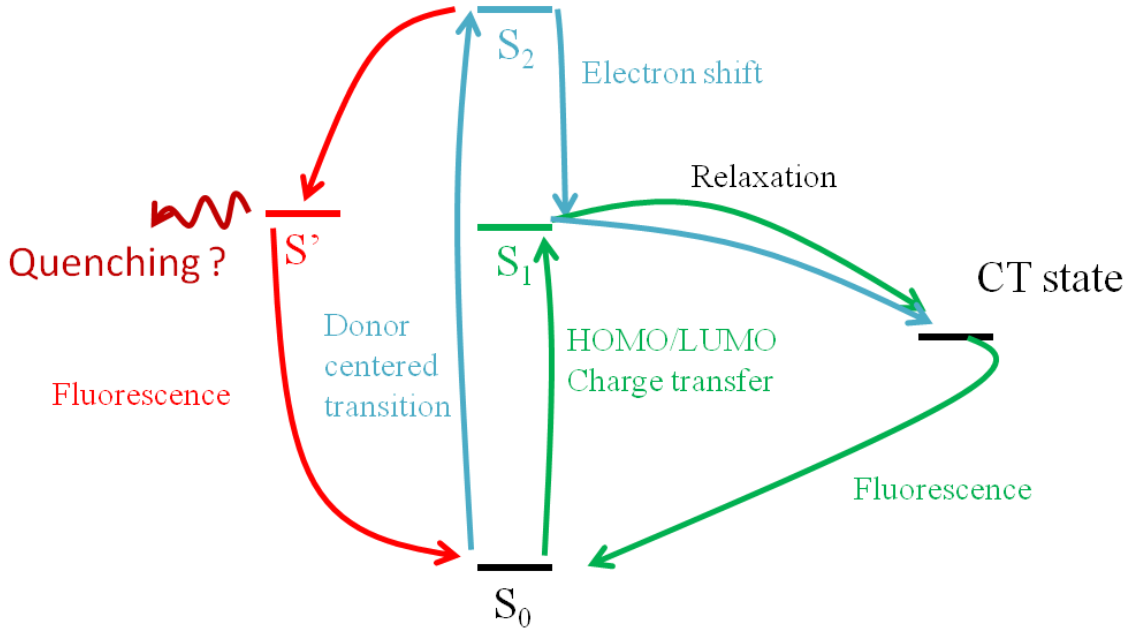


Fig. 46- A possible and very simplified scheme for the different optical transitions involved for the dyes.

From the steady state absorption spectra, the $E_{0\text{-}0}$ transition energies were reasonably estimated from the intersection of the normalized absorption and emission spectrum (normalization performed at the low energy band level). The $E_{0\text{-}0}$ values, alongside all the properties of the charge transfer low energy band were gathered in Tab. 6.

Tab. 6- Summarized spectroscopic properties of the four bithiophen dyes for the low energy CT band, in DCM, on the protected version of the compounds.

Compound	$\lambda_{abs,max,CT}$	ε_{max} ($L.mol^{-1}.cm^{-1}$)	$\lambda_{em,max,CT}$ (nm)	$\Delta\lambda$ (nm) (a)	$E_{0\text{-}0}$ (eV) (b)
(7)	442	27 100	688	246	2.38 **(c)**
(10)	519	43 660	716	197	2.05
(13)	542	64 530	732	190	1.97
(16)	590	53 390	802	212	1.81

(a) Stoke shift of the compounds. $\Delta\lambda = \lambda_{em,max,CT} - \lambda_{abs,max,CT}$. **(b)** $E_{0\text{-}0}$ energy was calculated with the following equation $E_{0\text{-}0} = 1240 / \lambda_{0\text{-}0}$, were $\lambda_{0\text{-}0}$ is the intersection wavelength between the normalized absorption and emission spectra, for the CT band. The absorption spectrum had been normalized versus the CT band this time. **(c)** $E_{0\text{-}0}$ was also estimated considering at the 10% of the maximum amplitude level of the CT band, due to the complex structure of the fluorescence spectrum of **(7)**. The same value of 2.38 eV was found.

II.B.3. **Summary and conclusion**

The electrochemical work, as well as the quantum chemistry calculation, show that the four bithiophen dyes possess different HOMO / LUMO gaps. This is due to a gradual decrease of the LUMO level of the dye, when the strength of the acceptor is increased. This trend tunes the absorption wavelength and the energetic levels of the different molecules. The redox and optical properties of interest for p-type DSSC application of the four bithiophen dyes are summarized in Tab. 7. The excited state reduction potential was calculated according to the formula described in the first chapter of the thesis. From this, the hole injection driving force (ΔG_{inj}) was also calculated, in the case of NiO. All the compounds show high hole injection driving force (between 740 mV and 840 mV), that renders them suitable for integration in a p-type DSSC device.

Tab. 7- Optical and redox information of interest of the four bithiophen dyes for p-type DSSC application. The properties were assessed in DCM, on the *tert*-butyl ester protected version of the compounds. The potentials are given *vs* NHE reference electrode. Hole injection driving force was calculated regarding NiO and dye regeneration driving force was calculated regarding iodine electrolyte.

Compound	$\lambda_{abs,max,CT}$ (nm)	ε_{max} ($L.mol^{-1}.cm^{-1}$)	E_{0-0} (eV)	E_{ox} (V)	E_{red} (V)	E_{red}^{*} (V)	ΔG_{inj} (eV)	ΔG_{reg} (eV)
(7)	442	27 100	2.38	1.20/ 1.44	-0.98	1.4	-0.84	-0.80
(10)	519	43 660	2.05	1.27	-0.75	1.3	-0.74	-0.57
(13)	542	64 530	1.97	1.28	-0.58	1.4	-0.83	-0.40
(16)	590	53 390	1.81	1.27	-0.41 / -0.86	1.4	-0.84	-0.23

Regarding the recent highlight in the work of Udo Bach [32] (see chapter 1), this high hole injection driving force, though representing an important energy loss, could be an important advantage for these push-pull dyes. Another point is the dye regeneration driving force (ΔG_{reg}), which appears to be high enough to permit efficient photocurrent generation with iodine-based electrolyte with this dye series. These favorable energetic properties, alongside the high to very high molar extinction coefficients, render the synthesized molecules interesting candidates for application in p-type DSSC. This aspect is tackled in the chapter dedicated to the solar cell tests of this thesis (chapter 4). We finish this conclusion by emphasizing the red absorption behavior of the indane dicyano derivative **(17)** of the dye series. The red absorption of this dye is permitted by the low-energy position of its LUMO, which comes from the fact that the LUMO position of the acceptor is more or less conserved in the push-pull dye, when coupling with the triarylamine is done (details were given in annex 3). Judging by the 230 mV driving force, the low lying of the LUMO should still allow for an efficient dye regeneration process with iodine electrolyte, as shown by recent results by Gibson et al. for another red absorbing dye [31]. Efficient red absorbing dye are scarce (at the beginning of this PhD, in 2012, only two of them were reported, see annex 4) and constitute an important step toward the building of efficient tandem solar cells.

References

1. Qin, P. *et al.* Synthesis and Mechanistic Studies of Organic Chromophores with Different Energy Levels for p-Type Dye-Sensitized Solar Cells. *J. Phys. Chem. C* **114,** 4738–4748 (2010).
2. Bredas, J.-L. Mind the gap! *Mater. Horiz.* **1,** 17–19 (2013).
3. Lennox, A. J. J. & Lloyd-Jones, G. C. Selection of boron reagents for Suzuki–Miyaura coupling. *Chem. Soc. Rev.* **43,** 412–443 (2013).
4. Weidelener, M. *et al.* Synthesis and characterization of perylene–bithiophen–triphenylamine triads: studies on the effect of alkyl-substitution in p-type NiO based photocathodes. *J. Mater. Chem.* **22,** 7366–7379 (2012).
5. Cremer, J. Novel head-to-tail coupled oligo(3-hexylthiophen) derivatives for photovoltaic applications. (2005).
6. Chang, C.-H., Chen, Y.-C., Hsu, C.-Y., Chou, H.-H. & Lin, J. T. Squaraine-Arylamine Sensitizers for Highly Efficient p-Type Dye-Sensitized Solar Cells. *Org. Lett.* **14,** 4726–4729 (2012).
7. Cai, L. *et al.* Effects of solvent and base on the palladium-catalyzed amination: PdCl2(Ph3P)2/Ph3P-catalyzed selective arylation of primary anilines with aryl bromides. *Tetrahedron* **70,** 4754–4759 (2014).
8. Wood, C. J., Robson, K. C. D., Elliott, P. I. P., Berlinguette, C. P. & Gibson, E. A. Novel triphenylamine-modified ruthenium(II) terpyridine complexes for nickel oxide-based cathodic dye-sensitized solar cells. *RSC Adv.* **4,** 5782–5791 (2014).
9. Ghosh, K., Masanta, G. & Chattopadhyay, A. P. Triphenylamine-Based Pyridine N-Oxide and Pyridinium Salts for Size-Selective Recognition of Dicarboxylates. *Eur. J. Org. Chem.* **2009,** 4515–4524 (2009).
10. Liu, B. *et al.* Synthesis, crystal structures and two-photon absorption properties of a series of terpyridine-based chromophores. *Dyes Pigments* **95,** 149–160 (2012).
11. Hirai, Y. & Uozumi, Y. Clean synthesis of triarylamines: Buchwald–Hartwig reaction in water with amphiphilic resin-supported palladium complexes. *Chem. Commun.* **46,** 1103–1105 (2010).
12. Zhang, G.-F. *et al.* General Synthetic Approach toward Geminal-Substituted Tetraarylethene Fluorophores with Tunable Emission Properties: X-ray Crystallography, Aggregation-Induced Emission and Piezofluorochromism. *Chem. Mater.* **26,** 4433–4446 (2014).
13. Vaccaro, G. *et al.* Direct monitoring of self-assembly of copolymeric micelles by a luminescent molecular rotor. *Chem. Commun.* **49,** 8474–8476 (2013).

14. Fu, G. C. The Development of Versatile Methods for Palladium-Catalyzed Coupling Reactions of Aryl Electrophiles through the Use of P(t-Bu)3 and PCy3 as Ligands. *Acc. Chem. Res.* **41,** 1555–1564 (2008).
15. Weidelener, M. *et al.* Synthesis and Characterization of Organic Dyes with Various Electron-Accepting Substituents for p-Type Dye-Sensitized Solar Cells. *Chem. – Asian J.* **9,** 3251–3263 (2014).
16. *Microwaves in Organic Synthesis* (ed. Loupy, A.) V–XXVI (Wiley-VCH Verlag GmbH, 2006). doi/10.1002/9783527619559.
17. Gronnow, M. J., White, R. J., Clark, J. H. & Macquarrie, D. J. Energy Efficiency in Chemical Reactions: A Comparative Study of Different Reaction Techniques. *Org. Process Res. Dev.* **9,** 516–518 (2005).
18. Moseley, J. D. & Kappe, C. O. A critical assessment of the greenness and energy efficiency of microwave-assisted organic synthesis. *Green Chem.* **13,** 794–806 (2011).
19. Click, K. A. *et al.* A double-acceptor as a superior organic dye design for p-type DSSCs: high photocurrents and the observed light soaking effect. *Phys. Chem. Chem. Phys.* **16,** 26103–26111 (2014).
20. Lafleur-Lambert, A., Rondeau-Gagné, S., Soldera, A. & Morin, J.-F. Synthesis and characterization of a new ethynyl-bridged C60 derivative bearing a diketopyrrolopyrrole moiety. *Tetrahedron Lett.* **52,** 5008–5011 (2011).
21. Zou, Y. *et al.* A High-Mobility Low-Bandgap Poly(2,7-carbazole) Derivative for Photovoltaic Applications. *Macromolecules* **42,** 2891–2894 (2009).
22. Stas, S., Sergeyev, S. & Geerts, Y. Synthesis of diketopyrrolopyrrole (DPP) derivatives comprising bithiophen moieties. *Tetrahedron* **66,** 1837–1845 (2010).
23. Tamayo, A. B., Tantiwiwat, M., Walker, B. & Nguyen, T.-Q. Design, Synthesis, and Self-assembly of Oligothiophen Derivatives with a Diketopyrrolopyrrole Core. *J. Phys. Chem. C* **112,** 15543–15552 (2008).
24. Frebort, Š. *et al.* O- and N-alkylated diketopyrrolopyrrole derivatives. *Tetrahedron Lett.* **52,** 5769–5773 (2011).
25. Wallquist, O. in *High Performance Pigments* (ed. Smith, H. M.) 159–184 (Wiley-VCH Verlag GmbH & Co. KGaA, 2001). doi/10.1002/3527600493
26. Favereau, L. *et al.* Diketopyrrolopyrrole derivatives for efficient NiO-based dye-sensitized solar cells. *Chem. Commun.* **49,** 8018–8020 (2013).

27. Qu, S. *et al.* New Diketopyrrolopyrrole (DPP) Dyes for Efficient Dye-Sensitized Solar Cells. *J. Phys. Chem. C* **114,** 1343–1349 (2010).

28. Zhang, F. *et al.* A novel compact DPP dye with enhanced light harvesting and charge transfer properties for highly efficient DSCs. *J. Mater. Chem. A* **1,** 4858–4863 (2013).

29. Meier, H., Gerold, J., Kolshorn, H. & Mühling, B. Extension of Conjugation Leading to Bathochromic or Hypsochromic Effects in OPV Series. *Chem. – Eur. J.* **10,** 360–370 (2004).

30. Oliva, M. M. *et al.* Structure−Property Relationships in Push−Pull Amino/Cyanovinyl End-Capped Oligothiophens: Quantum Chemical and Experimental Studies. *J. Org. Chem.* **71,** 7509–7520 (2006).

31. Wood, C. J. *et al.* Red-Absorbing Cationic Acceptor Dyes for Photocathodes in Tandem Solar Cells. *J. Phys. Chem. C* **118,** 16536–16546 (2014).

32. Daeneke, T. *et al.* Dominating Energy Losses in NiO p-Type Dye-Sensitized Solar Cells. *Adv. Energy Mater*. **5,** 1401387 (2015).

III. NiO formation through ink-jet printing

III.A. The different NiO synthesis techniques

In this paragraph, the two NiO preparation methods that gave, up to now, the best results in p-type DSSCs are presented. The NiO prefabricated paste way, essentially developed by the group of Udo Bach, in Australia, is firstly described. Then, the method using a sol-gel ink for a direct formation of NiO on FTO, initially developed by Nakasa and Sumikura in Japan, is depicted. Besides, several other methods for NiO preparation for DSSC exist (the most straightforward and reproducible being the spray deposition of a NiO nanoparticle slurry, by the group of Danilo Dini [1]) as summarized in a recent review by Gibson et al. [2].

III.A.1. NiO prefabricated nanomaterial paste

III.A.1.a. General method for the paste preparation

The preparation of a NiO paste, out of prefabricated nano/micro NiO objects is a common way to obtain efficient NiO materials for p-type DSSCs. In the first publication dealing with this method of preparation, by Bach et al. in 2008 [3], NiO nanoparticles were dispersed in a water/acetylacetone mixture, with the surfactant triton X100. This type of paste is no longer used and was replaced by a preparation similar to the one used for TiO_2, for n-type DSSCs [4]. Nano/micro NiO objects were actually suspended in a mixture of terpineol (a high boiling point solvent, to avoid cracking), ethanol, in which ethyl-cellulose had been dissolved (ethyl cellulose plays the role of a binder and is also a viscosity enhancer) [5]. After ethanol removal under reduced pressure, a viscous paste was obtained. This important viscosity rendered the paste suitable for doctor-blading and especially for screen-printing. Importantly, the use of a semi-automated screen-printer, like in Bach et al. work [5], permits to obtain reproducible results. Also, the thickness of the deposited layer can be tuned, by multiple layers deposition or by the use of different meshes, with tunable types and sizers, for the screen. Typically, reported values for one layer of as-deposited NiO is 1.25 µm thick [5]. Thicker films can be obtained, by superimposition of layers, which is very important to increase the amount of light absorbed by the photocathode. Between each layer, only a drying step is necessary, since the contact between the squeegee and the NiO film is limited, then the risks of former layer alteration when passing the squeegee is low.

Also, another advantage of screen-printing is that it makes it easy to accurately superimpose layers, since the FTO glass is accurately placed and a frame is used for screen-printing. Finally, sintering at relatively high temperatures (300-550 °C) permits to eliminate the organic binders and to link nano/micro objects between one another.

III.A.1.b. NiO nanoparticles as the preformed object

The 2.5% actual record PCE for p-type DSSCs was obtained with a commercial nano-powder (20 nm diameter nanoparticles, purchased from Inframat) [6]. The efficient PMI-6T-TPA (which formula has been given in Fig. 47) was employed, in conjunction with an iron complex, $Fe^{II/III}(acac)_{2/3}$ in the electrolyte. Previously to that work, straightforward results with an iodine based electrolyte were obtained and permitted to reach the value of 0.6 % for PCE[7]. The optimal thickness depends on the electrolyte used. For an {Iodine + additives}[o] based electrolyte, it was found to be 2.7 µm[7] and the J_{sc} was 5.11 mA.cm^{-2}. For Fe-based electrolyte, it was possible to build 4.2 µm thick efficient NiO films, and the current could even reach 7.65 mA.cm^{-2} [6].

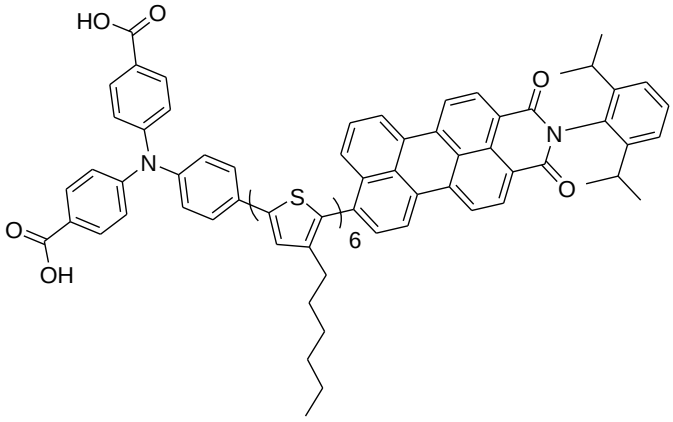


Fig. 47- PMI-6T-TPA

An optimized sintering program was settled by A. Nattestad in his PhD thesis [8]. It consists of two steps: a first step at 400°C (30 min) and an additional post-treatment at 550°C with a quite short duration (10 min). Zhang et al. accurately studied the effects of this post-treatment [7]. Heating at 550°C increases the particle size and then also the inter-particles necking. Hence, the active surface area of such electrodes is smaller and should exhibit, due to less important dye loading, a

[o] The exact composition of the {iodine + additives} electrolyte was: [I_2] = 0.03M, [*t*BP] (*tert*-butyl pyridine) = 0.5M, [1-butyl-3-methylimidazolium iodide] = 0.6M and [guanidinium thyocyanate] = 0.1 M, in acetonitrile[6] or in a mix of acetonitrile and valeronitrile (volume ratio of 85:5)[7].

drop in the photocurrent. This was actually not the case since, with the 550°C post treatment, the J_{SC} kept a high value of 5.11 mA.cm^{-2} (without the post-treatment, the J_{SC} value was 5.4 mA.cm^{-2}). The reason for such a behavior is the increase in crystallinity of the material. However, the crystallinity of the NiO material did not enhance hole transport properties, judging by its almost unchanged transport resistance (R_{TR}). Yet, charge recombinations between the holes in NiO and I^- oxidizing agent, present in the electrolyte, were reduced, and this explains the still high J_{SC} value after post treatment. It was assumed that increasing the crystallinity of the material decreased the number of defects at the surface of the NiO particles and then decreased the possibility for photo-generated charge carriers to recombine. The less important surface area of the as-fabricated material (bigger particles and more important inter-particle necking) was also pointed out for reducing charge recombination probability. Consequently, when the material was post treated, the charge collection efficiency was increased (from 90% to 95% at the positive bias of 170 mV, for instance). Very importantly, due to the limited charge recombination between the holes in NiO and the electrolyte, a very high V_{OC} value for an iodine based electrolyte, could be obtained (around 300 mV, compared to ca. 200 mV without the post treatment). One should also notice that 550°C is an optimized temperature. As suggested by the pristine work of Nattestad et al.[9] heating at higher temperature than 550°C is detrimental for device efficiency. This is probably due to the prominent loss of specific surface area and/or the complete loss of surface hydroxyl groups, which then renders dye grafting at the NiO surface impossible (as suggested in the supporting information of reference [10]). Besides, the same remark may be valid for the relative short time of the post-treatment (10 min).

III.A.1.c. Other prefabricated materials

Other nano-materials have been implemented into a cellulose based paste by the group of Bach. They reported on the synthesis of NiO highly crystalline octahedral nanoparticles, for a record V_{OC} (beyond 300 mV) for p-type DSSCs with an {iodine + additives}^{o} electrolyte. However, the high processing temperature required for the particles pre-fabrication (950°C) induced stoichiometric NiO formation (slight green color) and then less charge carriers were present in the material. Also, the high sintering temperature employed for the nanoparticle synthesis enhanced

their stability at the usual sintering temperature on glass FTO (450°C/500°C). Then inter-particle necking was dramatically reduced and this was responsible for the low photo-current observed (40 µA.cm^{-2}). The same group also successfully implemented a 2D transport material, composed of preformed NiO nanorods [11]. The nanorods were synthesized at a reasonable temperature (500°C) via a solid templated way. An optimized thickness of 1.7 µm films was established and a 550°C post-treatment was also employed to enhance the nanorods crystallinity. The nanorods additionally presented advantageous light scattering properties. Again, high V_{oc} was reached (around 300 mV), and quite high photocurrents could be obtained (3mA.cm^{-2}). Moreover, good device performance were obtained as a PCE of 0.40%, with an {Iodine + additives}^{o} electrolyte was reached. Besides, for the first time, using nanorods for p-type DSSCs was shown successful. Finally, another NiO material, exotic but efficient, was implemented by the same group: NiO micro-balls. Due to reduced NiO self-absorption, NiO films formed with NiO microballs gave high photocurrents, such as 7mA.cm^{-2} for a 6 µm thick film [12]. The microballs were synthesized by the thermolysis of Ni^{II} nitrate salt at 100°C, in an aqueous solution containing oxalic acid and a tetramine. After sintering at the reasonable temperature of 400°C for NiO, the micro-balls were obtained. After deposition of a paste containing the microballs, a 550°C post treatment was here again applied. As said in chapter 1, it was pointed out that the reduced self-absorption of NiO could stem from the higher surface area provided by the microball structure (then higher dye loading), and/or by the lower degree of defect of NiO, which was more crystalline than the "classical" nanoparticles.

III.A.1.d. Other pastes

Another group recently reported on the synthesis of $Ni(OH)_2$ nano-platelets colloids and their incorporation, after drying, into a paste similar to the one developed by Bach et al [10]. The spreading of the paste onto FTO was realized by spin-coating and 1 to 3 µm-thick films could be obtained. Various sintering temperature were tested (from 100°C to 600°C), in order to optimize the device performance. Indeed, 450°C happened to be an optimal temperature for device performance. This new material was tested in p-type DSSC configuration, with coumarin-343 as the dye. Despite low photocurrents (between 300 and 700 µA.cm^{-2}), an interesting 10-fold

increase in electron mobility, compared to NiO nanoparticles was remarked for these NiO nanoplatelets.

III.A.2. NiO sol-gel route

III.A.2.a. The $Ni(OH)_2$ slurry way

The preparation of a sol-gel ink has historically been the first route developed for the synthesis of NiO films for p-type DSSCs. In the pristine works, $Ni(OH)_2$ colloids were prepared through the partial hydrolysis of Ni^{II} acetate precursors, with water [13,14,15]. The film was doctor-bladed onto FTO and annealed at 500°C for 1 hour, 1µm-thick films were obtained. In 2001, another similar route was employed by Boschloo and Hagfeldt, but this time with the use of $NiCl_2$ precursors [16]. Hydrolysis of the precursors was favored by the use of a strong base, NaOH, and the annealing temperature was reduced to 300-315 °C. The use of NaOH as the base however induced the presence of NaCl residues. In 2007, Zhu et al. modified the method by operating the $NiCl_2$ hydrolysis in ethanol, rather than in water[17]. The thickness of the film could not exceed 1µm due to cracking or poor mechanical stability. In 2009, Sun et al. reported that it was possible to deposit 2 layers of NiO, so as to increase the thickness of the film and to reach 1 to 1.4 µm [18], which is almost double of the one-layer samples that they had prepared in 2008 [19] (600µm thickness). A thermal annealing at high temperature (then, not a simple drying step), between each layer, was necessary to obtain the thicker film[p]. Once annealed, nano-crystalline nanoparticles were obtained. With such a two-layer structure, J_{SC} reached 2.5 $mA.cm^{-2}$ with the efficient push-pull dye P1 (its formula was given on Fig. 48) and an iodine based electrolyte (0.1 M I_2 / 1M LiI).

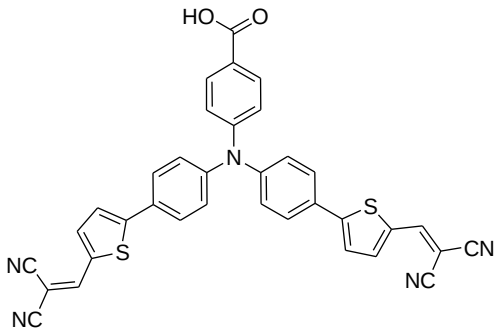


Fig. 48- P1

[p] This precision was obtained in the review by Gibson et Coll[2] .

III.A.2.b. The sol-gel templated way

The performance of the NiO photocathodes prepared through the sol-gel way were greatly enhanced by the incorporation of pluronic triblock copolymers as a templating, structuring agent and permitted to largely exceed the 2.5 $mA.cm^{-2}$ obtained by Sun et al.

III.A.2.b.i. Templating NiO films with pluronic tribloc copolymers

Pluronic triblock copolymers represent a class of non-ionic surfactants. They are made of two hydrophilic poly-ethylenoxide (PEO) chains, linked to one hydrophobic polypropylene oxide (PPO) chains, with a general formula as follows: $(PEO)_m$-$(PPO)_n$-$(PEO)_m$ (also see Fig. 49). They have actually been widely used for the formation of well-defined mesostructured oxides, such as SiO_2 or TiO_2 [20]. Several kinds of such polymers exist, they are actually divided by family. The hydrophilic/hydrophobic ratio (m/n) determines to which family the polymer belongs. Polymers with high m/n ratio belong to the "F" family and those with smaller m/n ratio to the "P" family (there is even a third family, the "L" family, for very hydrophobic triblock copolymers).

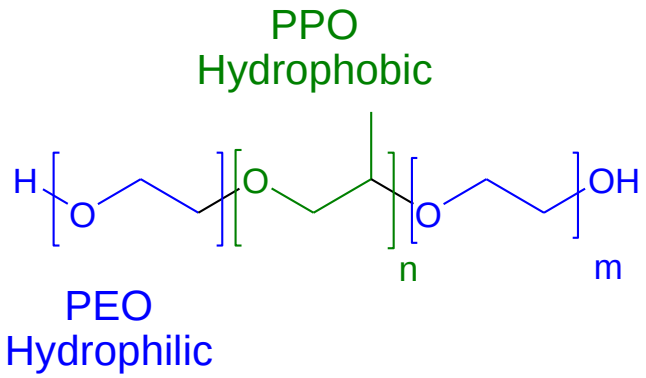


Fig. 49- General formula for a $(PEO)_m$-$(PPO)_n$-$(PEO)_m$ copolymer triblock

Actually, Nakasa et al., in 2005, reported on the use of a pluronic triblock copolymer P_{123} for NiO synthesis, for p-type DSSCs [21]. Interestingly, in the same year, the group of Grätzel reported on the use of pluronic triblock copolymers in n-type DSSCs [22]. This polymer was incorporated into a mixture of ethanol and water and $NiCl_2$ was used as the nickel precursor source. Then, this ink was spin-cast onto FTO and NiO films were formed after calcination.

In 2008, Sumikura et al. studied more precisely this way to form the NiO films for DSSC [23]. They also investigated the influence of the triblock copolymer's family over the solar-cell performance.

Actually, four copolymers were tested: F_{88}, F_{108}, P_{105} and P_{123} (see for each polymer characteristics).

Tab. 8- The four pluronic triblock copolymers used by Sumikura et al. (reproduced from their publication ref 23)

Polymer	m	n	MW ($g.mol^{-1}$)	m/n	Group
F_{88}	104	39	11 400	2.67	F
F_{108}	133	50	14 600	2.66	F
P_{105}	37	56	6 500	0.66	P
P_{123}	20	69	5 750	0.29	P

The general formulation of the ink was the following: 1g of pluronic copolymer, 1g of anhydrous $NiCl_2$, 3 mL of water and 6 g of EtOH. After doctor-blading, the film was dried at room temperature and then annealed at 400°C. The thickness of the as-formed film was reported to be about 0.5 µm. SEM images of the as-prepared films showed highly ordered and structured NiO nanoparticles. They suggested that a high organization of the $NiCl_2$ precursors existed prior to sintering and was managed by the presence of pluronic copolymers (see Fig. 51). Actually, due to the hydrophilic character of the solvent, micelles are spontaneously formed (see Fig. 50). Nickel salt precursors are then segregated into the hydrophilic zone, this is supposed to permit the mesoporous structuration of the NiO film after polymer annealing and NiO formation.

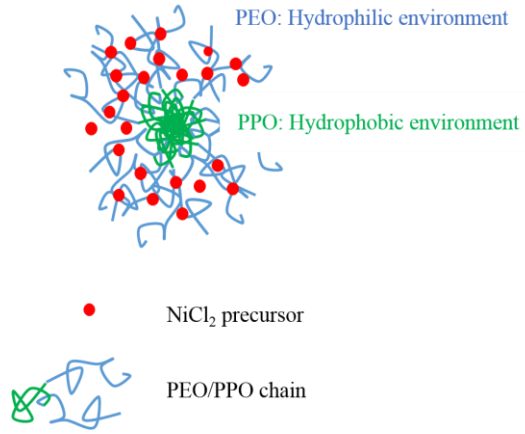


Fig. 50- A representative view of the micellar structure of pluronic bloc copolymers in a hydrophilic environment (water + ethanol), with $NiCl_2$ precursors.

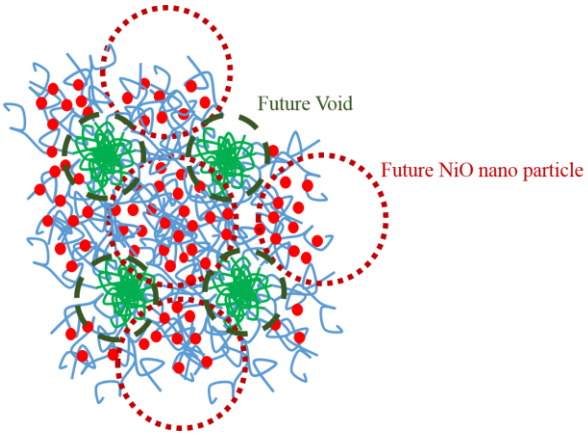


Fig. 51- A representative view of the possible arrangement of the PEO/PPO micelles prior to sintering.

Sumikura et al. found that lower hydrophilic/hydrophobic ratios (m/n) induced less densely packed NiO particles. Hence, F group pluronic copolymers with a higher hydrophilic/hydrophobic ratio than P group ones, induced smaller voids between particles of NiO, in agreement with the micellar ordering prior to sintering (see Fig. 51). Polymers of the P group then induced a smaller NiO surface area and then smaller amounts of grafted dye (confirmed by the dye desorption measurements). This explains the poorer performance of p-type DSSCs when polymers of the P group were employed for NiO fabrication.

After selecting a F family copolymer, the ratio polymer/$NiCl_2$ was also studied. It was found that a mass ratio of 1/1 was the optimum to obtain well-packed NiO nanoparticles after sintering.

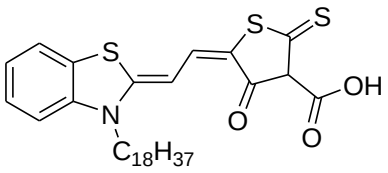


Fig. 52- NK-2684

They also observed that for polymers of the F family, the size of the particles was linked to the PEO, hydrophilic, chain length. Indeed, the longer the hydrophilic chain, the smaller the particle. For instance, F_{88}, has a shorter hydrophilic chain than F_{108} (see Tab. 12). The obtained particle diameter is 18.6 nm for F_{88} and 12 nm for F_{108}. In the study of Sumikura et al., it seemed that the particle size has a minor influence over the DSSC performance. For these two polymers, J_{SC} was between 1.0 and 1.2 $mA.cm^{-2}$, V_{OC} around 80 mV and PCE efficiency between 30 m% and 40 m%, with NK-2684 as dye (in Fig. 52, the chemical formula of NK-2684). These values are quite high for such a low film thickness. In order to increase further the photocathode performance, thicker films have to be employed. This was achieved by the work of Sun and Hammarström, in Sweden.

III.A.2.b.ii. Tuning the thickness of the F_{108} templated NiO films

The formulation of the ink was kept set compared to Sumikura's work and doctor blade was employed for ink spreading over FTO. Eventually, in 2010, Sun and coworkers presented an optimized way for the formation of NiO through the F_{108} templated sol-gel way [24]. Briefly, so as to double the thickness of the film, it was shown that the best method was to perform an annealing step between the two layers. Denser films were obtained in the first case, and this permitted to enhance LHE, which was attributed to an increase in dye loading. The film as deposited also presented enhanced mechanical stability. Besides, the temperature of 450°C was described as an optimum sintering temperature (see Tab. 9, taken from ref. [24]). At such a temperature, the average

crystal diameter was 16 nm. This is actually a more important value than the 12 nm described by Sumikura et al. when sintering was performed at 400°C.[q]

Tab. 9- Sintering temperature optimization described by Sun et coll. with F_{108} as the templating polymer, for a two layers of NiO photocathode.

T (°C)	Crystal diameter (nm)	IPCE (%)	J_{SC} ($mA.cm^{-2}$)	V_{OC} (mV)	FF	η (%)
400	12	1 (480 nm)	0.09	100	0.43	0.004
450	16	64 (475 nm)	5.48	80	0.34	0.150
500	19	39 (460 nm)	3.52	110	0.36	0.140

Then, a high J_{sc} value could be obtained: 5.48 $mA.cm^{-2}$, again with P1 as the sensitizer and an iodine based electrolyte. The V_{OC} obtained was substantially lower (84 mV), compared to the one obtained in the work by the Bach group, presented above, but the electrolyte did not contain additives (electrolyte composition: $[I_2]$ = 0.1M, [LiI] = 1M, in acetonitrile). The group of Licheng Sun clearly mentioned that the deposition of 3 layers did not lead to substantial improvement of the solar cell performance, despite an increase in LHE. In 2014 [26] the group of Wu, reported that it was possible to doctor-blade more than two layers of NiO with the method developed by Sun. An optimal value of approximately 2.5 µm was reported. It is however true that the formulation of their ink was slightly more concentrated in polymer and in $NiCl_2$ salt. The J_{SC} was multiplied by three for dye O_3 (see Fig. 53 for the formula), when passing from 600 nm (0.8 $mA.cm^{-2}$), to 2.3 µm (2.6 $mA.cm^{-2}$) and was found to plateau at higher film thickness. Like in the work of Sun and coworkers, small VOC were obtained (100 mV for dye O_3).

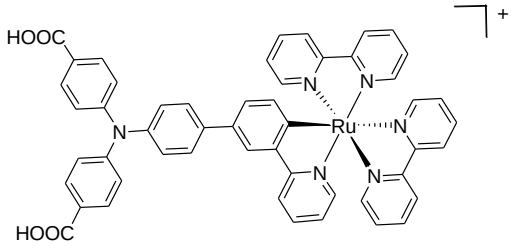


Fig. 53- Dye O_3

Recently, very high J_{sc} values (with an iodine based electrolyte, see above for the formulation) were obtained with films deposited via the sol-gel template method. Wu et al. obtained 7.4

[q] Previously, in 2009, Hammarström et coll. had actually reported a synthesis of 5 µm thick NiO electrodes, obtained by depositing 3 layers of precursors and sintering at 500°C between each step [25].

$mA.cm^{-2}$ [27], with NiO substrate thickness range of 2.0 to 2.5 µm. Zhang et al.[28] reported a high value of 8.20 $mA.cm^{-2}$ for two layers of NiO. Gibson et al. reported an impressive 8.21 $mA.cm^{-2}$ value [29], for a five layer of NiO sample with CAD3 [r].

One can remark that if it is clear that thicker than 600nm, one layer of NiO sample must be prepared for increasing LHE, the optimal thickness for NiO for p-type DSSC is not a fixed value and also depends on the dye which is employed. This was actually remarked by Gibson et al. [30]. It was emphasized that for dye CAD 1 dye, 3 layers were optimal and on the other hand, for CAD 2 (see), 2 layers gave better performance. A possible explanation mentioned was that CAD 2 was very bulky and then could not diffuse efficiently through the NiO porous network. These high J_{SC} actually rival the ones reported for the NiO paste way (7.57 $mA.cm^{-2}$ by Liu et al in 2014 [31]).

III.A.2.c. Using other templates than pluronic block copolymers

Interestingly, in 2014, Yang et al. reported another templating way to fabricate NiO films. They actually used ethyl-cellulose as a so called "environmental friendly" template [32]. The nickel precursor was again $NiCl_2$. Two scales of arrangement were obtained: a small scale nano-particular arrangement, and a meso-scale arrangement, which could be varied by changing the drying temperature of the film. The drying temperature of 90°C was actually optimal so as to obtain porous hollow spheres of NiO after sintering at 450°C (see Fig. 54, remark the two-scale arrangement of NiO: small nanoparticles, assembled in hollow spheres of approximately 500 nm of diameter). Interestingly, in order to increase contacts between the NiO hollow spheres, the photocathodes were dip-coated into a nickel acetate solution (0.05M), three times, and sintered again at 450°C for 30 min.

[r] Actually, in the communication by Gibson et coll., the number of layers of NiO employed was not directly mentioned. However, the amount of dye grafted on NiO was displayed as a function of the number of layers in the supporting information. Based on the data on the number of dyes grafted on NiO for the solar cell performance displayed, it was possible to find the number of NiO layers employed for CAD_3 NiO photocathodes.

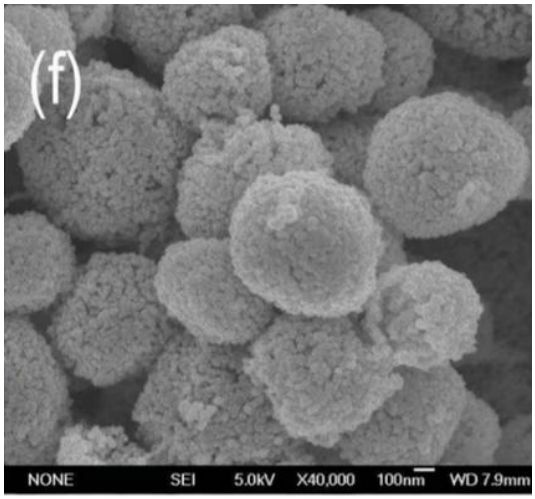


Fig. 54- The Porous NiO hollow spheres obtained by Yang et al. . Reproduced from their publication.

These nanospheres were reported to favor a dense assembly of the dye used in this publication (T1), compared with the nanoparticle way. At similar level of specific surface area per volume unit [s], the dye loading for the nanospheres was more important. This indicated a dense packing of dye at the NiO surface and clearly permitted to obtain higher V_{OC} values (150 mV rather than 113 mV). Besides, the reasons for the dense packing of dyes on the nanospheres was not clearly identified. Indeed, at similar thickness, the performance of the nanospheres were lower than for nanoparticles (PCE = 0.125 % *vs* PCE = 0.106%), due to a lower J_{SC} value.

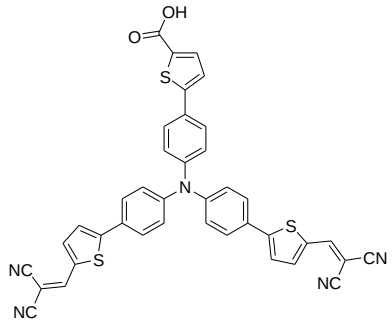


Fig. 55- T1

[s] Which was calculated from the publication data: Specific surface area per volume unit = BET*(mass of NiO per cm^2 of electrode) / electrode thickness. It was found 1136 $m^2.cm^{-3}$ for the nanoparticles and 1129 $m^2.cm^{-3}$ for the nanospheres.

III.A.3. Comparison of the different methods and conclusions

III.A.3.a. Comparison of the actual "two best NiO"

The actual record performance for p-type DSSCs, have been obtained with a NiO resulting from an optimized screen printing of a nanoparticle paste, by the group of Udo Bach. However, the high efficiency of these cells is also greatly due to the use of a very efficient dye PMI-6T-TPA. The other method, "sol-gel templated", in which the templating agent is a pluronic copolymer triblock with a high hydrophilic/hydrophobic ratio, has also permitted to obtain good performances in recent publications. These two methods seem to be the best ones for NiO film formation for p-type DSSCs.

It is actually interesting to point out that no real comparison was ever done in the literature between those two methods. However, by combining two references, it was possible to find comparable experimental conditions for the two NiO fabrication methods, and a tentative comparison is given here. The first publication is a reference publication by Licheng Sun (see ref [24]) that studies P1 dye as the sensitizer in association with a sol-gel templated NiO. The second publication is a publication about $CuGaO_2$ by the group of Udo Bach, with dye P1 also and for which a reference NiO electrode was synthesized by the screen-printing of a nanoparticle ink. For both, the sensitization conditions are the same (16 hours in a 0.3 mM acetonitrile solution of P1) and the electrolyte composition are also identical (1.0 M LiI / 0.1 M I_2). It is true that being thicker than the sol-gel NiO, the NiO paste electrode may exhibit more hole/electrolyte recombination, however, it seems obvious that the sol-gel method provides better performance for p-type DSSCs with dye P1.

Tab. 10- Performance of the p-type DSSCs based on dye P1 with the two different NiO. This table is based on the combination of two publications.

NiO Deposition method	Film thickness (µm)	J_{SC} (mA.cm^{-2})	V_{OC} (mV)	PCE (%)	FF (%)	LHE (%) at 500 nm
NPs-Sol-gel templated [(a)]	1.1 -1.2 µm	5.48	106	0.12	0.37	~ 90%
NPs-Sol-gel template [(a)]	1.6 µm	~ 5.5	~ 78	Not precised	Not precised	~ 95%
NPs-Paste [(b)]	2.4	1.89	108.4	0.072	0.35	~ 80%

*(a) Sun et al., Adv. Mat., **2010**, 22, 1759-1762*
*(b) Cheng et al. J. Mater Chem. A, **2014**, 2, 2968-2976*

How to explain these differences? A first explanation may reside in the differences in terms of LHE between the two NiO. There is a greater LHE for P1 with sol-gel NiO, despite a thinner layer of NiO. This reveals the more important dye loading at the sol-gel NiO surface. In order to go further, the available texture properties of the two different NiO were also summarized in Tab. 11. Here a comparison is also intended on the basis of the combination of results presented in different publications. The interesting parameter should have been the dye/NiO absorption ratio. However, to the best of the author efforts, this parameter was not available for the sol-gel templated doctor-bladed NiO in any publication. It is interesting to remark that the BET of sol-gel templated NiO is lower than for the paste way, while the substrate is also more porous. This all should induce a less important specific surface per volume unit. However since the dye loading is more important for sol-gel NiO, it suggests a bigger pore size / surface accessibility for the sol-gel NiO. Besides the fact that the porosity of sol-gel NiO is more important, suggests its self-absorption is less important two since less material is present in a given volume. This could be a reason for the better performance of the sol-gel templated NiO (confirmation of this should be brought about by clear publications on this aspect).

Tab. 11- Comparison of the texture properties of sol-gel NiO and nanoparticle paste based NiO. Different publications were used to build this table.

NiO Deposition method	BET (m^2/g)	Porosity (%)	Absorbance at 450 nm of the bare NiO film (A_{NiO})	Absortivity at 450 nm of the bare NiO film	Transmittance at 450 nm of the bare NiO film
NPs-Sol-gel templated	40.6 [(a)]	76 [(b), (c)]	Not mentioned	Not mentioned	Not mentioned
NPs-Paste	56 [(d)]	51[(d)]	~ 0.22 [(d)] (1 µm thick)	40 % (1 µm thick)	60 % (1µm thick)

NiO absortivity is defined as follows: Absortivity = $1\text{-}10^{-ANiO}$.

Transmittance is defined as follows: Transmittance = 10^{-ANiO}

*(a) Gibson et al., Appl. Mat. Int., **2015**, 24556-24565*
*(b) Sun et al., Adv. Mat., **2010**, 22, 1759-1762*
*(c) Sumikura et al. J. Photochem. Photobiol. A : Chem., **2008**, 199, 1-7*
*(d) Bach et al., J. Phys. Chem C, **2014**, 16375-16379*

III.A.3.b. Conclusions

From the two major ways for NiO photocathode fabrication a precise comparison of different publications dealing with these two types of NiO, both employing P1 dye permits to suggest that the sol-gel way gives better results, due to a possible less important NiO self-absorption and also to an increased amount of grafted dyes at the NiO surface. This was an important argument for the choice of the sol-gel templated method, for NiO electrode preparation in this thesis.

III.B. Doctor-blading NiO films with F_{127} as the copolymer block

III.B.1. Use of a "Classical" ink

III.B.1.a. Preparation of "classical" doctor-bladed NiO film with F_{127} as the templating agent

As it name reads, F_{127} belongs to the F family of pluronic triblock copolymers. Then this polymer should be suitable for templating NiO film for a p-type DSSC application. Surprisingly however, F_{127} has actually never been investigated in that purpose.

Tab. 12- Structural parameters for F_{127} and F_{108} pluronic copolymers, compared with P_{123}

Pluronic	MW ($g.mol^{-1}$)	m	n	m/n
F_{127}	12 600	100	65	1.53
F_{108}	14 600	133	50	2.66
P_{123}	5 750	20	69	0.29

In order to assess if this polymer was suitable for NiO photocathode fabrication, an ink was prepared with F_{127}, in a same trend as the one "classically" prepared with F_{108} polymer (see experimental part) [24]. The obtained ink was very liquid, which rendered its doctor-blading uneasy. Still, doctor-blading was performed on a glass slide (previously cleaned), with one layer of magic-tape. The filmed was dried at room temperature for 30 min, gelation was visibly noticed, and then it was sintered at 450°C for 30 min (like in Sun et al. work[24] with F_{108}). A crack free, but inhomogeneous film was obtained (see Fig. 56). The upper part of the film was thick and black, while the bottom part was thin and almost transparent.

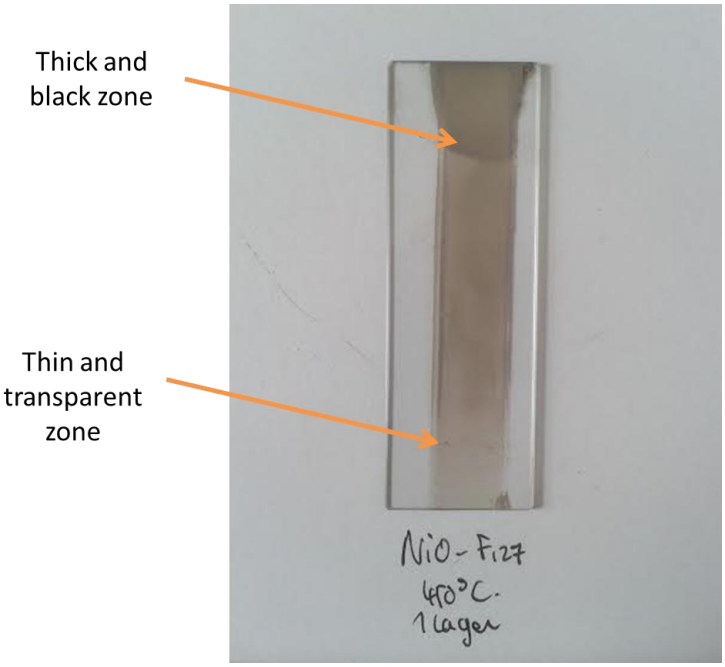


Fig. 56- A NiO film, fabricated with F_{127} as the templating agent, doctor-bladed and sintered at 450°C.

III.B.1.b. SEM analysis

III.B.1.b.i. Thick black zones

As expected, the visibly thick and black zone displayed an inhomogeneous morphology (see Fig. 57). An irregular crust, consisting of densely packed nanoparticles was observed. Several cracking were remarked in the crust, like the one exemplified in Fig. 57. Very interestingly, this permitted to reveal that under the crust, NiO nanofibers had been formed. Actually, the nanofiber displayed a "dual" structure, as they were consisted of nanoparticles. The fiber diameter was around 500 nm and their length, though it could not be measured precisely from the SEM pictures was higher than 5 µm.

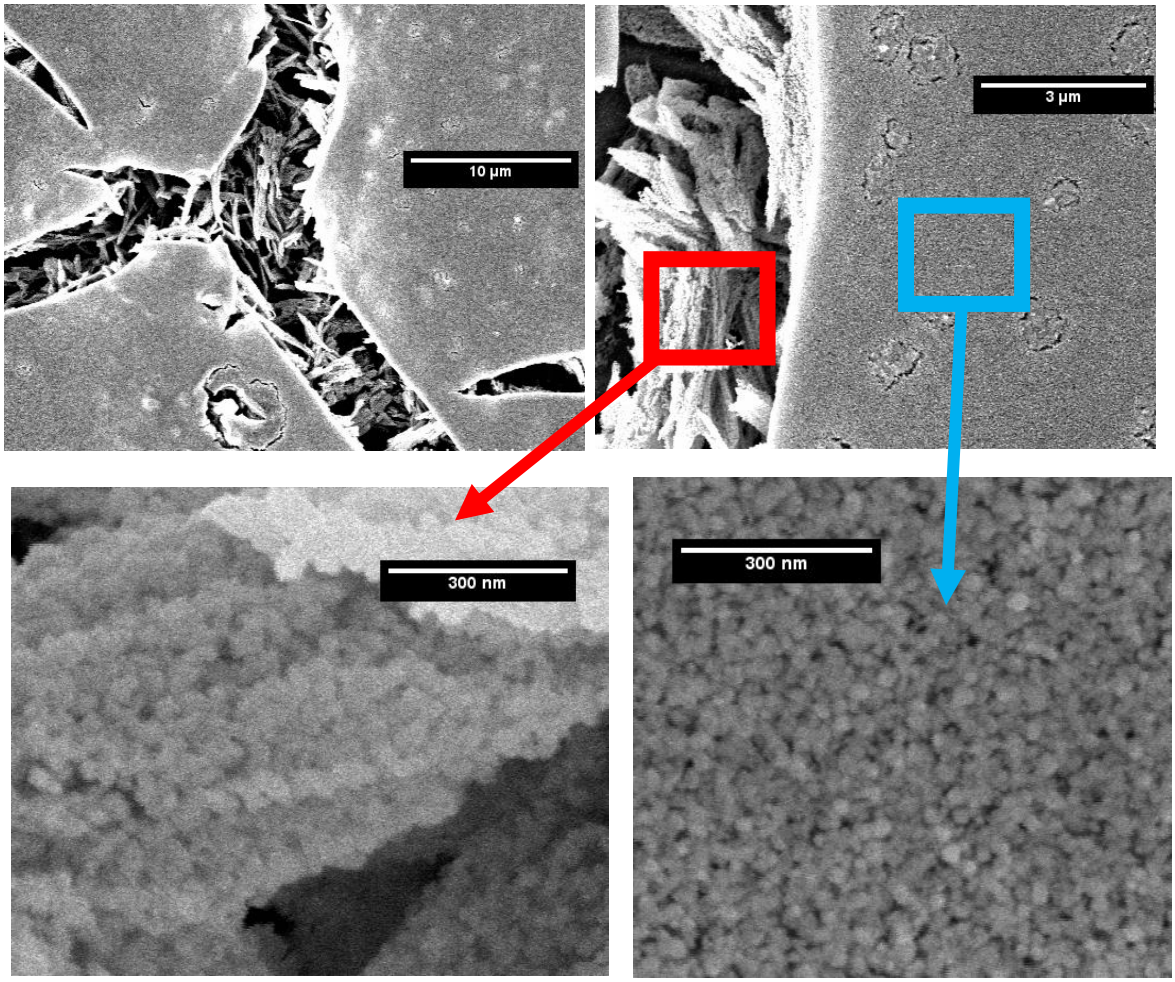


Fig. 57- SEM top-view of the NiO film in the black and thick zone at different zooms, showing the crust like structuration (in blue) and the "dual" nanoparticle nanofiber structuration (in red).

III.B.1.b.ii. Thin transparent zone

The visibly thinner and more transparent zone, which then represents the attractive part of the film for a p-type DSSC application was also observed with SEM. It was found that this thinner zone

was more densely organized and the film resembled to the one obtained by Sumikura et al.[23] (see Fig. 58). Cross-sections SEM pictures were also acquired and revealed a thickness of around 0.9 µm which is actually slightly thicker than for the F_{108} films obtained by Sumikura and coworkers. The film actually revealed a very dense, highly organized packing of NiO nano-crystals, with an average crystal diameter (measured on 20 nanoparticles on the SEM picture) of 16 nm. Then from this point of view, despite its smaller m/n ratio of 1.53 compared to F_{108}, (see Tab. 12), F_{127} seemed to meet requirements for NiO morphology, for a p-type DSSC application.

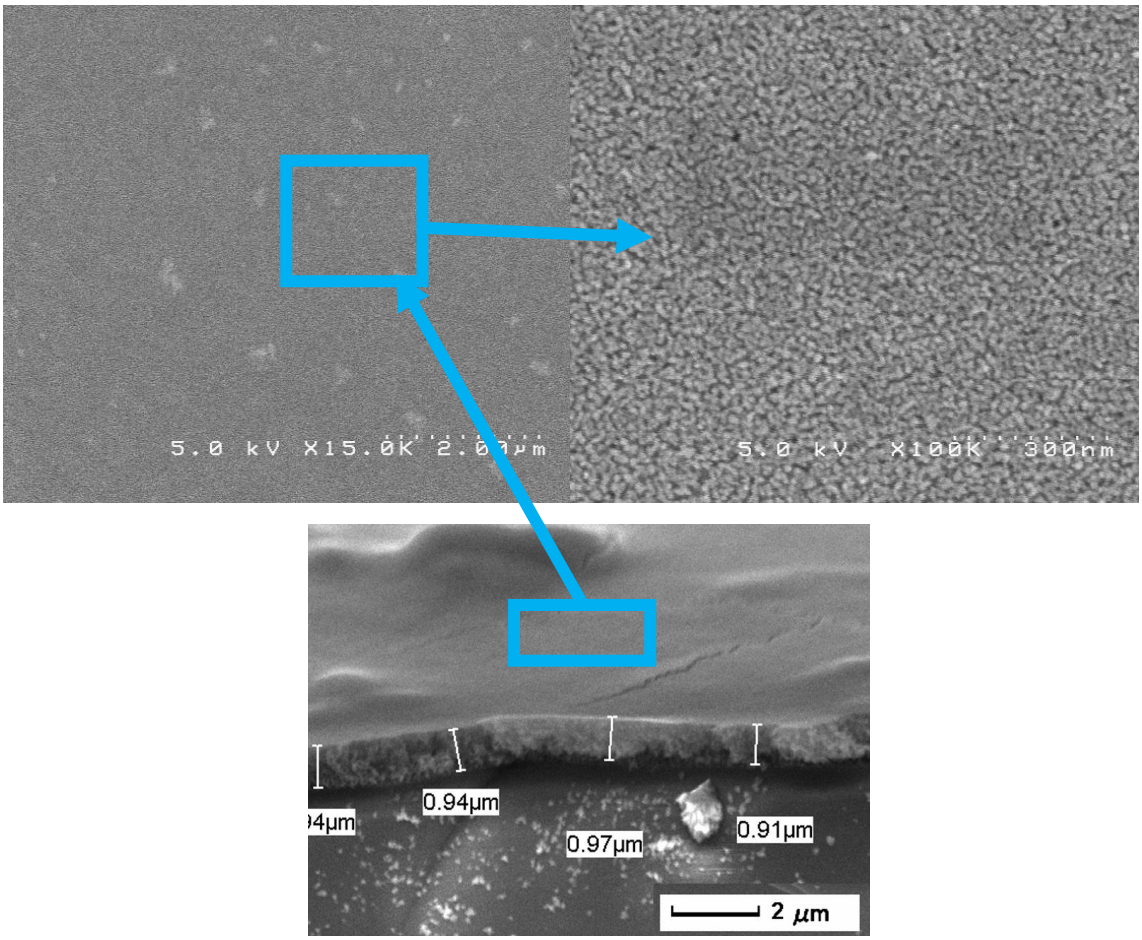


Fig. 58- TOP view and SEM cross section of a doctor blade NiO film in the transparent thin zone where a compact arrangement of nanoparticles was noticed.

However, the thinner zone displayed irregularities and the thickness and morphology of the film were far from being uniform. Actually, even in this thinner zone, a similar morphology as for the thicker zone described above could be observed and the "dual" nanofiber structure, surrounded with a crust was present in some parts of the film (see Fig. 59). The nanofiber diameter was high but irregular: between 200 nm and 800 nm. The crust thickness was between 500 and 600 nm.

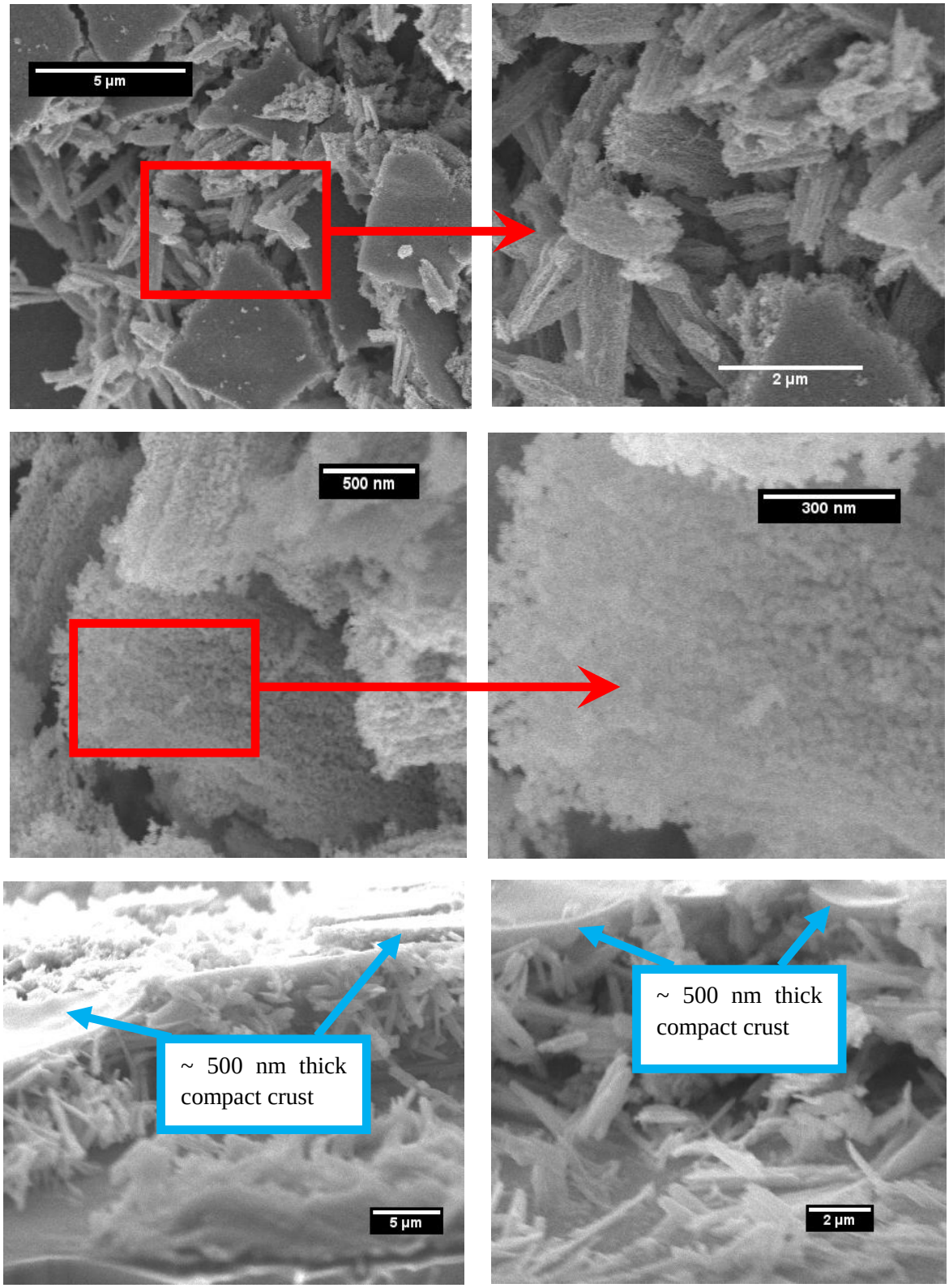


Fig. 59- SEM pictures (top-view and cross sections) of the porous NiO fibers formed in the thinner zone of the NiO doctor bladed film.

III.B.1.c. Possible mechanism for film morphology

The F_{127} concentration in the ink, prior to deposition is about 9 mM, largely higher than its CMC ($2.8.10^{-6}$ M [33]) Then, micelles are likely to be formed in the ink. However, the gelation point has not been reached yet since the pristine ink is very liquid; gelation occurs only after evaporation of the solvent, as described in III.B.2). From this, one can induce that micelles are not well organized in the pristine ink. The arrangement of micelles into an organized network occurs afterwards, with the help of solvent evaporation and eventually gives a gel, as observed. In this case, one can say that an Evaporation Induced Self Assembly (EISA) process occurs, as described by Sanchez et al [34,t]. This explains that NiO structuration after sintering is the "negative picture" of F_{127} polymer arrangement once it has gelled. This means that the meso-structuration of the F127 micelles is exactly transferred to the NiO film.

In order to check if the NiO structuration which was observed with SEM was compatible with F_{127} structuration once gelled, the ternary phase diagram of F_{127} in an ethanol/water medium was analyzed. Such a diagram was obtained by Ivanova et al [35]. It revealed that depending on the concentration in the {water/ethanol} solvent mixture, F_{127} micelles can arrange into dense packing of either cylinders, lamellas or nanospheres. Then, we can assume that the observed "crust", as well as the thinner zones of the film correspond to the nanosphere compact arrangement of F_{127} in the gel prior to sintering. However, no "dual-order" organization of F_{127} polymer was described by Ivanova et al. And the cylinder organization of micelles that they described cannot correspond to the nanofiber organization observed in the case of this thesis, simply because the nanofiber diameter observed is about 500 nm, which is far beyond the micelle dimension "order of magnitude" which can be estimated to be at maximum 80 nm (F_{127} bears 265 monomer units, each unit has approximately 3 atoms, then one F_{127}, has a theoretical maximum length of about 800Å = 80 nm).

Hence, the following mechanism is proposed for the film structuration. Solvent evaporation occurs first at the surface of the deposited film. During this process, micelles arrange themselves into a dense nanosphere packing, which respects the phase diagram described by Ivanova et al.

[t] However, one should note that in their paper, Sanchez et al. described the EISA by starting from an ink in which the polymer concentration is below CMC.

Afterwards, this densely packed arrangement extends to the deeper part of the film. If the amount of ink is low (like at the bottom of the film described in Fig. 56), the dense arrangement of micelles can reach FTO glass (in Fig. 60, a simplified chart represents this mechanism). On the other hand, if the amount of ink is more important (like in the upper part of the film described in Fig. 56), the dense arrangement of micelles at the surface of the film gradually evolves in a "crust" which keeps the solvent trapped.

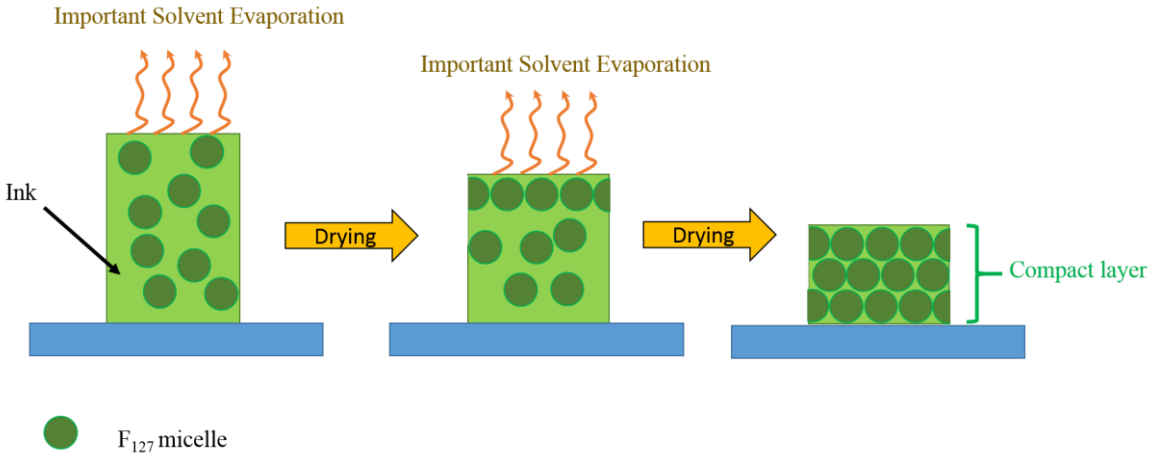


Fig. 60- Proposed mechanism for a compact layer formation of F127 micelles during gelation of the film, after doctor blading of the ink, when a thin amount of ink is deposited.

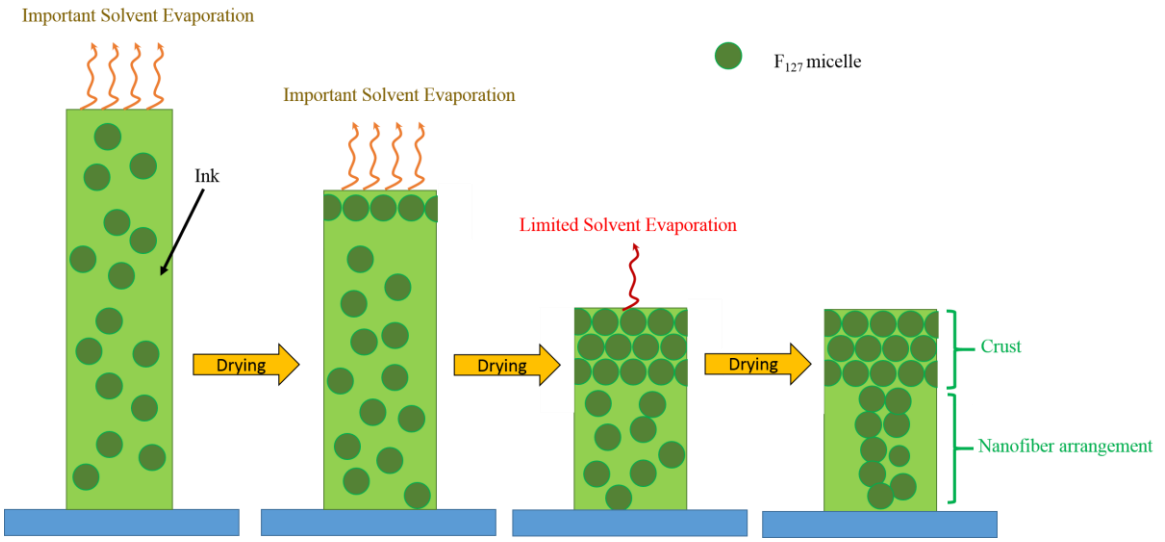


Fig. 61- Proposed mechanism for crust formation and nanofibers arrangement during drying of doctor blade ink, when a thick amount of ink is deposed.

Then, as the solvent cannot evaporate, EISA cannot occur under the "crust" and the compact arrangement of micelles cannot extend to the whole film. Hence, micelles arrange themselves in another way, less compact, such as nanofibers. However, the explanation for the "dual" nanofiber

structuration remains unclear. A simplified chart for this possible mechanism has been depicted Fig. 61.

III.B.1.d. Reproducibility issues

As shown in Fig. 56, NiO films prepared by doctor blading a $NiCl_2$ pluronic template ink induced non uniform films. This is due to the high sensitivity of the method to its operator (strength, speed at which doctor blading is performed *etc.*); this sensitivity is even higher since the ink is quite fluid. Then this film formation method suffers from an important lack of reproducibility. This was actually already pointed out by Odobel et al. [36]. To illustrate the lack of reproducibility of the doctor-blade method, it also interesting to quote a publication by the group of Wu, who detailed very precisely how it was unhandy to perform the spreading of the $NiCl_2$ sol by using "doctor-blading":

[A "square well" of 0.5 cm edge length was constructed onto an FTO substrate using scotch tape. Ten µL of the slurry was placed on the scotch tape near the top of the defined area using a micropipet and was quickly spread onto the FTO using the sharp edge of a glass slide placed at an acute angle to the substrate. Care was taken not to allow a back-flow of the slurry onto the film] [37].

III.B.2. Increasing the viscosity of the ink

In order to enhance the reproducibility of the doctor blade method, we tried to increase the ink's viscosity. For this purpose, the solvent was slowly and gently evaporated from the ink, till a gel was formed (see Fig. 62). It took approximately three days for the gel to be formed at room temperature.



Fig. 62- The formed gel after solvent gentle evaporation.

However, the obtained gel texture was not adapted for doctor-blading, as the gel stuck to the glass rod. This led to important uniformity and cracks after the film sintering at 450°C (Fig. 63). Also, the film was largely too thick to consider its application for p-type DSSCs. In agreement with the results shown above, a similar nanotubular meso-structuration was observed. Interestingly, sometimes, the tubular structure observed was massive and breathtaking (see Fig. 63).

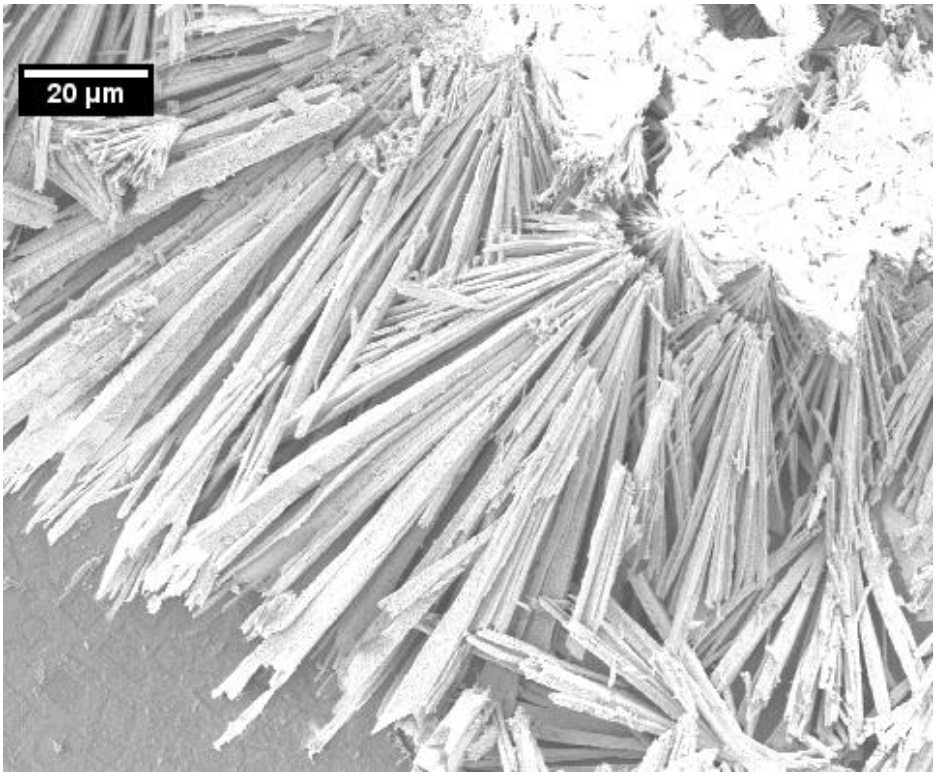


Fig. 63- Breath-taking nanotubular structure with NiO film formed with an ink previously gently gelled.

III.B.3. Conclusions

As expected, the use of F_{127} as a templating agent in the NiO sol-gel ink led to important structuration of the NiO film. When a thin film of ink was spread over the glass, the presence of F_{127} triblock copolymer permitted to obtain densely packed, small (16 nm diameter) NiO nanoparticles, films. The thickness of the film was below 1 µm. This structuration is similar to the one obtained in the literature with F_{108} as the templating agent for p-type DSSCs. As a consequence it appeared that F_{127} is a successful candidate as the templating agent for NiO film formation for p-type DSSCs. Moreover it was remarked that when the amount of ink spread over the glass substrate is high, a typical structuration was noticed:

➔Presence of a densely packed NiO nanoparticles crust on the top of the film (500/600 nanometers thick)

➔Presence of NiO nanofibers below the crust. The nanofibers are themselves consisted of nanoparticles, then one can refer to a "dual" structuration.

The mechanism for crust formation was attributed to the favored solvent evaporation at the surface of the film. The mechanism for the nanofibers to be formed is not very clear. This structuration could actually be profitable for type DSSCs construction, in the aim of creating a NiO material with increased charge transport properties, like what was done by Udo Bach et al. [11]. There is however a substantial lack of reproducibility for the NiO film formation when using the doctor-blade method. This spreading method is not suitable for spreading such a low viscosity ink in a reproducible manner. This is one of the reasons why the deposition of NiO through ink-jet printing was intended in this thesis. This is the object of the following paragraphs.

III.C. NiO films fabrication through ink-jet printing

III.C.1. Introduction

III.C.1.a. Generalities- Ink-jet printing for materials applications

III.C.1.a.i. An attractive technique

Ink-jet printing materials for technological applications has gained an important interest over the last twenty years, due to a good level of compatibility for several material synthesis. Indeed, ink-

jet printing (IJP) has the important advantage to be a digital technology. A numeric pattern is loaded to the printer program and then drops are accurately printed. No mask is required, drops are deposited at a desired place, and no stress is applied to the substrate, which is very advantageous for multiple layer deposition. Then a high level of tuning is possible, and patterning of the film is very easy. Indeed, multiple layers can be successively printed (additive patterning). Also, being digital, IJP drastically reduces the amount of ink or construction materials which is wasted compared to other printing or coating techniques, like photolithography. Finally, being automated, IJP also has the important interest to have a good level of reproducibility.

III.C.1.a.ii. Industrial challenges

The recent marketing of high-rate ink-jet printer[u] nowadays allows many start-ups to emerge in the field of IJP (such as Kateeva, supported by DuPont, ISET, which commercializes ink-jet printed CIGS solar cells or Genes'Ink in France, a nano-ink producer). The field of printed electronics is for instance attracting an important industrial interest. One should think about RFID tags, OLEDs, thin-film organic transistors, solar cells, sensors, or electronic contacts, which are subject to intense investigations for industrial transfer [38,39,v]. Still, there are some technological challenges for the above mentioned ink-jet printed applications to truly emerge. As IJP is a solution process, solvents orthogonality for multi-layers components (such as for organic transistors) is an important issue. Film/substrate adhesion issues or film homogeneity problems are also reported (the fact that drops are printed induces specific effects, such as the famous "coffee ring" effect for instance, which was pointed out by Deegan et al. [40]). Also, ink-jet printing is limited in terms of resolution. A record minimal value of 1µm for ink-jet printed Au contacts was for instance reported [38]. The lack of resolution for IJP is one of the reason explaining it is still not competitive with more traditional methods, such as photolithography, when high resolution is required.

[u] See the web site of one of the leader in the sector of piezoelectric ink-jet printers http://www.domino-printing.com/Global/en/Home.aspx.
[v] See the web site of AFELIM, Association Française de l'Electronique IMprimée, http://www.afelim.fr).

III.C.1.b. IJP basic principles and requirement

III.C.1.b.i. Continuous IJP and Drop on demand IJP

There are actually two kinds of IJP process: continuous IJP and drop on demand (DOD) IJP. Continuous IJP was created first, in 1960 [41] and requires that the inks can be electrically charged. A continuous drop flow is formed under the periodic application of a pressure wave into an ink reservoir. At the nozzle's exit, the drops which will be printed are electrically charged by two electrodes. Then these drops can be deflected toward the desired positions on the substrate and the image is formed. The drops which are not printed are not charged at the nozzle's exit and can be collected (see Fig. 64). This method induces then lots of waste and has a low resolution, this is why it is only used for basic applications, such as printing on textile or printing bar codes[42].

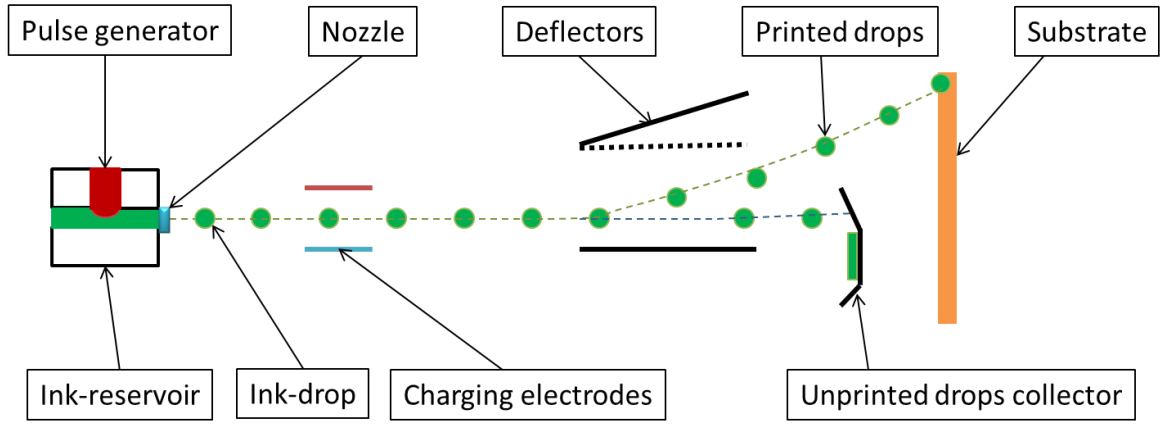


Fig. 64- Continuous IJP schematized principle.

DOD IJP was developed in the 70's and is today the most used IJP technique [41]. For this technique, a piezo-electric actuator or a thermic resistance induces a pressure pulse which results in drop ejection from an ink cartridge at selective places. The image is built upon the combined movement of the cartidge and of the substrate. The piezo-electric actuator (which has been schematized on Fig. 65) is generally prefered since it is more compatible with volatile inks. DOD also have the advantage of generating tiny drops (1 to 10 pL), which gives a better resolution.

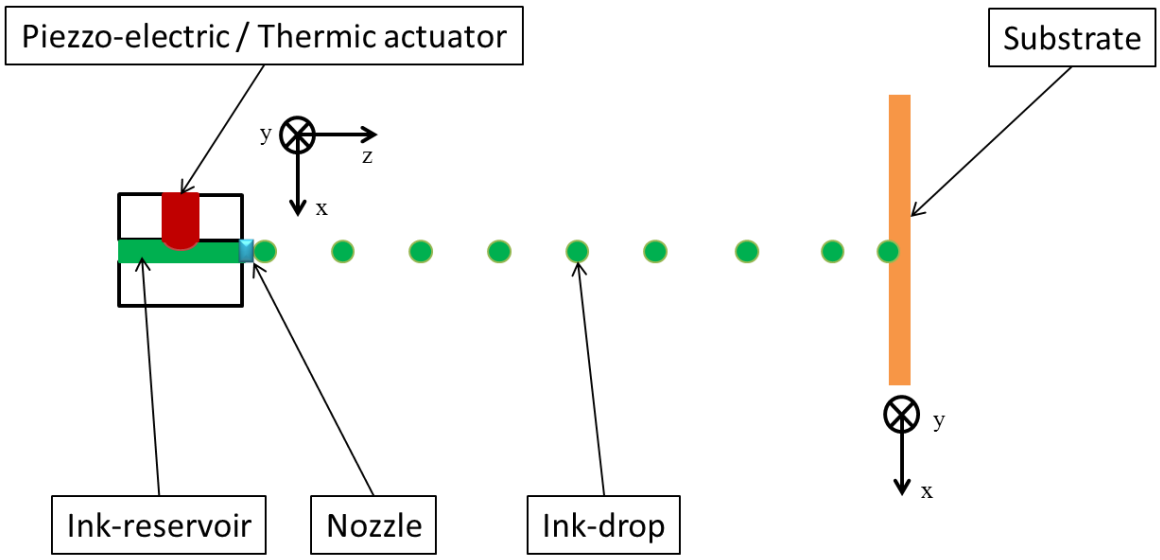


Fig. 65- DOD IJP schematized principle.

III.C.1.b.ii. The successive steps of IJP

The first step of IJP is the drop generation. This step is mastered by the electric voltage applied to the piezo-electric actuator situated in the injection chamber (see Fig. 66). Actually, the applied voltage is not constant during the drop generation process and the function which manages this voltage alongside time is called the waveform. A typical waveform has been described on Fig. 66. The waveform must be optimized, depending on the ink used, in order to guarantee optimal drop ejection. The first step is to apply the 0V voltage to the piezoelectric actuator, in order to increase the injection chamber volume; this induces that the ink is pumped into the injection chamber. Then the voltage is rapidly increased (step 2 on Fig. 66) to reach its maximum value. This leads to drop formation at the level of the nozzle. Then (step 3 on Fig. 66), the drop is ejected by reducing the piezo-electric actuator voltage till the “equilibrium” value. This steps is performed gradually, so that the injection chamber is not backfilled with air.

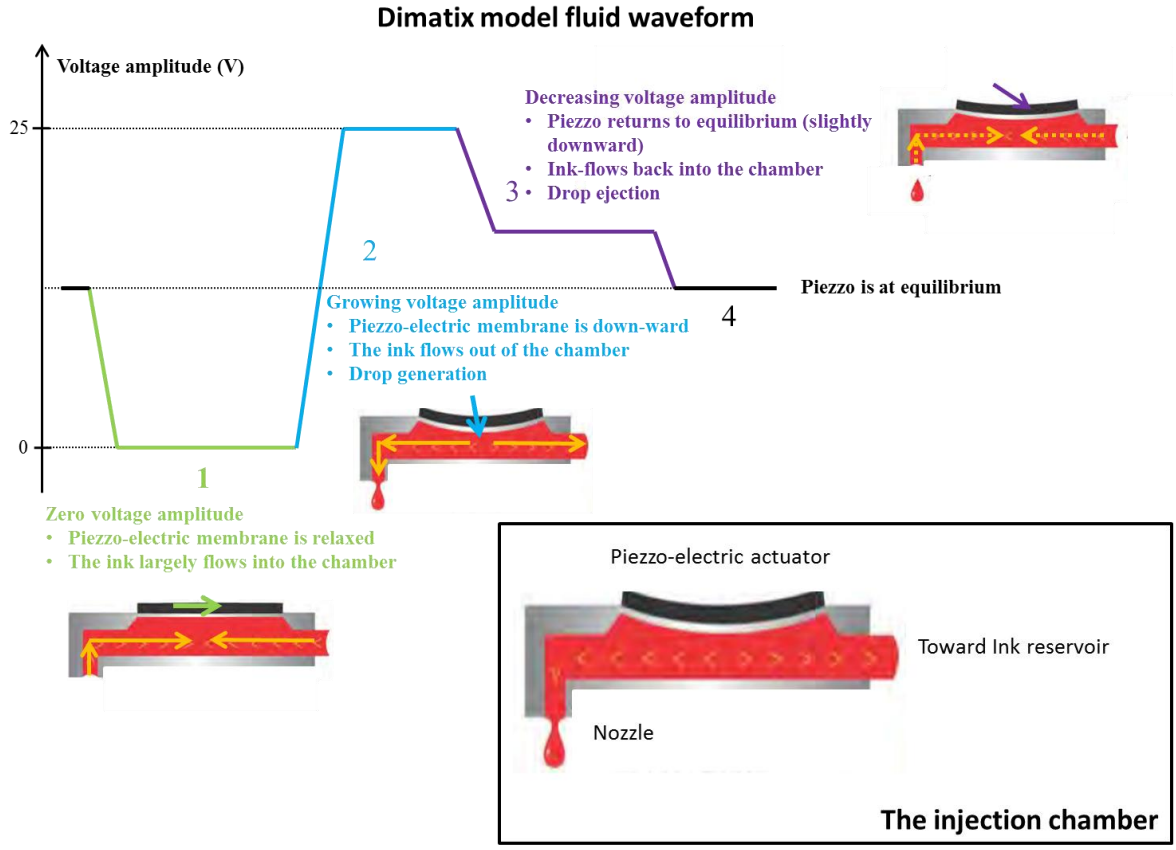


Fig. 66- Typical Dimatix model fluid waveform (with an arbitrary voltage applied) and representation of the injection chamber (the chart of the piezo electric actuator was reproduced from the Dimatix user guide). The voltage which is exemplified here is set at 25 V.

One should notice that the presence of debris in the nozzle can induce parasitic drops formation, or even nozzle clogging. The presence of bubbles into the ink can also be detrimental for drop generation. Finally, the temperature of the nozzle is a parameter which can be adjusted in order to get optimal drop generation.

Once ejected, the drop flies to the substrate. At the beginning of this step, a tail is formed behind the drop. If the proper voltage has been applied in the cartridge, the tail is reintegrated into the drop during drop flight, if not, satellite, detrimental drops are formed. Too high voltages generally induce drops with a too high velocity, and then, satellite drops are formed. Moreover, during drop flight, drop evaporation occurs. In link with the volatility of the solvent used, the nozzle to substrate distance has then to be correctly chosen in order to avoid total drop evaporation.

Finally, the drop impacts the substrate. The velocity of the drop should not be too important, in order to avoid parasitic "splashing". After that, the ink spreads onto the substrate and then drying occurs. An important parameter for IJP is that substrates can be heated during printing and then drying conditions can be tuned. This heating possibility can be very interesting for material properties tuning.

III.C.1.b.iii. Ink design and formulation for IJP

In order to ensure proper ink-jet printing (the nozzle diameter is small: 21 µm for Dimatix printers), the ink's viscosity should be low, ideally between 1 and 20 mPa.s [43].Also, the ink has to be designed so as to prevent nozzle clogging. For this, the objects contained in the ink should not overstep 1/100 of the nozzle diameter. Hence a filtering step, to remove possible debris or too big objects, is needed prior to IJP. Also, the ink has to be designed not to evolve and generate clogging species once into the cartridge. Finally, the ink's surface tension must fulfill compromised requirements. That is, is has to be high enough to prevent ink leakage through the nozzle, but also it has to be low enough to ensure good wetting to the substrate. Ideally, according to Dimatix user manual, the ink surface tension should be between 28 and 33 $mN.m^{-1}$. In order to ensure that the ink was correctly formulated and the suitable jetting parameters were chosen, so that proper drops are formed during printing (no parasitic drops, no tails …), investigations are performed with the help of a "drop-watcher" (see III.C.2.b), which is nothing more than a stroboscopic camera.

III.C.1.c. Ink-jet printing oxides via the sol-gel way

III.C.1.c.i. State of the art

Realization of oxide films through IJP is gaining a constant interest among researchers, regarding the tuning possibilities and the reproducibility provided by this deposition technique[43]. Either nanoparticle or "sol-gel" inks can be formulated. The nanoparticle based inks have to be made out of small particles (below 100 nm), so as not to induce nozzle clogging. However, as small particles are more prone to coalesce, generally, stabilizing agents have to be added (which means they need to be removed after printing, by combustion for instance). For the sol-gel inks, the requirement is to avoid gelation into the nozzle. This problem can be solved by suitable design of

the ink (ligand controlling the gelation process for instance, pH adjustment, the use of non-aqueous solvents …).

An increasing number of publications is dedicated to oxide deposition by IJP through the sol-gel way. Actually, it seems that the first paper referring to this topic dates back 1997, with the work of Atkinson et al. [44]. They actually ink-jet printed sol-gel inks onto ceramics, for a decorative application, via continuous IJP. A Chrome Alumina Pink pigment and a Nickel Alumina blue pigment were fabricated, through the ink-jet printing of a simple mixing of nitrate or chloride salts in aqueous solutions.

The first non-decorative application appeared in 1998, by the work of Danzebrink's team. They reported on the fabrication of hybrid silica based microlenses [45,46]. In 2000 and 2001, the group of Brinker reported on the IJP of porous silica composite through the incorporation into the sol silica precursor ink, of structuring agents such as the non-ionic Brij-56 [47,48]. From 2006 to recently (2012) Lejeune et al.[49,50,51] reported on the fabrication of mesoporous SiO_2 microdots array. It appears this team was the first to use "pluronic type polymer" F_{127} as a mesoporous structuring agent in a sol-gel ink for IJP. Besides, in the most recent publication a possible "artificial nose", futuristic application was mentioned [51]. The layer by layer local patterning possibility of IJP was here fully utilized. TiO_2 was also ink-jet printed by several groups through the sol-gel way[52,53,54,55,56]. A wide variety of other materials were allowed to be ink-jet printed via a sol-gel ink: Cerium oxide [57], tungsten oxide [58], $YBa_2Cu_3O_{7-\delta}$ oxide [59, 60, 61, 62] or ZIO (Zinc Indium Oxide) [63]. Actually, only one publication was found to report on NiO ink-jet printing, to the best of our knowledge. However the ink contained NiO nanoparticles and the resulting film did not display the desired structuration for DSSCs [64]. NiO was never reported to be ink-jet printed through the sol-gel way.

III.C.1.c.ii. Combinatorial material synthesis

Interestingly, some groups took advantage of IJP being compatible with several sol gel precursors and used it as a tool for combinatorial studies. For instance, Parkinson et al. [65] used various nitrate salt based sol-gel inks ($Fe(NO_3)_3$, $Cu(NO_3)_2$, $CsNO_3$, $Nd(NO_3)_3$, $Co(NO_3)_2$ and $Al(NO_3)_3$) which they respectively placed into cartridges. With a commercial printer, they obtained oxides

with a great variety of compositions, which could then be tested for their water photo-electrolysis activity. Optimization of the method led to the discovery of new photo-electrocatalysts, and to the optimization of their design [66]. This group largely exploited this combinatorial analysis for other materials, such as $BiVO_4$ (via $BiNO_3$)[67], Fe_2O_3[68] or Ru and Ir metal oxide catalyst for Oxygen Evolution Reaction[69]. Lewis et al. also reported on a screening session based on a combinatorial IJP approach, with nitrate metal salt inks[70]. Finally, a slightly different approach by Stucky et al. produced mesoporous materials, through combinatorial IJP [71]. They formulated sol-gel inks, out of metal salts (which are not necessary nitrate salts, like for the Parkinson et al. and Lewis et al. approach), and block copolymer as the mesoporous structuring agent (such as F_{127}). The use of F_{127} polymer (for its surfactant role) was pointed out to be beneficial for the ink rheological properties, for IJP.

III.C.1.d. Conclusions

IJP is an innovative and suitable technique for oxide film formation, out of a sol-gel ink. A few groups even successfully incorporated the structuring agent F_{127} as a templating agent in the ink, with metal salts as oxide precursors. But pure NiO synthesis was never mentioned.

Then, it appeared that the ink used for NiO photocathode films described above (see III.B.1.a) deserved to be tested as an IJP ink. Another motivation was that IJP being a digital and automated technology, was expected to largely increase the reproducibility of NiO film formation, compared to the traditionally used doctor-blade method.

III.C.2. Fabrication of NiO films for DSSC through ink-jet printing

III.C.2.a. Ink preparation

III.C.2.a.i. Ink formulation for IJP

III.C.2.a.i.(i) First investigations

In order to establish if the ink which is normally used for NiO formation through doctor-blading method was suitable for IJP, its viscosity was measured. Measurements were performed at different shear rates (see Fig. 67). At low shear rates (10 Hz), the ink viscosity was about 60 mPa.s at the beginning and rapidly increased to higher values (130 mPa.s). When the shear rate was increased to 100 Hz, the ink behavior was quite similar, though the viscosity value was

slightly increased to 70 mPa.s. When very high shear rates were applied to the ink (10 000 s^{-1}), a pronounced shear thickening behavior was observed. Shear-thickening behavior is not suitable for IJP, because high shear rates are applied to the ink during printing. Thickening of the ink must be prevented to rule out nozzle clogging. One can conclude that the ink used for doctor-blading, though being very liquid, has still a viscosity which is ten times higher than what it should be for being ink-jet printable.

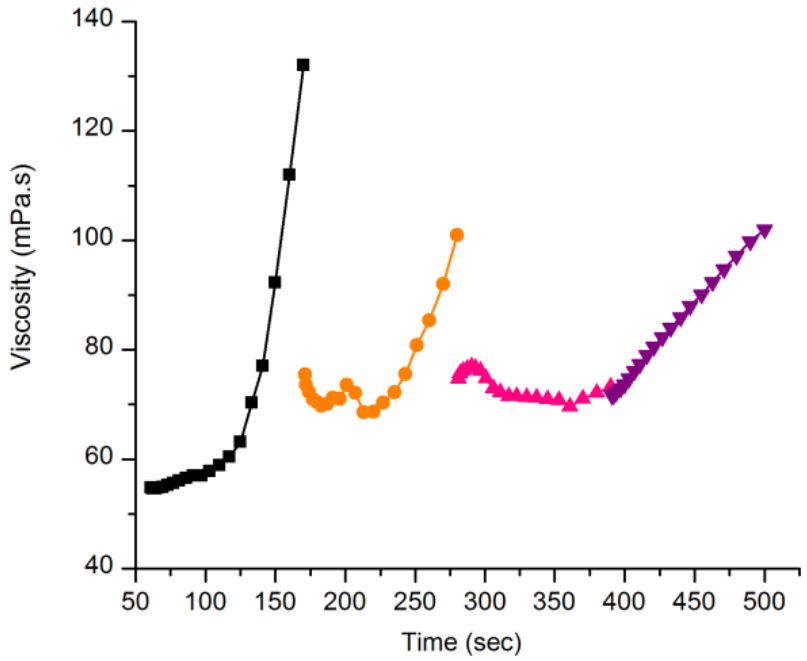


Fig. 67- Viscosity as a function of time, for different shear rates (SR), for the non-diluted ink. Black (squares), SR=10 s^{-1}; Orange (rounds), SR=100 s^{-1}; Pink (triangles), SR = 1000 s^{-1}; Purple (inverted triangles), SR=10 000 s^{-1}.

III.C.2.a.i.(ii) Decreasing the ink viscosity

In order to decrease its viscosity, the ink was tentatively diluted in water, by addition of one mass equivalent of this solvent. A picture of the obtained ink has been shown on Fig. 69). Then, the rheological properties of this diluted ink were assessed. The results are presented on Fig. 68. At low shear rate, the viscosity of the system oscillated between 5.18 and 5.28 mPa.s and the average value was comprised between 5.20/5.22 mPa.s. When the shear rate was increased up to 5000 s-1, the system was found even more stable and the small oscillations around the average value disappeared. The viscosity value was found to be 5.22 mPa.s. This low value is actually

compatible for IJP use. One can remark that this time, the fluid does not display any shear thickening behavior. The fluid rather presents the rheological properties of a Newtonian fluid (viscosity independent of the shear rate). This is expected, considering the large amount of water (which is the Newtonian fluid by excellence) which are present in the diluted ink. Considering that during IJP, very high shear rates are applied to the ink (*vide supra*), it is beneficial that the ink viscosity remains constant at these high shear rates, in order for instance to avoid nozzle clogging.

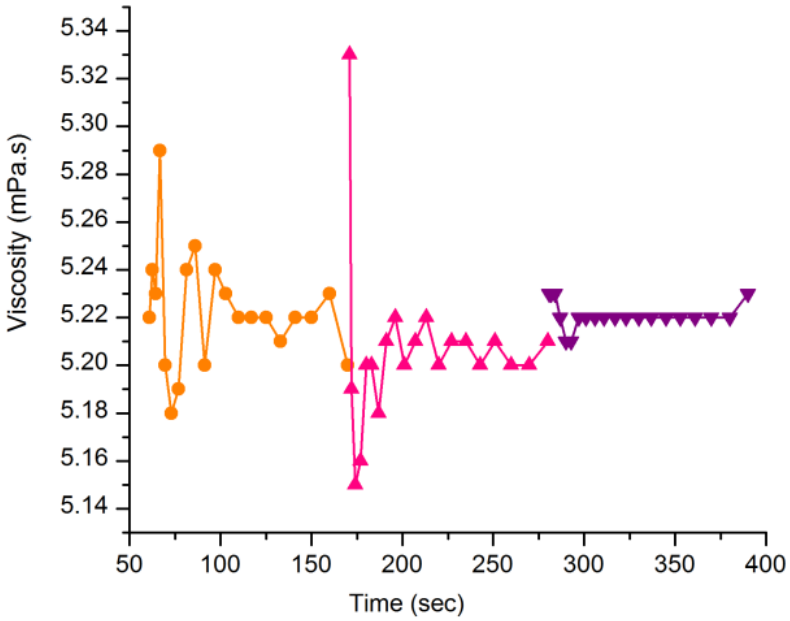


Fig. 68- Viscosity as a function of time, for different shear rates (SR), for the diluted by two with water ink, after. Orange (rounds), SR=100 s^{-1}; Pink (triangles), SR = 1000 s^{-1}; Purple (inverted triangles), SR = 5 000 s^{-1}.



Fig. 69- The diluted ink

III.C.2.a.i.(iii) Surface tension and contact angle

The surface tension of the ink was calculated to be 31.5 $mN.m^{-1}$. This value is in the optimal range for IJP (see III.C.1.b.iii. Finally, in order to evaluate the compatibility of the diluted ink with FTO glass, its contact angle was measured, after UVO treatment of FTO, like for printing conditions (see experimental part). The contact angle was found to be 17° ± 1° (see Fig. 70**).** This means that the ink wets well its substrate, which is beneficial for IJP since it could avoids pinholes formation.

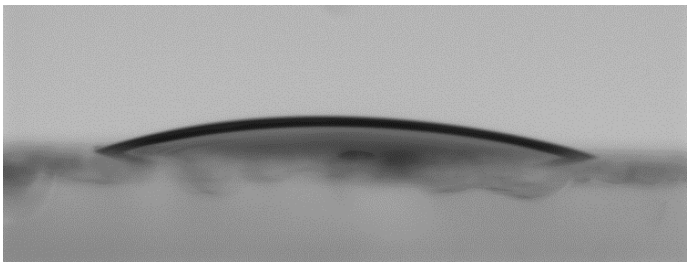


Fig. 70- Contact angle measurement picture for the diluted ink on FTO glass, after UVO

III.C.2.a.ii. Aging of the ink

Aging sol-gel inks is a common procedure for optimizing the sol preparation. In the case of the ink studied here, two aging process were considered:

➔ the starting of $NiCl_2$ inorganic polymerization, to form hydroxilated species, such as $Ni(OH)_2$

➔ the self organization of the F_{127} polymer in the aqueous medium (as the polymer concentration is above CMC when the ink is prepared).

Actually, if the $NiCl_2$ inorganic polymerization occurs during ink aging, $Ni(OH)_2$ species should be formed. This should be visually detectable since $Ni(OH)_2$ species are known to precipitate in aqueous and ethanolic media [72,73]. To the best of our efforts, no such precipitate was actually noticed within one week of ink conservation in a sealed bottle, at room temperature. XPS on NiO films confirmed this hypothesis (see III.C.3.b).

On the other hand, we could not monitor the organization of F_{127}, which could happen too. However, an arbitrary minimum aging time of 20 hours was employed for ink preparation in this thesis.

III.C.2.b. Printer description

The ink-jet printer employed was a Fujifilm Dimatix DMP-2800 (see Fig. 71). This type of printer is composed of a carriage, with a cartridge holder. The cartridge is plugged into the cartridge holder during printing. The cartridges used in this thesis were 16 nozzle cartridges, with a nozzle diameter of 21.5 µm . The substrate is placed onto the platen at a desired position and can be heated up to 60°C during printing. The cartridge can also be heated up to 70°C during printing. In order to monitor the drop evolution after its ejection from the nozzle, a stroboscopic camera (so called "drop-watcher") is available. One should remark that when using the drop watcher, due to its location, the possible influence of the platen temperature on the drop formation process cannot be taken into account.

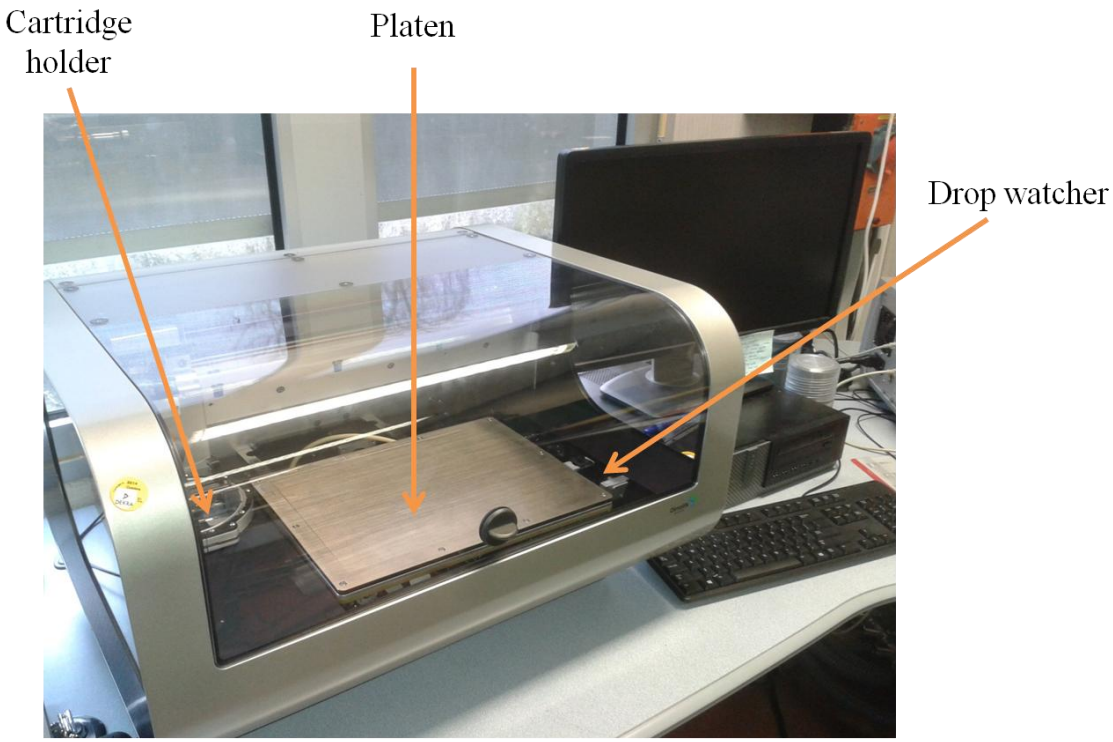


Fig. 71- The Dimatix printer (DMP 2800) used in this thesis

III.C.2.c. Printing parameters for NiO film preparation

In order to build NiO films with a good quality the numerous printing parameters allowed by the Dimatix printer needed to be adjusted first.

III.C.2.c.i. First-step required: preparing the cartridge

A first very important requirement was to ensure that no bubbles were present in the printing chambers. For this, after the ink was introduced into the cartridge, the cartridge was left at rest for

at least 30 min in the printer. During this session, cleaning cycles were performed, in order to avoid detrimental gelation of the ink in the nozzles. Besides, it was important to operate with a very clean cleaning pad. Importantly, the print-head was gently and carefully cleaned by wiping with ethanol prior to printing (attention was paid not to turn the cartridge up and to introduce bubble in the chambers). Further details can be found in the experimental part.

Then actually two sets of parameters were tested for the NiO film formation. Actually, these sets of parameters share many common points, which are first described here.

III.C.2.c.ii. Common parameters for all films formation

0.5 cm per 0.5 cm tinted area (*i.e.* no patterning) films were formed. Drops were uniformly deposited with resolution (distance between the drops in the x direction and in the y direction) of 20µm. The Dimatix model fluid waveform was used. This waveform is typically used for IJP, and is adapted to the Newtonian character of the ink. For both sets of parameters, the maximum jetting frequency was set at 3 kHz. This is a low value, then it increases printing duration, however, it permits to avoid nozzle clogging and to increase the film quality. The platen temperature was set at 30°C, in order to permit gelation of the films. One can remark that it was important to ensure thermalization of the FTO substrates at the platen temperature before printing (see experimental part).

III.C.2.c.iii. First set of parameters (« set-1 »)

III.C.2.c.iii.(i) Drop generation

At the beginning of the study, it was thought that good quality drops would permit to obtain good quality films. For this, we first tried to obtain good quality drops. This drop optimization step was performed with the help of the drop watcher. Then, two parameters were optimized: the applied voltage and the temperature of the cartridge. It was found that a 17 V applied voltage, and a cartridge temperature of 32°C give good quality drops: well defined, without satellites (see Fig. 72) and with a reasonable velocity around 7.5 / 8 $m.s^{-1}$ (see Fig. 73). Importantly, all the nozzles ejected similar drops, with similar velocity (see Fig. 73, right). For a dynamic illustration, the drop formation movies with set-1 parameters can be found in the electronic version of this thesis.

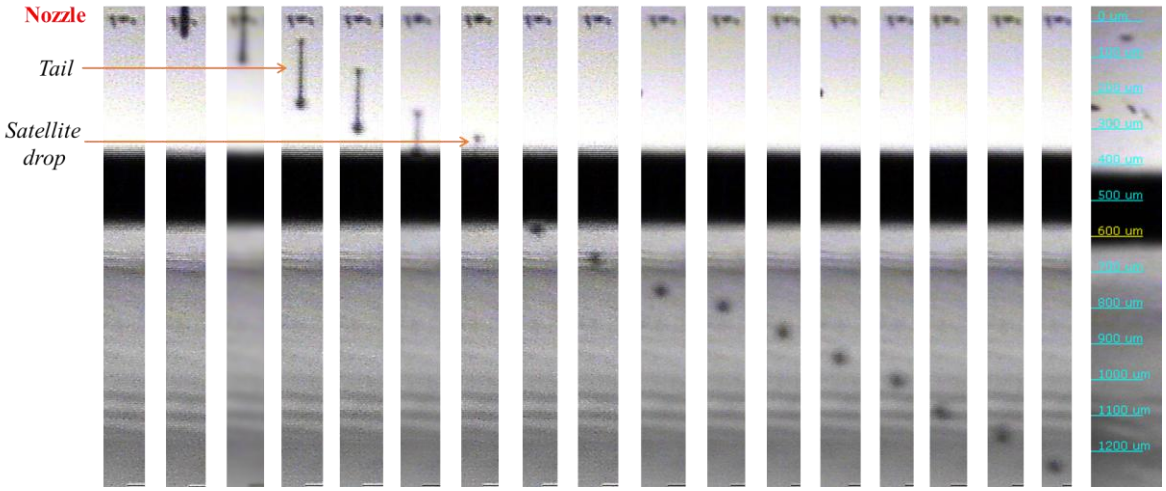


Fig. 72- Evolution of the drop after its ejection from the nozzle with « set-1 » parameters.

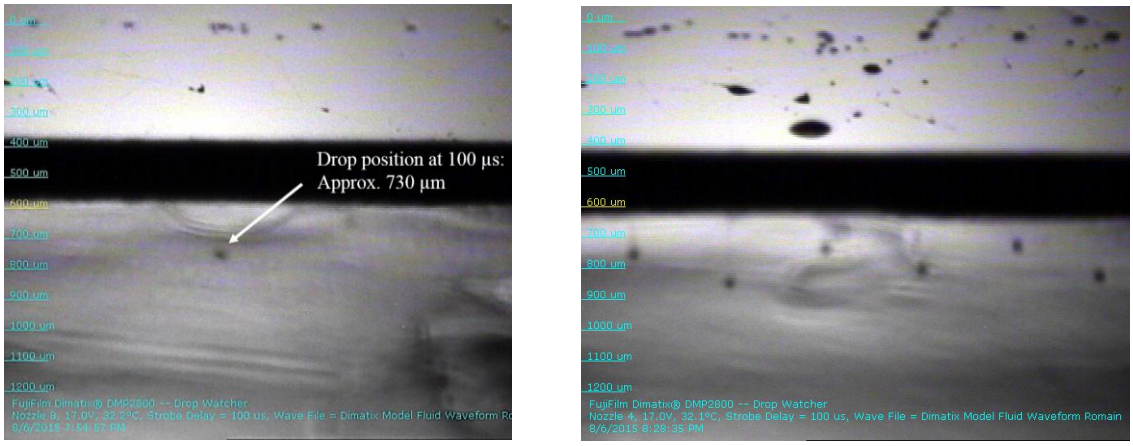


Fig. 73- Drop position 100µs after its ejection from the nozzle with « set-1 » parameters. Left : one nozzle was activated, right : all the nozzles were activated.

III.C.2.c.iii.(ii) Film formation

When the nozzle to substrate distance was set at a reasonable value, 650 µm, at which the tail of the drop was not present anymore (see Fig. 72), it was very surprising to discover that no film was visibly formed on FTO. Then, the print-head was tentatively set closer to the FTO glass, but no film was neither detected … As the drop watcher indicated no nozzle clogging, it was interpreted that, due to the proximity with the platen, which is at 30°C, the drops totally dried during their flight, and the film could not be visible. This is why we decided to increase drop velocity, so as to decrease the flight time, and avoid full drying of the drops before reaching the FTO substrate.

III.C.2.c.iv. Second set of parameters (« set-2 »)

III.C.2.c.iv.(i) Drop generation

The voltage applied to the piezo-electric actuator was increased at 25V, in order to increase drop velocity. This was successful since a velocity of approximately 14 $m.s^{-1}$ could be obtained (see Fig. 75-left, the drop approximately travels 700 µm within 50µs), which is twice faster than with "set-1" parameters. Also, in order to avoid ink overflowing off the cartridge, the temperature of the nozzle was lowered to room temperature (i.e. around 23°C). With these parameters, nozzle clogging was actually scarcely noticed and all the nozzles ejected drops of similar velocities (see Fig. 75-right, also see the film of the drop generation process in the electronic version of this thesis).

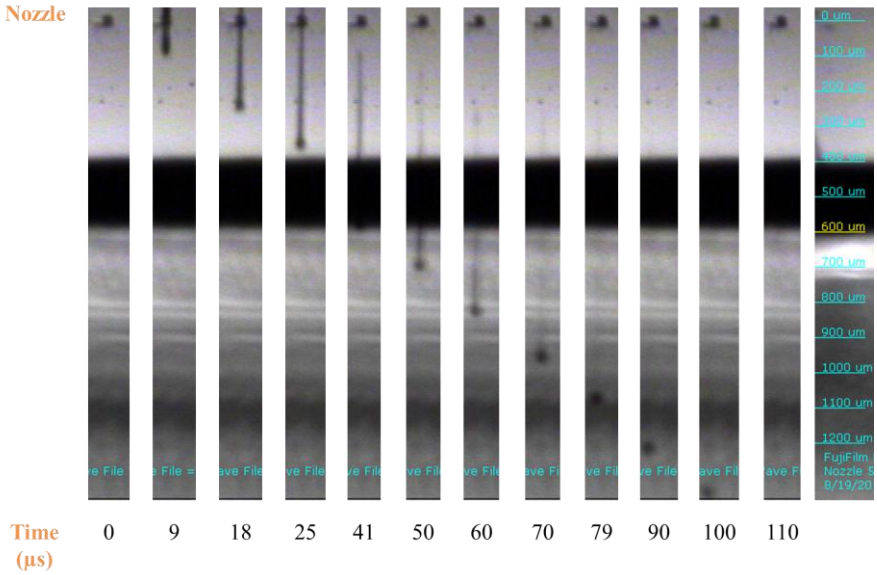


Fig. 74- Evolution of the drop during its flight along time with « set-2 » parameters.

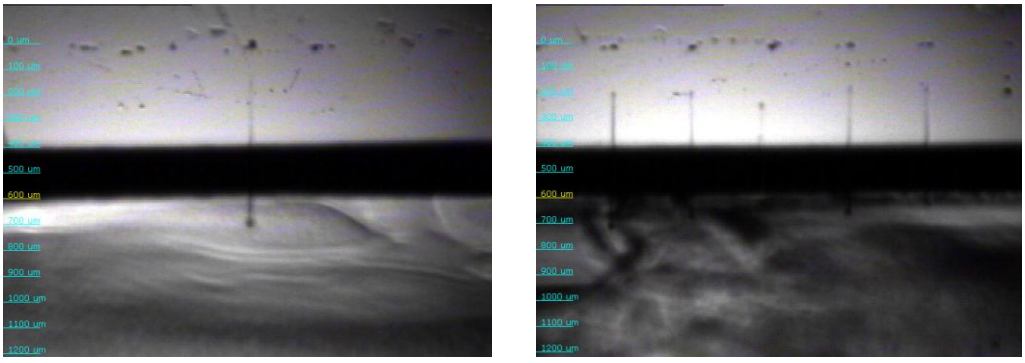


Fig. 75- Drop position 50 µs after ejection from the nozzle, with « set-1 » parameters. Left: one nozzle was activated. Right: all the nozzles were activated.

III.C.2.c.iv.(ii) Film formation

The substrate to nozzle distance was adjusted at 650µm and this time, a film was formed. Hence increasing drop velocity, in order to decrease the drop flight time, and the solvent evaporation prior to deposition, was successful. The formed film appeared to be of good quality (no splashing effect, nor pinhole, were visibly detected) and was actually used for implementation into all the p-type DSSCs presented in this chapter.

III.C.2.d. Role of humidity

The relative humidity of the room appeared to play a very important role in the IJP of sol-gel NiO process. If humidity was below 30 % / 35 %, large pinholes were noticed in the film, prior to drying. It is possible that low humidity induces a high rate of solvent evaporation at every step of the printing. Then, ink gelation inside the nozzle is more likely to occur, which leads to nozzle clogging. Also, speed-up drying of the drops during their flight between the nozzle and the substrate can be favored at low humidity values. Interestingly, the role of humidity during the IJP process is often mentioned in a recent review by Jabbour et al.[74]. In order to control the humidity of the room, a humidifier was settled in the printing room. It ensured humidity values between 30% and 45%, which appeared to be adapted for efficient IJP.

III.C.2.e. Deposition of one layer of NiO substrates (NiO-1L samples)

III.C.2.e.i. Drying and sintering conditions

Just after printed, the film is very liquid. Then, in order to prevent the ink from flowing over the substrate during manipulation of the substrate, the film was first of all dried at the platen temperature (30°), during one minute. After that, a 10 minute drying session at 100°C on a hot plate, external to the printer, was performed in order to remove the solvent from the film. Finally, likewise what is usually done when the sol-gel ink is doctor bladed, the film was sintered at 450°C for 30 min, at air [24]. As described in III.C.3.b, such a high temperature is required for NiO formation. **NiO-1L** (**1L** for one layer) films were formed this way.

III.C.2.e.ii. Film morphology

NiO-1L films were crack-free and transparent, with slight color iridescence. The center and major part of the film was blue, while the edges of the film displayed an orange/yellow coloration. This

difference indicates that the film is slightly thicker in the edges. This could be attributed to a slight "coffee-ring" effect during printing of the NiO film [75]. The color iridescences due to the high transparency of the {FTO/NiO} film and to its thickness which is in the range of visible light wavelengths (see SEM pictures, see Fig. 77).



Fig. 76-NiO-1L sample after sintering at 450°C

The cross-section and top view pictures of NiO formed revealed a uniform and very compact nano-particular structure for NiO (see Fig. 77). The particle diameter was measured on 20 particles and the average value was 17 nm. From the cross-section image (see Fig. 77) the thickness of the **NiO-1L** sample was measured at 320 nm (± 10 nm).

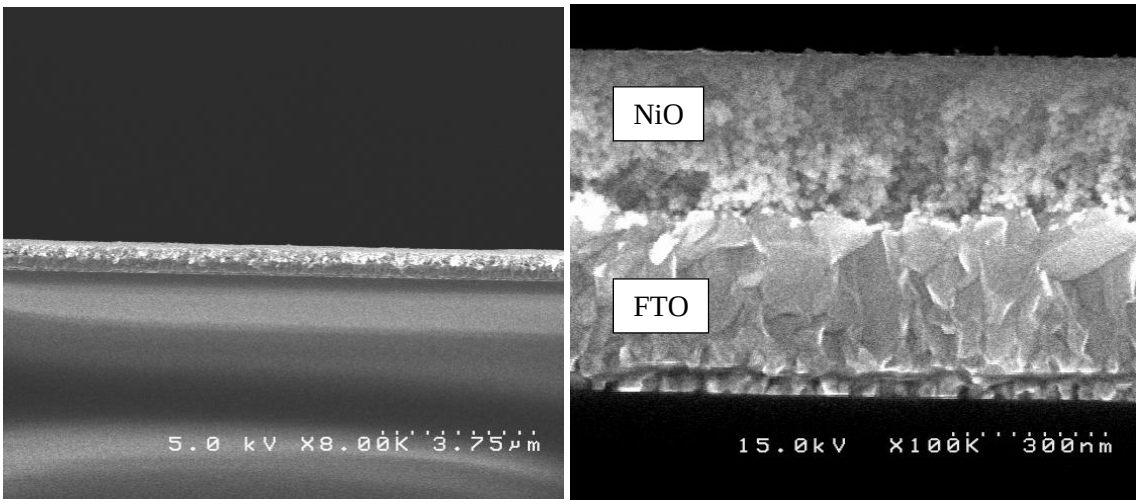


Fig. 77- SEM cross section of a NiO-1L film

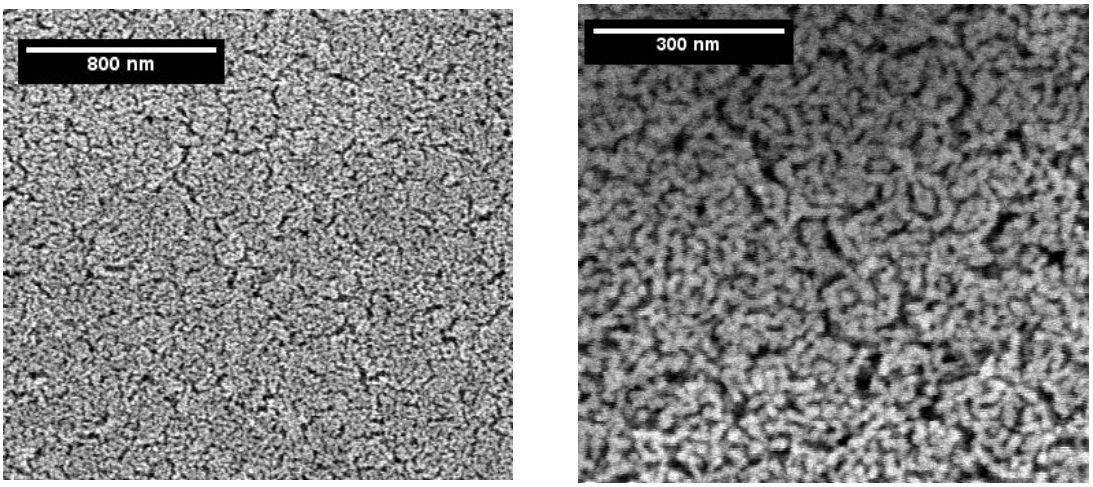


Fig. 78- Top view SEM image of a NiO-1L film

III.C.2.f. Increasing the number of NiO layers

In order to be suitable for integration in p-type DSSCs (in particular, in order to increase LHE), it is necessary to increase the thickness of the NiO film. As said above, the traditional thickness of NiO layers in p-DSSCs is between 1 and 2 micrometers, while only layer NiO IJP films provides only 0.3µm-thick films. Different interlayer drying conditions strategies were then tested in the purpose of increasing the film thickness via repetitive IJP steps.

III.C.2.f.i. Interlayer drying of 30°C

The first interlayer drying trial was to perform only a one minute 30°C drying step between each layer. Two to four layers of ink were deposited and the cross section SEM pictures after final drying at 100°C during 10 minutes and sintering at 450°C during 30 min are shown in Fig. 79.

In this case, a "nano-fiber like" nano-particles dual structuration which resembles the one obtained for doctor-bladed films, was observed. The nano-fiber like structuration was more pronounced as the number of layers increased and the surrounding crust was also observed in all cases.

Actually, this result finds an echo with the idea that increasing the amount of liquid ink deposited (that is at a given time, at a given place, the amount of liquid ink is important) induces nanofiber structuration, with a crust at the top of the film (see III.B.1.c). We assume that after its printing, the additional layer partly dissolves the former one, or does not wet it well. This induces a local more important amount of ink and thus the nanofiber / crust structuration. The nanofibers

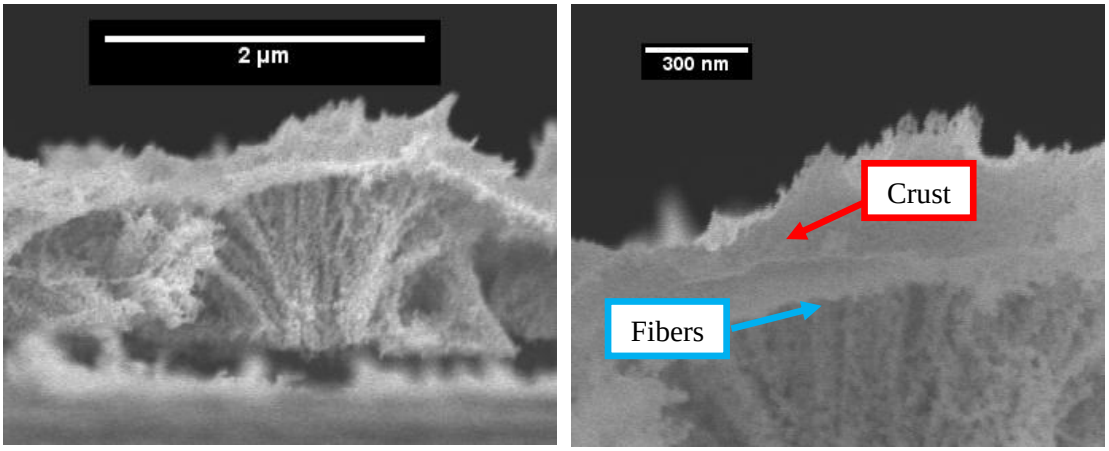
formation induced that the obtained films are dramatically less densely packed and the thickness reached are then important. The thickness of the films was around 1.5/2 µm for the two-layer sample (**NiO-F-2L**, **F** for "Fiber"), 2/3µm for the three-layer sample (**NiO-F-3L**) and about 4 µm for the four-layer sample (**NiO-F-4L**).

This structuration was found interesting for p-type DSSCs for two reasons:

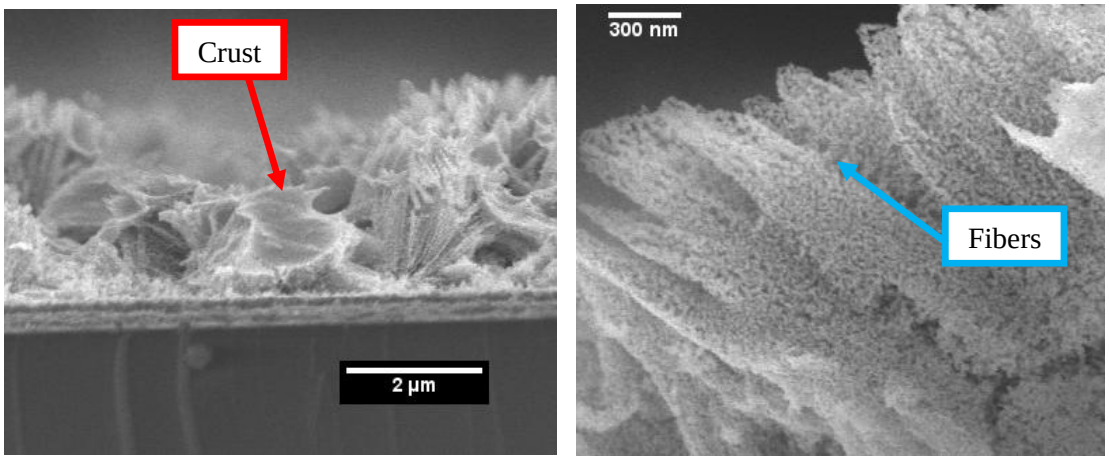
➔The nanofiber like structuration, which could provide better hole transport properties

➔The porosity of the material, which may induce better light harvesting properties

NiO-F-2L:



NIO-F-3L:



NiO-F-4L:

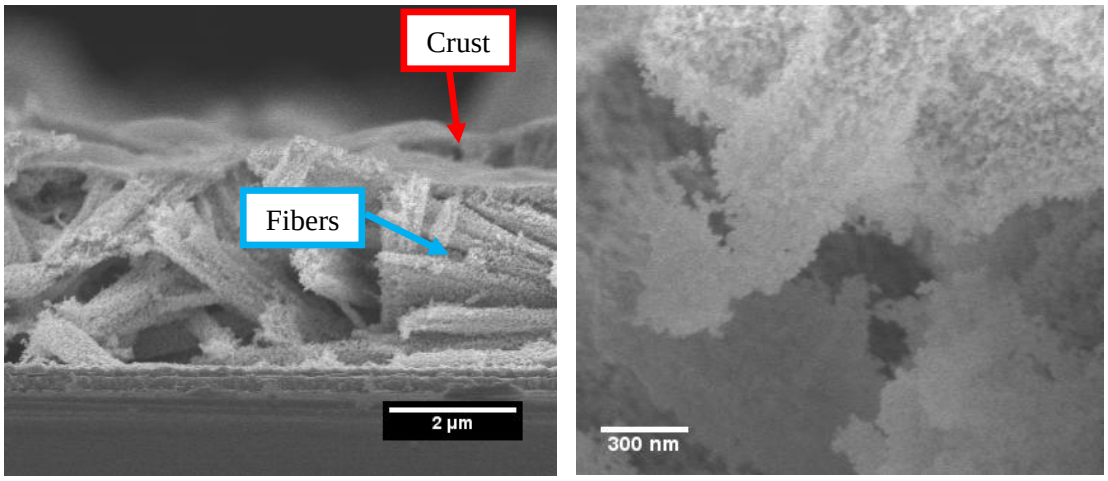


Fig. 79- SEM cross sections of more than one layer IJP NiO films with a drying temperature of 30°C.

III.C.2.f.ii. Interlayer drying of 100°C

In order to obtain more compact NiO films, an additional interlayer drying step, of 100°C during 10 min was introduced. The morphology of a four-layer NiO film fabricated this way, after the final 30min, 450°C sintering step is shown on Fig. 80. The structure is actually quite similar to the one obtained when a simple drying at 30°C between each layer was performed and the nanofibers were still observed.

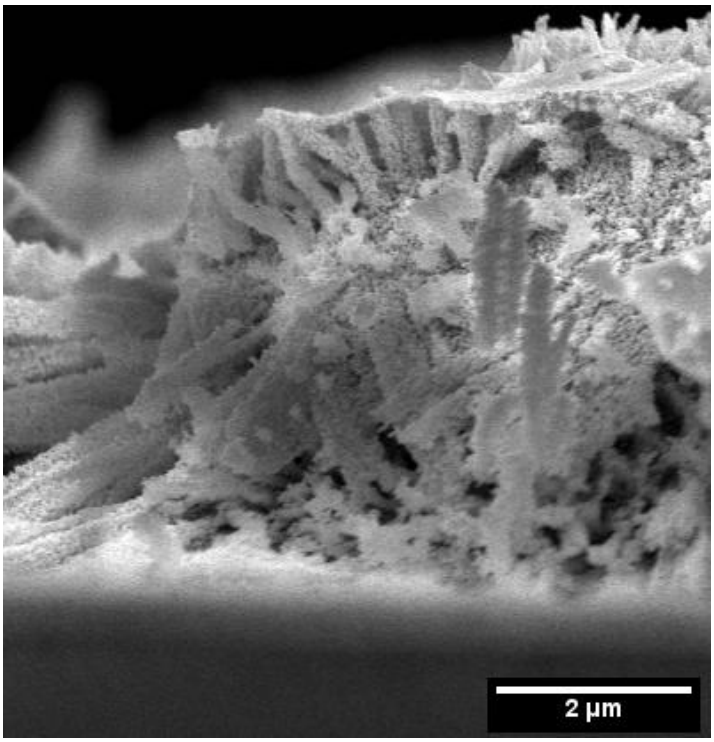


Fig. 80- SEM cross section image of four layers of NiO, with 100 °C drying steps between each layers.

III.C.2.f.iii. Interlayer sintering at 450°C

We finally tried to add a sintering step at 450°C in the interlayer treatment process, in order to avoid the formation of nanofibers. From a practical point of view, the 30°C one minute drying step was conserved, the 100°C drying step was also kept, but its duration was shortened to 3 min. The 450°C drying step duration was 4 min. This duration visibly permitted to remove the organic F_{127} and to form NiO (iridescence of the film was noticed). After the last layer was deposited, the film was finally sintered during 30 min (this comprises the 4 minutes of sintering of the last layer) for photocathode formation. One can notice that the duration of the interlayer sintering was

minimized to 4 min in order to prevent at maximum the formation of large NiO particles which could reduce the specific surface area of the film.

In this thesis, four-layer NiO samples synthesized this way are reported (**NiO-4L** samples). The picture of the obtained film for the deposition is depicted on Fig. 81. This time, the morphology is compact and dense. The film is uniform and no nanofiber structuration is noticed. This shows that the 450°C sintering step permitted to fix the morphology of the former layer deposited, before the next one is printed over.

The additional layers are all 170 nm thick (± 20 nm), which is thinner than the first one (320 nm (±10 nm). This is attributed to the penetration of the ink in the prior layer during its deposition. The overall thickness of the **NiO-4L** film is 850 nm (± 20 nm). The morphology resembles the one obtained by Sun and cowokers [24], who showed SEM pictures for two layers of NiO, with a 450°C interlayer drying step. Top-view SEM pictures of the film are also displayed in Fig. 82 and revealed a uniform, crack free structure, suitable for future study in p-type DSSCs.

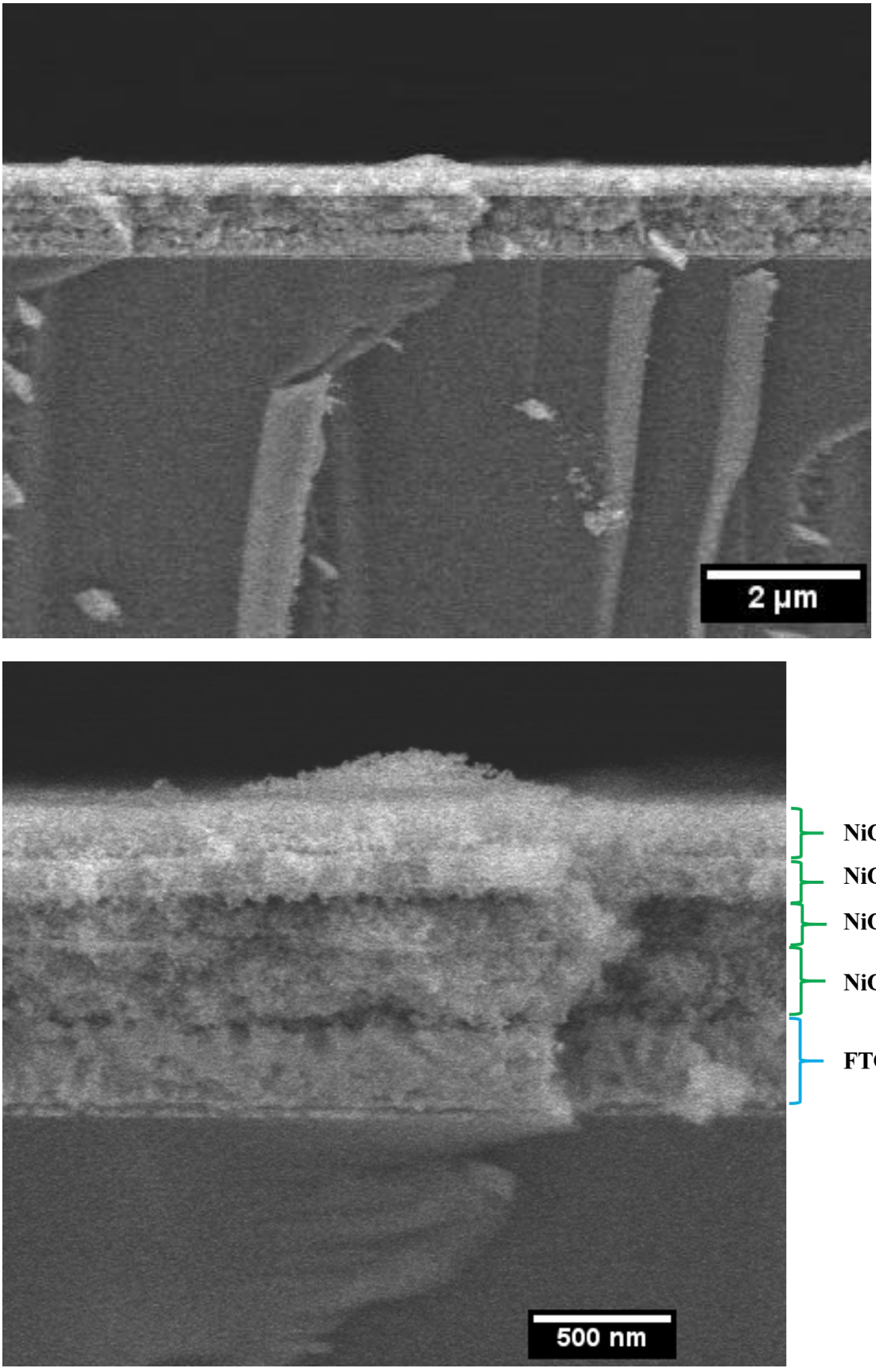


Fig. 81- Four-layer NiO sample with a 450°C interlayer drying step between each layer.

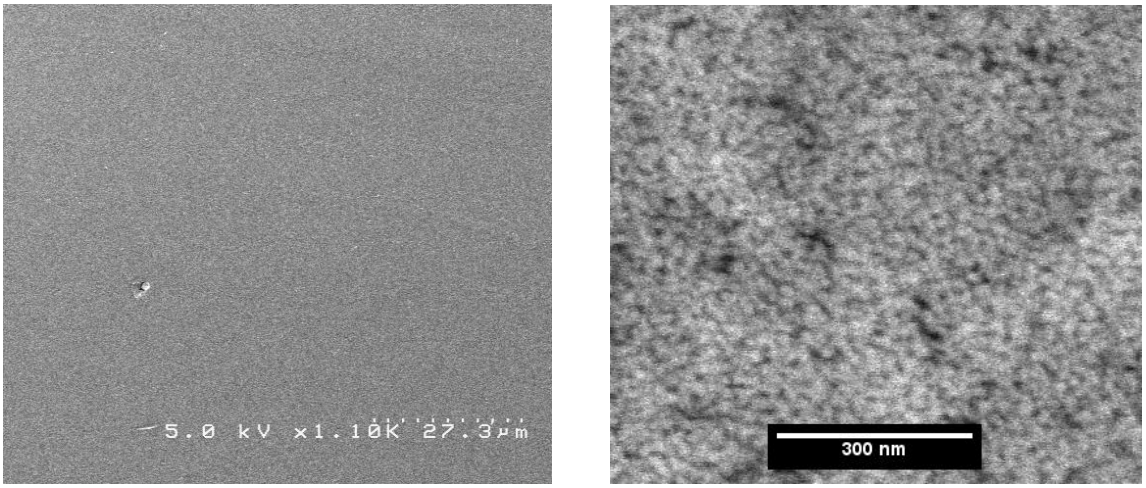


Fig. 82- Top view SEM pictures of the NiO-4L film.

III.C.3. Study of NiO formation mechanism

As described in the introduction of this chapter, Sun and coworkers depicted that the optimum sintering temperature for p-type DSSCs for which NiO had been made with sol-gel templated polymer ink was 450°C. However, to the best of our knowledge, the mechanism for NiO formation with this method has never clearly been published. Here, it is proposed to better understand this mechanism with the help of TGA and XPS analysis.

III.C.3.a. TGA analysis

TGA analysis was performed for the ink used for printing (see Fig. 83). In order to better understand this TGA graph, the weight percentage of each ink constituent were calculated in Tab. 13. The amount of expected NiO was calculated with a model equation for NiO formation (**eq. 1**). On should note that this equation is a model equation (and the aim of this paragraph is to investigate NiO formation mechanism). On the TGA graph, an important initial weight loss (89%) is assigned to an almost complete loss of water and ethanol, and stopped at 100°C. It is considered that the slight difference (1%) regarding the expected value (see Tab. 13) is comprised in the experimental error. After a plateau over a 70°C range, a 5% weight loss starts. This loss is centered on 180°C and is assigned to the burning of F_{127}. Afterwards, two processes occur:

a first one starts at 220°C and is centered at around 300°C; it can tentatively be assigned to the formation of $Ni(OH)_2$, which would be consistent with the suggestion of Lepleux et al.[36], who assigned a formation of $Ni(OH)_2$ from nickel acetate salts starting at around 300°C.

Another thermal process occurs between 350°C and 480°C, which can be assigned to the effective formation of NiO. The final weight percentage is the one expected for NiO formation (*eg.* 3%).

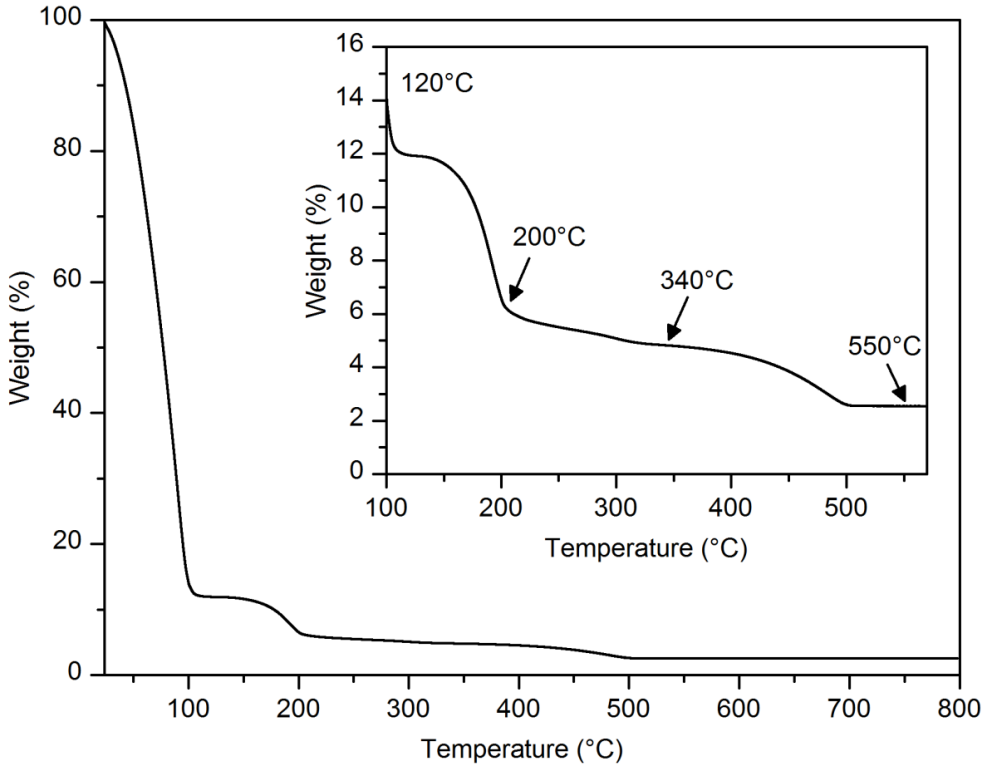


Fig. 83- TGA analysis for the diluted ink, with a 5°C/ min ramp, under air

Tab. 13- Initial absolute weight and weight percentage of the different elements of the ink used for printing.

Compound	Weight (g)	Weight (%)
H_2O	12.89	65
EtOH	4.85	25
F_{127}	1	5
$NiCl_2$	1	5
Total	19.74	100

$$NiCl_2 + H_2O \rightarrow NiO + 2\ HCl \quad (\textbf{eq.1})$$

Tab. 14- Reagent table for the formation of NiO (M_{NiCl2} = 130 g.mol^{-1}, M_{HCl} = 36 g.mol^{-1}, M_{NiO} = 75 g.mol^{-1}).

$NiCl_2$	H_2O	NiO	2 HCl
1g = 7.7 mmol (5%)	7.7 mmol = 0.14 g (≈1%)	0	0
0	0	7.7 mmol = 0.58 g (≈ 3 %)	15.4 mmol = 0.55 g (≈ 3 %)

III.C.3.b. NiO formation mechanism study with XPS

In order to investigate deeper the NiO formation mechanism, an XPS study was performed on IJP NiO. One-layer IJP NiO electrodes were fabricated on FTO and sintered at the different temperatures: 120°C, 200°C, 340°C, 450°C and 550°C (see experimental section for more details). Each electrode was analyzed by X-ray Photoelectron Spectroscopy (XPS).

In agreement with the material formulation, the survey spectra, displayed on Fig. 84 clearly show peaks due to nickel, oxygen and carbon elements for all the samples, and in some cases to chlorine. The atomic ratio of each element was reported to nickel at each temperature (see Tab. 15). The high content of carbon on the spectra at low temperature (120°C and 200°C) is attributed to the F_{127} organic polymer that is present in the formulated ink. At higher temperature, thanks to the heat treatment performed under air, the polymer is burnt, so as to create the mesoporous structuration. It should be noted that in this study, the burning of the polymer occurs at higher temperature than for TGA. This could be a consequence of the structuration of the film into well packed micelles, which only occurs when a thin film of ink is formed, as described above (which

may not be the case for TGA analysis). The carbon present on the samples heated at 450°C and 500°C corresponds to contamination carbon, with characteristic peak centered at 284.9 eV [76]. Indeed, the samples were manipulated in ambient condition after their heat treatment.

In the Ni_{2p} region, two broad sets of signals corresponding to $2p_{3/2}$ (860 eV) and $2p_{1/2}$ (876 eV) core levels are observed. The heat treatment from 200°C to 450°C leads to an increase of peak intensity and the emergence of new peaks particularly in the $2p_{3/2}$ region that can be respectively explained through the increase of Ni content in the sample since the organic polymer has been removed and through the formation of NiO. Indeed, on this last point, the new peaks at 853.6 eV and 866.2 eV on the 450°C and 500°C samples are characteristics of NiO[76] and confirm that NiO formation needs high temperatures in the case of the sol-gel templated synthesis. The most intense peak in the $2p_{3/2}$ region shifts during the heat treatment from 856.4 eV (120°C and 200°C), to 855.8 eV (340°C) and 853.6 (450°C and 500°C). These three binding energies as well as the shape of the Ni_{2p} curves are respectively in agreement with the previously reported $NiCl_2$, $Ni(OH)_2$ and finally NiO species [76]. In link with the remark concerning the aging of the ink (see III.C.2.a.ii, one can notice that nickel oxide and hydroxide derivatives are only formed at high temperature. Then, aging of the ink at room temperature may not imply starting of the sol-gel condensation for the $NiCl_2$ precursors. This is why the duration of the aging process was limited to 20h in this thesis, compared to previous literature.

The evolution of the $Ni_{2p3/2}$ peak is in harmony with the evolution of the chlorine and oxygen content. The Cl_{2p} core level spectra, displayed in Fig. 84 and Tab. 15, show a decrease of chlorine in the sample after 200°C before its complete vanishing at 450°C. It is worth to mention that the loss of chlorine between 200°C and 320°C is more important than shown by the small intensity decrease on the spectra since this loss is compensated by the reduction of carbon content in the sample.

Concerning the O_{1s} core level spectra, the peak centered at 529.2 eV for the 450°C and 500°C samples is attributed to bulk O_2^- ligands in NiO [77]. The other peak at 530.9 eV (30% of the oxygen atoms) is commonly seen in NiO samples [76,78,77]. It has been described to be the consequence of hydroxyl groups that are bonded to Ni atoms of the NiO network [78]. The chemical

reactivity of the surface induces huge formation of -OH surface functions and explains the high Oxygen/Nickel ratio of 1.36 for the sample heated at 500°C. The peak at 533.1 eV on the 200°C and 320°C samples is due to the ether and hydroxyl functions present in F_{127} polymer. Finally, the well-defined peak at 531.6 eV for the 340°c sample is proposed to be related to $Ni(OH)_2$ formation. The possibility of NiOOH formation is ruled out since the presence of this species should induce two peaks of similar intensity in the O_{1s} region (one for the hydroxyl oxygen "OH^-", the other for the Oxide "O^{2-}"oxygen) [79]. This interpretation is in agreement with the hypothesis of the intermediate formation of $Ni(OH)_2$ species in the course of NiO formation mechanism (*vide supra*). It is the first time that such an intermediate species is identified for the sol-gel template synthesis of NiO.

Tab. 15- Evolution of the different atomic ratio of Ni, O, Cl and C, as a function of the sintering temperature of the one layer NiO film. Ni was taken as a reference.

Temperature (°C)	Nickel	Oxygen	Chlorine	Carbon
120	1.0	3.7	2.0	9.4
200	1.0	4.5	1.9	10.8
340	1.0	2.0	0.7	2.7
450	1.0	1.4	0.0	0.6
550	1.0	1.2	0.0	0.4

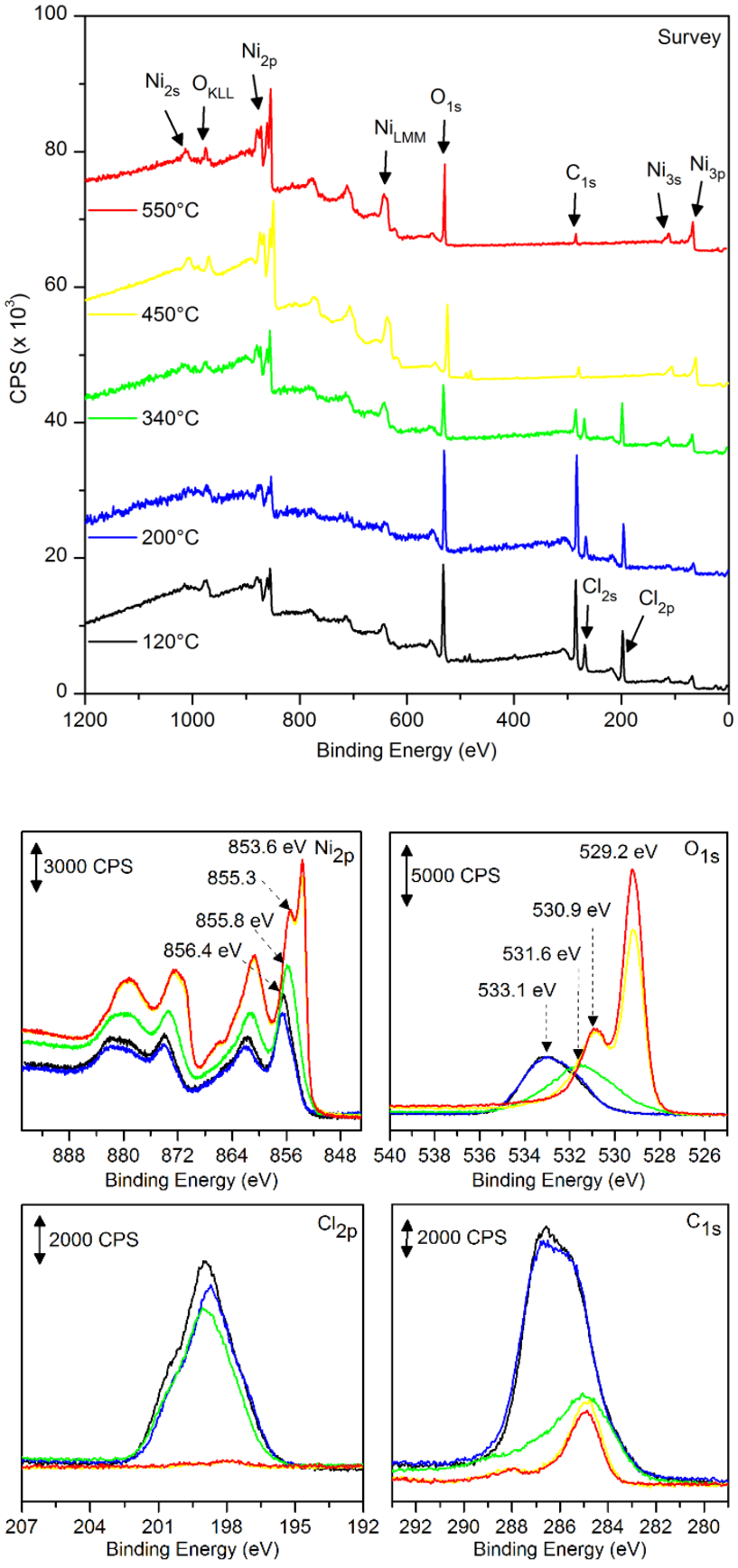


Fig. 84- XPS survey and Ni_{2p}, O_{1S}, Cl_{2p} and C_{1s} core level spectra of one layer IJP NiO electrode heated at different temperature: 120°C (black), 200°C (blue), 340°C (green), 450°C (yellow) and 550°C (red).

III.C.4. **Conclusions**

The dilution by one mass equivalent of water of the "traditional" ink used for sol-gel templated NiO film preparation made that ink suitable for ink-jet printing. The viscosity of the ink obtained was 5.2 mPa.s and the surface tension was 31.5 $mN.m^{-1,}$ which corresponds to optimal parameters for ink-jet printing.

Printing conditions were established and one-layer NiO films were first prepared. Uniform films, with a dense packing of nanoparticle morphology was obtained and displayed a thickness of 320 nm $^{\pm}$ 10 nm. In order to increase the thickness of the NiO film, different interlayer processing conditions were tested. It was observed that at low drying temperatures, a nano-fiber like dual-pore structure was formed. One to four micrometer thick films were obtained. When a sintering step at 450°C was introduced, a compact stacking of NiO nanoparticles was obtained. The thickness of the four-layer films prepared was 850 nm (± 20 nm). The implementation of these films into p-type DSSC device is described in the next chapter.

Interestingly, XPS investigations were also performed in link with TGA analysis, so as to better understand the mechanism of NiO formation with the sol-gel polymer templated method. It is confirmed that NiO requires high temperature for its formation (superior to 340°C). Interestingly, it is proposed that an intermediate $Ni(OH)_2$ species is formed between 200°C and 340°C in the course of the $NiCl_2$ salt transformation into NiO.

References

1. Gibson, E. A. *et al.* Dye sensitised solar cells with nickel oxide photocathodes prepared via scalable microwave sintering. *Phys. Chem. Chem. Phys.* **15,** 2411–2420 (2013).
2. Dini, D., Halpin, Y., Vos, J. G. & Gibson, E. A. The influence of the preparation method of NiOx photocathodes on the efficiency of p-type dye-sensitized solar cells. *Coord. Chem. Rev.* **304–305,** 179–201 (2015).
3. Nattestad, A., Ferguson, M., Kerr, R., Cheng, Y.-B. & Bach, U. Dye-sensitized nickel(II)oxide photocathodes for tandem solar cell applications. *Nanotechnology* **19,** 295304 (2008).
4. Ito, S. *et al.* Fabrication of thin film dye sensitized solar cells with solar to electric power conversion efficiency over 10%. *Thin Solid Films* **516,** 4613–4619 (2008).
5. Nattestad, A. *et al.* Highly efficient photocathodes for dye-sensitized tandem solar cells. *Nat. Mater.* **9,** 31–35 (2010).
6. Perera, I. R. *et al.* Application of the Tris(acetylacetonato)iron(III)/(II) Redox Couple in p-Type Dye-Sensitized Solar Cells. *Angew. Chem. Int. Ed*, **54**, 3758-3762 (2015).
7. Zhang, X. L. *et al.* Sensitization of nickel oxide: improved carrier lifetime and charge collection by tuning nanoscale crystallinity. *Chem. Commun.* **48,** 9885–9887 (2012).
8. Nattestad, A. Development of photocathodes for incorporation into tandem dye sensitised solar cells. (Monash University. Faculty of Engineering. Dept. of Materials Engineering, 2010). at <http://arrow.monash.edu.au/vital/access/manager/Repository/monash:63141>
9. Nattestad, A., Ferguson, M., Kerr, R., Cheng, Y.-B. & Bach, U. Dye-sensitized nickel(II)oxide photocathodes for tandem solar cell applications. *Nanotechnology* **19,** 295304 (2008).
10. Flynn, C. J. *et al.* Hierarchically-Structured NiO Nanoplatelets as Mesoscale p-Type Photocathodes for Dye-Sensitized Solar Cells. *J. Phys. Chem. C* **118,** 14177–14184 (2014).
11. Zhang, X. L. *et al.* Charge transport in photocathodes based on the sensitization of NiO nanorods. *J. Mater. Chem.* **22,** 7005–7009 (2012).
12. Powar, S. *et al.* Improved photocurrents for p-type dye-sensitized solar cells using nano-structured nickel(II) oxide microballs. *Energy Environ. Sci.* **5,** 8896–8900 (2012).
13. He, J., Lindström, H., Hagfeldt, A. & Lindquist, S.-E. Dye-Sensitized Nanostructured p-Type Nickel Oxide Film as a Photocathode for a Solar Cell. *J. Phys. Chem. B* **103,** 8940–8943 (1999).

14. He, J., Lindström, H., Hagfeldt, A. & Lindquist, S.-E. Dye-sensitized nanostructured tandem cell-first demonstrated cell with a dye-sensitized photocathode. *Sol. Energy Mater. Sol. Cells* **62,** 265–273 (2000).
15. Liu, K.-C. & Anderson, M. A. Porous Nickel Oxide/Nickel Films for Electrochemical Capacitors. *J. Electrochem. Soc.* **143,** 124–130 (1996).
16. Boschloo, G. & Hagfeldt, A. Spectroelectrochemistry of Nanostructured NiO. *J. Phys. Chem. B* **105,** 3039–3044 (2001).
17. Zhu, H., Hagfeldt, A. & Boschloo, G. Photoelectrochemistry of Mesoporous NiO Electrodes in Iodide/Triiodide Electrolytes. *J. Phys. Chem. C* **111,** 17455–17458 (2007).
18. Qin, P. *et al.* High Incident Photon-to-Current Conversion Efficiency of p-Type Dye-Sensitized Solar Cells Based on NiO and Organic Chromophores. *Adv. Mater.* **21,** 2993–2996 (2009).
19. Qin, P. *et al.* Design of an Organic Chromophore for P-Type Dye-Sensitized Solar Cells. *J. Am. Chem. Soc.* **130,** 8570–8571 (2008).
20. Soler-Illia, G. J. de A. A., Crepaldi, E. L., Grosso, D. & Sanchez, C. Block copolymer-templated mesoporous oxides. *Curr. Opin. Colloid Interface Sci.* **8,** 109–126 (2003).
21. Nakasa, A. *et al.* A High Voltage Dye-sensitized Solar Cell using a Nanoporous NiO Photocathode. *Chem. Lett.* **34,** 500–501 (2005).
22. Zukalová, M. *et al.* Organized Mesoporous TiO2 Films Exhibiting Greatly Enhanced Performance in Dye-Sensitized Solar Cells. *Nano Lett.* **5,** 1789–1792 (2005).
23. Sumikura, S., Mori, S., Shimizu, S., Usami, H. & Suzuki, E. Syntheses of NiO nanoporous films using nonionic triblock co-polymer templates and their application to photo-cathodes of p-type dye-sensitized solar cells. *J. Photochem. Photobiol. Chem.* **199,** 1–7 (2008).
24. Li, L. *et al.* Double-Layered NiO Photocathodes for p-Type DSSCs with Record IPCE. *Adv. Mater.* **22,** 1759–1762 (2010).
25. Gibson, E. A. *et al.* A p-Type NiO-Based Dye-Sensitized Solar Cell with an Open-Circuit Voltage of 0.35 V. *Angew. Chem. Int. Ed.* **48,** 4402–4405 (2009).
26. He, M., Ji, Z., Huang, Z. & Wu, Y. Molecular Orbital Engineering of a Panchromatic Cyclometalated Ru(II) Dye for p-Type Dye-Sensitized Solar Cells. *J. Phys. Chem. C* **118,** 16518–16525 (2014).
27. Click, K. A. *et al.* A double-acceptor as a superior organic dye design for p-type DSSCs: high photocurrents and the observed light soaking effect. *Phys. Chem. Chem. Phys.* **16,** 26103–26111 (2014).

28. Zhang, Q.-Q. *et al.* A push–pull thienoquinoidal chromophore for highly efficient p-type dye-sensitized solar cells. *J. Mater. Chem. A* **3,** 7695–7698 (2015).
29. Wood, C. J., Summers, G. H. & Gibson, E. A. Increased photocurrent in a tandem dye-sensitized solar cell by modifications in push–pull dye-design. *Chem. Commun.* **51,** 3915–3918 (2015).
30. Wood, C. J. *et al.* Red-Absorbing Cationic Acceptor Dyes for Photocathodes in Tandem Solar Cells. *J. Phys. Chem. C* **118,** 16536–16546 (2014).
31. Liu, Z. *et al.* Fine Tuning of Fluorene-Based Dye Structures for High-Efficiency p-Type Dye-Sensitized Solar Cells. *ACS Appl. Mater. Interfaces* **6,** 10614–10622 (2014).
32. Yang, H. B. *et al.* One-Step Fabrication of Unique Mesoporous NiO Hollow Sphere Film on FTO for High-Performance P-Type Dye-Sensitized Solar Cells. *Adv. Mater. Interfaces* **1,** n/a–n/a (2014).
33. Kabanov, A. V., Batrakova, E. V. & Alakhov, V. Y. Pluronic® block copolymers as novel polymer therapeutics for drug and gene delivery. *J. Controlled Release* **82,** 189–212 (2002).
34. Soler-Illia, G. J. de A. A., Crepaldi, E. L., Grosso, D. & Sanchez, C. Block copolymer-templated mesoporous oxides. *Curr. Opin. Colloid Interface Sci.* **8,** 109–126 (2003).
35. Ivanova, R., Alexandridis, P. & Lindman, B. Interaction of poloxamer block copolymers with cosolvents and surfactants. *Colloids Surf. Physicochem. Eng. Asp.* **183–185,** 41–53 (2001).
36. Lepleux, L. *et al.* Simple and Reproducible Procedure to Prepare Self-Nanostructured NiO Films for the Fabrication of P-Type Dye-Sensitized Solar Cells. *Inorg. Chem.* **48,** 8245–8250 (2009).
37. Natu, G. *et al.* Valence Band-Edge Engineering of Nickel Oxide Nanoparticles via Cobalt Doping for Application in p-Type Dye-Sensitized Solar Cells. *ACS Appl. Mater. Interfaces* **4,** 5922–5929 (2012).
38. Singh, M., Haverinen, H. M., Dhagat, P. & Jabbour, G. E. Inkjet Printing—Process and Its Applications. *Adv. Mater.* **22,** 673–685 (2010).
39. Kamyshny, A., Steinke, J. & Magdassi, S. Metal-based inkjet inks for printed electronics. *Open Appl. Phys. J.* **4,** 19–36 (2011).
40. Deegan, R. D. Pattern formation in drying drops. *Phys. Rev. E* **61,** 475–485 (2000).
41. Wijshoff, H. The dynamics of the piezo inkjet printhead operation. *Phys. Rep.* **491,** 77–177 (2010).
42. Mougenot, M. Réalisation par un procédé d'impression jet d'encre de réseaux de microplots de silice mesoporeuse fonctionnalisée.Thèse de doctorat : matériaux céramiques et traitements de surface. Université de Limoges. Disponible sur http://epublications.unilim.fr/theses/2007/mougenot-marion/mougenot-marion.pdf>. (2007).

43. Liu, X., Tarn, T.-J., Huang, F. & Fan, J. Recent advances in inkjet printing synthesis of functional metal oxides. *Particuology* **19,** 1–13 (2015).
44. Atkinson, A., Doorbar, J., Hudd, A., Segal, D. L. & White, P. J. Continuous ink-jet printing using sol-gel 'Ceramic' inks. *J. Sol-Gel Sci. Technol.* **8,** 1093–1097 (1997).
45. Biehl, S., Danzebrink, R., Oliveira, P. & Aegerter, M. A. Refractive Microlens Fabrication by Ink-Jet Process. *J. Sol-Gel Sci. Technol.* **13,** 177–182 (1998).
46. Danzebrink, R. & Aegerter, M. A. Deposition of micropatterned coating using an ink-jet technique. *Thin Solid Films* **351,** 115–118 (1999).
47. Fan, H. *et al.* Rapid prototyping of patterned functional nanostructures. *Nature* **405,** 56–60 (2000).
48. Fan, H. *et al.* Hierarchically structured functional porous silica and composite produced by evaporation-induced self-assembly. *Microporous Mesoporous Mater.* **44–45,** 625–637 (2001).
49. Mougenot, M. *et al.* Ink Jet Printing of Microdot Arrays of Mesostructured Silica. *J. Am. Ceram. Soc.* **89,** 1876–1882 (2006).
50. Fousseret, B. *et al.* Inkjet-Printing-Engineered Functional Microdot Arrays Made of Mesoporous Hybrid Organosilicas. *Chem. Mater.* **22,** 3875–3883 (2010).
51. De Los Cobos, O. *et al.* Tunable Multifunctional Mesoporous Silica Microdots Arrays by Combination of Inkjet Printing, EISA, and Click Chemistry. *Chem. Mater.* **24,** 4337–4342 (2012).
52. Černá, M., Veselý, M. & Dzik, P. Physical and chemical properties of titanium dioxide printed layers. *Catal. Today* **161,** 97–104 (2011).
53. Arin, M. *et al.* Inkjet printing of photocatalytically active TiO2 thin films from water based precursor solutions. *J. Eur. Ceram. Soc.* **31,** 1067–1074 (2011).
54. Chouiki, M. & Schoeftner, R. Inkjet printing of inorganic sol–gel ink and control of the geometrical characteristics. *J. Sol-Gel Sci. Technol.* **58,** 91–95 (2010).
55. Xu, Q., Smått, J.-H., Peltonen, J. & Ihalainen, P. Fabrication of nanoperforated ultrathin TiO2 films by inkjet printing. *J. Mater. Res.*, 1–10 (2015).
56. Morozova, M. *et al.* Thin TiO2 films prepared by inkjet printing of the reverse micelles sol–gel composition. *Sens. Actuators B Chem.* **160,** 371–378 (2011).
57. Yoshimura, M. & Gallage, R. Direct patterning of nanostructured ceramics from solution—differences from conventional printing and lithographic methods. *J. Solid State Electrochem.* **12,** 775–782 (2008).

58. Vidmar, T., Topič, M., Dzik, P. & Opara Krašovec, U. Inkjet printing of sol–gel derived tungsten oxide inks. *Sol. Energy Mater. Sol. Cells* **125,** 87–95 (2014).

59. Mouganie, T. & Glowacki, B. A. Chemical synthesis and microstructural analysis of superconducting YBa2Cu3O7-δ ink deposited by drop-on-demand ink-jet printing on silver substrates. *J. Mater. Sci.* **41,** 8257–8264 (2006).

60. Feys, J. *et al.* Ink-jet printing of YBa2Cu3O7 superconducting coatings and patterns from aqueous solutions. *J. Mater. Chem.* **22,** 3717–3726 (2012).

61. Obradors, X. *et al.* Chemical solution deposition: a path towards low cost coated conductors. *Supercond. Sci. Technol.* **17,** 1055 (2004).

62. Driessche, I. V. *et al.* Chemical solution deposition using ink-jet printing for YBCO coated conductors. *Supercond. Sci. Technol.* **25,** 065017 (2012).

63. Lee, D.-H., Chang, Y.-J., Herman, G. S. & Chang, C.-H. A General Route to Printable High-Mobility Transparent Amorphous Oxide Semiconductors. *Adv. Mater.* **19,** 843–847 (2007).

64. Sakai, Y., Futakuchi, T. & Adachi, M. Preparation of Inkjet-Printed NiO Films for Ba (Ti, Zr) O3-Based Ceramics and Application to Multilayer Ceramics with Ni Electrodes. *Jpn. J. Appl. Phys.* **47,** 7630 (2008).

65. Woodhouse, M., Herman, G. S. & Parkinson, B. A. Combinatorial Approach to Identification of Catalysts for the Photoelectrolysis of Water. *Chem. Mater.* **17,** 4318–4324 (2005).

66. Woodhouse, M. & Parkinson, B. A. Combinatorial Discovery and Optimization of a Complex Oxide with Water Photoelectrolysis Activity. *Chem. Mater.* **20,** 2495–2502 (2008).

67. Jiang, C., Wang, R. & Parkinson, B. A. Combinatorial Approach to Improve Photoelectrodes Based on BiVO4. *ACS Comb. Sci.* **15,** 639–645 (2013).

68. He, J. & Parkinson, B. A. Combinatorial Investigation of the Effects of the Incorporation of Ti, Si, and Al on the Performance of α-Fe2O3 Photoanodes. *ACS Comb. Sci.* **13,** 399–404 (2011).

69. Seley, D., Ayers, K. & Parkinson, B. A. Combinatorial Search for Improved Metal Oxide Oxygen Evolution Electrocatalysts in Acidic Electrolytes. *ACS Comb. Sci.* **15,** 82–89 (2013).

70. Katz, J. E., Gingrich, T. R., Santori, E. A. & Lewis, N. S. Combinatorial synthesis and high-throughput photopotential and photocurrent screening of mixed-metal oxides for photoelectrochemical water splitting. *Energy Environ. Sci.* **2,** 103–112 (2008).

71. Liu, X. *et al.* Inkjet Printing Assisted Synthesis of Multicomponent Mesoporous Metal Oxides for Ultrafast Catalyst Exploration. *Nano Lett.* **12,** 5733–5739 (2012).
72. Liu, K.-C. & Anderson, M. A. Porous Nickel Oxide/Nickel Films for Electrochemical Capacitors. *J. Electrochem. Soc.* **143,** 124–130 (1996).
73. Boschloo, G. & Hagfeldt, A. Spectroelectrochemistry of Nanostructured NiO. *J. Phys. Chem. B* **105,** 3039–3044 (2001).
74. Choi, H. W., Zhou, T., Singh, M. & Jabbour, G. E. Recent developments and directions in printed nanomaterials. *Nanoscale* **7,** 3338–3355 (2015).
75. Derby, B. Inkjet printing ceramics: From drops to solid. *J. Eur. Ceram. Soc.* **31,** 2543–2550 (2011).
76. Biesinger, M. C., Lau, L. W. M., Gerson, A. R. & Smart, R. S. C. The role of the Auger parameter in XPS studies of nickel metal, halides and oxides. *Phys. Chem. Chem. Phys.* **14,** 2434–2442 (2012).
77. Uhlenbrock, S., Scharfschwerdt, C., Neumann, M., Illing, G. & Freund, H.-J. The influence of defects on the Ni 2p and O 1s XPS of NiO. *J. Phys. Condens. Matter* **4,** 7973 (1992).
78. Marrani, A. G., Novelli, V., Sheehan, S., Dowling, D. P. & Dini, D. Probing the Redox States at the Surface of Electroactive Nanoporous NiO Thin Films. *ACS Appl. Mater. Interfaces* **6,** 143–152 (2014).
79. Legrand, D. L., Nesbitt, H. W. & Bancroft, G. M. X-ray photoelectron spectroscopic study of a pristine millerite (NiS) surface and the effect of air and water oxidation. *Am. Mineral.* **83,** 1256–1265 (1998).

IV. Building efficient DSSCs with the new dyes and IJP NiO

IV.A. Introduction

In order to establish the viability of IJP for NiO-based p-type DSSCs, the films described above were implemented into p-type DSSCs (**NiO-1L**, **NiO-4L** and **NiO-F-1L** to **4L**). The dye that was used for these tests was dye **(8)** (cf. Fig. 85). The results for the implementation of the other bithiophen dyes, described in chapter 2 (dye **(11)**, dye **(14)** and dye **(17)**) are also presented at the end of this chapter.

IV.B. p-Type DSSCs with NiO-1L films, sensitized with dye (8)

IV.B.1. Sensitizing the NiO-1L electrodes with dye (8)

For DSSCs, sensitization of the oxide is generally performed by immersion of the photoelectrode into a dye solution. For NiO electrodes, it is important to notice that sensitization should be done just after an annealing step at 450°C, which "activates" NiO and removes organic contaminants and water. As pointed out in the work by Cheng et al., NiO contamination by dust or water is very rapid [1]. Also, it is important to stress that in the work presented here, the photocathodes were thermalized at 60°C prior to their introduction in the dye solution, and immersed "still hot". The sensitization conditions vary from one publication to another, but concentration values in the 10^{-4} M range are generally used for the dye, and the duration of this step varies from one hour to one night. The solvent used for sensitization depends on the dye and there are actually some studies describing the effect of the dye solvent over the solar cell performances [2]. Eventually, in order to remove the unattached dyes, a rinsing step is always performed when sensitization is completed.

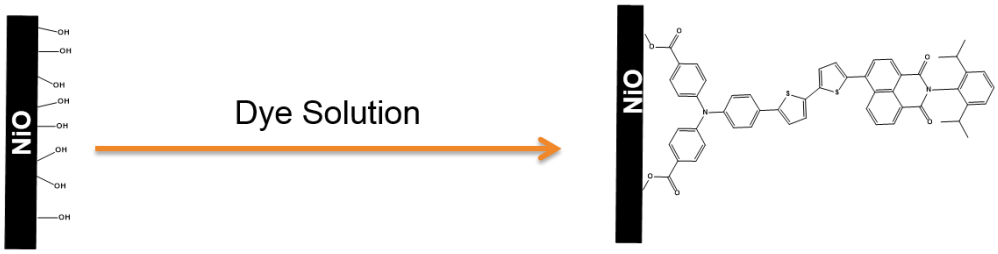


Fig. 85-Simplified view of dye grafting at the surface of NiO, an ester link between NiO and dye (8) is drawn here

IV.B.1.a. Solvent choice

Dye **(8)** shows good solubility in ethanol, then, as a first attempt, a 5.10^{-4} M solution of **(8)** in ethanol was prepared, and used for sensitization. Sensitization of a one-layer NiO electrode was

performed during 16 hours. The NiO sensitization was surprisingly very weak, and no specific coloration of the film was visible (see Fig. 86).

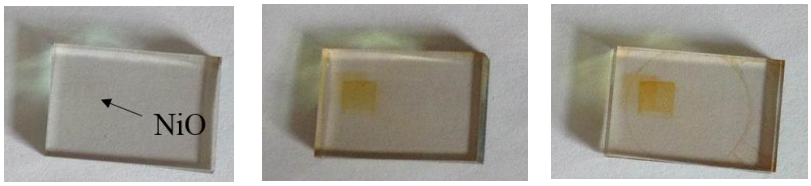


Fig. 86- Picture of NiO-1L electrodes, dyed with different baths of dye (8), overnight. From left to right, dyed with a freshly prepared ethanol solution, the NiO film was barely distinguishable; dyed with the same solution but after this solution re-precipitated (it took two days); dyed with a freshly prepared methanol solution.

However, the ethanol solution was kept at room temperature in a closed vessel. And after two days, an orange precipitate was noticed. It was tentatively assessed to perform the sensitization of a NiO electrode with this solution. After the electrode was generously rinsed with ethanol, the NiO coloration was actually observed (see Fig. 86, middle), attesting for an effective dying of NiO. We propose that the dye exist in the form of a soluble aggregate in the freshly prepared EtOH solution, corresponding to a super-saturation phenomenon. The presence of the aggregate could explain the absence of dye grafting on the NiO electrode. When the super-saturation is broken, a precipitate is formed, the effective concentration of the dye in solution is reduced and the dye exists in a form which could be monomers, easier to graft on NiO.

For practical reasons, operating the sensitization step with a solution that requires two days of reprecipitation is not straightforward. For this reason, it was intended to find a solvent in which dye **(8)** instantaneously formed a precipitate. Methanol, was logically found to be suitable for this purpose and was then employed as the solvent used for sensitization. For the preparation of the saturated solution, the same amount of product per liter of solvent as with the ethanol solution described above was used (5.10^{-4} mol of product per liter of methanol). This strategy revealed to be successful and an effective dying was observed (see Fig. 86, right).

IV.B.1.b. Dying bath duration

Finally, we tried to decrease the duration of the dye sensitization step. It was found that only one hour in methanol was sufficient, rather than one night, for effective sensitization of the NiO electrode (see Fig. 87). The as-sensitized NiO electrode was called **NiO-1L-(8)**.



Fig. 87- NiO-1L-(8) photoelectrode. Sensitization was performed during one hour, in a saturated methanol solution of dye (8).

IV.B.1.c. Solid state UV/Vis spectra of the sensitized NiO film

The solid state UV/Visible spectrum of the **NiO-1L** electrode was performed before and after sensitization of NiO with a saturated methanol solution of dye **(8)**, during one hour. The spectra of the NiO electrode before (A_{NiO}) and after sensitization ($A_{dye,NiO}$) are shown in Fig. 88. From these spectra, effective sensitization of NiO by dye **(8)** was confirmed.

After subtraction of the NiO signal, the spectrum $A_{dye}(\lambda)$ (see Fig. 88, inset) was obtained through the following equation: $\mathbf{A_{dye} = A_{dye,NiO} - A_{NiO}}$.

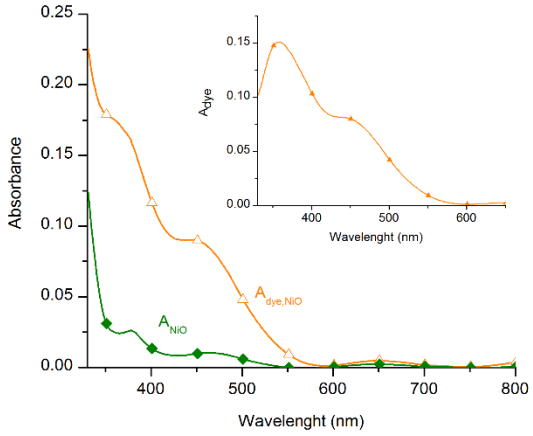


Fig. 88- Absorbance of bare NiO-1L film, A_{NiO} (green trace, filled diamonds). Absorbance of the same electrode after sensitization with dye (8) (NiO-1L-(8) electrode), $A_{dye,NiO}$ (orange trace, empty triangles). Inset: Dye Absorbance, A_{dye}. The FTO absorbance signal was subtracted in all cases.

The dye / NiO absorbance ratio was also evaluated at the peak absorption wavelength (440 nm), (ratio = A_{dye} / A_{NiO}). A high value of 9 was found. This value is three times higher than for the NiO microballs reported by Udo Bach et al, for which the dye/NiO absorbance was already maximized compared to NiO nanoparticles (see chapter 1) [3]. That high value should however be taken with caution, considering the uncertainty of measurement for A_{NiO}. This experimental error

could be important, because A_{NiO} is very low ($A_{NiO,440nm}$ = 0.009). The study of thicker NiO films, described later will allow to draw better comparisons about the dye / NiO absorbance ratio.

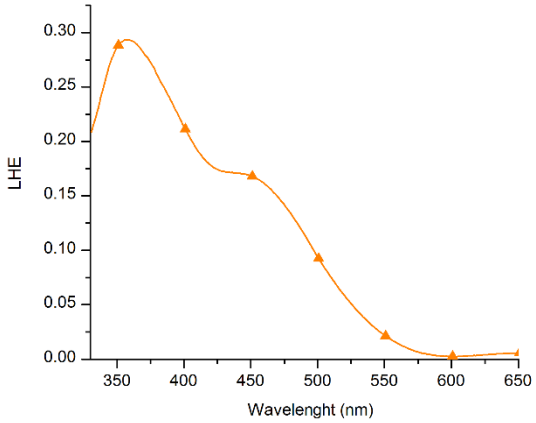


Fig. 89- LHE of dye (8) on a NiO-1L-(8) film. The formula used was LHE = 1 – 10^{-Adye}.

From $A_{dye}(\lambda)$ spectrum, the LHE (Light Harversting Efficiency) of the film was also calculated and displayed on Fig. 89. LHE represents the percentage of photons that are absorbed by the dye layer accross the NiO electrode. The formula that was used [4]: LHE = 1–10^{-Adye}, does not take into account NiO self-absorption and was used here for sake of simplicity. At the peak absorption wavelenght of the charge transfer band (440 nm), LHE is 17%. This low value is due to to the very low thickness of the film and is not easily comparable with literature values, since such thin NiO films were never used for p-type DSSCs. Wu and coworker reported a LHE in the range of 84% for 600 nm NiO films, with a dye (dye "O_2") that absorbs in the same range as dye **(8)**, with a similar molar extinction coefficient [5]. It is noteworthy that the NiO absorbance was taken into account in the calculation in that work. As it seems that the NiO used by Wu et al. absorbed more light than the one used in the present work, their reported LHE value can be considered as artificially increased by the NiO contribution.

Interestingly, after normalization, the A_{dye} spectrum was also compared with the one of dye **(7)** [w] in dichloromethane (see Fig. 90): There are only small differences between the solution and the solid state spectra. First of all, this suggests there is few electronic interactions between grafted

[w] Dye **(7)** is the *tert*-butyl ester protected version of dye **(8)**.

dye **(8)** and NiO. Secondly, dye **(8)** aggregation is limited [x]. It is proposed that the *tert*-butyl group that are present on the NI part of the molecule, as well as the large torsion angle between the bithiophen bridge and the NI part, help preventing for dye aggregation during sensitization.

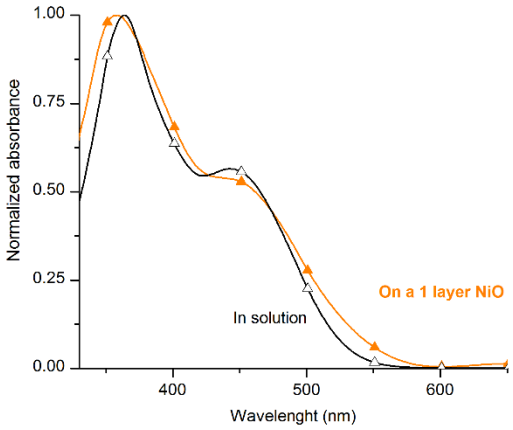


Fig. 90- Normalized solid state spectrum of dye (8) (A_{dye}) on NiO-1L (orange trace, filled triangles). Normalized absorbance of dye (7) in solution (black trace empty triangles).

IV.B.2. p-Type DSSCs tests methodology

IV.B.2.a. Fabrication of the DSSC

The fabricated photocathodes were coupled to an activated pre-drilled hole Pt electrode (Solaronix), with Surlyn spacer (60µm) between each electrode. Care was taken to avoid overheating of the sensitized electrode during this step. A classical iodine electrolyte [6] was prepared in the glovebox, which composition was the following: $[I_2]$ = 0.1M, [LiI] = 1M, in acetonitrile. The electrolyte was introduced in the solar cell with an adapted syringe (Solaronix), in a glovebox. The work was operated in a protected atmosphere in order to guarantee reproducibility of the water content in the DSSCs. Water content is sometimes thought to have an influence over the cell efficiency [7]. Finally, contacts were made via ultrasonic soldering (see Fig. 91) with incrusted wires. An example of a final p-type DSSC is shown on Fig. 92. It is also important to underline the dimensions of the NiO film, which are 0.5cm*0.5cm for all the p-type DSSC fabricated for this thesis.

[x] To confirm this hypothesis, the spectrum of the dye in solution at different concentration should be performed at different concentration. This would permit to detect aggregate formation. It is however worth mentioning that the solution spectrum displayed on Fig. 90 was performed on the *tert*-butyl protected version of the dye, which are not prone to form aggregates in DCM, where they are very soluble.

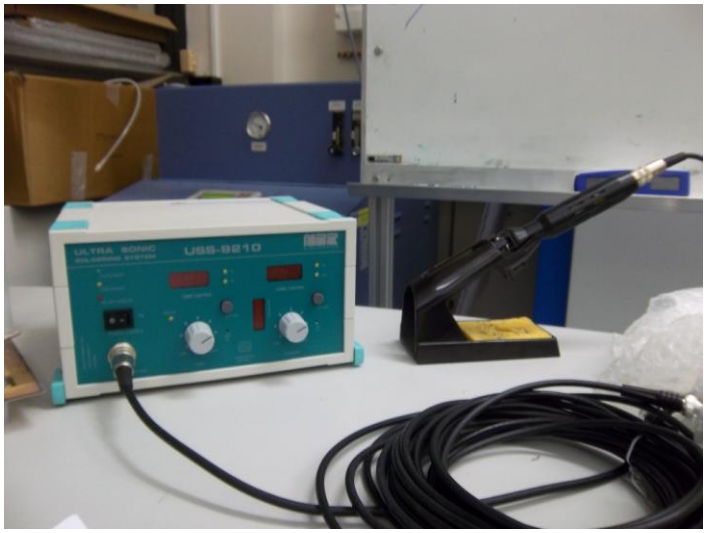


Fig. 91- The soldering system which was used for contacts formation

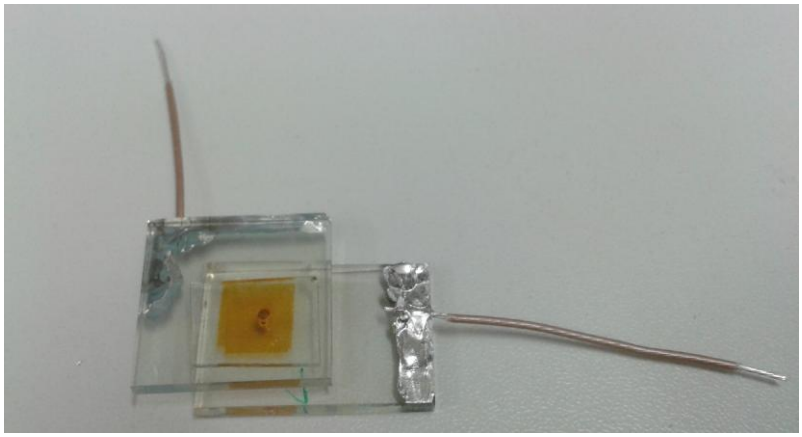


Fig. 92-An example of a fabricated p-type DSSC.

IV.B.2.b. Parameters for the solar cell tests

The solar cell tests were performed under 1 Sun, with the AM 1.5 standard. The J-V characteristics was acquired from negative value to positive values, with a 2 mV step and the settling time was 250 ms. The long settling time was used so as to take into account the capacitive nature of NiO according to the Udo Bach's work [8]. The characteristics under illumination were always performed prior to the one in the dark. Also, in order to minimize the light soaking effect (see annex 5), the tests under irradiation were always started just after the cell was placed in the irradiation zone and rapidly removed from this zone when the test was finished.

IV.B.3. **Results**

The J-V curves obtained for the **NiO-1L-(8)** film, under illumination and in the dark are shown in Fig. 93. The performance, averaged on three different devices, are summarized in Tab. 16.

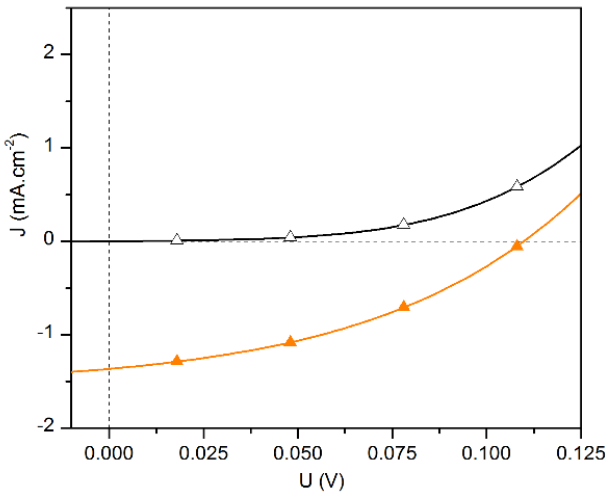


Fig. 93- J-V characteristic of a NiO-1L-(8) p-type DSSC, measured in the dark (black trace, empty triangle) and under 1 Sun (AM 1.5 standard) (orange trace, filled triangles).

The J-V trace under-illumination displays the typical features of a p-type DSSC characteristic. The overall PCE yield is 0.0571% which is considered to be a good performance considering the small thickness of the NiO film (320 nm ± 10 nm), and its limited LHE (see Fig. 89). The short-circuit current (1.36 ± 0.02 mA.cm^{-2}) largely oversteps the symbolic value of 1mA.cm^{-2}, and the V_{OC} (108 ± 1 mV) is in the average range for the reported V_{OC} in the literature with iodine electrolyte, as well as the fill factor (38.7 ± 0.3%). The performances are actually similar to the one obtained by Wu and coworker, with dye O_2[5], but they employed a twice thicker NiO film (PCE_{O2} = 0.050 % / $J_{SC,O2}$ = 1.43 mA.cm^{-2} / $V_{OC,O2}$ = 94 mV / FF_{O2} = 37%).

Tab. 16- Photovoltaic performance of the NiO-1L-(8), under 1 Sun (AM 1.5 standard). The results were averaged on three different devices.

PCE (%)	0.057 (± 0.001)
J_{SC} (mA.cm^{-2})	1.36 (± 0.02)
V_{OC} (mV)	108 (± 1)
FF (%)	38.7 (± 0.3)

The relative good performance of that device can be attributed to multiple parameters. First of all, the small thickness of the NiO film may result in reduced electrolyte / hole recombination and

then efficient charge collection. The dark-current value is also limited (0.44 $^{\pm}$ 0.04 mA.cm^{-2} at 100 mV), however, this value is not easily comparable with literature, due to the small thickness of NiO. Another point is the apparently high dye / NiO absorbance ratio, which is partly due to the good transparency of the NiO film. The fact that the LUMO of the dye is far from the surface and shielded by bulky *tert*-butyl groups may help preventing geminate charge recombination. Finally, the apparent absence of dye aggregation at the NiO surface may prevent dye-to-dye de-excitation and be beneficial for photocurrent generation.

Another interesting point is the reproducibility of the method as the errors are very small. The reproducibility of the method is even more striking when superimposing the different experimental curves (see Fig. 94).

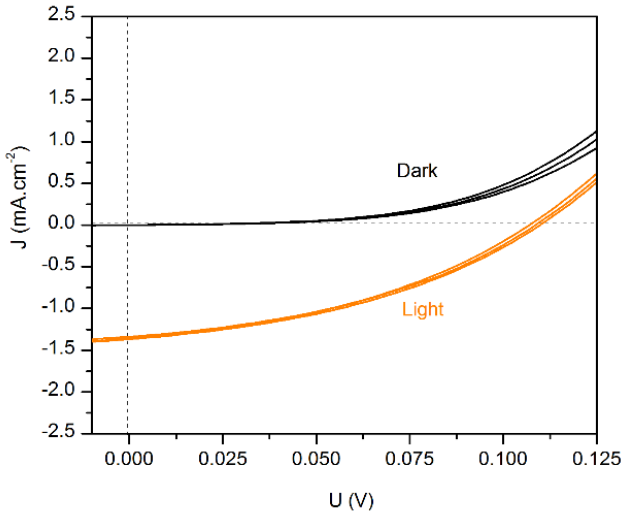


Fig. 94- Superimposition of the three J-V characteristics obtained for a NiO-1L-(8) p-type DSSC, measured in the dark (black trace) and under 1 Sun (AM 1.5 standard) (orange trace).

IV.B.4. Conclusion

The good performance of the one **NiO-1L** electrodes, sensitized with the push-pull dye **(8)**, allows to validate the concept of "ink-jet printing a templated sol-gel" ink for NiO material synthesis for p-type DSSCs. The obtained performance seems to be promising regarding the low thickness of the NiO film (320 nm ± 10 nm). However, that same low thickness limits the performance of the solar cell. The next paragraphs are dedicated to the performance study of p-type DSSC fabricated with thicker ink-jet printed NiO films (see chapter 3 for their fabrication).

IV.C. p-Type DSSCs performances with thicker NiO films

In this paragraph, the two different NiO morphologies that were obtained by changing the interlayer drying conditions: NiO nanofiber morphology (**NiO-F**), and NiO compact nanoparticles arrangement morphology, are tested in p-type DSSC configuration and compared.

IV.C.1. Solar cell fabrication and test parameters

The fabrication conditions of the p-type DSSCs are identical to the ones used for the **NiO-1L-(8)** electrodes: one-hour immersion into a saturated methanol solution of dye **(8)**, iodine electrolyte which composition is the following: $[I_2]$ = 0.1M, [LiI] = 1M, in acetonitrile, prepared and introduced into the DSSCs in a glovebox (see IV.B.2.a). The solar cell tests conditions are also identical (see IV.B.2.b).

IV.C.2. Dual pore, nanofiber like morphology

The electrodes for which the interlayer drying temperature was 30°C (two layers: **NiO-F-2L**, three layers: **NiO-F-3L** and four layers: **NiO-F-4L**) were successfully sensitized with dye **(8)**[y]. The picture of the sensitized electrodes can be seen in Fig. 95. From this picture, one can see a gradual increasing coloration of the NiO film, suggesting an increased amount of dye grafted, in agreement with the increasing NiO thickness.

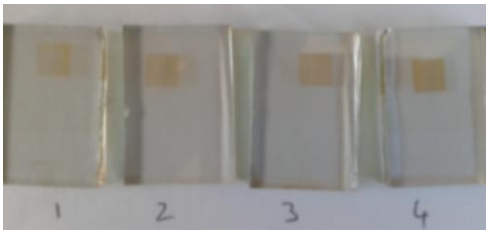


Fig. 95- From left to right: NiO-1L-(8), NiO-F-2L-(8), NiO-F-3L-(8) and NiO-F-4L-(8)

The performance of the p-type DSSCs fabricated with one to four layers of NiO, with the nano-fiber like morphology (interlayer drying at 30°C) have been summarized in Tab. 17 and the photovoltaic characteristics obtained are displayed in Fig. 96.

[y] The as sensitized photocathode are logically called: **NiO-F-2L-(8)**, **NiO-F-3L-(8) and NiO-F-4L-(8)**.

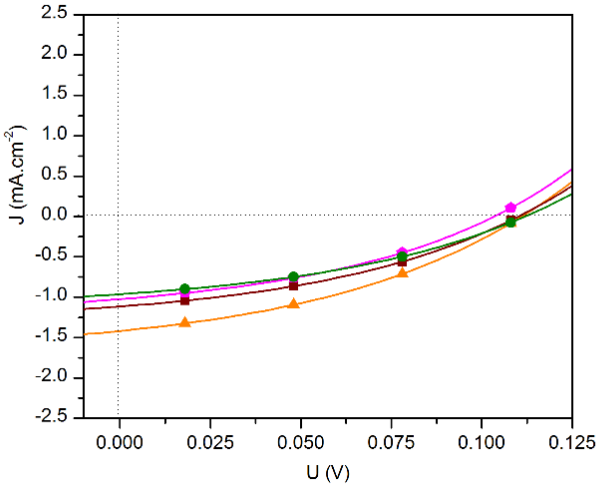


Fig. 96- Photovoltaic characteristics of NiO-1L-(8) (orange trace, filled triangles), NiO-F-2L-(8) (red trace, filled squares), NiO-F-3L-(8) (magenta trace, filled diamonds) and NiO-F-4L-(8) (green trace, filled circles). Measurements were performed under 1 Sun, with the AM 1.5 standard.

Tab. 17- Photovoltaic performance of the NiO-1L-(8), NiO-F-2L to 4L-(8). Electrolyte was an iodine solution in ACN ($[I_2]$ = 0.1M, [LiI] = 1M)

Sample Reference	Thickness	J_{sc} (mA.cm^{-2})	V_{OC} (mV)	FF (%)	PCE (%)
NiO-1L-(8)	320 nm)	1.36	108	38.7	0.0571
NiO-F-2L-(8)	~1 µm)	1.12	111	37	0.046
NiO-F-3L-(8)	~2 µm)	1.03	103	37	0.040
NiO-F-4L-(8)	(~3 µm)	0.97	111	38	0.040

One can observe that the PCE of the solar cell decreases when increasing the thickness of the NiO film. The V_{OC} remains in the same range, as well as the FF, when increasing the thickness of the film. The short-circuit current reaches a plateau value around 1 mA.cm^{-2} with thicker electrodes. The lower PCE of the thicker NiO electrode is then due to an important J_{SC} drop when using thicker photocathodes.

We can conclude that the dual-pore, nanofiber like morphology, induced by the 30° interlayer drying conditions, is not suitable for building efficient thick NiO electrodes. This could be attributed to the double effect of increased porosity of the overall film (less NiO material in a given volume, then less dye grafted in this given volume) and the possibility of increased injected-hole / electrolyte recombination, due to the low hole mobility in NiO, which has effects when the thickness of the film is increased.

IV.C.3. **Compact nanoparticle morphology:**

IV.C.3.a. Optical properties

NiO-4L films, with the dense nanoparticle morphology, described previously (see chapter 3) were also successfully sensitized (see Fig. 97) in one hour in methanol solution. One can notice the striking difference in terms of color, at similar levels of thickness for the mesoporous NiO film, between the dense morphology (**NiO-4L-(8)**) and the nanofiber like morphology (see **NIO-F-2L-(8)** on Fig. 95), confirming that the dense structure allows to graft more dye molecule in a given volume of film. The solid state UV / Vis spectra of the **NiO-4L** electrode was performed before and after sensitization (see Fig. 98). It confirmed the sensitization of the film by dye **(8)**.

After subtraction of the bare NiO signal, the spectrum ($A_{dye}(\lambda)$) was obtained (see Fig. 98, inset). At 440 nm, A_{dye} value was 0.206, this is actually 2.6 times more than for the 320 (± 10 nm) film (in this case, A_{dye} was 0.008). This results fits perfectly the 2.7 times increase of the NiO thickness (from 320 to 850 nm) and clearly suggests that sensitization occurred through all the NiO film.

The dye / NiO absorbance ratio was also calculated at 440 nm and the value obtained was 1.4. This value is lower than the one obtained by Udo Bach's group [3] with NiO films fabricated from a NiO nanoparticle paste (the ratio was also around 2.5). However, if one considers that our dye, dye **(8)**, absorbs twice as less light as PMI-6T-TPA, which was used in Udo Bach's work [z], the result from the analysis of the dyed and un-dyed **NiO-4L** spectrum suggests that in the experimental conditions of this thesis, our NiO electrode displays optical properties in the range of Udo Bach'group electrodes. In addition our NiO electrodes are more transaparent than Udo Bach's ones. Indeed, in our case, we have: $A_{NiO,\ \lambda=450\ nm,850\mu m} = 0{,}13$, which for a 1µm film would give $A_{NiO,\ \lambda=450\ nm,\ 1\mu m} = 0.15$, that is 29% of absorbed photons for a bare NiO film. This value is largely lower than the NiO paste based electrodes (see chapter 3, Tab. 11). This could be an advantage as NiO self-absorption is an important issue.

[z] PMI-6T-TPA has a molar exctinction coefficient in the range of 50 000 $mol^{-1}.L.cm^{-1}$, dye **(8)** molar exctinction coefficient at the peak of its CT band is 27 000 $mol^{-1}.L.cm^{-1}$.

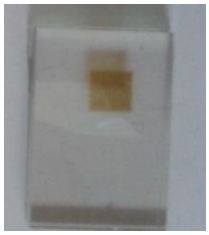


Fig. 97- NiO-4L-(8) electrode

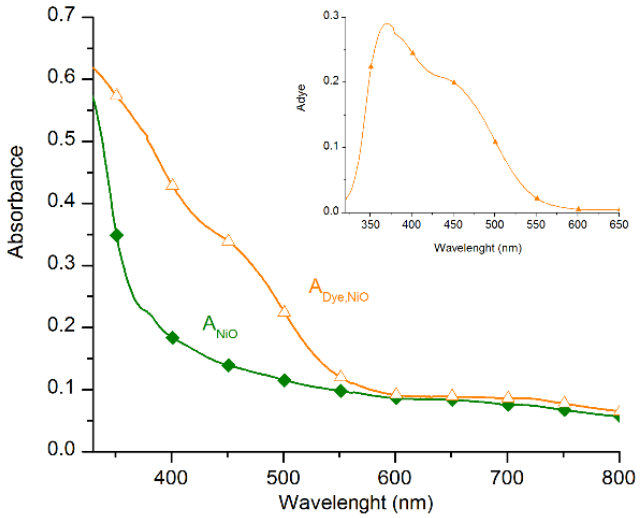


Fig. 98- Absorbance of NiO-4L electrode, A_{NiO} (green trace, filled diamonds). Absorbance of the same electrode after sensitization with dye (8): NiO-4L-(8), $A_{dye,NiO}$ (orange trace, empty triangles). Inset: Dye Absorbance, A_{dye}. The FTO absorbance signal was subtracted in all cases.

The comparison between the solid state and the solution spectrum (see Fig. 99) revealed a different situation as for the **NiO-1L-(8)** spectrum. The solid state spectrum is wider and more shapeless than the spectrum in solution. It reveals that aggregation was pronounced this time. The reason for such a discrepancy with our previous conditions is unclear. It is possible that the rinsing step with ethanol is less efficient in the case of thicker NiO films.

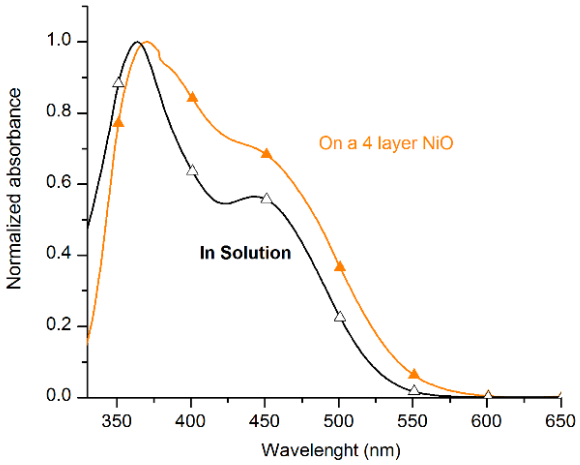


Fig. 99- Normalized solid state spectrum of dye (8) (A_{dye}) on NiO-4L electrode (orange trace, filled triangles). Normalized absorbance of dye (7) in solution (black trace empty triangles).

The LHE of the 850 nm-thick film was also calculated and the obtained trace is given on Fig. 100. In agreement with the increase of the thickness of the film, LHE was increased by approximately two folds compared with **NiO-1L-(8)** electrode (from 17 % to 38% at 440 nm, see Fig. 89).

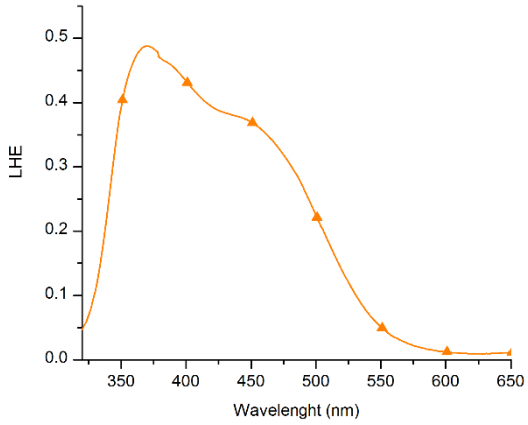


Fig. 100- LHE of a NiO-4L-(8) electrode. The formula used was LHE = $1 - 10^{-Adye}$.

IV.C.3.b. Photovoltaic performance

The photovoltaic performances of the as-built photocathodes are summarized in Tab. 18 and an example of J-V trace is shown on Fig. 101.

Tab. 18- Photovoltaic performance of the IJP NiO-4L-(8) electrode, under 1 Sun (AM 1.5 standard). The results were averaged on three different devices.

PCE (%)	0.096 ± 0.008
J_{SC} (mA.cm^{-2})	2.88 ± 0.23
V_{OC} (mV)	90 ± 4
FF (%)	36.7 ± 0.1

Compared to the **NiO-1L** electrode, the performances are dramatically improved. The overall PCE yield is almost doubled and is now close to 0.1%. The J_{SC} value is also doubled and reaches 2.88 mA.cm^{-2}, which is a high value considering that the electrode is 850 nm thick. These results are consistent with the two-fold increase in LHE of the **NiO-4L-(8)** electrode, compared with the **NiO-1L-(8)**. The FF is kept constant (37/38 %) and the V_{OC} is decreased from 108 $^{\pm}$ 1 mV to 90 $^{\pm}$ 4 mV. Compared to the fiber like morphology, at similar thickness value (see **NiO-F-2L-(8),** Tab. 17), the superiority of the compact nanoparticle morphology is obvious.

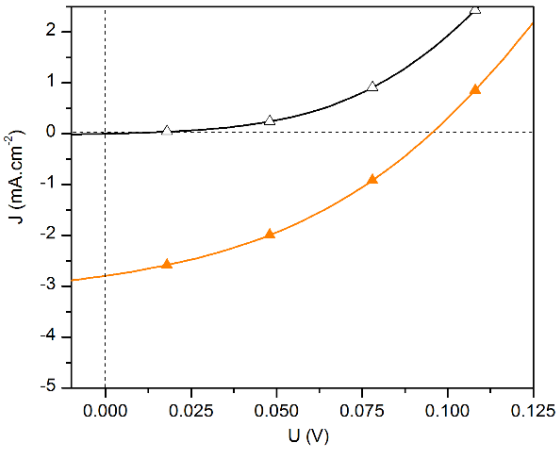


Fig. 101- Representative J-V characteristic of a NiO-4L-(8) electrode measured in the dark (black curve, empty triangle) and under 1 Sun (AM 1.5 standard) (orange curve, filled triangles).

The suitability of the ink-jet printing method for preparing efficient thick mesoporous electrodes is proved by our results. This is an important argument which validates IJP as a promising technique for efficient NiO-based p-type DSSCs.

IV.D. Introducing a NiO_x contact layer between FTO and NiO

IV.D.1. NiO_x thin layer deposition

In the next paragraph, the introduction of a NiO_x dense sub-layer, between FTO and the NiO mesoporous network was investigated (see Fig. 102). As described in chapter 1, it is thought that a NiO_x compact layer brings a better contact between FTO and the NiO mesoporous network, in the case of an iodine electrolyte. In Tab. 19, the state of the art for NiO_x deposition for p-type DSSCs is described. To the best of our knowledge, despite it has been used by some authors (see Tab. 19), there is no study on the influence of a NiO_x layer over the performance of a p-type DSSC, with iodine electrolyte for a spin-cast NiO_x layer [aa].

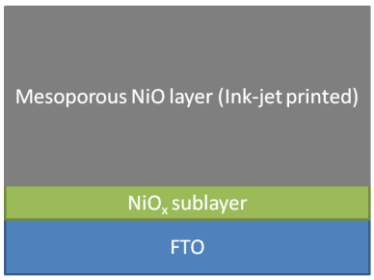


Fig. 102- Representative scheme of a NiO photocathode, with a NiO_x sub-layer.

More precise references about spin-coated NiO_x layer can be found in the field of polymer based solar cells [9, 1, 10, 11], as well as the field of inverted perovskite solar cells [12,13]. In those fields of research, NiO_x is used to replace the corrosive PEDOT:PSS, as an electron blocking layer. The state of the art for NiO_x layer formation by spin-coating, in this field of research has been represented in Tab. 20. Based on these works, we first tried to spin-cast the ethylene diamine solution proposed by Garcia et al.[14], since this method was described to provide good performance for OPV and perovskite solar cells [15]. However, we did not succeed in obtaining uniform NiO_x films with this method. As a matter of fact, many pinholes could be noticed after film drying. This could be explained by the high viscosity of the ink (presence of glycol).

[aa] Which was the only technique available in our lab

Tab. 19- the state of the art for NiO_x deposition for p-type DSSCs.

Reference and electrolyte used	Ni precursors formulation	Deposition technique
Gibson et al. (2009) [16] Iodine-based electrolyte	Ni^{II} acetate in EtOH (0.5M)	Three times 30µL spin-coating on FTO, followed by sintering at 300°C for 15 minutes (thickness not stated)
Zhang et al. (2011) [17] Iodine-based electrolyte	Ni^{II} acetate in EtOH (0.05M)	Five-time dip-coating. Drying and screen printing of NiO mesoporous (50 nm thick)
Zhang et al. (2012) [18] Iodine-based electrolyte	Ni^{II} acetate in EtOH (0.05M)	Dip-coating and screen-printing (no drying step mentioned in the publication).
Zhang et al. (2012) [19] Iodine-based electrolyte	Ni^{II} acetate in EtOH (0.05M)	Dip-coating, drying and screen-printing.
Perera et al. (2015) [20] Fe-based electrolyte	$Ni^{II}(acac)_2$ in MeOH (5 mM)	Spray pyrolysis. Exact experimental conditions were not stated. Approximately 10 nm thick
Yang and coworkers (2014) [21,22] Iodine-based electrolyte	Ni^{II} acetate in EtOH (0.2M)	Spin coating and sintering at 150°C for 15 min. Thickness not stated.



Fig. 103- The emerald green NiO_x precursor solution prepared following the Manders et al. route

It was thus chosen to spin-cast the solution described in the work by Manders et al.[9]. This solution was indeed less viscous and very uniform films could be obtained with high reproducibility. The experimental details can be found in the experimental section and are slightly modified compared to the work by Manders et al. Indeed a 10-min. drying step was introduced prior to sintering at higher temperatures, for practical reasons. Also, the sintering temperature of the NiO_x layer was raised up to 450°C, rather than 275°C (as anyway, the photocathode is finally annealed at 450°C for NiO sintering). In their paper, Manders et al. described the fabrication of a 5 nm-thick NiO_x film. In our conditions, a thickness of approximately 10 nm ($^{\pm}$3 nm) was measured with a stylus profilometer. This thickness is thinner as for the one reported by Zhang et al (see Tab. 19), and in the same range as for Perera et al., which used NiOx sub-layer, with a Fe-based electrolyte.

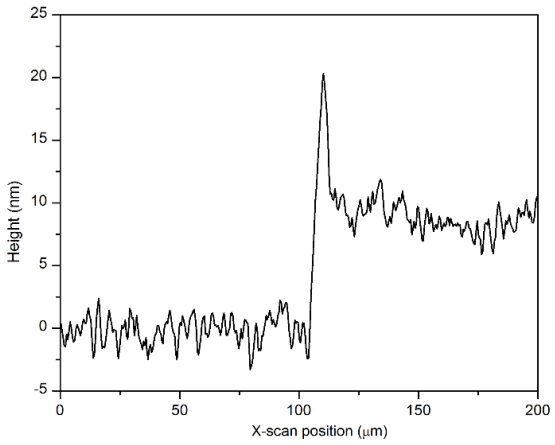


Fig. 104- Thickness measurement of the NiO_x compact layer, deposited on ITO, according to a modified method from the initial work of Manders et al.

Tab. 20- State of the art for NiO_x spin-coating in the field of OPV or perovskite solar cells

Reference	Solution formulation	Comments
[23, 24,25,26,27]	« diluted ink » of a $[Ni(en)_2](HCO_2)_2$. (en = ethylene diamine)	Exact formulation was not stated.
[12, 15, 14]	Ethylene glycol solution containing 0.5M of nickel formate dihydrate, with one molar equivalents of ethylene diamine.	Good performance for OPV or Perovskite based solar cells.
[28]	$Ni(acac)_2$ in toluene (15 mg/mL)	Weak performance (PCE = 3%) for a PCD/TBT photoactive layer)
[9]	Ethanol solution of Nickel acetate tetrahydrate (0.1M) and monoethanolamine (0.1M).	A 5 nm film was obtained. Good performance (PCE = 7.8% with pDTG-TPD:PC71BM photoactive layer)

IV.D.2. Influence of the NiOx sub layer on the p-type DSSC performance

The 10 nm-thick NiO_x underlayer layer described above was used as a compact sub-layer in the case of a **NiO-4L-(8)** photocathode. For simplicity, such a photocathode was called **NiO*-4L-(8)**. It is worth mentioning that in order to avoid contamination, it was important that the deposition of the mesoporous layer was performed rapidly after the 450°C sintering step of the thin layer (for more details, see experimental part). For mesoporous NiO synthesis, sensitization and device performance tests, the experimental conditions were kept identical to what was described above.

The J-V curve characteristic is represented in Fig. 105 and the performance were summarized in Tab. 21.

Tab. 21- Photovoltaic performances of the NiO*-4L-(8), under 1 Sun (AM 1.5 standard). The results were averaged on three different devices.

PCE (%)	0.124 ± 0.007
J_{SC} (mA.cm^{-2})	3.42 ± 0.26
V_{OC} (mV)	99 ± 2
FF (%)	36.7 ± 0.1

Obviously, introducing the NiO_x layer between the FTO electrode and the mesoporous NiO network increases the PCE of the cell, by 30%, which reaches now the value of 0.124 $^{\pm}$ 0.007%. This is essentially due to a significant increase, by 20%, of the short-circuit current (from 2.88 mA.cm^{-2}, to 3.42 mA.cm^{-2}) as the V_{OC} change is not very significant and the FF is stable, when comparing to the situation without NiO_x sub-layer (see IV.C.3.b, **NiO-4L-(8)**). It seems that in average, the dark current is slightly more important in the case of the **NiO*-4L** at 100 mV: 2.39 ± 0.22 mA.cm^{-2} *vs* 1.94 ± 0.02 mA.cm^{-2} for **NiO-4L**). This phenomenon was observed by Bach et al.[17] and reflects the catalytic activity of the NiO_x film toward I^- oxidation. The results shown in this thesis then confirm that with iodine electrolyte, the role of a 10 nm-thick NiO_x layer is to improve contacts between the NiO mesoporous network and FTO.

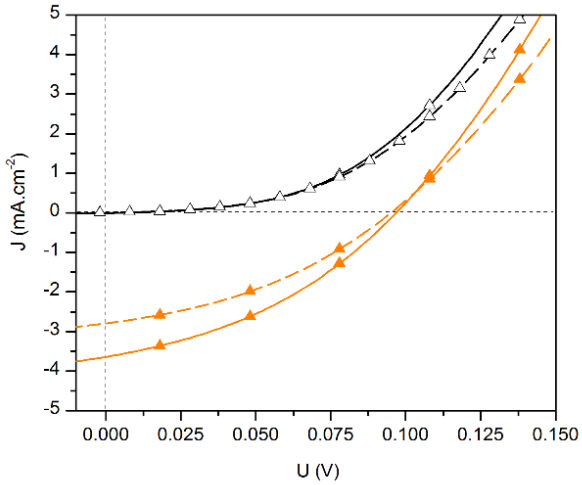


Fig. 105- Example of J-V characteristics of a NiO*-4L-(8) (plain trace) and NiO-4L-(8) (dashed trace), under 1 Sun (AM 1.5 standard) (orange traces, filled triangles) and in the dark (black traces, empty triangles.

IV.E. Performance of the IJP NiO electrodes with other bithiophen dyes

The three bithiophen dyes (**(11)**, **(14)** and **(17)**) which synthesis was described in chapter 2 have been implemented into **NiO-4L** based p-type DSSCs (without the NiO_x contact layer). The first results are presented in this chapter. It is important to note that for all the studies presented here, the electrodes were prepared according to the method described above and the same experimental conditions were also carefully used.

IV.E.1. Sensitization of the NiO electrode

In this paragraph, the establishment of the sensitization conditions for each dye is described. Indeed, **NiO-1L** electrodes were used to validate the sensitization conditions.

IV.E.1.a. Solutions preparation

In order to follow the example of dye **(8)** for NiO sensitization, we prepared saturated solutions for each bithiophen dye. The purpose was to find solvents in which the solubility of the dye is correct (substantial coloration of the solution should occur) but also permits to prepare saturated solution, without using excessive amounts of dye. Like for dye **(8)**, the target concentration was 5.10^{-4} mol of dye per liter of solvent.

IV.E.1.a.i. Dye (14)

As a matter of fact, with the help of its two ethyl groups, dye **(14)** is soluble enough in MeOH for the preparation of a methanol solution as for dye **(8)**. The obtained solution is displayed on Fig. 106.

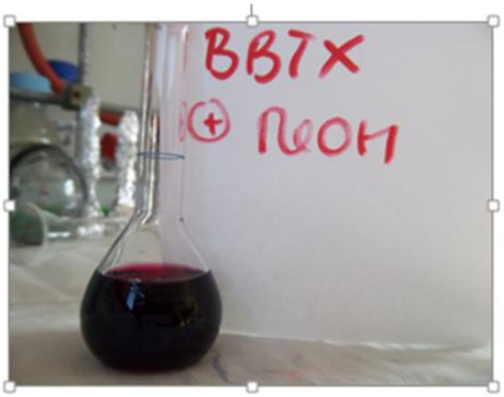


Fig. 106- The dye (14) saturated solution in MeOH which was used for NiO sensitization.

IV.E.1.a.ii. Dye (11) and (17)

The flatness of dye **(11)** and **(17)** and the absence of alkyl groups on their chemical structure render them hardly soluble in common organic solvents. Only DMF or DMSO are able to sufficiently solubilize these dyes, but we decided to avoid these high boiling point solvents. We found that a {1/1 : DCM/MeOH} mixture was suitable for dye **(11)** and **(17)** to prepare the desired solutions. Interestingly, neither dye **(11)** nor **(17)** were soluble in MeOH, or in DCM. However, their solubility was quite important in a mixture of these solvents. In order to exemplify this phenomenon, pictures are shown for dye **(11)** in Fig. 107. This result is quite uncommon and underlines the cooperative effect of solvents for dye molecule solubilization.

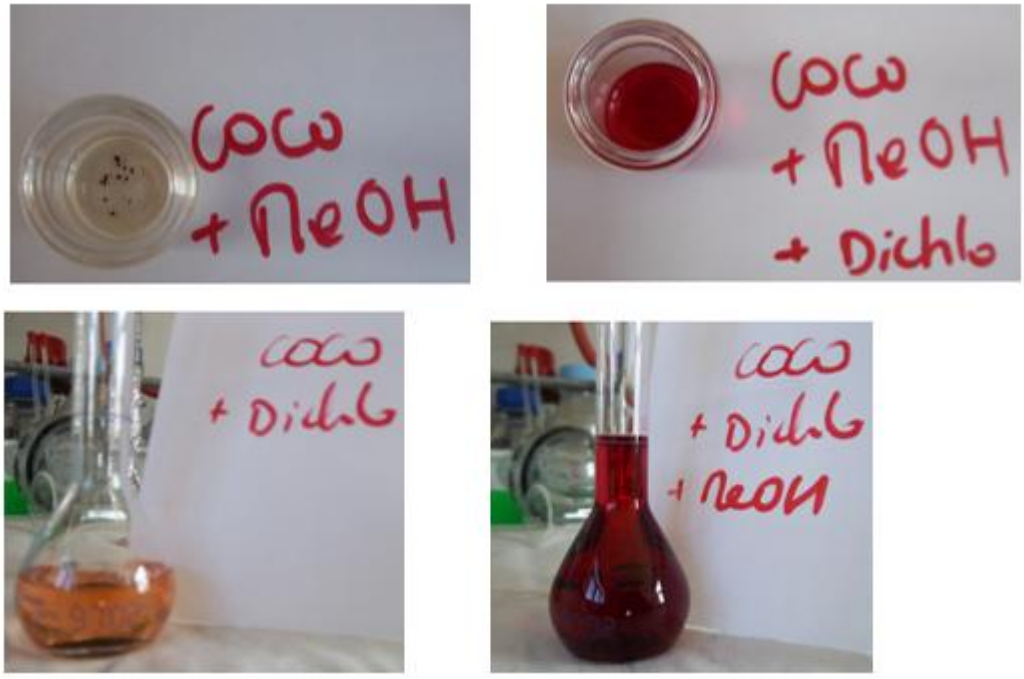


Fig. 107- The surprising behavior of dye (11) (« COCO » here, owing to the two C=O bounds in its formula) in methanol and DCM solvent mixtures. A saturated solution of dye (11) was prepared by adding 5.10^{-4} mol of (11) per liter of a {DCM/MeOH mixture : 1/1}, according to two ways. First way (up): One volume of MeOH is first added (left), then, one volume of DCM is added (right). Second way (down): One volume of DCM is first added (left), then, one volume of MeOH is added (right).

IV.E.1.b. Sensitization of NiO

The sensitization tests were performed with **NiO-1L** electrodes. They were sensitized by immersion into the saturated sensitization solutions during one hour. Judging by the pictures of such photocathodes, sensitization was visibly successful (see Fig. 108).



Fig. 108- NiO-1L films after dye sensitization. Then from left to right, NiO-1L-(14), NiO-1L-(11), NiO-1L-(17) and NiO-1L-(8).

The solid state spectra of dyes **(11)**, **(14)** and **(17)**, one **NiO-1L** electrodes confirmed the sensitization of NiO. These spectra are displayed on Fig. 109, the spectrum of dye **(7)** is recalled on this figure.

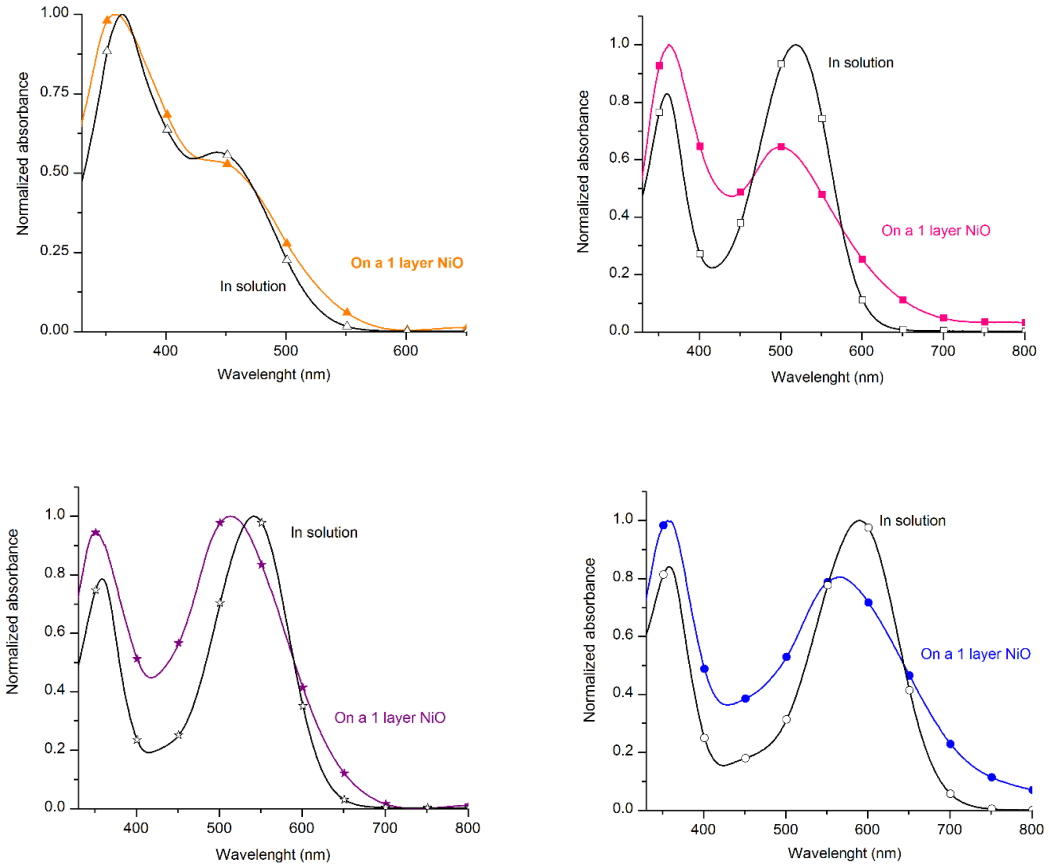


Fig. 109- Normalized absorption spectra "A_{dye}" of the four bithiophen dyes, on NiO (filled shapes) and in solution (empty shapes). Orange trace (triangles): dye (8), pink trace (squares): dye (11), purple trace (stars): dye (14), blue trace (circles): dye (17).

Except for dye **(8)** (which was studied above), the solid state spectra of the bithiophen dyes are very different from the ones in solution. They actually all clearly show an important

hypsochromic shift (40/50 nm for dye **(14)** and dye **(17)**, 20/30 nm for dye **(11)**) and their shape is wider than in solution.

The large hypsochromic shift can be attributed either to important interactions of the dyes with the NiO electronic states, due to the high dipolar moment of these dyes (see chapter 2) or to their aggregation at the NiO surface [29]. Aggregation of the dyes at the surface of the **NiO-1L** electrode also explains that the solid state spectra are wider than the solution spectra. This phenomenon was expected, considering the important flatness of the dyes, which induces Pi-stacking. It is true that the solid state spectrum of dye **(14)** seems to be slightly less different of the solution spectrum, regarding the spectra of dye **(11)** and **(17)**. This could be an effect of the presence of the two ethyl groups on the accepting part of dye **(14)**, which may reduce dye aggregation at the NiO surface.

IV.E.1.c. Device tests on NiO-4L electrode

The device tests were performed with **NiO-4L** electrodes, without the NiO_x compact sub-layer. Sensitization of these electrodes was effective, regarding the pictures of these as prepared photocathodes (see Fig. 110).

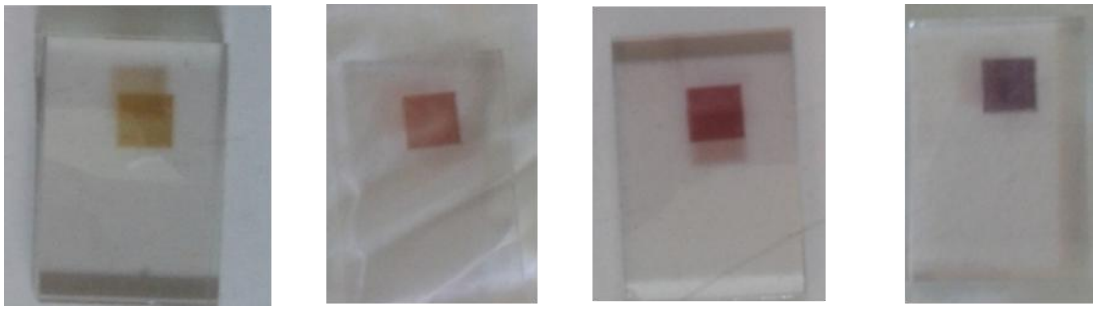


Fig. 110- NiO-4L electrode, after sensitization with the four bithiophen dyes. From left to right: NiO-4L-(8), NiO-4L-(11), NiO-4L-(14) and NiO-4L-(17)

The different photovoltaic characteristics of these photocathodes are displayed in Fig. 111. The superimposition of the different traces under 1 Sun irradiation is shown on Fig. 112 and the performances are summarized in Tab. 22.

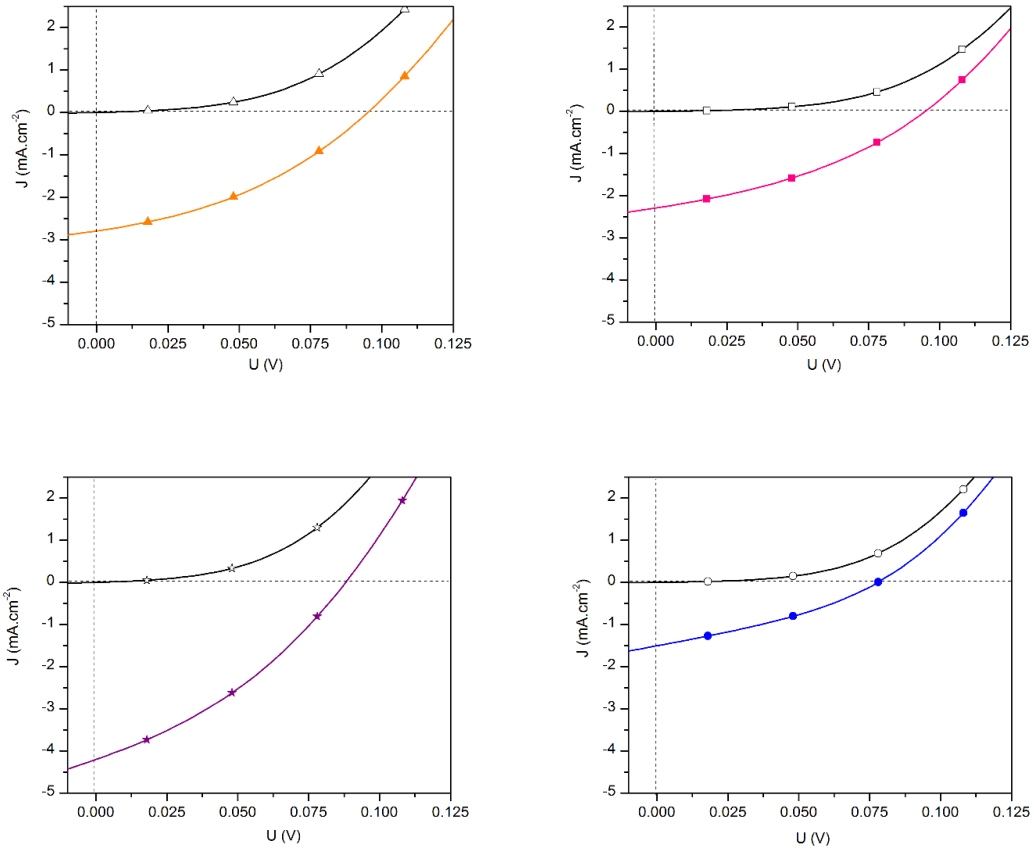


Fig. 111- J-V characteristics of NiO-4L-(8) (orange trace, triangles), NiO-4L-(11) (pink trace, squares), NiO-4L-(14) (purple trace, stars) or NiO-4L-(17) (blue trace, circles. Measurements were performed in the dark (black curve, empty shapes) and under 1 Sun (AM 1.5 standard) (color curve, filled shapes).

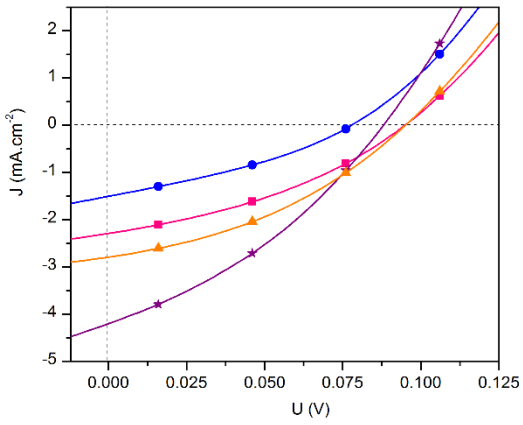


Fig. 112- Superimposition of the J-V characteristics for the four bithiophen dyes, used as a sensitizer for NiO-4L electrode (for more details, see Fig. 111).

Tab. 22- Summary of the photovoltaics performances of the NiO-4L electrodes, sensitized with the different bithiophen dyes synthesized in chapter 2 in p-type DSSC device.

	Dye **(8)**	Dye **(11)**	Dye **(14)**	Dye **(17)**
PCE (%)	0.096 ± 0.008	0.08 ± 0.01	0.126 ± 0.010	0.038 ± 0.003
J_{SC} (mA.cm^{-2})	2.88 ± 0.23	2.45 ± 0.30	4.32 ± 0.32	1.53 ± 0.10
V_{OC} (mV)	90 ± 4	91 ± 5	88 ± 2	77 ± 1
FF (%)	36.7 ± 0.1	35.9 ± 0.6	33 ± 0.5	32.3 ± 0.7

The best performance were obtained when dye **(14)** was used. A value largely above 0.1% (0.126%) could be reached. The second best perfoming device was the one with is dye **(8)**, followed by dye **(11)**. p-Type DSSCs based one dye **(17)** however shows lower performance than the other one.

We start the data analysis with dye **(8)**. This dye, despite its lower molar extinction value gives good performance. This can be attributed to multiple positive factors. First of all, the dihedral angle present between the bithiophen unit and the NI acceptor permits to further away this dye LUMO orbital (see anne 3). This should be beneficial for delaying geminate recombination, as said in the first chapter. This effect seem to largely compensate for the lower epsilon value of dye **(8)** induced by the same torsion angle, showing again the importance to fight against geminate recombination, with NiO-based p-type DSSCs. The certainly lower aggregation of this dye, in comparison with the other one may help to enhanced properties, by avoiding dye to dye dexcitation after light absorption. This lower aggregation is due to the presence of the *isopropyl* groups on the NI part of the dye and the dihedral angle of the molecule. Another interesting point for dye **(8)** could be a "electron-sheltering" effect by the *isopropyl* groups sandwiching the NI acceptor, also preventing charge recombination (once the electron is one the acceptor, the *isopropyl* keep it from recombine with the hole in NiO)

Dye **(11)** performance are lower than for dye **(8)**, despite an almost twice more intense charge transfer transition. Pronounced dye aggregation as well as the proximity of the LUMO toward NiO surface, compared with dye **(8)** may stand for an explanation.

For dye **(17)**, an important drop in the short-circuit current is observed. Considering the high molar extinction coefficient of this dye (53 390 mol^{-1}.L.cm^{-1} at 590 nm), the J_{SC} value is obviously

low. First, we could attribute these lower performances to lower driving force for dye regeneration (calculated to be 230 mV in chapter 2), likewise in the work by Sun and coworkers with dye P7 [30]. However, we rather propose that dye **(17)** aggregation is too pronounced and isolates NiO surface. This hypothesis is supported by the low value of the dark current for dye **(11)**, which is lower than expected (see Fig. 111), considering the important dipolar moment of this dye, which is directed toward the surface and should then induce NiO VBE to shift upward [31]. In this case, the dark-current start "sooner", when the Fermi level of the electrode is raised to positive bias. We have then god hope that provide the aggregation issue is mastered, this dye should work better.

Eventually, the results with dye **(14)**, with a PCE reaching 0.126% $^{\pm}$ 0.010 are interesting considering the low thickness of the **NiO-4L** film (850 nm-thick). An important J_{sc} value of 4.32 $^{\pm}$ 0.32 mA.cm^{-2} was obtained. This high value is attributed to the high molar extinction coefficient of dye **(14)** (64 530 mol^{-1}.L.cm^{-1}, at the peak wavelength, 542 nm). Also, the possibly limited aggregation of this dye at the NiO surface, and, why not, a "shielding" effect of the ethyl groups on the acceptor part can be responsible of the good performance of this sensitizer.

The V_{OC} value of the three dyes described above are similar. It is possible that compensation mechanisms between high photo-current generation, NiO VB edge shift at negative potential when the dipolar moment of the dye is increased or the effect of the dye's LUMO distance to NiO, account for these similar value of V_{OC}. Concerning the FF, it seems that it decreases when increasing the strength of the acceptor part in the dye, this could be an effect of the reducing of the driving force for charge recombination when increasing the acceptor strength (by LUMO gradual stabilization). This phenomenon was observed by Smeigh et al.[32] for a series of perylene imide dyes.

IV.E.2. **Conclusion**

The strong absorption of dye **(14)** allows to increase the performances of the four-layer NiO photocathodes and a PCE value of 0.126% ($^{\pm}$ 0.010) was obtained. This is a high value for a 850 nm-thick NiO electrode. The two other dyes give lower performances, which we attribute to the

detrimental effect of aggregation at the NiO surface. This aggregation also seems to limit the performances of the strongly red absorbing dye **(17)** on thick electrodes, when compared to the one-layer electrode. Overcoming this issue could validate the use of this dye for future implementation in efficient iodine-based tandem dye sensitized solar cells.

IV.F. **Conclusions**

In this part, the validity of ink-jet printing a sol-gel ink for NiO p-type DSSC photocathode formation was demonstrated. By increasing the thickness of the NiO film, in a compact way, it was possible to obtain a PCE of 0.096 $^{\pm}$ 0.008 for the 850 nm-thick electrode, sensitized with TPA-2T-NI **(8)**. The more porous, dual-pore nanofiber like morphology did not permit to enhance the photocathode efficiency. When a 10 nm-thick NiO_x sublayer, synthesized by spin-coating, was introduced between FTO and NiO mesoporous network, the PCE was enhanced by 30% and reached 0.124 ± 0.007. This increase seems to be due to electric interfacial contact enhancement and not a decrease of the dark-current. Finally, the three other bithiophen dyes were investigated as sensitizers for the four-layer NiO film, in absence of the NiO_x sublayer. The strongly absorbing dye **(8)** gave the highest J_{SC} value of this thesis: 4.32 $^{\pm}$ 0.32 $mA.cm^{-2}$. The PCE yield of such a cell was found to be 0.126 $^{\pm}$ 0.010 %. These good results are other proofs of concept for using IJP for NiO photocathode fabrication. Further improvement are necessary to enhance the performance of the strongly red absorbing dye **(17)**, but the working principle of this dye was validated, which permit to reasonably consider its future use in efficient tandem DSSCs.

References

1. Chen, S., Manders, J. R., Tsang, S.-W. & So, F. Metal oxides for interface engineering in polymer solar cells. *J. Mater. Chem.* **22,** 24202–24212 (2012).
2. Wu, F., Zhu, L., Zhao, S., Song, Q. & Yang, C. Engineering of organic dyes for highly efficient p-type dye-sensitized solar cells. *Dyes Pigments* **124,** 93–100 (2016).
3. Powar, S. *et al.* Improved photocurrents for p-type dye-sensitized solar cells using nano-structured nickel(II) oxide microballs. *Energy Environ. Sci.* **5,** 8896–8900 (2012).
4. Li, L. *et al.* Double-Layered NiO Photocathodes for p-Type DSSCs with Record IPCE. *Adv. Mater.* **22,** 1759–1762 (2010).
5. Ji, Z., Natu, G., Huang, Z. & Wu, Y. Linker effect in organic donor–acceptor dyes for p-type NiO dye sensitized solar cells. *Energy Environ. Sci.* **4,** 2818–2821 (2011).
6. Wood, C. J., Summers, G. H. & Gibson, E. Increased photocurrent in a tandem dye-sensitized solar cell by modifications in push-pull dye-design. *Chem. Commun.* **51**, 3915-3918 (2015).
7. Marrani, A. G., Novelli, V., Sheehan, S., Dowling, D. P. & Dini, D. Probing the Redox States at the Surface of Electroactive Nanoporous NiO Thin Films. *ACS Appl. Mater. Interfaces* **6,** 143–152 (2014).
8. Powar, S. *et al.* Highly Efficient p-Type Dye-Sensitized Solar Cells based on Tris(1,2-diaminoethane)Cobalt(II)/(III) Electrolytes. *Angew. Chem. Int. Ed.* **52,** 602–605 (2013).
9. Manders, J. R. *et al.* Solution-Processed Nickel Oxide Hole Transport Layers in High Efficiency Polymer Photovoltaic Cells. *Adv. Funct. Mater.* **23,** 2993–3001 (2013).
10. Irwin, M. D., Buchholz, D. B., Hains, A. W., Chang, R. P. H. & Marks, T. J. p-Type semiconducting nickel oxide as an efficiency-enhancing anode interfacial layer in polymer bulk-heterojunction solar cells. *Proc. Natl. Acad. Sci. U. S. A.* **105,** 2783–2787 (2008).
11. Ratcliff, E. L. *et al.* Evidence for near-Surface NiOOH Species in Solution-Processed NiOx Selective Interlayer Materials: Impact on Energetics and the Performance of Polymer Bulk Heterojunction Photovoltaics. *Chem. Mater.* **23,** 4988–5000 (2011).
12. Wang, K.-C. *et al. p-Type* Mesoscopic Nickel Oxide/Organometallic Perovskite Heterojunction Solar Cells. *Sci. Rep.* **4,** (2014).
13. Chen, W. *et al.* Hybrid interfacial layer leads to solid performance improvement of inverted perovskite solar cells. *Energy Environ. Sci.* **8,** 629–640 (2015).

14. Garcia, A. *et al.* Improvement of Interfacial Contacts for New Small-Molecule Bulk-Heterojunction Organic Photovoltaics. *Adv. Mater.* **24,** 5368–5373 (2012).
15. Jeng, J.-Y. *et al.* Nickel Oxide Electrode Interlayer in CH3NH3PbI3 Perovskite/PCBM Planar-Heterojunction Hybrid Solar Cells. *Adv. Mater.* **26,** 4107–4113 (2014).
16. Gibson, E. A. *et al.* A p-Type NiO-Based Dye-Sensitized Solar Cell with an Open-Circuit Voltage of 0.35 V. *Angew. Chem. Int. Ed.* **48,** 4402–4405 (2009).
17. Zhang, X. L. *et al.* Enhanced open-circuit voltage of p-type DSC with highly crystalline NiO nanoparticles. *Chem. Commun.* **47,** 4808–4810 (2011).
18. Zhang, X. L. *et al.* Charge transport in photocathodes based on the sensitization of NiO nanorods. *J. Mater. Chem.* **22,** 7005–7009 (2012).
19. Zhang, X. L. *et al.* Sensitization of nickel oxide: improved carrier lifetime and charge collection by tuning nanoscale crystallinity. *Chem. Commun.* **48,** 9885–9887 (2012).
20. Perera, I. R. *et al.* Application of the Tris(acetylacetonato)iron(III)/(II) Redox Couple in p-Type Dye-Sensitized Solar Cells. *Angew. Chem. Int. Ed*, **54**, 3758-3762 (2015).
21. Yang, H. B. *et al.* One-Step Fabrication of Unique Mesoporous NiO Hollow Sphere Film on FTO for High-Performance P-Type Dye-Sensitized Solar Cells. *Adv. Mater. Interfaces* **1,** n/a–n/a (2014).
22. Zhu, L., Yang, H. B., Zhong, C. & Li, C. M. Rational design of triphenylamine dyes for highly efficient p-type dye sensitized solar cells. *Dyes Pigments* **105,** 97–104 (2014).
23. K. Xerxes Steirer, Joseph J. Berry, Jordan P. Chesin, Matthew T. Lloyd, Nicodemus Edwin Widjonarko, Alex Miedaner, Calvin J. Curtis, David S. Ginley, Dana C. Olson. Solution processed metal oxide thin film hole transport layers for high performance organic solar cells. (2012).
24. Steirer, K. X. *et al.* Enhanced Efficiency in Plastic Solar Cells via Energy Matched Solution Processed NiOx Interlayers. *Adv. Energy Mater.* **1,** 813–820 (2011).
25. Ratcliff, E. L. *et al.* Energy level alignment in PCDTBT:PC70BM solar cells: Solution processed NiOx for improved hole collection and efficiency. *Org. Electron.* **13,** 744–749 (2012).
26. Steirer, K. X. *et al.* Optimization of organic photovoltaic devices using tuned mixed metal oxide contact layers. in *2010 35th IEEE Photovoltaic Specialists Conference (PVSC)* 000102–000104 (2010). doi:10.1109/PVSC.2010.5614501
27. Steirer, K. X. *et al.* Solution deposited NiO thin-films as hole transport layers in organic photovoltaics. *Org. Electron.* **11,** 1414–1418 (2010).

28. Mustafa, B., Griffin, J., Alsulami, A. S., Lidzey, D. G. & Buckley, A. R. Solution processed nickel oxide anodes for organic photovoltaic devices. *Appl. Phys. Lett.* **104,** 063302 (2014).
29. Ameline, D. *et al.* Isoindigo derivatives for application in p-type dye sensitized solar cells. *RSC Adv.* **5,** 85530–85539 (2015).
30. Qin, P. *et al.* Synthesis and Mechanistic Studies of Organic Chromophores with Different Energy Levels for p-Type Dye-Sensitized Solar Cells. *J. Phys. Chem. C* **114,** 4738–4748 (2010).
31. Rühle, S. *et al.* Molecular Adjustment of the Electronic Properties of Nanoporous Electrodes in Dye-Sensitized Solar Cells. *J. Phys. Chem. B* **109,** 18907–18913 (2005).
32. Smeigh, A. L. *et al.* Ultrafast recombination for NiO sensitized with a series of perylene imide sensitizers exhibiting Marcus normal behaviour. *Chem. Commun.* **48,** 678–680 (2011).

Conlusion of the Thesis

In the aim of improving the performance of NiO-based photocathodes, a new method for NiO film fabrication, ink-jet printing, was developed is this thesis, alongside a series of new push-pull sensitizers.

For NiO film formation we had selected the sol-gel templated ink, for the good performance offered for p-type DSSC construction. Dilution of this ink was a key step for the compatibility with ink-jet printing. p-Type DSSCs were constructed with NiO ink-jet printed films, and the performances compete with actual good literature, validating the new method for the photocathode fabrication purpose. The films were formed in a reproducible way, which is a crucial advantage. Another benefit resides in the several NiO morphology tuning properties that could be offered. A first example in this trend was shown in the present work. Being a non-contact coating technology, ink-jet printing actually permitted to get rid of the stress problem, inherent to other coating technology employed for NiO formation when depositing additional layers. This allowed for the use of different the interlayer drying conditions, and especially low temperature drying conditions, the coating technology which is commonly used for sol-gel NiO formation. The NiO morphology could therefore be tuned. Fiber-like NiO structures were obtained when the low temperature drying conditions were employed. Even-if the performance of as-built photocathodes were not cutting-edge, the possibilities of ink-jet printing were shown. Annealing the successive layers at high temperature actually permitted to avoid fiber formation and this was dramatically beneficial for device performance.

The series of new push-pull type dyes developed, all triphenylamine-based, with various electron acceptors permitted to cover a wide range of the UV/Visible spectrum, reaching the red-part of the solar spectrum, which is important for future efficient Tandem Dye-Sensitized Solar Cells to be constructed. Some organic synthesis hurdles should however be overcome in the future, in

order to go further, in the NIR part of the spectrum. The efficiency of the different dyes was corroborated with their physical properties and promising results were obtained.

Another important aspect of this thesis was the study of the influence of a thin NiO_x sub-layer, synthesized by spin-coating. In conjunction with an iodine-based electrolyte, this sub-layer permits to improve the contact between mesoporous NiO and FTO. The overall performance of the device was enhanced by 30%.

Clearly, increasing the NiO thickness, which was 850 nm for the thicker films presented here, is expected to offer “facile” further improvements. Not to mention that ink-jet printing technology should be compatible with various NiO doping approach that were recently highlighted … Demonstrating the usefulness of our new NiO formation method.

Experimental part

I. Organic synthesis (chapter 2, part I)

I.A. General conditions

All chemical reagents were purchased at Aldrich (if not, supplier information are specified) and used as received. Solvents (Aldrich, VWR, Carlo Erba) were used as received, except if specified.

For inert reactions:

- Reagents and solvents charging were performed in a water free and oxygen free glove-box.
- Previously to reaction, vessels had been stored in a 200°C hoven and powders dried in a desiccator.
- Liquids (solvent or liquid reagents) were dried with 4Å activated molecular sieves in the glove box. The resulting concentration of water in the dried liquid was measured with a Karl-Fisher apparatus (737 KF Coulometer) and has been specified every time.
- After charging, the set-up was transferred out of the glove box and protected with an argon atmosphere during reaction time.

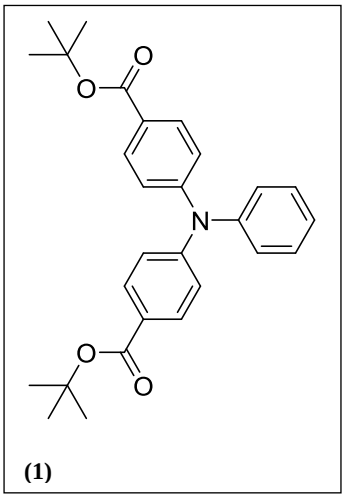
For microwave assisted synthesis, a Microsynth Milestone laboratory microwave hoven was used.

Silica-gel chromatography columns were performed with Merck Silica gel 60 (0.040-0.063 mm).

NMR spectra were recorded with a Bruker AVANCE DRX 400 (^{1}H, 400 MHz and ^{13}C, 100 MHz) otherwise, it was specified. FTIR spectra were recorded with a Bruker Alpha-P.

I.B. **Synthesis of the different intermediates and final molecules**

(1)



(1)

This reaction was carried out in inert atmosphere. Aniline (0.99 g, 10.65 mmol, 1.00 eq.), 4-Bromo-benzoic acid tert-butyl ester (5.99 g, 23.31 mmol, 2.19 eq.), $Pd_2(dba)_3$ (282 mg, 0.31 mmol, 0.03 eq.), $[HP(^tBu)_3]BF_4$ (150 mg, 0.52 mmol, 0.05 eq.), NaO^tBu (2.52 g, 26.25 mmol, 2.46 eq.) and 60 mL of dry toluene were introduced into a 100 mL three necked flask, topped with a refrigerant. A spontaneous exothermic process was noticed. The solution was then stirred for 2 hours at 110 °C, under argon protection. The color, initially dark red, finally turned yellowish. A white precipitate (NaBr) was also noticed. Dichloromethane was added to the mixture which was then washed three times with brine. The combined organic phases were dried over $MgSO_4$. So as to remove the catalytic residues, the solution was filtered over a short celite pad. After removal of the solvents, a brown oil was obtained. Upon the addition of 25 mL of boiling MeOH, a white precipitate rapidly appeared and after one night at 4°C it was collected. This solid was dried under vacuum (3.45 g, 72 % yield).

M.W. (g.mol^{-1}): 446

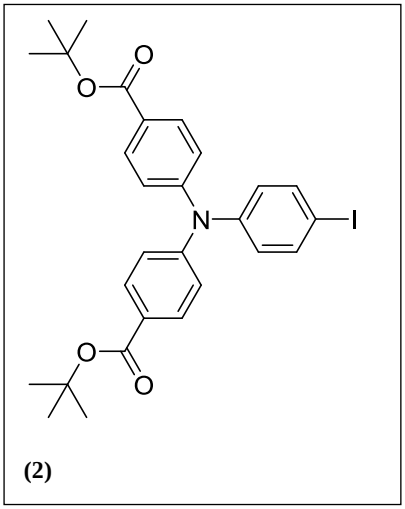
F.P.:138°C

^{1}H NMR ($CDCl_3$, ppm): 7.87 (d, ^3J = 8.96 Hz, 4H, $H_{aro(-COOtBu)}$), 7.33 (t, ^3J = 7.32 Hz, 2H, H_{aro}), 7.18 (d, ^3J = 7.32 Hz, 1H, H_{aro}), 7.13 (d, ^3J = 8.62 Hz, 2H, H_{aro}), 7.07 (d, ^3J = 8.96 Hz, 4H, $H_{aro(-Nphenyl)}$), 1.58 (s, 18H, H_{CH3})

IR (ν, cm^{-1}): 2977 (C-H), 1701 (C=O), 1590 (C=C), 1504 (C=C), 1482 (C=C).

(2)

This synthesis was performed according to ref [1].



(2)

Iodine chloride (2.80 g, 17.28 mmol, 2.40 eq.) and zinc acetate (1.90 g, 10.38 mmol, 1.44 eq.) were introduced into 13 mL of 1,4-dioxane. The mixture was stirred for one hour, zinc acetate did not dissolve entirely. Triphenylamine **(1)** (3.20 g, 7.19 mmol, 1.00 eq.) was mixed with 13 mL of 1,4-dioxane and 2 mL of dichloromethane. After heating, **(1)** was totally dissolved into the solvent, and was added dropwise, with a seringy, to the reaction mixture (it took 20 min). After four hours of stirring at room temperature, the mixture was poured into 100 mL of a saturated sodium thiosulfate aqueous solution. This aqueous phase was extracted three times with dichloromethane. The organic phase was then dried over magnesium sulfate. Solvents were removed under reduced pressure and a brown oil was obtained. Upon the addition of 50 mL of boiling MeOH, a white, snow flake like, precipitate rapidly appeared. After filtration and drying, a white solid was obtained (3.58 g, 85% yield).

M.W. ($g.mol^{-1}$): 571

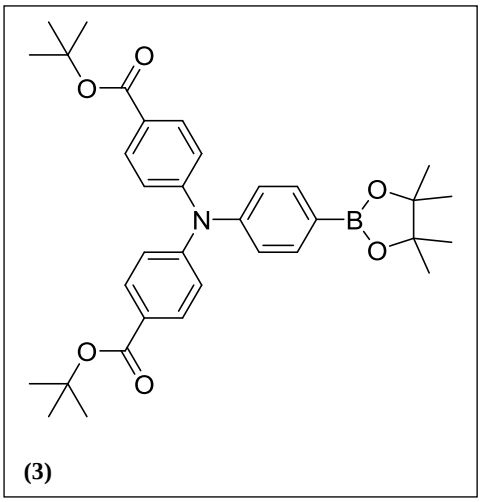
F.P.:172°C

^{1}H NMR ($CDCl_3$, ppm): 7.87 (d, ^3J = 8.78 Hz, 4H, $H_{aro(-COOtBu)}$), 7.61 (d, ^3J = 8.78 Hz, 2H, $_{Haro(-I)}$), 7.06 (d, ^3J = 8.78 Hz, 4H, H_{aro}), 6.88 (d, ^3J = 8.78 Hz, 2H, H_{aro}), 1.59 (s, 18H, H_{CH3})

IR (ν, cm^{-1}): 3001 (C-H, CH_3), 1703 (C=O), 1576 (C=C), 1505 (C=C), 1480 (C=C).

(3)

This synthesis was inspired from ref [2]. Care was taken to employ strictly inert conditions.



(3)

In a 50 ml one-necked flask the iodine derivative **(2)** (1.00 g, 1.75 mmol, 1.00 eq.), the bis(pinacolato)diboron (489 mg, 1.97 mmol, 1.10 eq., *Frontier chemicals*), the $PdCl_2$(dppf) (66 mg, 0.09 mmol, 0.05 eq.) and potassium acetate (515 mg, 5.25 mmol, 3.00 eq.) were mixed with 13 mL of DMSO ([H_2O]=2 ppm, KF). An orange suspension was obtained and after a few minutes, it turned greenish. Then it was stirred at room temperature for one hour (the iodine derivative solubility in DMSO was poor). The resulting brown suspension was heated for an additional hour at 80°C. After cooling at room temperature (ten minutes), it was poured into a large volume of water (300 mL). A white precipitate appeared. After 30 min at 4°C, the solid was collected, generously washed with water and finally re-solubilized into dichloromethane. A filtration over a short $MgSO_4$ pad was performed and after solvent removal under reduced pressure, a brown solid was obtained. The remaining iodine derivative was removed with the help of a short silica-gel chromatography column (dichloromethane as the eluent). After solvent removal and upon the addition of hot MeOH (50 mL), a white solid appeared. It was finally collected and dried under vacuum (553 mg, 55% yield).

M.W. ($g.mol^{-1}$): 571

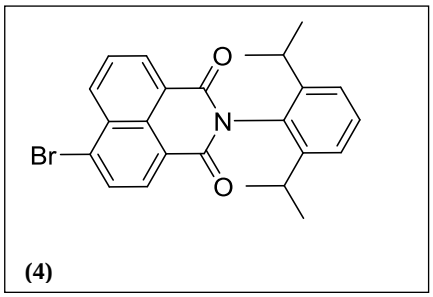
F.P.: 240 °C

^{1}H NMR (CDCl3, ppm): 7.86 (d, ^{3}J = 8.78 Hz, 4H, $H_{aro(-COOtBu)}$), 7.74 (d, 3J = 8.42 Hz, 2H, H_{aro}), 7.09 (m, 6H, H_{aro}), 1.58 (s, 18H, $H_{CH3,carboxylic\ ester}$), 1.34 (s, 12H, $H_{CH3,boronic\ ester}$)

IR (ν, cm-1): 3001 (C-H, CH3), 1703 (C=O), 1576 (C=C), 1505 (C=C), 1480 (C=C).

(4)

This reaction was inspired from a literature synthesis [3]. Other publications also reported for the synthesis of **(4)** [4,5].



(4)

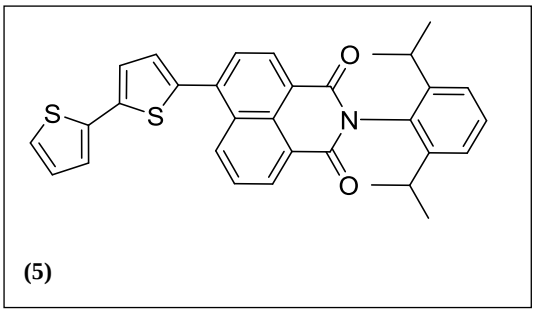
In a one-necked flask, 4-Bromo-1,8-naphtalic anhydride (7.66 g, 0.028 mol, 1.00 eq.), 2,6 –diisopropylaniline (4.90 g, 0.028 mol, 1.00 eq.) were mixed with acetic acid (120 mL) and the resulting yellow suspension was stirred for 3 days at reflux. After cooling at room temperature, a pale yellow precipitate was collected, washed with water and then ethanol. After one night of drying at 60°C in vacuum, the remaining brominated derivative was removed thanks to a chromatography column on Silica-gel (dichloromethane as the eluent). A white solid was obtained as **(4)** (8.99g, 75% yield).

M.W. (g.mol^{-1}): 436

^{1}H NMR ($CDCl_3$, ppm): 8.75 (dd, ^3J = 7.32 Hz, ^2J = 1.10 Hz, 1H, $H_{aro,naphtalene}$), 8.68 (dd, ^3J = 8.60 Hz, ^2J = 1.10Hz, 1H, $H_{aro,naphtalene}$), 8.51 (d, ^3J = 7.87 Hz, 1H, $H_{aro,naphtalene}$), 8.11 (d, ^3J = 7.87 Hz, 1H, $H_{aro,naphtalene}$), 7.92 (dd, $^3J_1$ = $^3J_2$ = 7.32 Hz, 1H, $H_{aro,naphtalene}$), 7.50 (t, ^3J = 8.05 Hz, 1H, $H_{aro,phenyl,para}$), 7.35 (d, ^3J = 7.68 Hz, 2H, $H_{aro,phenyl,meta}$), 2.73 (sept, ^3J = 6.8 Hz, 2H, $CH_{isopropyl}$), 1.17 (d, ^3J = 6.77 Hz, 12H, CH_3).

IR (ν, cm^{-1}): 1709 (C=O), 1670 (C=O), 1343 (C-N), 1236 (C-N)

(5)



(5)

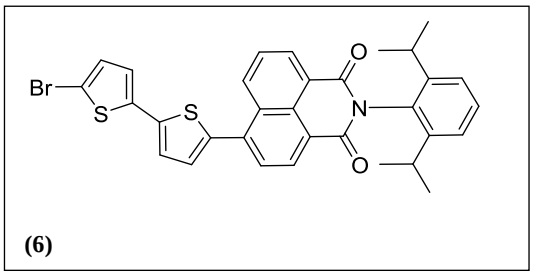
This synthesis was microwave assisted. In a 250 mL two necked flask, 2,2′-Bithiophen-5-boronic acid pinacol ester (543 mg, 1.86 mmol, 1.20 eq.), **(4)** (675 mg, 1.55 mmol, 1.00 eq.), $Pd(dba)_2$ (89 mg, 0.16 mmol, 0.10 eq.), $[HP(t\text{-}bu)_3]BF_4$ (45 mg, 0.16 mmol, 0.10 eq.) and grinded potassium phosphate (987 mg, 4.65 mmol, 3.00 eq.) were introduced. The flask was placed in the microwave hoven and carefully degassed with nitrogen. Hence, 110 mL of the solvent (a {THF/H_2O: 1/0.1} mixture, which has been carefully degassed before) was introduced into the flask. The solution was heated and stirred for 35 min under microwave irradiation. The reaction conditions were the following: t = 0 to t = 5min, P = 150 W, from room temperature to 65°C; t = 5min to t = 35 min, P = 100W, T = 65°C. After cooling at room temperature, the solvent was removed under reduced pressure. The solid obtained was solubilized into dichloromethane and washed three times with brine. The organic phases are dried over $MgSO_4$. After solvent removal, the residue was purified over silica gel column (eluent gradient, from {dichloromethane/petroleum ether : 1/1}, to reach 100% dichloromethane). A pure orange solid (672 mg, 83% yield) was finally obtained.

M.W. ($g.mol^{-1}$) 522

^{1}H NMR ($CDCl_3$, ppm): 8.81 (dd, $^3J_1$ = 8.5 Hz, $^4J_2$ = 0.6 Hz, 1H, $H_{aro,naphtalene}$), 8.74 (dd, $^3J_1$ = 7.1 Hz, $^4J_2$ = 0.6 Hz , 1H, $H_{aro,naphtalene}$), 8.69 (d, ^3J = 7.6 Hz, 1H, $H_{aro,naphtalene}$), 7.91 (d, ^3J = 7.6 Hz, 1H, $H_{aro,naphtalene}$), 7.85 (dd, $^3J_1$ = 8.4 Hz, $^3J_2$ = 7.5 Hz, 1H, $H_{aro,naphtalene}$), 7.49 (t, ^3J = 7.8 Hz, 1H, $H_{aro,phenyl,para}$), 7.36 to 7.31 (m, {2H, $H_{phenyl,meta}$} + {4H, $H_{thiophen}$}), 7.09 (dd, $^3J_1$ = 5.3 Hz, $^3J_2$ = 3.6 Hz, 1H, $H_{thiophen}$), 2.77 (sept, ^3J = 6.7 Hz, 2H, $H_{CH,isopropyl}$), 1.17 (d, ^3J = 6.8 Hz, 12H, $H_{CH3,isopropyl}$).

IR (ν, cm^{-1}): 1699 (C=O), 1658 (C=O), 1353 (C-N), 1234 (C-N).

(6)



(6)

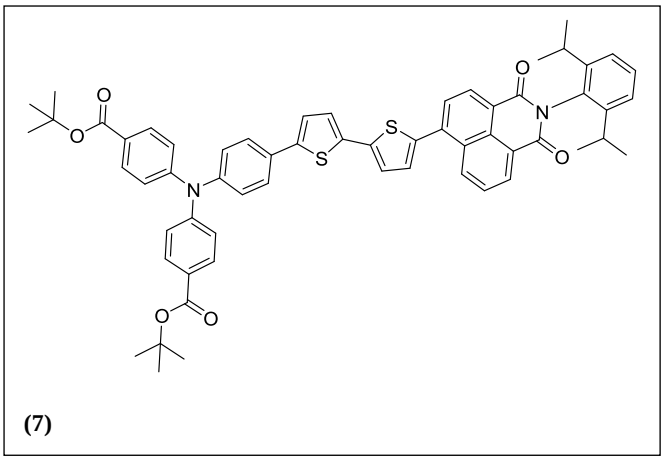
In a 50 mL three necked flask, containing **(5)** (700 mg, 1.34 mmol, 1.00 eq.*)* and 10 mL of DMF, NBS (286.6 mg, 1.61 mmol, 1.2 eq., diluted into 4 mL of DMF) was added slowly, in the dark, at room temperature. The mixture was stirred overnight in these conditions. After concentration under vacuum, water was added and the precipitate was filtered over a short silica-gel pad (dichloromethane as the eluent). After solvent removal, **(6)** was obtained as an orange solid (685mg, 85% yield).

M.W. ($g.mol^{-1}$): 601

^{1}H NMR ($CDCl_3$, ppm): 8.78 (d, ^3J = 8.4 Hz, 1H, $H_{aronaphtalene}$), 8.74 (d, ^3J = 7.2 Hz, 1H, $H_{aro,naphtalene}$), 8.69 (d, ^3J = 7.7 Hz, 1H, $H_{aro,naphtalene}$), 7.90 (d, ^3J = 7.7 Hz, 1H, $H_{aro,naphtalene}$) ,7.51 (dd, $^3J_1$ = 8.2 Hz, $^3J_2$ = 7.6 Hz, 1H, $H_{aro,naphtalene}$), 7.50 (t, ^3J = 7.8 Hz, 1H, $H_{aro,phenyl,para}$), 7.35 (d, ^3J = 7.7 Hz, 2H, $H_{aro,phenyl,meta}$), 7.31 (d, ^3J = 3.9 Hz, 1H, $H_{thiophen}$), 7.27 (d, ^3J = 3.9 Hz, 1H, $H_{thiophen}$), 7.05 (s, 2H, $H_{thiophen}$), 2.77 (sept, ^3J = 6.9 Hz, 2H, H_{CH}), 1.18 (d, ^3J = 6.8 Hz, 12H, H_{CH3})

IR (ν, cm^{-1}): 1701 (C=O), 1662 (C=O).

(7)



(7)

This reaction was carried out under argon. In a 100 mL three necked flask, **(6)** (556 mg, 0.93 mmol, 1.00 eq.), **(03)** (557 mg, 1.01 mmol, 1.09 eq.), $Pd(dba)_2$ (26 mg, 0.05 mmol, 0.05 eq.) and K_3PO_4 (579 mg, 2.76 mmol, 2.98 eq., previously grinded) were introduced. Then, 50 mL of degassed {THF/H_2O, 1/0.1} solvent mixture were introduced, under argon. The flask was heated and stirred in a microwave hoven, the following parameters were employed: 5 min at 150 W, from room temperature to 49°C; 55 min at 100W at 49°C. The initial orange color had turned to deep red. After solvent removal under reduced pressure, dichloromethane was added and the mixture was washed three times with water. The combined organic phases were dried over $MgSO_4$ and filtered over a short celite pad. After solvent removal, a red solid was obtained. It could be recrystallized from cyclohexane to give a sharp-orange solid (710 mg, 80% yield).

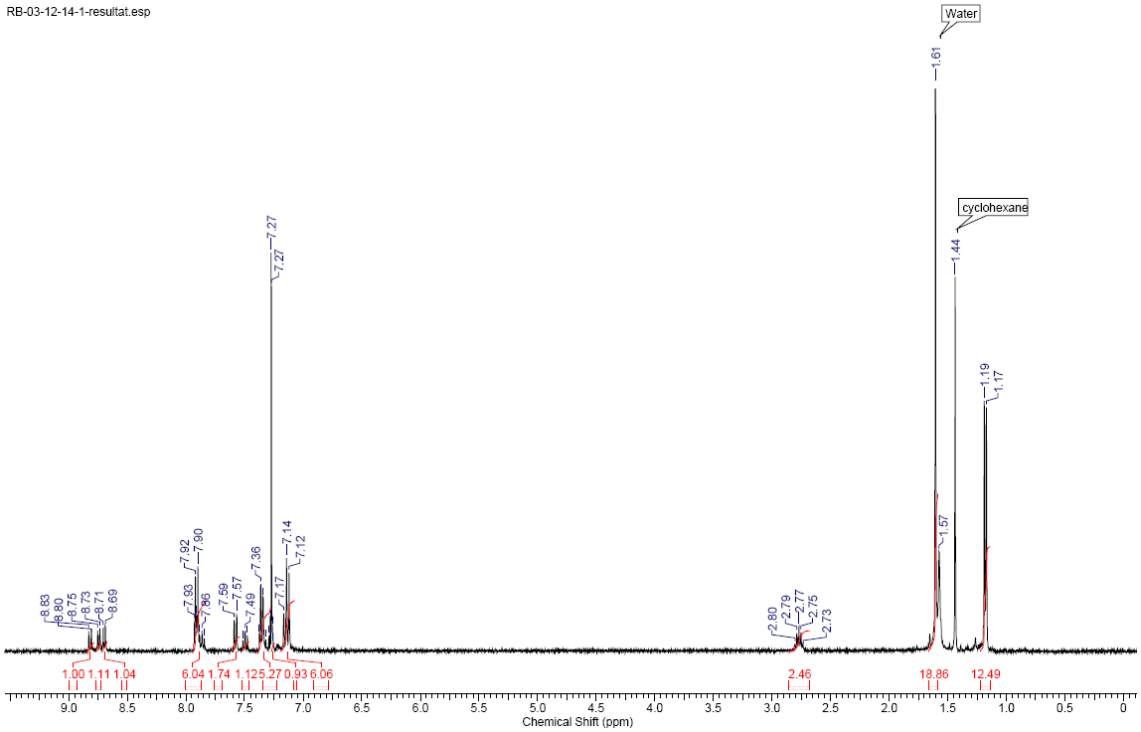
M.W. ($g.mol^{-1}$): 965

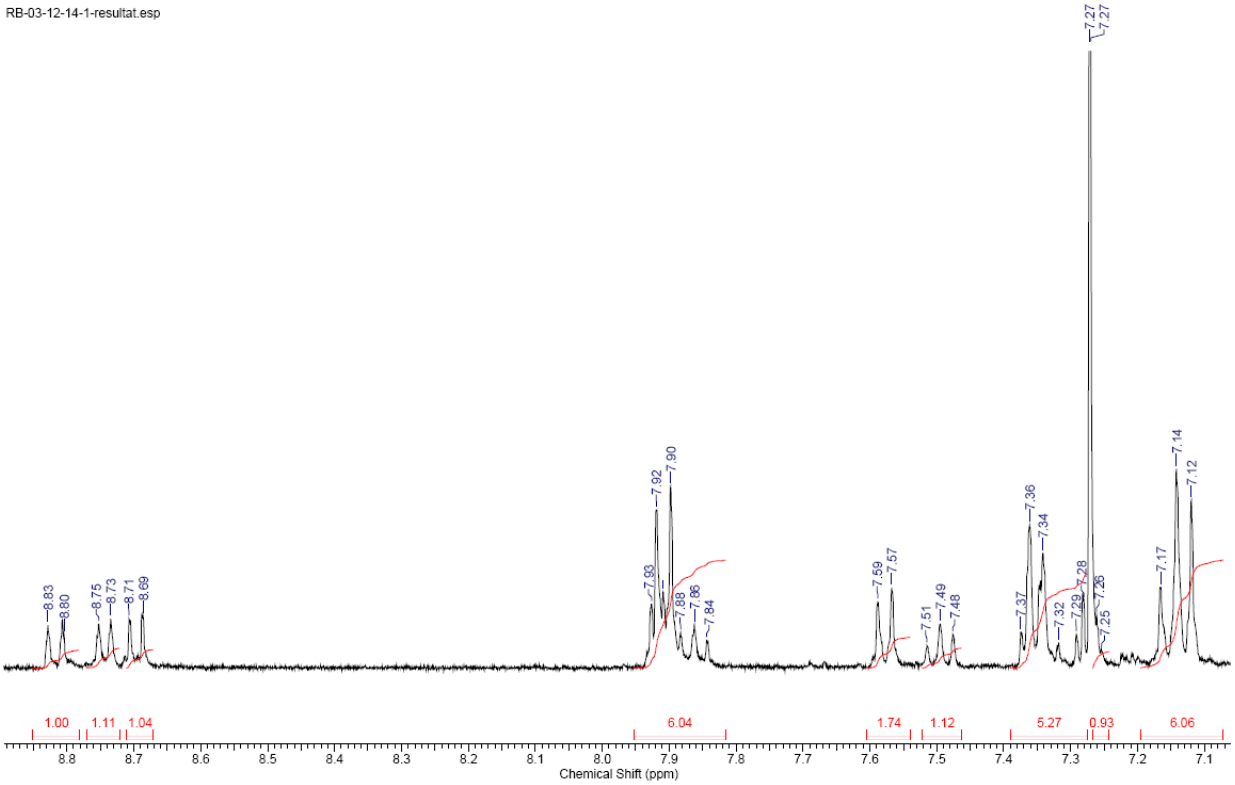
F.P.: 248°C

^{1}H NMR ($CDCl_3$, ppm): 8.82 (d, ^3J = 8.60 Hz, 1H, $H_{aro,naphtalene}$), 8.74 (d, ^3J = 7.14 Hz, 1H, $H_{aro,naphtalene}$), 8.70 (d, 1H, $H_{aro,naphtalene}$), 7.93 to 7.84 (m, 6H, $2H_{aro,naphtalene}$ / $4H_{aro,TPA\text{-}COOtBu}$), 7.58 (d, ^3J = 8.23 Hz, 2H, $H_{aro,TPA}$), 7.49 (t, ^3J = 7.87 Hz, 1H, $H_{aro,phenyldiisopropyl,para}$), 7.25 to 7.37 (m, 6 H, $4H_{thiophen}$ / $2H_{aro,phenyldiisopropyl,meta}$), 7.14 (m, 6H, $H_{aro,TPA}$), 2.77 (sept, 2H, ^3J = 6.77 Hz, $H_{CH,isopropyl}$), 1.61 (s, 18H, $H_{CH3,tert\text{-}butyl}$), 1.18 (d, 3J = 6.84Hz;12H, $H_{CH3,isopropyl}$)

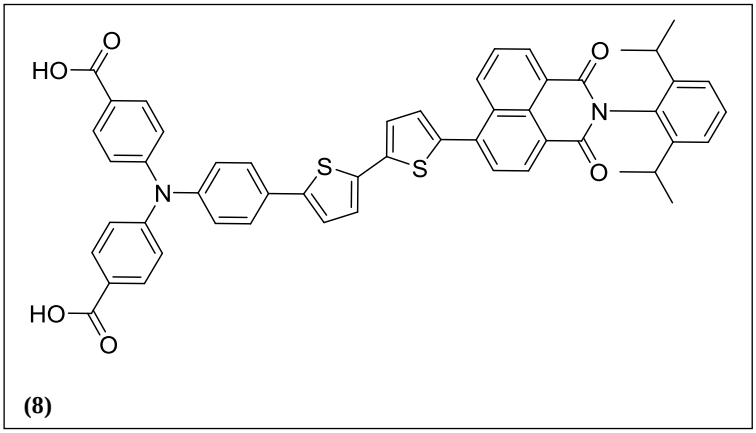
IR (ν, cm^{-1}): 3067, 2964, 2926, 2867, 2850 (C-H), 1703 (C=O), 1664 (C=O), 1580 (C=C), 1524 (C=C), 1503 (C=C), 1469 (C=C).

(7)- ^{1}H $CDCl_3$


RB-03-12-14-1-resultat.esp
Water
cyclohexane
Chemical Shift (ppm)


RB-03-12-14-1-resultat.esp
Chemical Shift (ppm)

(8)



(8)

In a 10 mL one necked flask, **(07)** (300 mg, 0.31 mmol, 1.00 eq.) was dissolved into 5 mL of dichloromethane. Then TFA (1.77 g, 15.5 mmol, 50 eq.) was added in the dark. After 5 hours of stirring, the mixture was poured into a large volume of water, and additional dichloromethane was added. The orange organic phase was separated, washed three times with water and dried over $MgSO_4$. After solvent removal under reduced pressure and drying with high vacuum, the solid was washed with hot cyclohexane to give **(08)** as a crystalline orange powder (245 mg, 0.29 mmol, 94% yield).

M.W. (g.mol^{-1}) 853

F.P.: 220-225°C

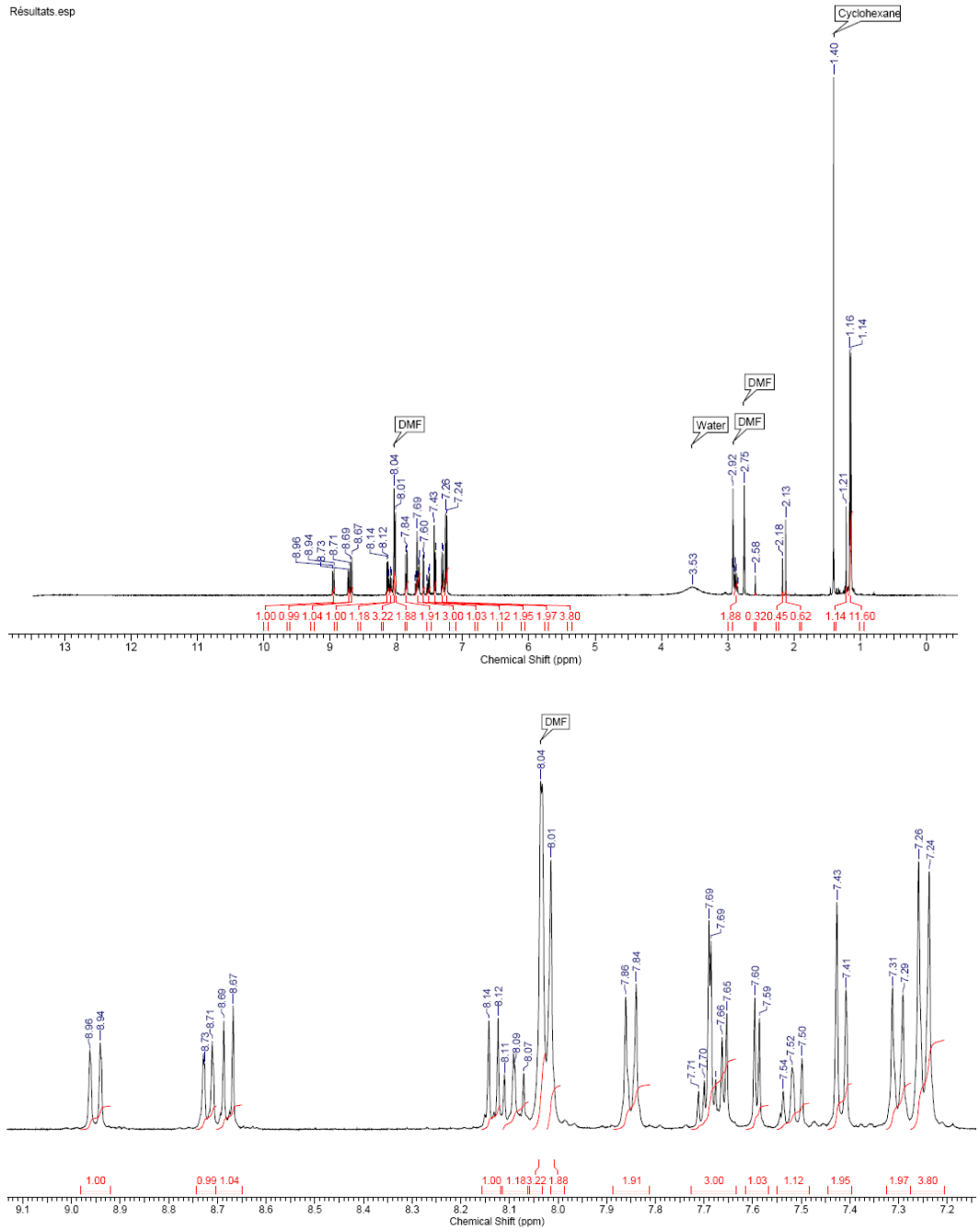
^{1}H NMR (N,N-DMF-d_7, ppm): 8.95 (d, ^{3}J = 8.60 Hz, 1H, $H_{aro,naphtalene}$), 8.72 (d, ^{3}J = 8.05 Hz, 1H, $H_{aro,naphtalene}$), 8.68 (d, ^{3}J = 8.68 Hz, 1H, $H_{aro,naphtalene}$), 8.13 (d, ^{3}J =7.68 Hz, 1H, $H_{aro,naphtalene}$), 8.09 (t, ^{3}J = 7.32Hz, 1H, $H_{aro,naphtalene}$), 8.02 (d,^{3}J = 8.42 Hz, 4H, $H_{aro,TPA,-COOH}$), 7.85 (d, ^{3}J = 8.60 Hz, 2H, $H_{aro,TPA}$), 7.71 to 7.65 (m, 3H), 7.59 (d, ^{3}J = 3.84 Hz, 1H, $H_{thiophen}$), 7.52 (t, ^{3}J = 8.05Hz, 1H, $H_{aro,phenyldiisopropyl,para}$), 7.42 (d, ^{3}J = 7.50 Hz, 2H, $H_{aro,TPA}$), 7.30 (d, ^{3}J = 8.60 Hz, 2H, $H_{aro,TPA}$), 7.25 (d, ^{3}J = 8.78 Hz, 4H, $H_{aro,TPA}$), 2.88 (sept, 2H, ^{3}J = 6.77 Hz, $H_{CHisopropyl}$), 1.15 (d, ^{3}J = 6.77 Hz, 12H, $H_{CH3,isopropyl}$)

^{13}C NMR (N,N-DMF-d_7, ppm): **$C_{carbox./amide}$**: 164.40, 164.10; **C_{aro}**: 150.87, 146.28, 143.25, 139.77, 138.89, 138.45, 135.60, 132.98, 131.94, 131.82, 131.51, 131.21, 129.97, 129.67, 129.59, 129.09, 128.45, 127.20, 126.77, 126.50, 125.51, 125.17, 124.15, 123.31, 123.25, 122.23; **$C_{aliphatic}$**: 26.93, 23.73

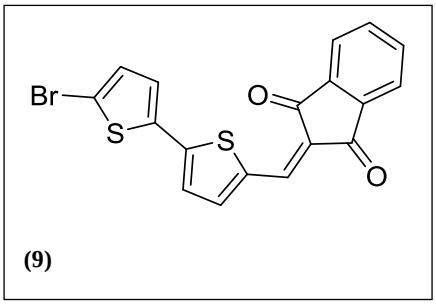
ESI-MS, (m/z): calculated for $[M]^+$: 852, found for $[M+H]^+$: 851

IR (ν, cm^{-1}): 3000 (O-H), 1706 (C=O), 1664 (C=O).

(8)- ^{1}H DMF-d_6



(9)



(9)

This synthesis was performed by Praveen Chandrasekar (CINAM, J.M. Raimundo). To a mixture of bromo-bithiophen aldehyde (1.0 eq) and 1H-indene-1,3(2H)-dione (1.0 eq) was added excess of acetic anhydride (~40 V). This was heated at 80°C for 24 h. Then it was cooled to

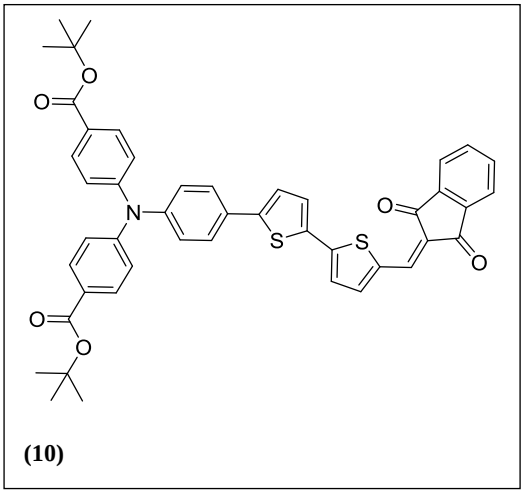
room temperature and the solid was filtered and washed with ice-cold ethanol. The solid was dried under vacuum at 40^{o} C for 24 h to afford the pure bithiophen adduct **(09)** as an orange powder (16% yield)

M (g.mol^{-1}): 401

ESI-MS, (m/z): calculated for $[M]^{+}$: , found for $[M+H]^{+}$:

^{1}HNMR (250 MHz, DMSO-d_6, ppm): 8.21 (d, ^{3}J = 4.0 Hz, 1H), 8.07 (s, 1H, $H_{ethylene}$), 7.95-7.968 (m, 4H), 7.61 (d, ^{3}J = 4.0 Hz, 1H, $H_{thiophen}$), 7.52 (d,^{3}J = 4.0 Hz, 1H, $H_{thiophen}$), 7.38 (d, ^{3}J = 3.7 Hz, 1H, $H_{thiophen}$).

(10) -



(10)

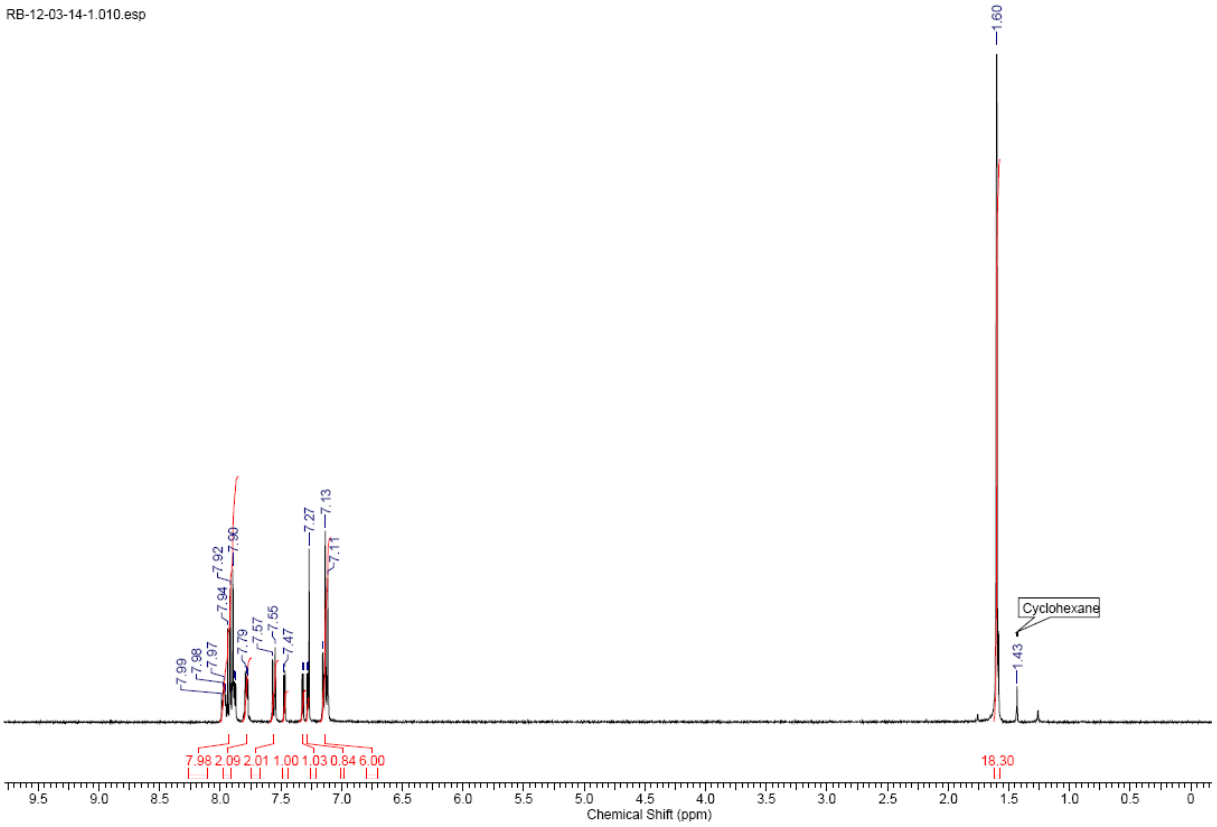
This reaction was microwave assisted. In a 10 mL three necked flask, **(09)** (26 mg, 0.06 mmol, 1.00 eq.), triphenylamine **(03)** (40 mg, 0.07 mmol, 1.17 eq.), $Pd(dba)_2$ (2 mg, 0.003 mmol, 0.05 eq.), $[HP(^tBu)_3][BF4]$ (1 mg, 0.003 mol, 0.05 eq.) and K_3PO_4 (40 mg, 0.19 mmol, 3.17 eq., previously grinded) were introduced. The set-up was degassed with nitrogen. Then, 2.5 mL of a {THF/H_2O: 1/0.1} solvent mixture, previously degassed with argon, were introduced. This mixture was stirred and heated in the microwave, following these parameters: 5 min at 150 W, from room temperature to 49°C; 55 min at 100W at 49°C. The color of the mixture rapidly turned bloody-red. After solvent removal under reduce pressure, dichloromethane was added and the mixture was washed three times with water. The combined organic phases were dried over $MgSO_4$ and filtered on a short celite pad. After solvent removal, a Parma-red solid was obtained. The recrystallization of this solid from cyclohexane gave a pure fuchsia powder (40 mg, 87% yield).

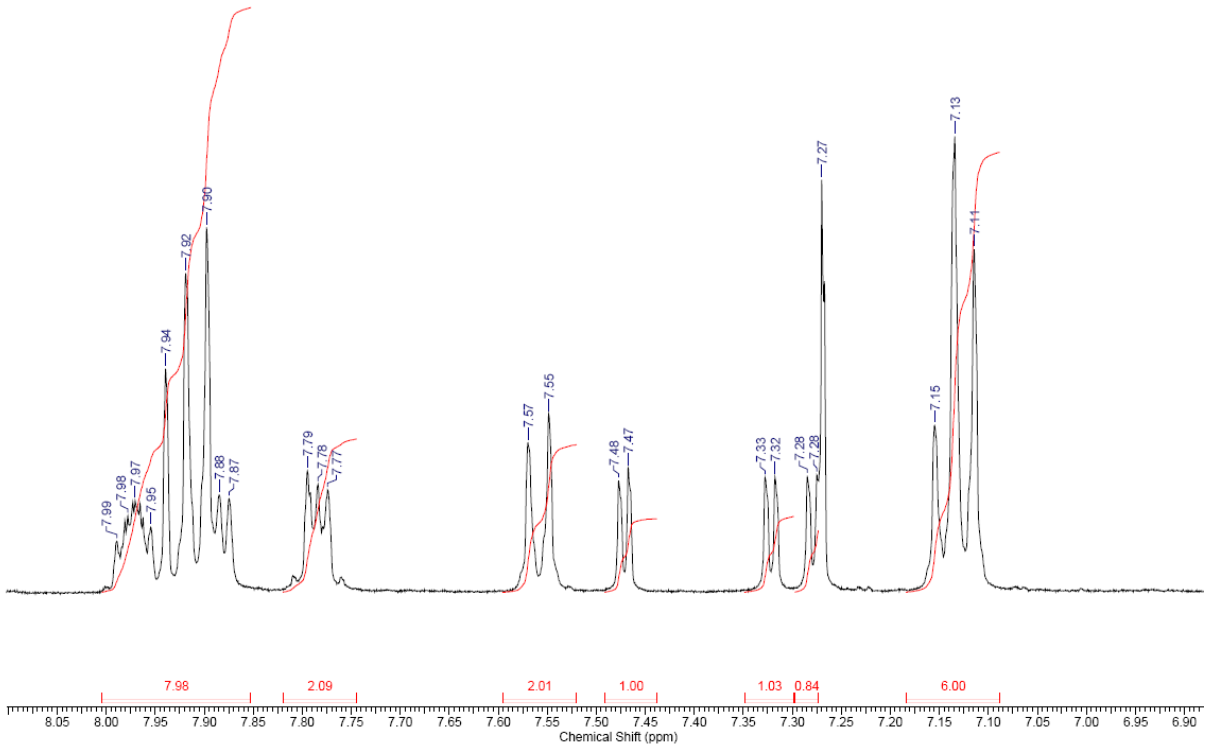
M.W. ($g.mol^{-1}$): 766

F.P.: 210 °C

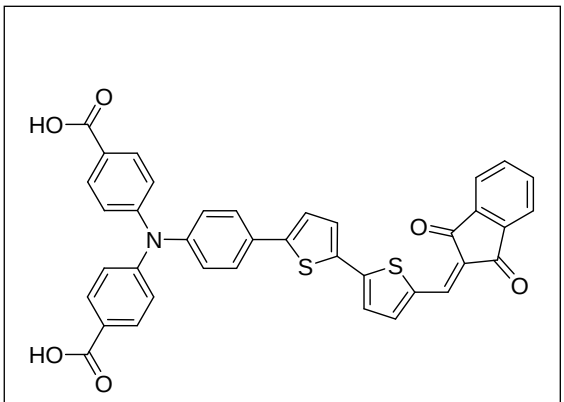
^{1}H NMR ($CDCl_3$, ppm): 7.97 (m, 2H, $H_{aro,phtal,H\text{-}C=C\text{-}C=O}$), 7.94 (s, 1H, $H_{ethylene}$), 7.91 (d, ^3J = 8.60 Hz, 4H, $H_{aro,TPA\text{-}COOtBu}$), 7.88 (d, 1H, $H_{thiophen}$), 7.78 (m, 2H, $H_{aro,phtal,H\text{-}C\text{-}C=C\text{-}C=O}$), 7.56 (d, ^3J = 8.42 Hz, 2H, $H_{aro,TPA}$), 7.47 (d, ^3J = 3.84 Hz, 1H, $H_{thiophen}$), 7.32 (d, 1H, $H_{thiophen}$), 7.28 (d, 1H, ^3J = 3.84 Hz, $H_{thiophen}$), 7.13 (m, 6H, $H_{aro,TPA}$), 1.61 (s, 18H, $H_{CH3tert\text{-}butyl}$).

(10)- ^{1}H $CDCl_3$


RB-12-03-14-1.010.esp
1.60
Cyclohexane
1.43
7.99
7.98
7.97
7.92
7.90
7.94
7.79
7.57
7.55
7.47
7.27
7.13
7.11
7.98 2.09 2.01 1.00 1.03 0.84 6.00
18.30
Chemical Shift (ppm)


7.99
7.98
7.97
7.95
7.94
7.92
7.90
7.88
7.87
7.79
7.78
7.77
7.57
7.55
7.48
7.47
7.33
7.32
7.28
7.28
7.27
7.15
7.13
7.11
7.98
2.09
2.01
1.00
1.03
0.84
6.00
Chemical Shift (ppm)

(11) -



(11)

In a vial, **(10)** (37 mg, 0.045 mmol, 1.00 eq.) was dissolved into 1 mL of dichloromethane. Then TFA (243 mg, 2.1mmol, 47 eq.) was added in the dark. After 18 hours of stirring, dichloromethane was added and solvents were removed under reduced pressure and drying with high vacuum was operated during 36h. **(11)** was obtained as a pure dark powder (31 mg, 99% yield).

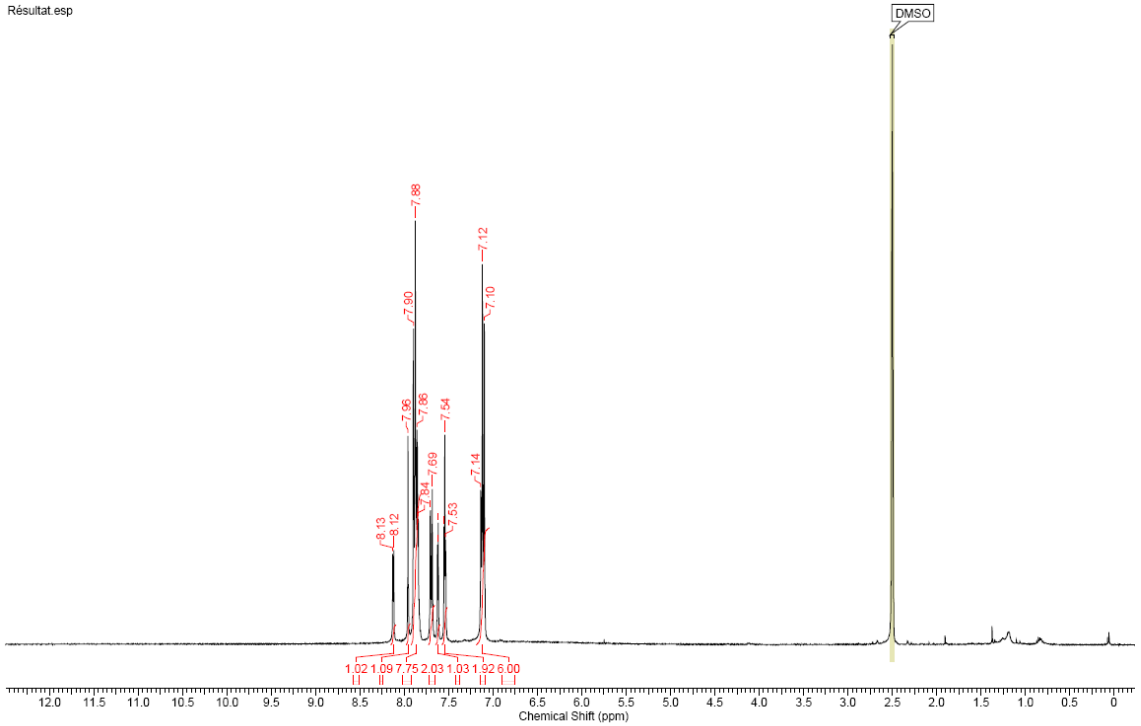
M.W. ($g.mol^{-1}$): 654

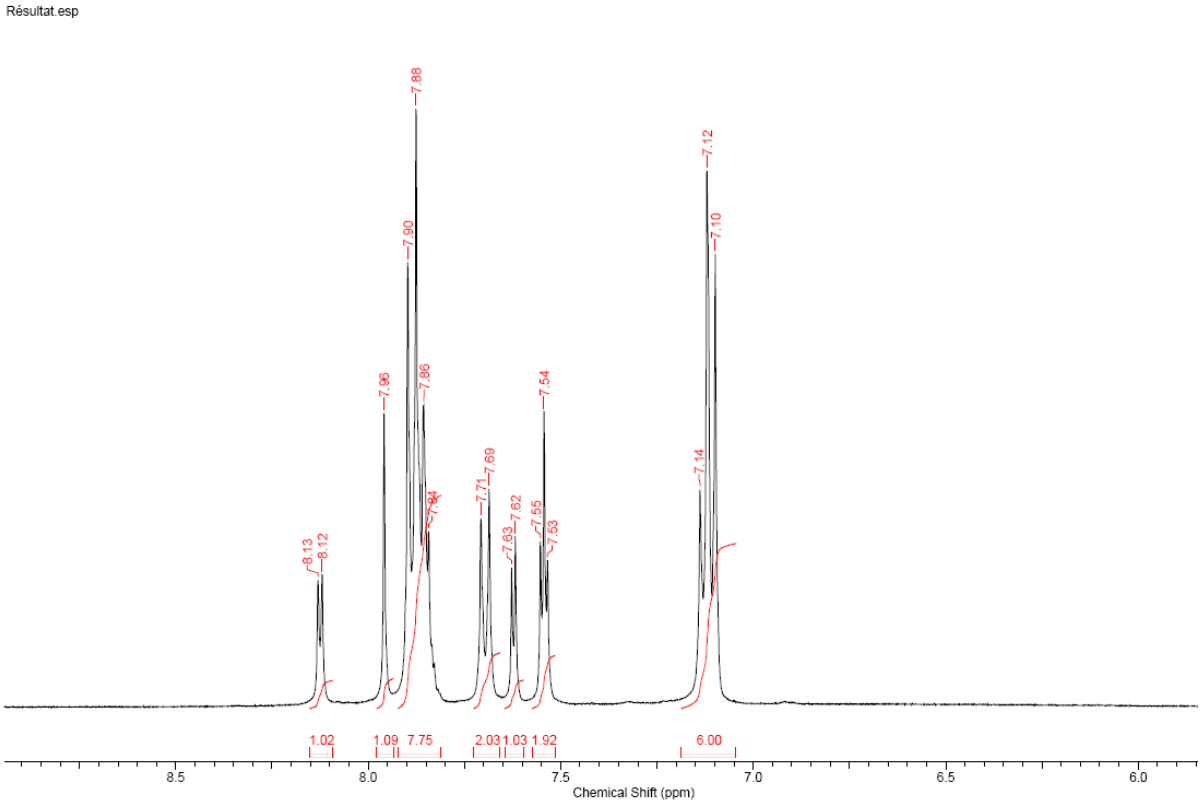
^{1}H NMR (DMSO-d_6,ppm): 8.12 (d, ^{3}J = 4.21 Hz, 1H, $H_{thiophen}$), 7.96 (s, 1H, $H_{ethylene}$), 7.88 (m, 8H), 7.70 (d, ^{3}J = 8.42 Hz, 2H, $H_{aro,TPA}$), 7.61 (d, 1H, ^{3}J = 3.84 Hz, $H_{thiophen}$), 7.54 (d, 1H, 3.84, $H_{thiophen}$), 7.53 (d, ^{3}J = 3.66 Hz, 1H, $H_{thiophen}$), 7.12 (m, 6H, $H_{aro,TPA}$)

^{13}C NMR (DMSO-d^6,ppm): $\mathbf{C_{ketone}}$: 189.32; $\mathbf{C_{carbox}}$: 168.80; $\mathbf{C_{aro}}$: 150.0, 148.9, 145.8, 144.9, 135.4, 134.5, 131.1, 127.1, 126.0, 125.4, 122.9.

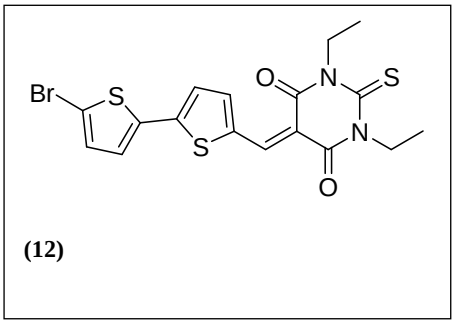
ESI-MS, (m/z): calculated for $[M]^+$: 653, found for $[M+H]^+$: 652

(11)- ^{1}H $CDCl_3$


Résultat.esp
DMSO
7.88
7.90
7.12
7.10
7.96
7.86
7.54
7.69
7.14
7.84
7.53
8.13
8.12
1.02 1.09 7.75 2.03 1.03 1.92 6.00
Chemical Shift (ppm)


Résultat.esp
7.88
7.90
7.12
7.10
7.96
7.86
7.54
7.69
7.14
7.71
7.84
7.62
7.83
7.55
7.53
8.13
8.12
1.02 1.09 7.75 2.03 1.03 1.92 6.00
Chemical Shift (ppm)

(12) -



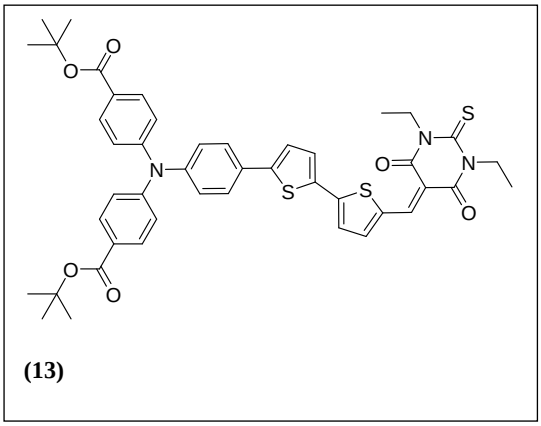
(12)

This synthesis was performed by Praveen Chandrasekar (CINAM, J.M. Raimundo). A similar procedure as for **(09)** was used. A brown solid was obtained (12% yield).

M.W. (g.mol^{-1}): 455

^{1}H NMR (250 MHz, DMSO-d_6): 8.67 (s, 1H), 8.29 (d, ^{3}J = 4.0 Hz, 1H, $H_{thiophen}$), 7.70 (d, ^{3}J = 4.0 Hz, 1H, $H_{thiophen}$), 7.62 (d, ^{3}J = 4.0 Hz, 1H, $H_{thiophen}$), 7.39 (d, ^{3}J = 4.2 Hz, 1H, $H_{thiophen}$), 4.46 (q, ^{3}J = 6.7 Hz, 4H, CH_2), 1.22 (t, ^{3}J = 7.0 Hz, 6H, CH_3).

(13)



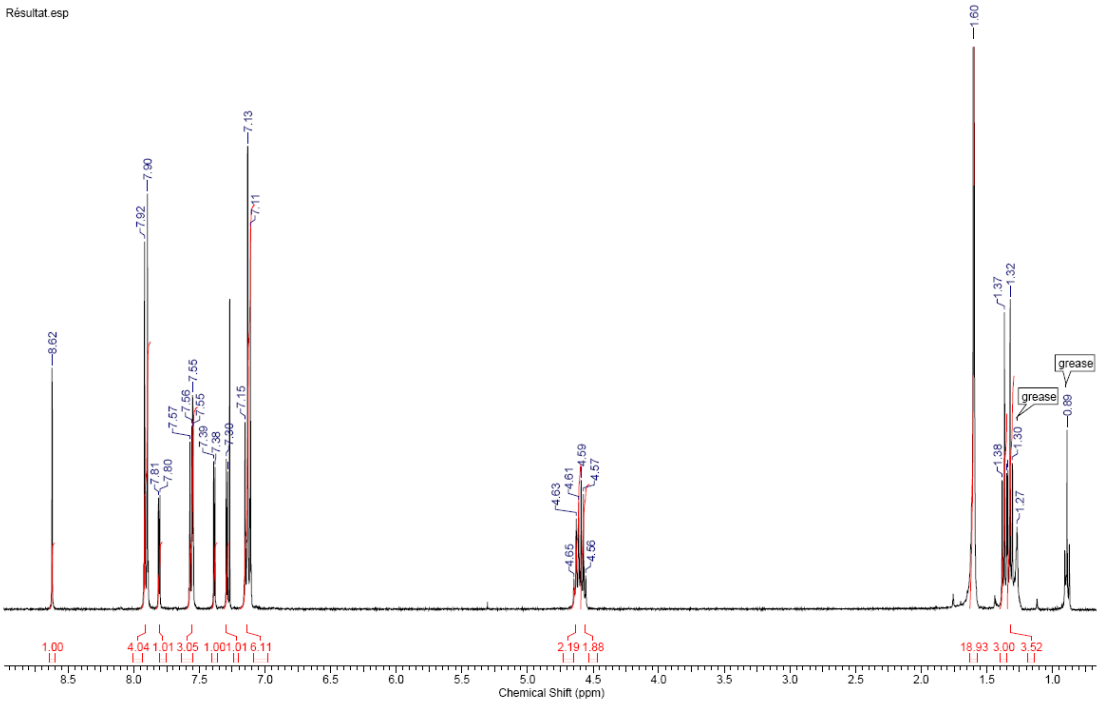
(13)

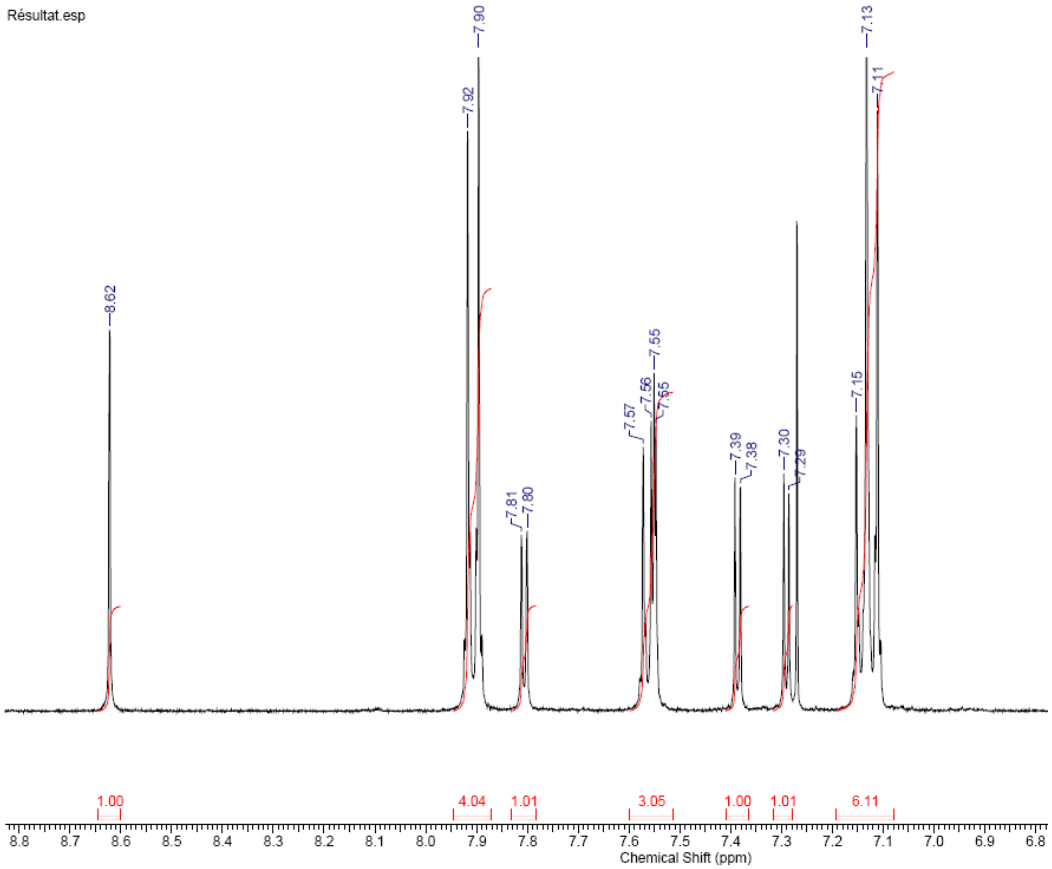
In a 10 mL three necked flask, (**12)** (76 mg, 0.17 mmol, 1.00 eq.), triphenylamine **(03)** (107 mg, 0.19 mmol, 1.12 eq.), $Pd(dba)_2$ (5 mg, 0.009 mmol, 0.05 eq.), $[HP(^tBu)_3][BF4]$ (3 mg, 0.010 mol, 0.06 eq.) and K_3PO_4 (115 mg, 0.55 mmol, 3.24 eq., previously grinded) were introduced, the set-up was degassed with nitrogen. Then, 7 mL of previously degassed with argon {THF/H_2O, 1/0.1} were introduced. The flask was heated and stirred in a microwave hoven. The following parameters were employed: 5 min at 150 W, from room temperature to 49°C; 55 min at 100W at 49°C. From red, the color of the mixture rapidly turned to fuchsia. After solvent removal under reduce pressure, dichloromethane was added and the mixture was washed three times with water. The combined organic phases were dried over $MgSO_4$. The obtained powder was purified over a silica-gel chromatography column (initial eluent: cyclohexane/dichloromethane: 0.55/0.45, a gradient of eluent was then applied to reach 100% dichloromethane). The purest fraction was recrystallized from hexane to give a highly pure dark purple solid (21 mg, 15% yield).

M.W. ($g.mol^{-1}$): 820

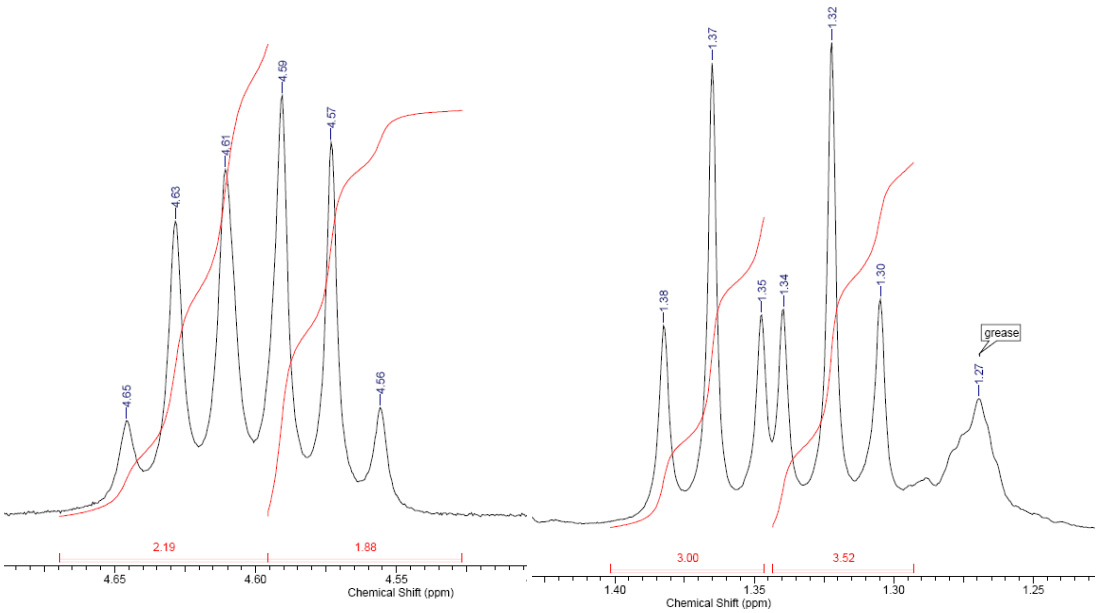
^{1}H NMR ($CDCl_3$, ppm): 8.62 (s, 1H, $H_{ethylene}$), 7.91 (s, 3J=8.76 Hz, 4H, $H_{aro,triphenylamine\text{-}COOtBu)}$, 7.80 (d, ^{3}J = 4.39 Hz, 1H, $H_{thiophen}$), 7.57 to 7.55 (m, 3H, 1$H_{thiophen}$ and 2$H_{aro,Triphenylamine}$), 7.38 (d, ^{3}J = 4.21Hz, 1H, $H_{thiophen}$), 7.29 (d, 3J = 4.03 Hz, 1H, $H_{thiophen}$), 7.13 (m, 6H, $H_{triphenylamine}$), 4.61 (qd, ^{3}J= 6.95 Hz, 2H, $H_{CH2\text{-}thiobarbituric}$), 4.59 (qd, ^{3}J= 6.95 Hz, 2H, $H_{CH2\text{-}thiobarbituric}$), 1.60 (s, 18H, $CH_{3tert\text{-}butyl}$), 1.37 (t, ^{3}J=6.95 Hz, 3H, $H_{CH3\text{-}thiobarbituric}$), 1.32 (t, ^{3}J=6.95 Hz, 3H, $H_{CH3\text{-}thiobarbituric}$).

(13)- ^{1}H $CDCl_3$

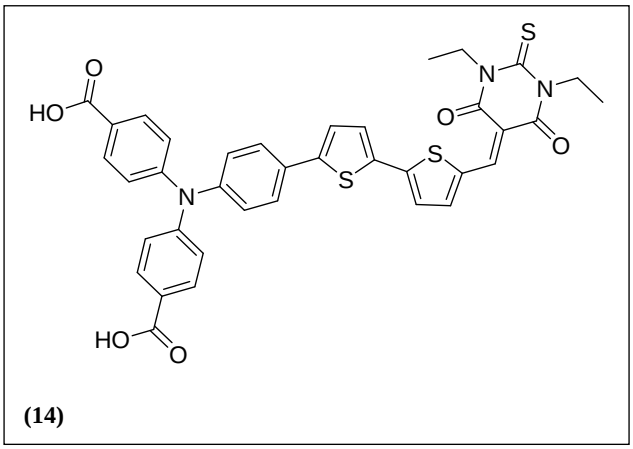

Résultat.esp
8.62
7.92
7.90
7.81
7.80
7.57
7.56
7.55
7.55
7.39
7.38
7.30
7.15
7.13
7.11
4.63
4.61
4.59
4.57
4.65
4.56
1.60
1.37
1.32
1.38
1.30
1.27
grease
grease
0.89
1.00
4.04
1.01
3.05
1.00
1.01
6.11
2.19
1.88
18.93
3.00
3.52
Chemical Shift (ppm)


Résultat.esp
8.62
7.92
7.90
7.81
7.80
7.57
7.56
7.55
7.55
7.39
7.38
7.30
7.29
7.15
7.13
7.11
1.00
4.04
1.01
3.05
1.00
1.01
6.11
Chemical Shift (ppm)

(13)- ^{1}H $CDCl_3$


4.65
4.63
4.61
4.59
4.57
4.56
2.19
1.88
4.65
4.60
4.55
Chemical Shift (ppm)
1.38
1.37
1.35
1.34
1.32
1.30
1.27
grease
3.00
3.52
1.40
1.35
1.30
1.25
Chemical Shift (ppm)

(14)



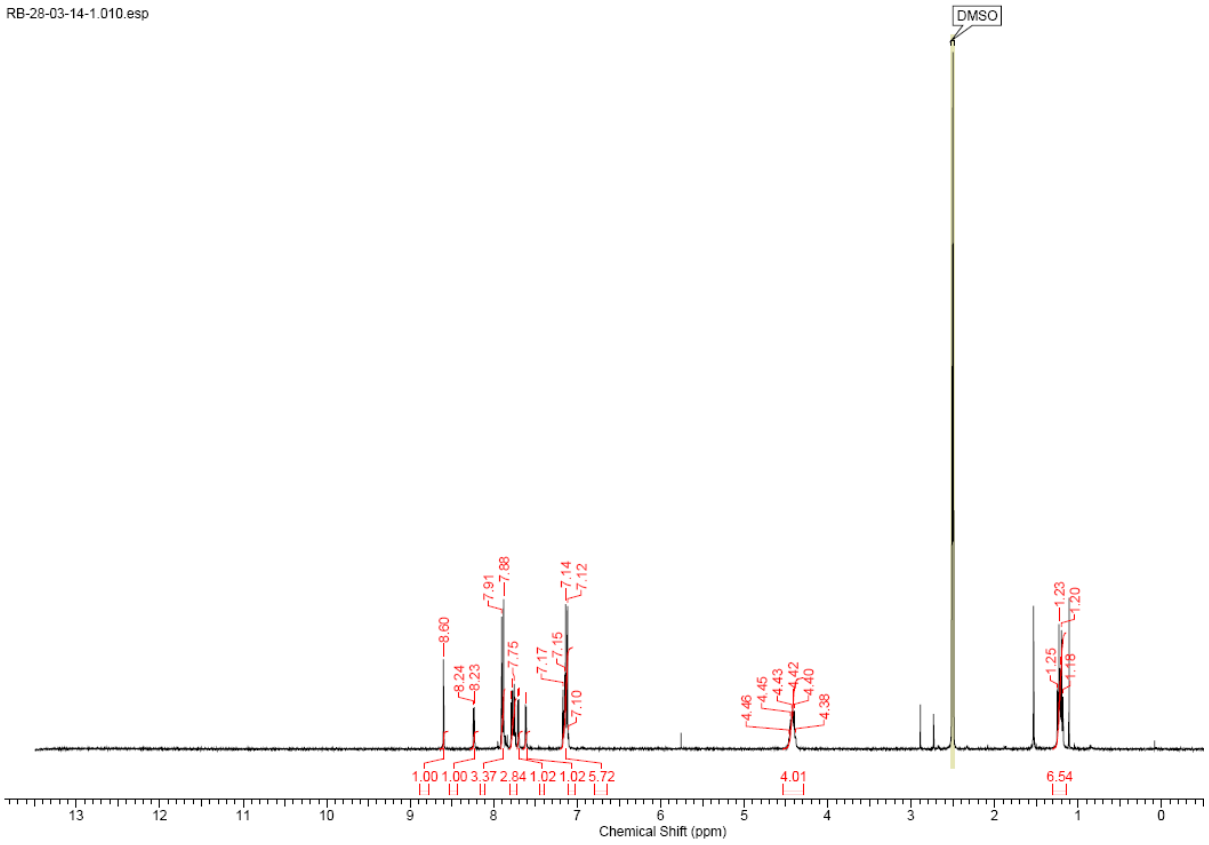
(14)

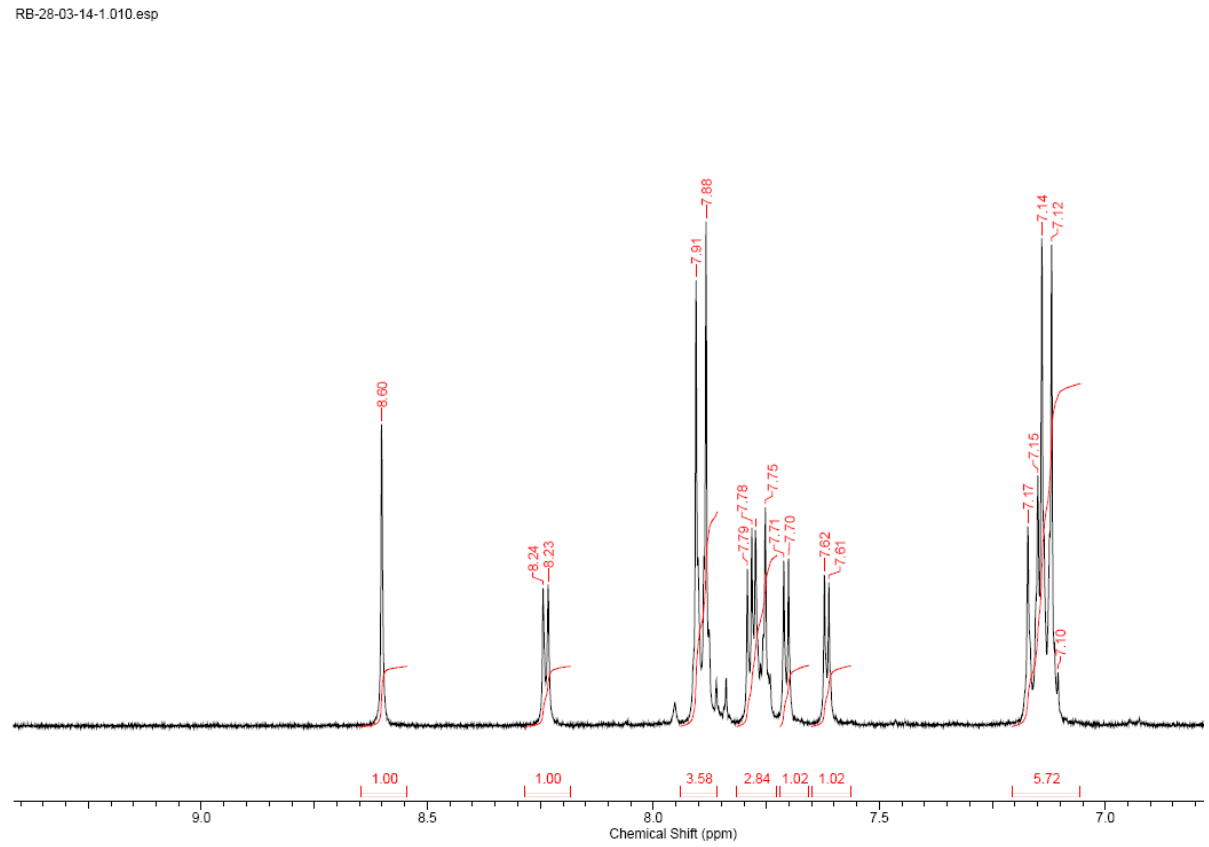
In a vial, **(13)** (33 mg, 0.04 mmol, 1.00 eq.) was dissolved with 1 mL of dichloromethane. Then TFA (230 mg, 2.0 mmol, 50 eq.) was added in the dark. After 18 hours of stirring, dichloromethane was added and solvents were removed under reduced pressure and drying with high vacuum was operated. The obtained solid was washed with hot cyclohexane. Eventually, **(14)** was obtained as a dark powder (27 mg, 0.038 mmol, 95% yield).

M.W. ($g.mol^{-1}$): 707

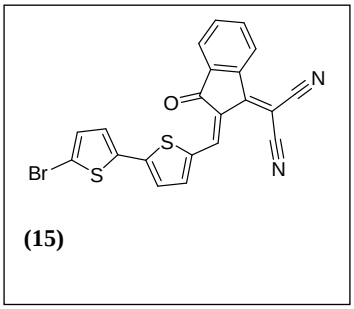
^{1}H NMR (DMSO-d_6, ppm): 8.60 (s, 1H, $H_{ethylene}$), 8.23 (d, ^3J = 4.57 Hz, 1H, $H_{thiophen}$),7.90 (d, ^3J = 8.78 Hz, 4H, $H_{aro,triphenylamine-COOtBu)}$, , 7.78 (m, 3H, $1H_{thiophen}$ and $2H_{aro,triphenylamine}$), 7.70 (d, ^3J = 4.21Hz, 1H, $H_{thiophen}$), 7.61 (d, ^3J = 4.03 Hz, 1H, $H_{thiophen}$), 7.14 (m, 6H, $H_{triphenylamine}$), 4.42 (m, 4H, $H_{CH2\text{-}thiobarbituric}$), 1.23 (t, ^3J=6.95 Hz, 3H, $H_{CH3\text{-}thiobarbituric}$), 1.20 (t, ^{3}J=7.14 Hz, 3H, $H_{CH3\text{-}thiobarbituric}$).

(14)- ^{1}H DMSO-d_6


RB-28-03-14-1.010.esp
DMSO
8.60
8.24
8.23
7.91
7.88
7.75
7.17
7.16
7.14
7.12
7.10
4.46
4.45
4.43
4.42
4.40
4.38
1.23
1.20
1.25
1.18
1.00 1.00 3.37 2.84 1.02 1.02 5.72
4.01
6.54
Chemical Shift (ppm)


RB-28-03-14-1.010.esp
8.60
8.24
8.23
7.91
7.88
7.79
7.78
7.75
7.71
7.70
7.62
7.61
7.17
7.15
7.14
7.12
7.10
1.00
1.00
3.58
2.84
1.02
1.02
5.72
Chemical Shift (ppm)

(15)



(15)

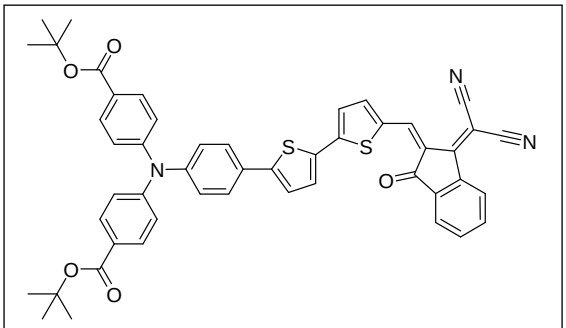
This synthesis was performed by Praveen Chandrasekar (CINAM, J.M. Raimundo). A similar procedure as for **(09)** was used. A greenish blue solid was obtained (70% yield).

M.W. (g.mol^{-1}): 448

^{1}H NMR (250 MHz, DMSO-$d_{6,}$ ppm): 8.82 (s, 1H), 8.66 (d, ^{3}J = 8.2 Hz, 1H), 8.06-8.11 (m, 4H), 7.77 (d, ^{3}J = 4.5 Hz, 1H, $H_{thiophen}$), 7.71 (d, ^{3}J = 4.2 Hz, 1H, $H_{thiophen}$), 7.51 (d, ^{3}J = 4.0 Hz, 1H, $H_{thiophen}$).

ESI-MS (m/z): $[M]^{+}$ calculated: 448, $[M+H]^{+}$ found 449.

(16)



(16)

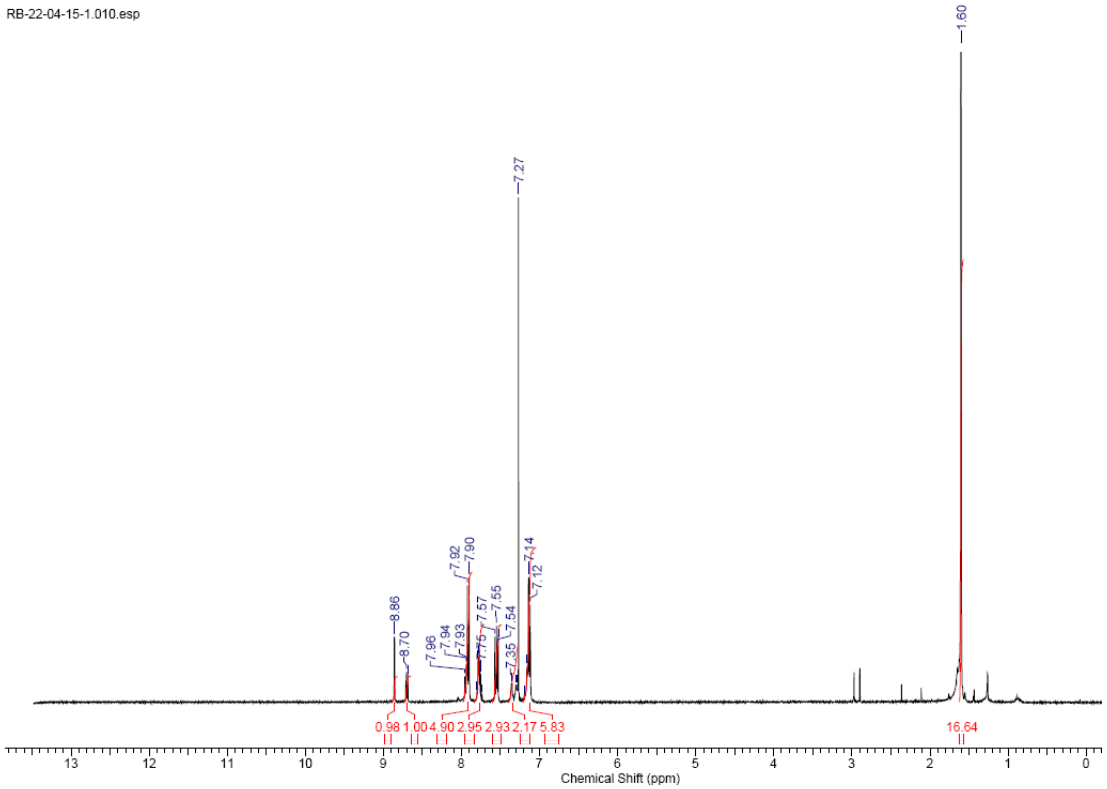
In a 10 mL three necked flask, **(15)** (31 mg, 0.06 mmol, 1.00 eq.), triphenylamine **(03)** (40 mg, 0.07 mmol, 1.16 eq.), $Pd(dba)_2$ (3 mg, 0.005 mmol, 0.04 eq.), $[HP(^tBu)_3][BF_4]$ (1 mg, 0.003 mol, 0.05 eq.) and K_3PO_4 (40 mg, 0.19 mmol, 3.17 eq., previously grinded) were introduced. The set-up was degassed with nitrogen. Then, 3 mL of a previously argon degassed {THF/H_2O, 1/0.1} solvent mixture were introduced. The flask was heated and stirred in a microwave hoven. The following parameters were employed: 5 min at 150 W, from room temperature to 49°C; 55 min at 100W at 49°C. Initially wine, the mixture was dark blue at the end of the reaction. After solvent removal under reduce pressure, dichloromethane was added and the mixture was washed three times with brine. The combined organic phases were dried over $MgSO_4$ and filtered on a short celite pad. After solvent removal, the blue powder was washed with large amounts of hot cyclohexane. A careful recrystallization from toluene (cyclohexane could be used to recuperate the remaining product in the flask) enabled the getting of a pure crystalline dark green powder (35 mg, 71% yield).

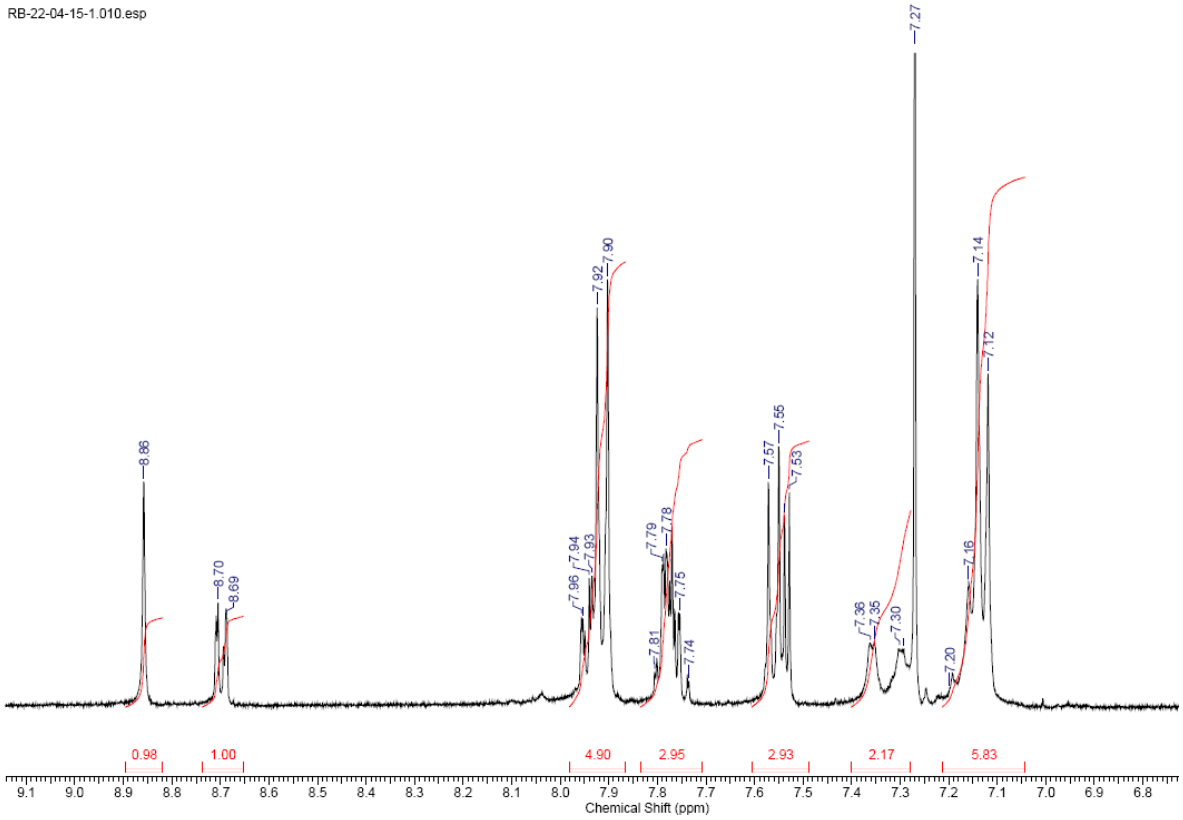
M.W. ($g.mol^{-1}$): 814

F.P.: 179 °C

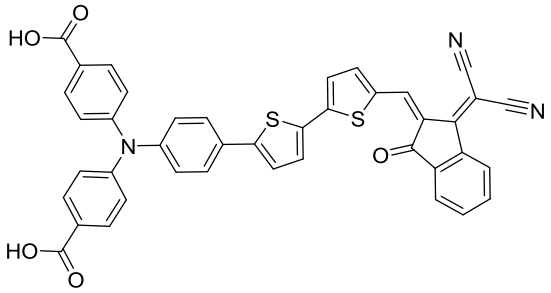
^{1}H NMR ($CDCl_3$, ppm): 8.86 (s, 1H, $H_{ethylene}$), 8.70 (d, ^3J = 6.95 Hz, 1H, $H_{aro,indane}$), 7.95 (d, ^3J = 7.87 Hz, 1H, $H_{aro,indane}$), 7.91 (d, ^3J = 8.78 Hz, 4H, $H_{aro,triphenylamine\text{-}COOtBu}$), 7.81 to 7.74 (m, 3H), 7.56 (d, ^3J = 8.60 Hz, 2H, $H_{aro,triphenylamine}$), 7.53 (d, ^3J = 3.84 Hz, 1H, $H_{thiophen}$), 7.36 (d, ^3J = 4.03 Hz, 1H, $H_{thiophen}$), 7.30 (d, ^3J = 4.03 Hz, 1H, $H_{thiophen}$), 7.14 (m, 6H, $H_{aro,triphenylamine}$), 1.60 (s, 18H, CH_3)

(16)- ^{1}H $CDCl_3$


RB-22-04-15-1.010.esp
1.60
7.27
7.92
7.90
7.14
7.12
8.86
8.70
7.96
7.94
7.93
7.75
7.57
7.55
7.54
7.35
0.98 1.00 4.90 2.95 2.93 2.17 5.83
16.64
Chemical Shift (ppm)


RB-22-04-15-1.010.esp
7.27
7.92
7.90
7.14
7.12
8.86
7.57
7.55
7.53
8.70
8.69
7.96
7.94
7.93
7.79
7.78
7.81
7.74
7.36
7.35
7.30
7.20
7.16
0.98 1.00 4.90 2.95 2.93 2.17 5.83
Chemical Shift (ppm)

(17)



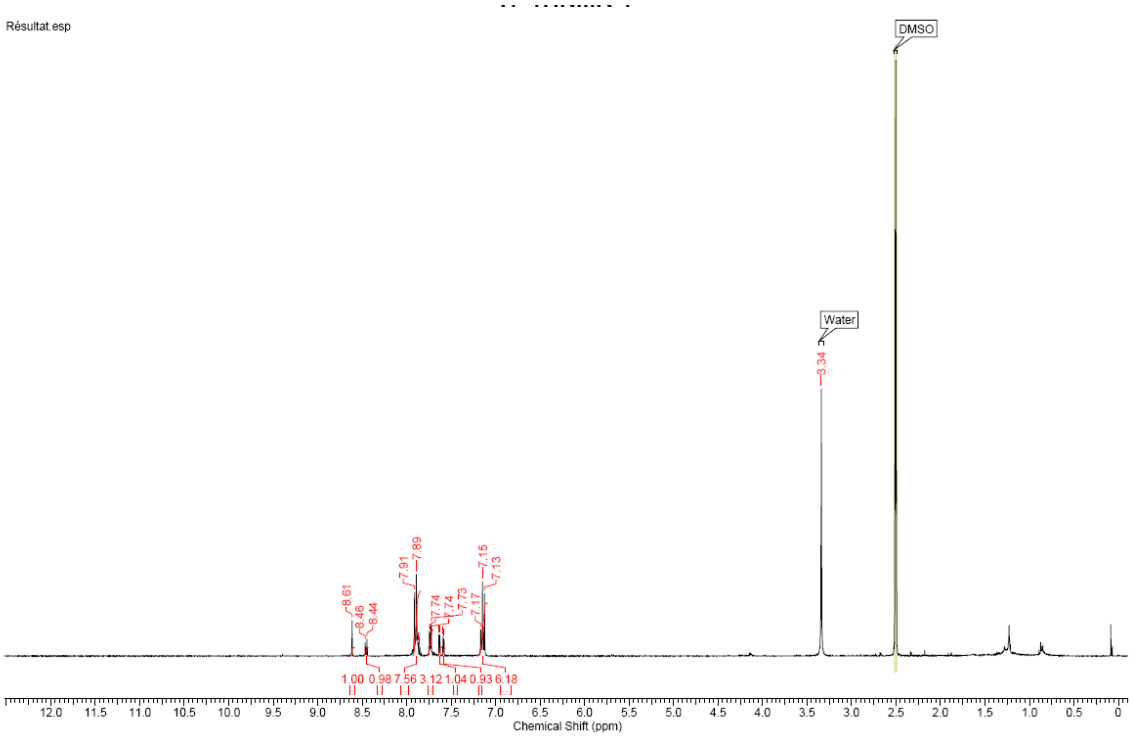
(17)

In a vial, **(16)** (37 mg, 0.045 mmol, 1.00 eq.) was dissolved in 1 mL of dichloromethane. Then, TFA (242 mg, 2.12 mmol, 42.0 eq.) was added in the dark and the mixture was stirred overnight. Dichloromethane helped rinsing the vial and after solvent removal and drying. **(17)** was obtained after recristalisation from dichloromethane, as a pure black, with blue reflects, powder (31 mg, 0.044 mmol, 98% yield).

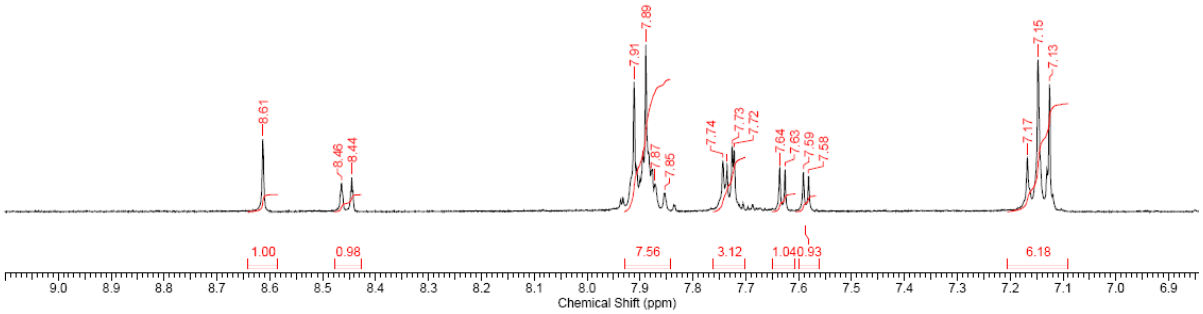
M.W. (g.mol^{-1}): 702

^{1}H NMR (DMSO-d$_6$, ppm): 8.61 (s, 1H, H$_{ethylene}$), 8.70 (d, ^{3}J = 6.68 Hz, 1H, H$_{aro,indane}$), 7.85 to 7.91 (m, 8H), 7.73 (m, 3H), 7.63 (d, ^{3}J = 4.03 Hz, 1H, H$_{thiophen}$), 7.58 (d, ^{3}J = 3.84 Hz, 1H, H$_{thiophen}$), 7.15 (m, 6H, H$_{aro,triphenylamine}$).

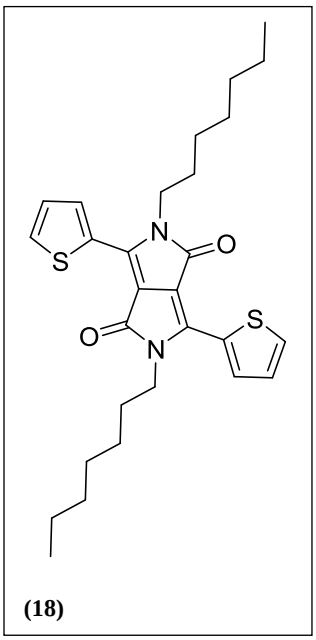
(17)- ^{1}H DMSO-d$_6$



(17)- ^{1}H DMSO-d_6



2,5-diheptyl-3,6-di(thiophen-2-yl)-2,5-dihydropyrrolo[3,4-c]pyrrole-1,4-dione- (20)



(18)

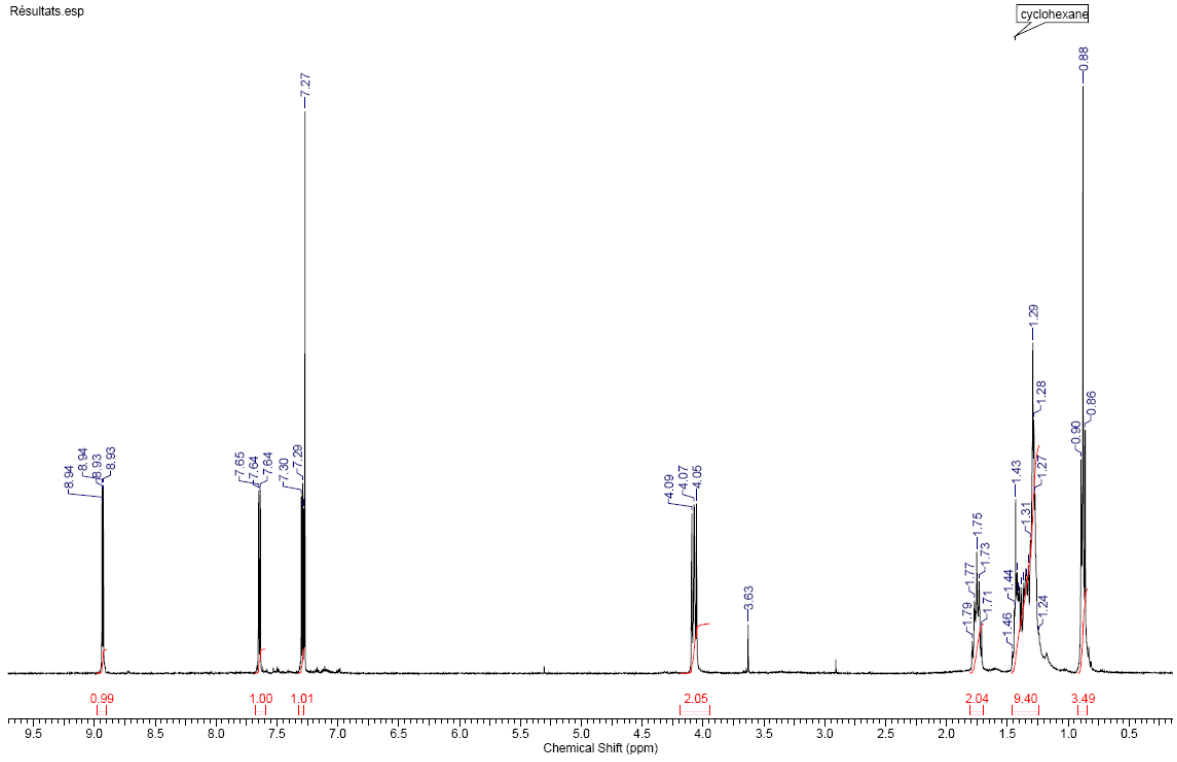
This reaction was carried out inert. In a 100 mL three necked flask topped with a refrigerant, 2,5-Dihydro-3,6-di-2-thienyl-pyrrolo[3,4-c]pyrrole-1,4-dione (Aldrich, 1.00 g, 3.33 mmol, 1.00 eq.), 1-iodohexane (4.33 g, 19.16 mmol, 5.75 eq.) and K_2CO_3 (1.84 g, 13.33 mmol, 4.00 eq.) were introduced. Then, 16 mL of dry DMF were added. The flask was placed out of the glove box, and was finally heated and stirred at 130°C during 60 hours, under argon. Dichloromethane was added to this purple thick and dark mixture and solvents were carefully removed under reduced pressure. The obtained solid was resolubilized into dichloromethane and washed three times with brine. The combined organic phases were dried over $MgSO_4$. After solvent removal, the product was purified over a silica gel chromatography column (eluent: {cyclohexane/dichloromethane: 1/1}). A first yellow fraction was not collected, the second one sharply pink but not very fluorescent was not analyzed. The desired fraction was the third one.

This fraction was orange and strongly fluorescent at ambient light. After solvent removal and drying, a pure wine color powder was obtained (420 mg, 25% yield).

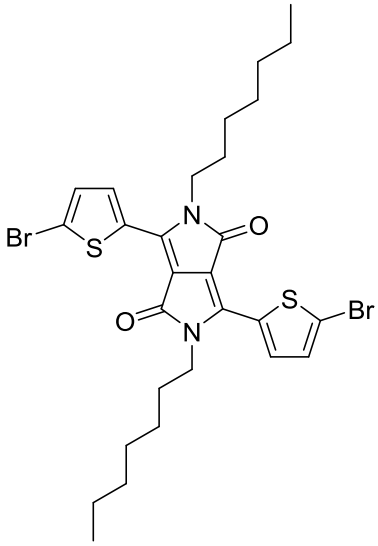
M.W. (g.mol^{-1}): 497

F.P.: 143-146 °C

^{1}H NMR ($CDCl_3$, ppm): 8.93 (dd, ^{4}J = 0.91 Hz, ^{3}J = 3.97 Hz, 1H, $H_{thiophen,\beta}$), 7.64 (dd, ^{4}J = 0.91 Hz, ^{3}J = 5.12 Hz, 1H, $H_{thiophen,\delta}$), 7.29 (dd, $^{3}J_1$ = 3.84 Hz, $^{3}J_2$ = 4.21 Hz, 1H, $H_{thiophen,\gamma}$), 4.07 (t, 2H, ^{3}J = 7.90 Hz, $CH_{2,\alpha}$), 1.75 (qt, 2H, $CH_{2,\beta}$), 1.46 to 1.24 (m, 8H, $CH_{2,\gamma\ to\ \zeta}$), 0.88 (t, 3H, ^{3}J = 6.85 Hz, CH_3).



3,6-bis(5-bromothiophen-2-yl)-2,5-diheptyl-2,5-dihydropyrrolo[3,4-c]pyrrole-1,4-dione- (21)



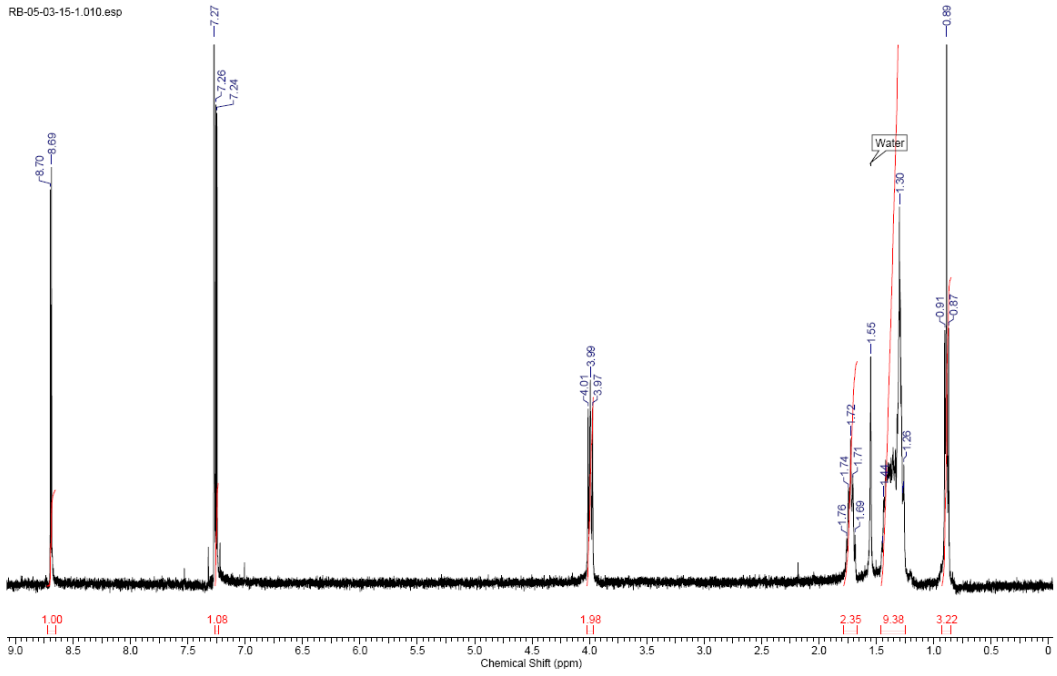
(19)

In a 100 mL three necked flask, **(14)** (381 mg, 0.77 mmol, 1.00 eq.) and 31 mL of chloroform were introduced. The mixture was degassed with argon during 4 hours. Then, NBS (283 mg, 1.59 mmol, 2.06 eq.) was rapidly introduced in the dark and at 0°C. After 18 hours, 20 ml of degassed methanol was added to the reaction, in the dark. Then, this mixture was plunged into 400 mL of MeOH and stirred during 30 minutes. After filtration, a purple precipitate was obtained (the filtrate was yellow). Hence, the solid was first washed with hot water and finally with hot methanol. After drying under vacuum, a highly pure blue purple solid was obtained (260 mg, 56% yield).

M.W. (g.mol^{-1}): 655

F.P.: 208°C

^{1}H NMR ($CDCl_3$, ppm): 8.69 (d, ^{3}J = 4.21 Hz, 1H, $H_{thiophen,\beta}$), 7.25 (d, ^{3}J = 4.39 Hz, 1H, $H_{thiophen,\gamma}$), 3.99 (t, 2H, ^{3}J = 8.05 Hz, $CH_{2,\alpha}$), 1.72 (qt, ^{3}J = 8.60 Hz, 2H, $CH_{2,\beta}$), 1.45 to 1.26 (m, 8H, $CH_{2,\gamma\ to\ \zeta}$), 0.89 (t, 3H, ^{3}J = 6.90 Hz, CH_3).



II. Physical properties (chapter 2, part 2)

II.A. Generalities

All chemicals in this part were purchased from Aldrich and used without additional purification in this part. Electrochemical measurements were carried out in a three electrodes set-up, with a Biologic VSP potentiostat. Steady-state absorption and emission spectra were recorded with a double-beam UV-visible spectrophotometer (Perkin Elmer lambda 900) and a spectrofluorimeter (SPEX Fluorolog 3, Horiba Jobin Yvon) in 1 cm optical path quartz cells. The solvent used were spectrometric grade in this later case.

II.B. Electrochemistry

The redox potentials of interest were determined in organic solvents (DCM or dry DMF) with $TBAPF_6$ as the support salt (10^{-1}M). Cyclic-voltammetry technique was employed, with a scan rate of 100 $V.s^{-1}$. A platinum wire was used in lieu of the working electrode and carbon graphite was the counter electrode. The reference electrode used was $AgNO_3$/Ag in DMF. Measurements were performed under nitrogen.

For every measurement session, the redox potential of the $\{Fc^+/Fc\}$ reference couple was also measured[bb]. This allowed the accurate conversion on the experimental potentials against NHE reference electrode [6,7] (see Tab. 23 and Fig. 113). Indeed, for clarity, all the potentials presented in this work are versus NHE.

[bb] A diluted solution of ferrocene in the supporting electrolyte was prepared for this purpose. The potential of the Fc^+/Fc couple was then measured.

Solvent	$E(Fc^+/Fc)^{solvent}$ *vs* SCE	$E(Fc^+/Fc)^{solvent}$ *vs* NHE
DMF	0.45	0.69
DCM	0.46	0.70
ACN	0.40	0.64

Tab. 23- Fc^+/Fc redox potentials in the organic solvents used in this work. The potentials versus SCE were taken from ref [6] and converted to NHE by the addition of 0.24 V [7].

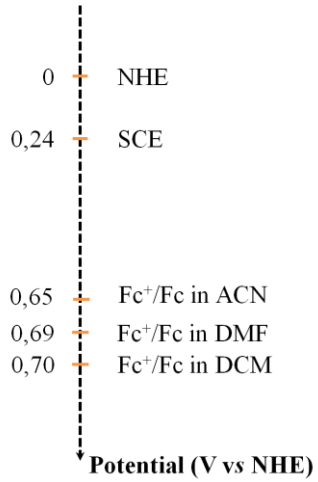


Fig. 113- Axis summarizing the redox potentials of the redox references used in this work

For redox potential determination, when the redox process was reversible, the redox potential was calculated from the average of the reduction and oxidation peak. On the other hand, when irreversible, it was always estimated from the peak potential.

II.C. UV-Visible spectra in solution

The studies were performed in DCM or dry DMF. The absorption spectra were corrected from the solvent contribution by subtraction of the pure solvent signal (blank experiment).

The fluorescence spectra were first corrected by subtraction of the pure solvent contribution. Then, they were also corrected for the wavelength-dependent response of the instrument (use of an adapted correction curve). Sometimes, fluorescence happened in an absorption band. As a consequence, in that case, re-absorption process was additionally corrected.

The molar extinction coefficients of the final dyes under their *tert*-butyl protected version were precisely measured by weighting the product with an error below 5%. Then, solutions were prepared using only one adapted volumetric flask and the absorption spectrum was acquired.

The “zero-zero” transition energies, for the low energy charge transfer band, was estimated from the intercept of the normalized absorption spectrum and the normalized fluorescence spectrum for dye **(10)**, **(13)** and **(16)**. For **(7)** it was estimated from the 10% maximum amplitude of the

normalized absorbance signal. Indeed in all casee, the normalization was performed regarding the lowest energy absorption band.

II.D. DFT/TDDFT calculations

Quantum chemical studies were carried out by using the Gaussian 3 package. DFT calculations were done so as to optimize the geometry of the compounds and to calculate the energies of their molecular orbitals. B3LYP was used as the hybrid functional and the 6-31G (d) basis set was employed. To ensure a true energy minimum was reached, the vibration frequencies were calculated and it was ensured there was no imaginary frequency. The molecular orbitals were also allowed to be plotted, with an isodensity value of 0.02 a.u. Finally, TDDFT permitted to calculate the 7 first vertical transitions energy. All the calculations were performed in vacuum.

III. DSSC fabrication through IJP. Solar cell tests. (chapter 3 and chapter 4)

III.A. Generalities

All the reagents were purchased from Aldrich or VWR (ethanol, 96%) and used without further purification. The water used was always deionized water (R = 12 Ω). The glass / FTO substrates were purchased from Solaronix (e_{FTO} = 330 nm, ρ = 32 Ω.cm^{-1}). For printing a Dimatix DMP 2800 was employed. 10pL-16 nozzle cartridges were used. The muffle-hoven that was used was Thermolyne 48 000 furnace. The predrilled FTO Pt electrode wer purchased from Solaronix, ref = test cell platinum electrode 74201. Meltonix 1170-60 (Solaronix) was used as the sealer for DSSC preparation (the space between the two electrodes was 60µm). MBR electronics USS-9210 Ultrasonic Soldering System, was used for making the electrical contacts of the final DSSC with Cerasolzer alloy. The current-voltage characteristics of p-type DSSCs were measured with a Keithley 2635 system Source Meter under 1 Sun (AM 1.5 standard)

III.B. DSSC fabrication

III.B.1. Cleaning the FTO substrates

The substrates were placed into an appropriate 20 slides glass support that was itself placed into a glass container for washing. Then, a succession of various cleaning media was used: {permuted water / DECON}, permuted water, ethanol, acetone and finally isopropanol. The cleaning process was always the following: the substrates were sonicated in the desired cleaning medium at maximum power, at 60° for 10 minutes. After that, the cleaning mixture was removed from the container. Then, the whole system was rinsed, three times with deionized boiling water, and three

times with the next cleaning mixture. The substrates were stored into isopropanol prior to a further use.

III.B.2. Preparing the NiO_x precursor solution

In the case of NiO_x deposition on FTO, prior to printing, the following experimental conditions were used. In the case of a FTO substrate, go directly to paragraph 6. The NiO_x precursor solution was prepared in a similar trend as described in the literature [8]. Nickel acetate (1.28 g, 5 mmol, 1.00 eq.), ethanol amine (315 mg, 5 mmol, 1.00 eq.) and ethanol (50 mL) were added, in this order, into a 100 mL round bottom flask. After 4 hours of stirring and refluxing at 70°C, an emerald-green clear solution was obtained. It was stored in the fridge (T = 4°C).

III.B.3. Deposing the NiO_x layer

So as to minimize dust contamination, at maximum 7 of the previously prepared substrates could be used in the same time for the NiO_x thin film deposition. The FTO substrates were plunged into boiling water for 15 sec. Then, they were carefully dried with nitrogen and eventually transferred to the UVO cleaner. UVO treatment lasted 10 minutes. Then, one substrate was taken out of the UVO cleaner and residual dusts were removed thanks to a nitrogen flux. The other substrates were kept inside the UVO cleaner so as to prevent pollution. The NiO_x precursor solution was spin-coated at 4000 rpm for 90 seconds (a 450µm PTFE filter was employed). The substrate was then rapidly transferred to a heat platen and was dried at 110°C for 10 minutes. FTO contacts were cleaned with ethanol during this process. The resulting thin film was visibly homogenous. It is worth mentionning that substrates were again protected from dust during the drying process. Once deposition of the NiO_x layer had been achieved for all the substrates, they were transferred to the pre-heated hoven and sintered at air, at 450°C, for 30 minutes. Hence, they were allowed to cool at room temperature, after that, they were stored in a clean place (protection from the dusts).

III.B.4. Preparation of the $NiCl_2$ diluted ink for printing

F_{127} (1g) was mixed with permuted water (2.19 g) and ethanol (4.85 g). When the polymer was totally dissolved, $NiCl_2$,$6H_2O$ (1.83 g) was added to the mixture. A green solution was obtained

(we called it **Ink-0**). This solution was dissolved into one massic equivalent of water and aged at least 20 hours at room temperature in a sealed glass bottle, before being used. **Ink-1** was thus obtained.

III.B.5. Preparation of the printer

A 200µm filter (PTFE) was employed to remove debris from **Ink-1** and to minimize the risks of nozzle clogging. The cartridge was placed into the print-carriage and the films were printed 30 min after, so as to ensure bubbles were not present into the injection chamber. During this period, "purge 0.3sec" cleaning cycles were performed every 300 sec, so as to avoid gelation of the ink inside the print head and thus clogging. The temperature of the print-head was comprised between 21°C and 23°C. Also, a 100µm sheet of paper was placed on the printer platen, so as to protect it during printing.

III.B.6. Preparation of the substrates

➔**FTO substrates**: after being (one by one) placed into boiling water for 15 seconds, the substrates were carefully dried with nitrogen. They were submitted to UVO treatment during 5 minutes just before printing.

➔**NiO_X substrates**: after being additionally sintered at 450°C for 15 minutes, cooled to room temperature, flushed with nitrogen, substrates were submitted to UVO during 5 minutes. The color of the thin film slightly changed: a light black coloration could be distinguished, suggesting NiO_x oxidation (see chapter 1).

Then for both type of substrates the same procedure was applied. Printing was performed rapidly after the UVO treatment was completed. Typically, a printing session could be performed for three substrates. One substrate (FTO or NiO_x) was taken out of the UVO cleaner, flushed with nitrogen and finally introduced into the printer. The others were kept in the UVO cleaner, waiting to be used.

Prior to printing, the substrate was thermalized at the platen temperature (30°C), it took the time of the last cleaning operations of the print-head (one minute approximately), *vide supra.*

III.B.7. **Mesoporous NiO Film deposition**

The following cleaning steps were performed before each film deposition. First of all, one "purge-spit-purge" cleaning cycle was performed. Then, the cartridge head was wiped with ethanol soaked kimswift paper. It was important to make sure the cleaning pad was not dirty.

The printing parameters were the following, for the deposition of one layer of the sol-gel ink.

- Dimatix model fluid waveform
- Maximum jetting frequency: 3 kHz
- Voltage applied to the piezo electric during printing: 25 V
- Resolution: 20µm (saber angle was set at 4.5°)
- Platen temperature was set at 30°C
- Nozzle to substrate distance: 650 µm
- Substrate thickness taken into account: 3300 µm (FTO thickness was 3200 µm, additionally, the 100µm sheet of paper was taken into account).
- One spit cleaning cycle was automatically performed before the layer deposition (the spitting frequency was 3kHz)
- Print-head temperature was comprised between 21°C and 23°C (it could not be precisely controlled)
- Relative humidity was comprised between 35% and 45%.

Once printed, the film was allowed to gellify one minute on the platen, at 30°C.

➔For the one-layer mesoporous NiO substrates (**NiO-1L**), the following procedure was used:

The substrate was transferred to a heat plate (100°C) and dried during 10 minutes. It was protected from the dusts during this drying session. Directly after, the substrate was sintered 4 min at 450°C, in the pre-heated hoven. The additional 26 min sintering were performed just before the sensitization step (see III.B.8). This last sintering step was performed in the same time for all the substrates of the session.

➔For the four-layer NiO substrates (**NiO-4L**), the following procedure was used:

The substrate was transferred to a heat plate (100°C) and dried during 3 minutes. It was protected from the dusts during this drying session. Directly after, the substrate was sintered 4 min at

450°C, in the pre-heated hoven. After cooling to RT, one layer of NiO was additionally printed, exactly in the same conditions as for the previous layer (though no UVO treatment was performed prior to printing). The whole operation was repeated until the 4 layers of NiO were deposited. Like for the **NiO-1L** substrate, the last sintering session was performed during 4 min. The additional 26 min sintering were performed just before the sensitization step (see III.B.8). This last sintering step was performed in the same time for all the **NiO-4L** substrates of the session.

III.B.8. Sensitization of the photocathode

III.B.8.a. Sensitization solution preparation

The same amount of dye (5.10^{-4} mol per liter of solvent) was used for all the sensitization solutions. All the prepared solutions were visibly saturated. Dye **(8)** and dye **(14)** saturated solutions were prepared in MeOH. Dye **(11)** and dye **(17)** saturated solutions were prepared in a {methanol / dichloromethane, 1/1} solvent mixture. Prior to use, the solutions were sonicated 10 minute at maximum power.

III.B.8.b. Substrate sensitization

After the 26 min sintering step (see III.B.7), the substrates were placed onto a heat plate (60°C), during 8 minutes. After that, they were plunged, still hot, into the sensitization solution (1hour orbital stirring, minimal power, in the dark). The sensitized films were taken out of the bath. A first quick rinsing step with ethanol was performed for all the substrates, so as to put them out of the bath in the same time. Then a second generous rinsing occurs, with ethanol two, followed by drying with nitrogen. The as-built photocathodes were rapidly used for solar cell construction.

III.B.9. Preparation of the Electrolyte

The electrolyte was prepared in a oxygen free glove box. Dry acetonitrile (Aldrich, 50 mL) was poured onto LiI (6.70 g, 50 mmol). Then iodine (1.27 g, 5 mmol) was added and the mixture was stirred till no solid could be distinguished.

III.B.10. Solar cell fabrication

The pre-drill platinum counter electrodes were sintered at 450°C for one hour. After being flushed with nitrogen, the NiO photocathodes and the Pt anodes were sealed together. For this purpose,

Meltonix sealer was placed onto the dyed electrode, Pt electrode was placed upon the sealer and this whole was heated at 110°C on the Pt side first. Pressure was applied, during approximately 30 seconds. Then, during more or less 15 sec, on the NiO side. The good quality of the sealing was a determining parameter for the success of the cell fabrication. Namely, the sealant must have turned perfectly transparent.

In a nitrogen free glove box, the space between the two electrodes was filled with the electrolyte thanks to an appropriate “Vac'n'Fill” syringe (Solaronix). The filling hole was then itself sealed this way: it was carefully cleaned first, then a Meltonix small piece was placed onto the hole, and this all was pressed against a hot (110°C) square of microscope slide, during 10 seconds. The as-fabricated solar cells were kept in the dark as much as possible. Electrical contacts were made using soldering iron. Conductive wires were strongly attached the FTO or Pt glass with Cerasolzer alloy. It was important that the back face of the soldered glass was in contact with a heat conducting surface during this soldering step. Ideally, the wire should hold on the glass upon strong stretching.

III.B.11. **Photovoltaic measurements**

Measurements were performed, in a nitrogen and water free glovebox, under 1 Sun (AM 1.5) or in the dark. The step was 2 mV and the settling time was 250 ms in order to take into account the NiO capacitive effect [9]. Measurements were performed just after the cell was placed under the irradiation zone. Measurement under light was performed first, then, the dark measurement was done. The cell was removed from the light zone as rapidly as possible after measurement under light.

IV. Miscellaneous information

IV.A. Doctor-bladed films Ink-0 morphology

Ink-0 was doctor-bladed onto previously a cleaned glass substrate (microscopic slide VWR), with a glass rod. One layer of magic-tap scotch (3M) were used for the doctor-blading. Thickness and morphology measurements were performed with SEM (MEB HITACHI S4500). Cross-section and top-view images were acquired.

IV.B. Rheological properties

Viscosity measurements were performed on **Ink-0** and **Ink-1** at different shear rates. The viscosity was measured using a MCR 302 rheometer (Anton Paar). The surface tension of the **Ink-1** was determined according the stalagmometric and the pendant drop methods using a contact angle apparatus (Apollo Instruments). The value found was 31.5 mN/m. The contact angle of **Ink-1** onto previously cleaned and UVO (5 min) treated FTO is 17 ± 1 °.

IV.C. NiO film thickness measurements

For **NiO-1L** and **NiO-4L** thickness measurements, the films were formed as decribed above, on FTO glass (see III.B.7). With help of a glass cutter, a line was drawn with on the glass side of the substrate. Then, an adapted "point-plier" was used to cut the substrate. The point was always placed on the FTO side.

IV.D. NiOx thickness measurements

The NiO_x thickness measurement was performed with a Stylus-Diktat apparatus. Care was taken to have a perfect horizontality.

IV.E. NiO sensitized film solid-state absorption measurements

In this study, the apparatus used was. The step was 1 nm.

The signal of a nude the FTO electrode was first acquired. Then, **NiO-1L** and **NiO-4L** substrates absorption were measured bare. After sensitization and drying with the various dye (*vide supra*) the spectrum was acquired. For dye **(8)**, **NiO-1L** and **NiO-4L** sensitized electrodes were analysed. For the other dyes **(11)**, **(14)** and **(17)**, the measurement was performed with **NiO-1L** films.

IV.F. NiO formation mechanism study with IJP film (Ink-1)

The TGA analysis was performed on Ink-1 apparatus was: TGA Q-50 de TA-Instruments (Air steam, 100 mL.min^{-1}). For the XPS analysis. five **NiO-1L** samples were used. For the drying sintering process, the following conditions were applied for all the substrates:

- 1 minute at 30°C
- 10 minutes at 100°C

All together, the 5 **NiO-1L** substrates were placed into a pre-heated at 120°C hoven. The first sample was taken out of the hoven after 10 minutes. The temperature of the hoven was set at 200°C (1°C/min ramp (approximately), to reach the temperature). The sample were sintered at 200°C for 10 min. The second sample was taken out of the hoven. The operation was repeated for the following temperatures: 340°C, 450°C and 500°C. XPS analysis was performed onto these substrates. XPS measurements are acquired using a Kratos Axis Ultra DLD spectrometer with a monochromatic Al Kα excitation (1486.7eV) and a charge compensation system. Photoelectron data are collected at take-off angle of 90° (normal emission). Survey spectra are taken at analyzer pass energy of 160 eV and high resolution spectra at pass energy of 40 eV (overall energy resolution, photons and spectrometer, is 0.5eV). The binding energy scale was calibrated using C 1s line at 284.8eV as a reference.

References

1. Weidelener, M. *et al.* Synthesis and characterization of perylene–bithiophen–triphenylamine triads: studies on the effect of alkyl-substitution in p-type NiO based photocathodes. *J. Mater. Chem.* **22,** 7366–7379 (2012).
2. Cremer, J. Novel head-to-tail coupled oligo(3-hexylthiophen) derivatives for photovoltaic applications. (2005).
3. Zhang, G.-F. *et al.* General Synthetic Approach toward Geminal-Substituted Tetraarylethene Fluorophores with Tunable Emission Properties: X-ray Crystallography, Aggregation-Induced Emission and Piezofluorochromism. *Chem. Mater.* **26,** 4433–4446 (2014).
4. Marom, H., Popowski, Y., Antonov, S. & Gozin, M. Toward the Development of the Direct and Selective Detection of Nitrates by a Bioinspired Mo–Cu System. *Org. Lett.* **13,** 5532–5535 (2011).
5. Choppawa, T., Sukwattanasinitt, M., Sahasithiwat, S., Ruangpornvisuti, V. & Rashatasakhon, P. Substituent effect on quantum efficiency in 4-aryloxy-N-(2′,6′-diisopropylphenyl)-1,8-naphthalimides: Experimental and computational investigations. *Dyes Pigments* **109,** 175–180 (2014).
6. Connelly, N. G. & Geiger, W. E. Chemical Redox Agents for Organometallic Chemistry. *Chem. Rev.* **96,** 877–910 (1996).
7. Pavlishchuk, V. V. & Addison, A. W. Conversion constants for redox potentials measured versus different reference electrodes in acetonitrile solutions at 25°C. *Inorganica Chim. Acta* **298,** 97–102 (2000).
8. Manders, J. R. *et al.* Solution-Processed Nickel Oxide Hole Transport Layers in High Efficiency Polymer Photovoltaic Cells. *Adv. Funct. Mater.* **23,** 2993–3001 (2013).
9. Powar, S. *et al.* Highly Efficient p-Type Dye-Sensitized Solar Cells based on Tris(1,2-diaminoethane)Cobalt(II)/(III) Electrolytes. *Angew. Chem. Int. Ed.* **52,** 602–605 (2013).

Annexes

I. Annex 1 - Another photocathode material than NiO ?

The number of p-type oxides that are available is weak and despite some trials were performed, no material was found to be better than NiO for p-type DSSCs. Efforts essentially focused on developing copper oxides derivative. This is the object of the following paragraphs.

I.A. A $Cu^{(II)}$ material, CuO:

Recently, a work by Guldi et al.[1] showed how $Cu^{(II)}O$ nanorods, associated to strongly red absorbing phtalocyanines could be a good candidate to compete with NiO photocathodes. Short-circuit photocurrents as high as 2.78 $mA.cm^{-2}$ were obtained and PCE reached the reasonably high value of 0.103%, with 4µm thick electrodes.

This work absolutely outperformed the former results obtained with CuO nanoparticles in 2008 by Sumikura et al. [2]. This is due to the change in the CuO morphology (nanorods, rather than nanoparticles) and certainly to the fact that the dyes used by Sumikura et al. were less efficient for photocathode use. Besides, Sumikura et al. had stressed the detrimental strong self-absorption behavior of CuO, due its small band-gap (Eg = 1.4 eV [2]). This aspect was actually not truly tackled in the publication by Guldi et al. but the performance of the photoelectrode are truly encouraging for future development. However, it is true that fundamental issues, such as the low fill-factor of p-type DSSCs were not solved with CuO, also CuO is presented to be unstable toward photocorrosion [3], which is an important drawback for solar cell application.

I.B. Delafossite $Cu^{(I)}$ materials :

Delafossite material is a class of copper (+I) material. Cu^{I} is mixed with an element which possess a +III oxidation number, and two atoms of oxygen: the general formula is $CuXO_2$. This type of

material was discovered to exhibit p-type conductivity by Hosono et al. in 1997 [4], in this case, X was Al.

Delafossite materials have undeniable advantages for photocathode implementation. They are generally presented as possessing good optical transparency [5]. This is due to the fact that, in delafossite structure, the Cu atoms are only linked between each-other in a 2D plane and then "conjugation is reduced" compared to the 3D situation and the band gap is wider than for CuO for instance (3.5 ev for $CuAlO_2$). Also, Cu^I has the d^{10} electronic configuration, consequently, it is not prone to internal d-d transitions, which could generate detrimental competing absorption with the dye molecule. The hole mobility is also better for delafossite materials (10^1-10^2 $cm^2V^{-1}s^{-1}$ [43]). Additionally, delafossite materials possess a VB which is 100/200 mV deeper than for NiO and this is beneficial so as to increase V_{OC}.

Actually, three types of delafossite material were tried for p-type photocathodes up to now: $CuAlO_2$, $CuGaO_2$ and $CuCrO_2$. If the performance do not equalize NiO, results are very encouraging and the challenge seems to be in the synthesis of the material (obtaining small size particles, densely packed and finding innovative deposition method, to avoid phase transformation into CuO for instance). Despite encouraging results, it is to be noticed that stability issues for this class of material are pointed out, due to the presence of Cu^I [5].

I.B.1. $CuAlO_2$

$CuAlO_2$ was implemented by the Australian team of Bach and Cheng in 2011[6] and gave better V_{OC} than NiO (330 mV, when PMI-6T-TPA was employed as the sensitizer) but low photocurrent (300µA.cm^{-2}). This was due to the large size of the particles employed, which conveys a small specific surface area to the photocathode. Wu et al.[7] could get photocurrents close to 1 mA.cm^{-2} by reducing particle size (to 35 nm), but in this case material synthesis was complex (very high temperature, restricted atmosphere conditions). Despite the limited performance for $CuAlO_2$, this material at least bear the advantage that Al is an Earth abundant element (rank 3).

I.B.2. $CuGaO_2$

$CuGaO_2$ was studied in parallel by Wu and Odobel groups. Thin (20/45 nm), but large (200/300 nm) nano-objects were obtained and if higher V_{OC} value were obtained, compared with NiO, the J_{SC} were again small (300/400 µA.cm^{-2}). This was again attributed to the low specific surface area of the delafossite material and, charge recombination seemed to be a remaining issue. Later Cheng et al. Reported on the synthesis of smaller $CuGaO_2$ nanoplates [8], and a mechanical pressing after spray deposition (spray was a solution to avoid resorting organic binder, which require high burning temperature, at which $CuGaO_2$ is unstable). Thanks to the pressing step, which increased material density, record J_{SC} of 2.05 mA.cm^{-2} were obtained and the high V_{OC} value was kept, with P_1 as the dye. The fill factor were above 41%, which is also an improvement compared with NiO. The author mentioned that thinner films may lead to better performance (the film thickness was 2.9 µm). This is probably due to the finally strong self-absorption of the film, depicted in fig. 3a) of ref [8] (the absorbance of bare $CuGaO_2$ film was around 1, at 500 nm, which corresponds to a 10% transmittance, which is very low). This result is actually surprising since as said above, $CuGaO_2$ are often presented as being very transparent. Interestingly, doping of $CuGaO_2$ material were reported to have positive effects: Fe doping [9], or Mg doping [10].

I.B.3. $CuCrO_2$

Cheng and Bach also explored the use of chromium as a component for the delafossite material. Small nanocrystals (with a diameter of 12 nm) were allowed to be synthesized through a quite simple hydrothermal synthesis[11]. When combined to PMI-6T-TPA, this material actually lead to interesting performance [12]. The J_{SC} was close to 2 mA.cm^{-2} and V_{OC} was enhanced by 42 mV, compared with NiO, reaching 268 mV, when iodine was employed in the electrolyte. Also, the fill factor was 44%, which is higher than for NiO (36%). When combined with the famous ethylene diamine cobalt complex $[Co(en)_3]^{2+/3+}$, a record V_{OC} , for a p-type DSSC, of 734 mV was obtained, almost 100 mV than for with NiO. In this work, despite efforts in order to increase the specific surface area of the material by resorting small size crystal, the material was found to be much more porous than NiO (79% of porosity for $CuCrO_2$, *vs* 51% of porosity for NiO). Then the

LHE of the $CuCrO_2$ electrode was less important than for NiO. However, the author mentioned that another important source of photocurrent limitation was the lower hole injection efficiency from the dye to $CuCrO_2$. This is due to the fact that, despite being very efficient, PMI-6T-TPA has a high lying HOMO, too close to the deep $CuCrO_2$ VB. It is to be noted that Mg doping had been reported to be an efficient strategy to increase the performance $CuCrO_2$ materials [13].

I.C. **ITO material**

Recently the group of Yiying Wu reported on an efficient use of mesoporous ITO electrodes as hole collector material, to generate high photo-cathodic currents [14]. Thick (11nm) photo-cathodes could be built, since ITO is a more transparent and more conductive material than NiO. High J_{SC} values were obtained (5.96 $mA.cm^{-2}$) and VOC around 100 mV were reached. The PCE yield and the fill-factors were not shown, though, in this this publication. This is probably due to the very high dark-current pointed out in this paper, which is was suggested to be overcome in the future by surface engineering of ITO.

An important difference with NiO and with other p-type semiconducting oxides used, up to now is that ITO is not p-type. ITO is a n-type, degenerate semi-conducting oxide, with a conduction band edge which lies at about 0.2 V *vs* NHE. Then the mechanism (not detailed here) is very different compared to traditional photocathode, based on p-type oxide.

I.D. **Other materials**

In the search of a new efficient photocathode material, other p-type material were assessed, such as potassium-doped ZnO [15], $Cu_5Ta_{11}O_{30}$ [16], LaOCuS [17], or $NiCo_2O_4$ [18]. The last one actually seems to represent a very promising material, since very high performance were actually depicted with N_{179} dye, which is a dye with no specific design for photocathodes. Actually, with an iodine based electrolyte, the J_{SC} value was as high as 8.35 $mA.cm^{-2}$, the V_{OC} reached 189 mV and the fill-factor was up to 50%, which is very high for p-type DSSCs. This all resulted in a PCE of 0.785 %, which could be the highest value for an iodine base electrolyte.

I.E. **Conclusions**

Despite encouraging research to replace NiO, up to now, a breakthrough still remains to be done to find another suitable material and obviously, the best cell performance have still been obtained by using NiO. This is why in this thesis, NiO was employed for the fabrication of the p-type DSSCs.

References

1. Langmar, O. *et al.* Combining Electron-Accepting Phthalocyanines and Nanorod-like CuO Electrodes for p-Type Dye-Sensitized Solar Cells. *Angew. Chem.* **127,** 7798–7802 (2015).
2. Sumikura, S., Mori, S., Shimizu, S., Usami, H. & Suzuki, E. Photoelectrochemical characteristics of cells with dyed and undyed nanoporous p-type semiconductor CuO electrodes. *J. Photochem. Photobiol. Chem.* **194,** 143–147 (2008).
3. Renaud, A. *et al.* CuGaO2: a promising alternative for NiO in p-type dye solar cells. *J. Mater. Chem.* **22,** 14353–14356 (2012).
4. Kawazoe, H. *et al. p-Type* electrical conduction in transparent thin films of CuAlO2. *Nature* **389,** 939–942 (1997).
5. Yu, M., Draskovic, T. I. & Wu, Y. Cu(I)-based delafossite compounds as photocathodes in p-type dye-sensitized solar cells. *Phys. Chem. Chem. Phys.* **16,** 5026–5033 (2014).
6. Nattestad, A., Zhang, X., Bach, U. & Cheng, Y.-B. Dye-sensitized CuAlO2 photocathodes for tandem solar cell applications. *J. Photonics Energy* **1,** 011103–011103–9 (2011).
7. Ahmed, J. *et al.* Scalable synthesis of delafossite CuAlO2 nanoparticles for p-type dye-sensitized solar cells applications. *J. Alloys Compd.* **591,** 275–279 (2014).
8. Xu, Z. *et al.* Remarkable photocurrent of p-type dye-sensitized solar cell achieved by size controlled CuGaO2 nanoplates. *J. Mater. Chem. A* **2,** 2968–2976 (2014).
9. Ursu, D., Miclau, M., Banica, R. & Vaszilcsin, N. Impact of Fe doping on performances of CuGaO2 p-type dye-sensitized solar cells. *Mater. Lett.* **143,** 91–93 (2015).
10. Renaud, A. *et al.* Impact of Mg Doping on Performances of CuGaO2 Based p-Type Dye-Sensitized Solar Cells. *J. Phys. Chem. C* **118,** 54–59 (2014).
11. Xiong, D. *et al.* Hydrothermal synthesis of ultrasmall CuCrO2 nanocrystal alternatives to NiO nanoparticles in efficient p-type dye-sensitized solar cells. *J. Mater. Chem.* **22,** 24760–24768 (2012).

12. Powar, S. *et al.* Improved Photovoltages for p-Type Dye-Sensitized Solar Cells Using CuCrO2 Nanoparticles. *J. Phys. Chem. C* **118,** 16375–16379 (2014).
13. Xiong, D. *et al.* Enhanced Performance of p-Type Dye-Sensitized Solar Cells Based on Ultrasmall Mg-Doped CuCrO2 Nanocrystals. *ChemSusChem* **6,** 1432–1437 (2013).
14. Huang, Z. *et al.* Dye-Controlled Interfacial Electron Transfer for High-Current Indium Tin Oxide Photocathodes. *Angew. Chem.* **127,** 6961–6965 (2015).
15. Bai, J. *et al.* Potassium-Doped Zinc Oxide as Photocathode Material in Dye-Sensitized Solar Cells. *ChemSusChem* **6,** 622–629 (2013).
16. Sullivan, I. *et al.* Photoinjection of High Potential Holes into Cu5Ta11O30 Nanoparticles by Porphyrin Dyes. *J. Phys. Chem. C* **119,** 21294–21303 (2015).
17. Renaud, A. *et al.* The first dye-sensitized solar cell with p-type LaOCuS nanoparticles as a photocathode. *RSC Adv.* **5,** 60148–60151 (2015).
18. Shi, Z. *et al.* NiCo2O4 Nanostructures as a Promising Alternative for NiO Photocathodes in p-Type Dye-Sensitized Solar Cells with High Efficiency. *Energy Technol.* **2,** 517–521 (2014).

II. Annex 2 - Choice of the catalytic system for SM coupling

In this work, {$Pd(dba)_2$/$[HP^tBu_3]BF_4$} has been employed as the catalytic system. As a matter of fact, catalytic systems which are similar to this one, have already been quite commonly employed for SM coupling [1,2]. The phosphine P^tBu_3 is well known for its high activity in SM coupling, the object of this paragraph is to remind why. Also, one should remark that the phosphonium salt form of the ligand, $[HP^tBu_3]BF_4$, was preferred since it is less sensitive to oxygen[2,3].

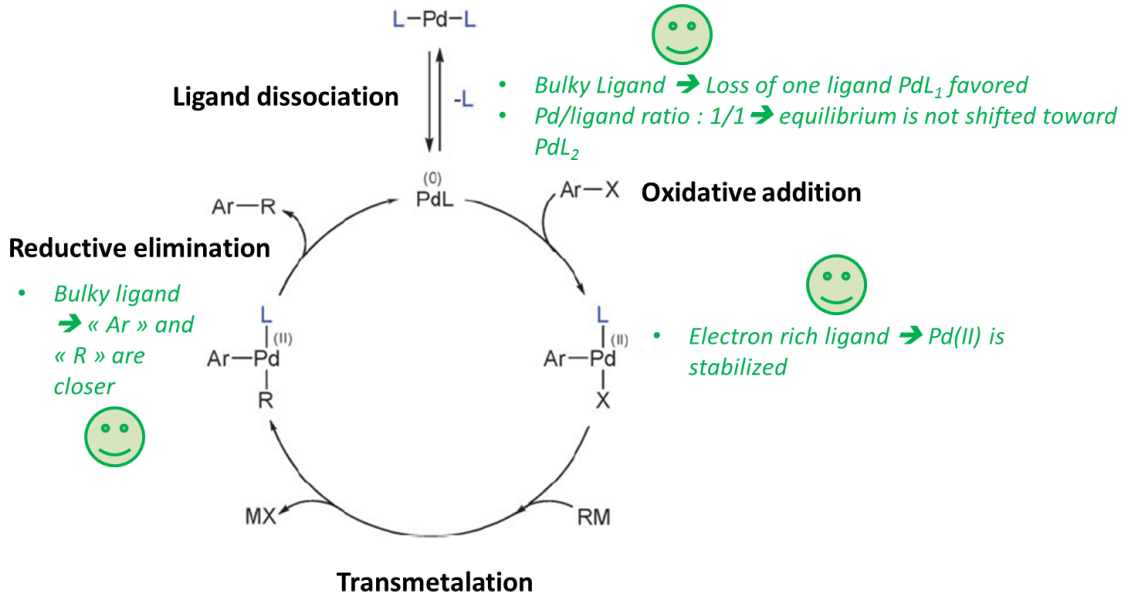


Fig. 114- General and simplified mechanism for palladium-catalyzed cross coupling reaction. Reproduced and modified for simplicity from the review by Fleckenstein and Plenio.

The bulkiness and the electron richness of the phosphine ligand P^tBu_3 is the origin of its superior activity for cross couplings reactions [4,5], typically, for Suzuki-Miyaura cross-coupling [6,7]. Some reviews [4,5] help understand the reasons for this high efficiency. From this reviews, a simplified and general mechanism for the reaction is depicted in Fig. 114. One can understand [5] that steric hindrance of the phosphine ligand may help generating the more stable, monolygated species $Pd(0)P^tBu_3$. It is advantageous to increase the formation of such a monolygated species since it is

more reactive for oxidative addition (for electron count reasons). Additionally, through sigma-donation, the electron richness of the phosphine generates an electron rich Pd(0) complex, prone to undergo oxidative addition. Moreover, in order to favor the formation of monophosphinated species, over the biphosphinated species, in this work, only one equivalent of phosphine source per mole of $Pd(dba)_2$ was introduced [5]. Interestingly, the Hartwig group described even more precisely the oxidative addition step in the case of brominated derivatives [6]. It is suggested that the mechanism of this key step is more complex than the one presented on Fig. 114. However it remains unclear, as two different pathways are possible (one is indeed involving the pre-dissociation of the Pd complex, presented on Fig. 114).

One should suggest that the electron richness of the phosphine ligand, permitting to stabilize the Pd(II) complex, may slow the reductive elimination step. However, as far as Christmann and Vilar are concerned [4], for P^tBu_3, "the steric properties of the phosphine overrides its electronic effect"[8]. Consequently, the bulkiness of the phosphine is thought to help the reductive elimination to happen (by "pushing" the "R" and the "Ar" groups, closer to one another).

The role of the ligand in the transmetalation step is not well defined and less understood

References

1. Weidelener, M. *et al.* Synthesis and Characterization of Organic Dyes with Various Electron-Accepting Substituents for p-Type Dye-Sensitized Solar Cells. *Chem. – Asian J.* **9,** 3251–3263 (2014).
2. Cremer, J. Novel head-to-tail coupled oligo(3-hexylthiophen) derivatives for photovoltaic applications. (2005).
3. Netherton, M. R. & Fu, G. C. Air-Stable Trialkylphosphonium Salts: Simple, Practical, and Versatile Replacements for Air-Sensitive Trialkylphosphines. Applications in Stoichiometric and Catalytic Processes. *Org. Lett.* **3,** 4295–4298 (2001).
4. Fleckenstein, C. A. & Plenio, H. Sterically demanding trialkylphosphines for palladium-catalyzed cross coupling reactions—alternatives to PtBu3. *Chem. Soc. Rev.* **39,** 694–711 (2010).
5. Christmann, U. & Vilar, R. Monoligated Palladium Species as Catalysts in Cross-Coupling Reactions. *Angew. Chem. Int. Ed.* **44,** 366–374 (2005).
6. Fu, G. C. The Development of Versatile Methods for Palladium-Catalyzed Coupling Reactions of Aryl Electrophiles through the Use of P(t-Bu)3 and PCy3 as Ligands. *Acc. Chem. Res.* **41,** 1555–1564 (2008).

7. Littke, A. F. & Fu, G. C. A Convenient and General Method for Pd-Catalyzed Suzuki Cross-Couplings of Aryl Chlorides and Arylboronic Acids. *Angew. Chem. Int. Ed.* **37,** 3387–3388 (1998).
8. Barrios-Landeros, F., Carrow, B. P. & Hartwig, J. F. Effect of Ligand Steric Properties and Halide Identity on the Mechanism for Oxidative Addition of Haloarenes to Trialkylphosphine Pd(0) Complexes. *J. Am. Chem. Soc.* **131,** 8141–8154 (2009).

III. Annex 3 - DFT/TDDFT Results

III.A. Introduction

The DFT and TDDFT calculation results are summarized in this last part. These calculations were performed on the deprotected, final, version of the dyes. The optimized geometry of the dyes was represented. The simulated transitions are also shown and corroborated to the experimental optical spectrum of protected dyes, in DCM. Finally, the orbital composition of each transition is detailed, as well as the shape of the orbitals implicated in the transitions.

An analysis of the push-pull interaction between the HOMO of the donor and the LUMO of the acceptor is also tentatively performed though a modular analysis.

III.B. **Results**

III.B.1. **Dye (8)**

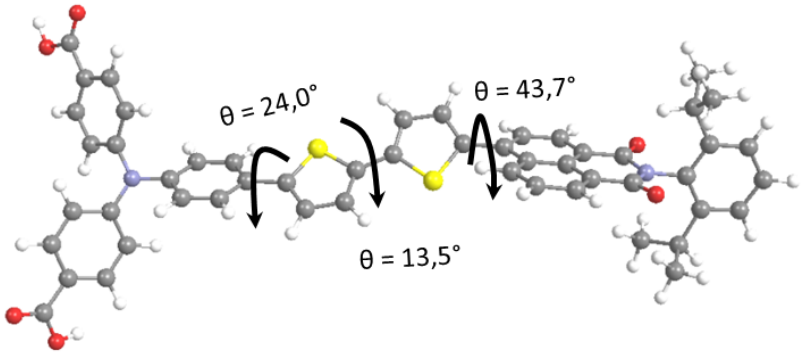


Fig. 115- Optimized geometry for (8) in vacuum

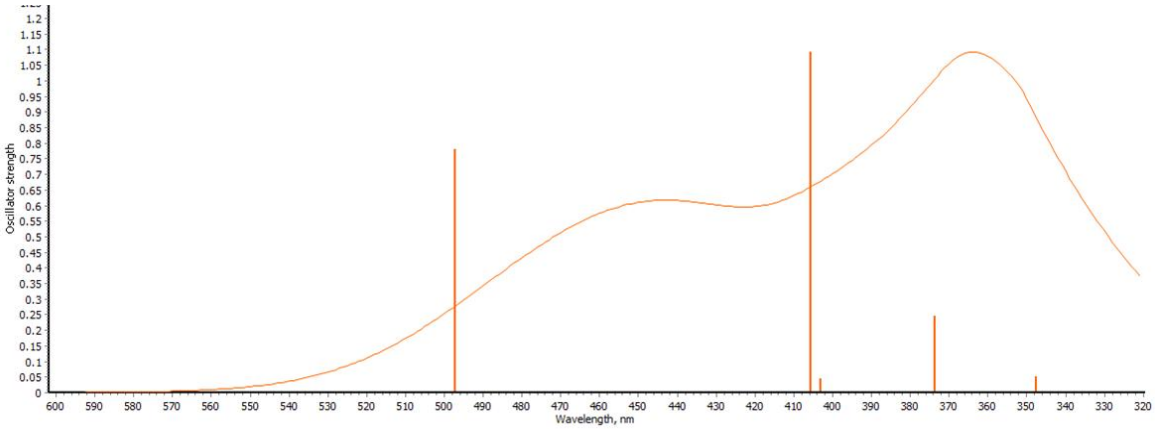


Fig. 116- Computed optical transitions of (8) in vacuum and the experimental spectrum in DCM for its *tert*-butyl ester protected version (7)

Tab. 24- Computed transition energies (λ_{max}), orbital contributions, associated oscillator strength and the calculated absorption molar extinction coefficient at λ_{max} (ε_{max}), in vacuum, for compound (8)

Computed λ_{max}	Orbitals contribution	Oscillator strength	Type of transition
497.15 nm/ 2.4939 eV	HOMO -> LUMO (91.65 %)	0.7804	CT
405.61 nm/ 3.0568 eV	HOMO-1 -> LUMO (26.36%) HOMO -> LUMO+1 (61.83%)	1.0930	- CT (26.36 %) - TPA-2T centered, partial CT (61.83%)
373.52 nm / 3.3193 eV	HOMO -> LUMO+2 (91.90%)	0.2440	TPA centered

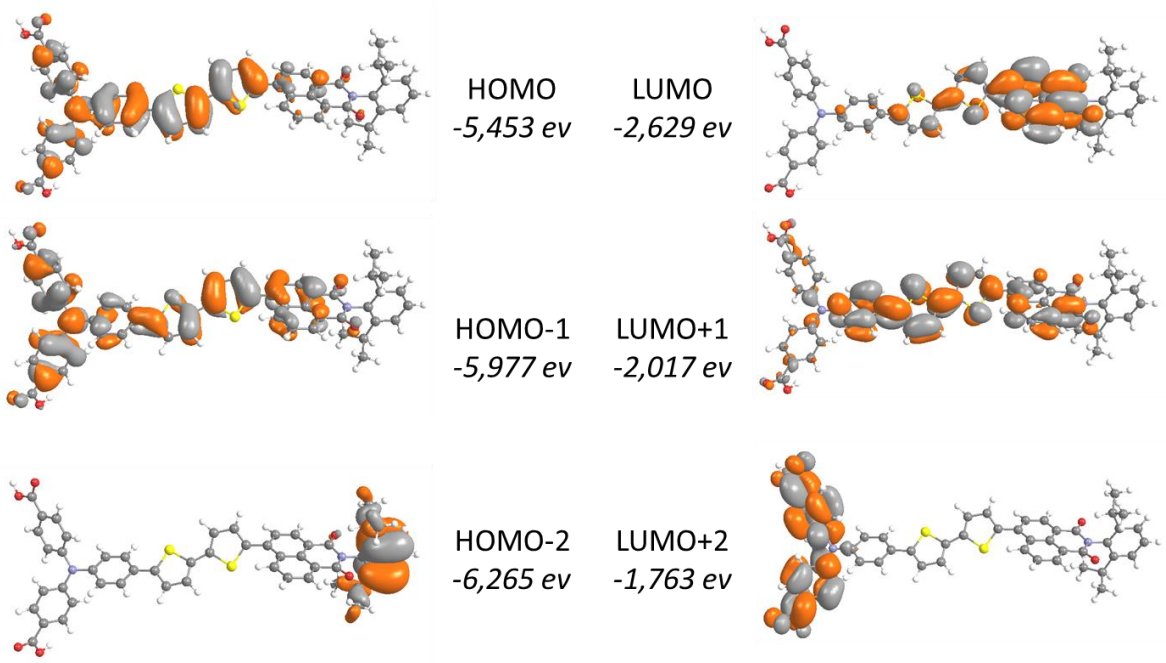


Fig. 117- Computed orbital for compound (8) in vacuum. In orange, the positive lobes and in grey, the negative lobes. Isovalue was set to 0.02 a.u.

III.B.2. **Dye (11)**

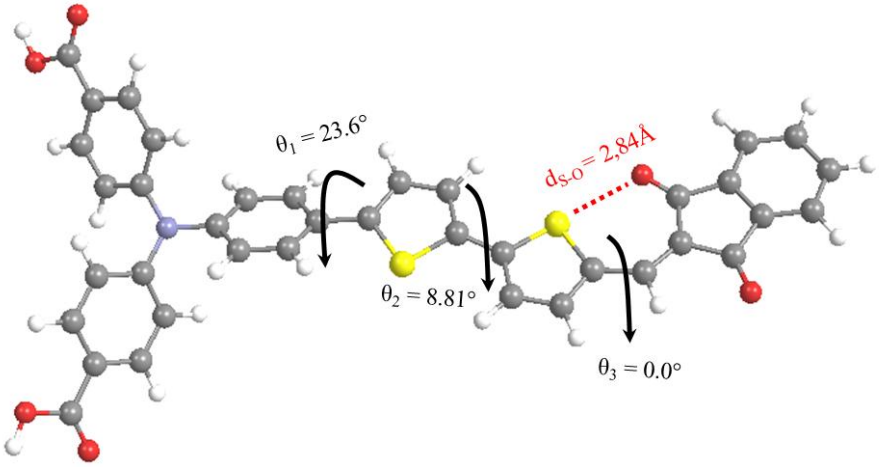


Fig. 118- Optimized geometry for (11) in vacuum

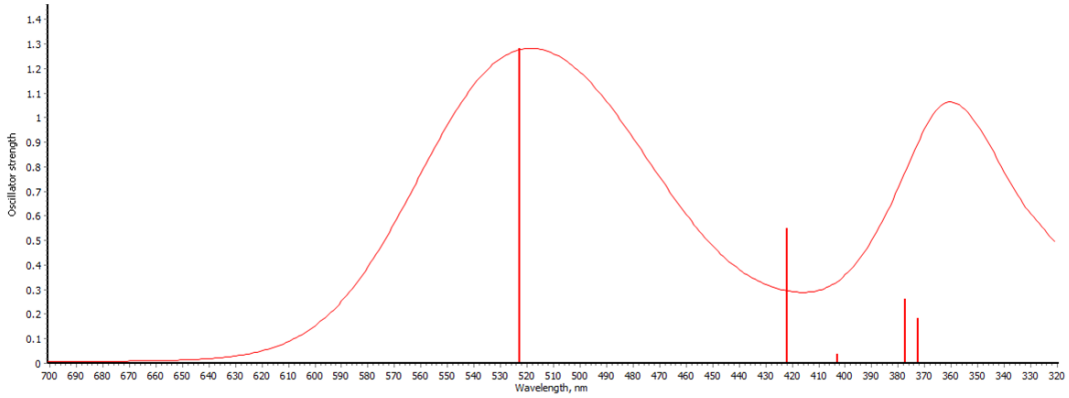


Fig. 119- Computed optical transitions for (11) in vacuum and the experimental spectrum in DCM for its *tert*-butyl ester protected version (10)

Tab. 25- Computed transition energies (λ_{max}), orbital contributions, associated oscillator strength and the calculated absorption molar extinction coefficient at λ_{max} (ε_{max}), in vacuum, for compound (11)

Computed λ_{max}	**Orbitals contribution**	**Oscillator strength**	**Type of transition**
522.62 nm/ 2.3723 eV	HOMO -> LUMO (85.83 %)	1.2833	CT
421.78 nm/ 2.9395 eV	HOMO-1 -> LUMO (84.6%)	0.5501	CT
377.50 nm / 3.2843 eV	HOMO -> LUMO+2 (91.55%)	0.2624	TPA centered
372.52 nm/ 3.3282 eV	HOMO->LUMO+3 (80.86%)	0.1845	The whole dye

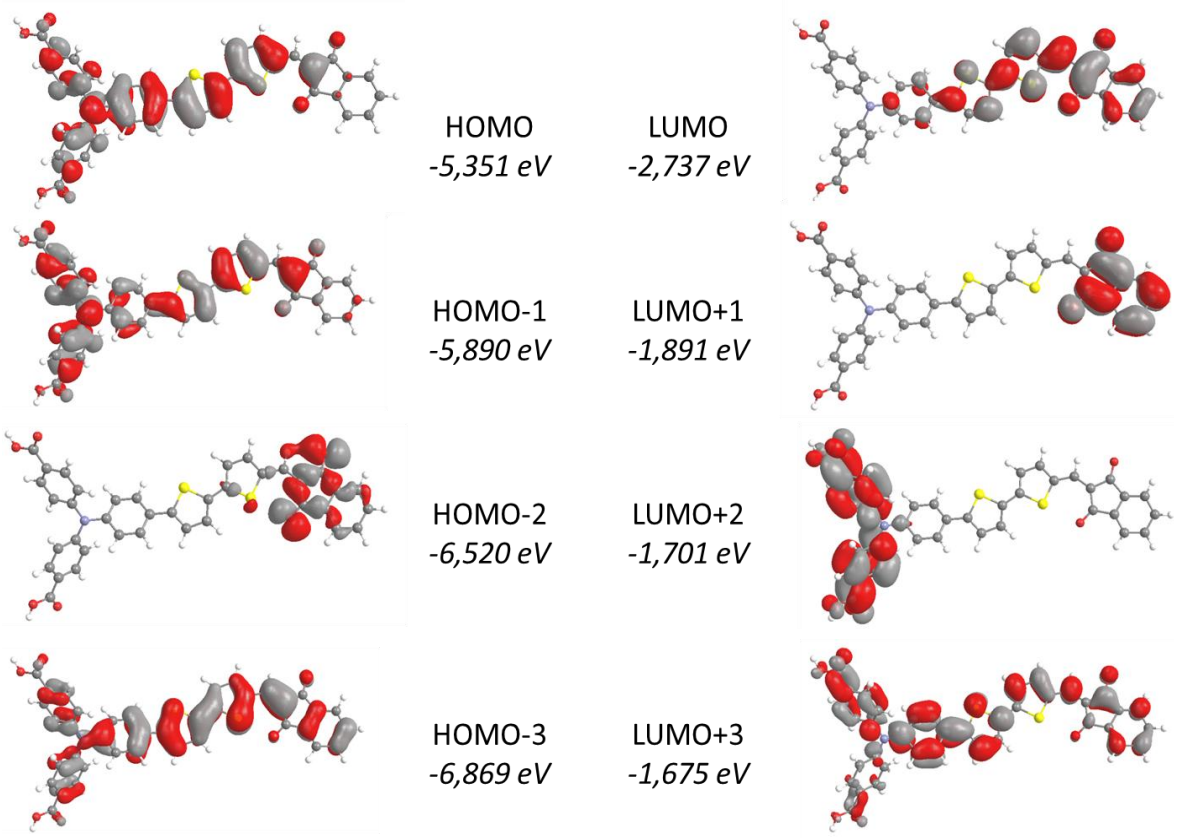


Fig. 120- Computed orbitals for compound (11) in vacuum. In red, the positive lobes and in grey, the negative lobes. Isovalue was set to 0.02 a.u.

III.B.3. **Dye (14)**

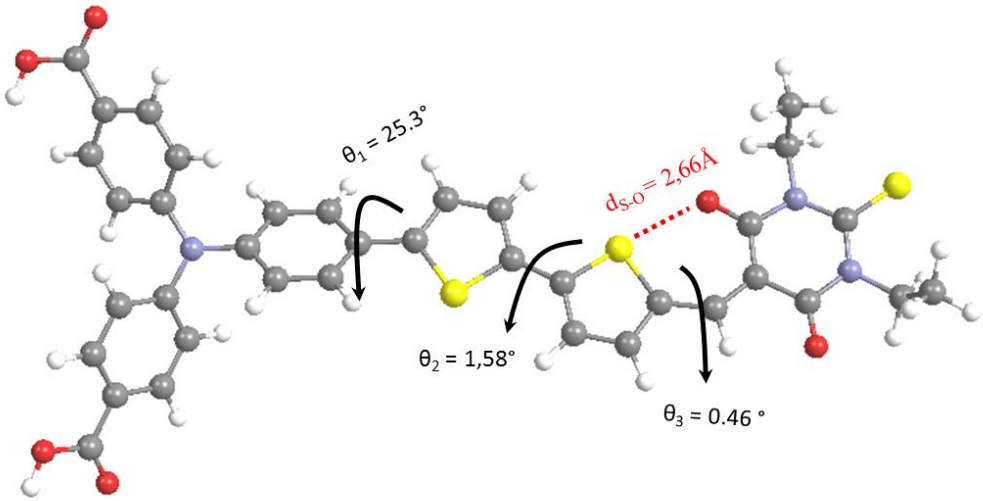


Fig. 121- Optimized geometry for (14) in vacuum

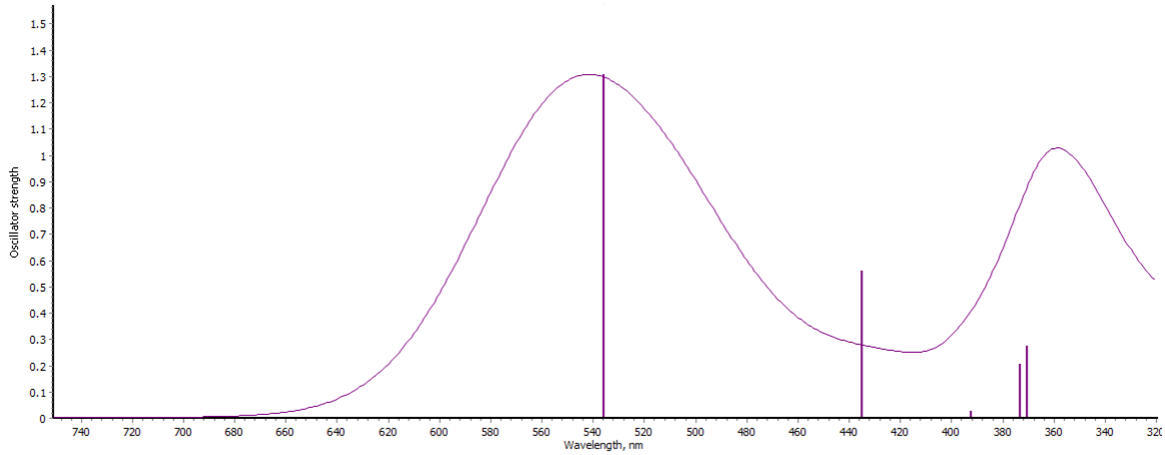


Fig. 122- Computed optical transitions for (14) in vacuum and the experimental spectrum in DCM for (13)

Tab. 26- Computed transition energies (λ_{max}), orbital contributions, associated oscillator strength and the calculated absorption molar extinction coefficient at λ_{max} (ε_{max}), in vacuum, for compound (14)

Computed λ_{max}	Orbitals contribution	Oscillator strength	Type of transition
535.71 nm/ 2.3144 eV	HOMO -> LUMO (85.48 %)	1.3080	CT
434.89 nm/ 2.8509 eV	HOMO-2 -> LUMO (85.25%)	0.5597	CT
373.23 nm / 3.3219 eV	HOMO -> LUMO+1 (65.52 %) HOMO-> LUMO+2 (25.53 %)	0.2062	-The whole dye (65.52%) - TPA centered (25.53%)
370.54 nm/ 3.3461 eV	HOMO -> LUMO+1 (20.75 %) HOMO-> LUMO+2 (63.45 %)	0.2733	-The whole dye (20.75%) - TPA centered (63.45%)

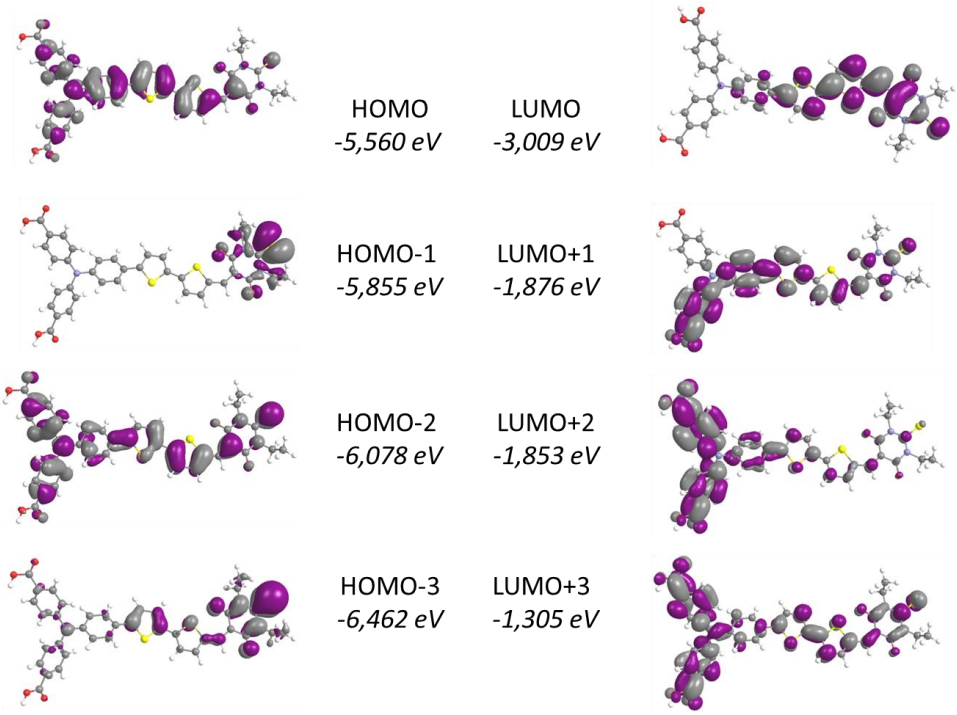


Fig. 123- Computed orbitals for compound (14) in vacuum. In purple, the positive lobes and in grey, the negative lobes. Isovalue was set to 0.02 a.u.

III.B.4. **Dye (17)**

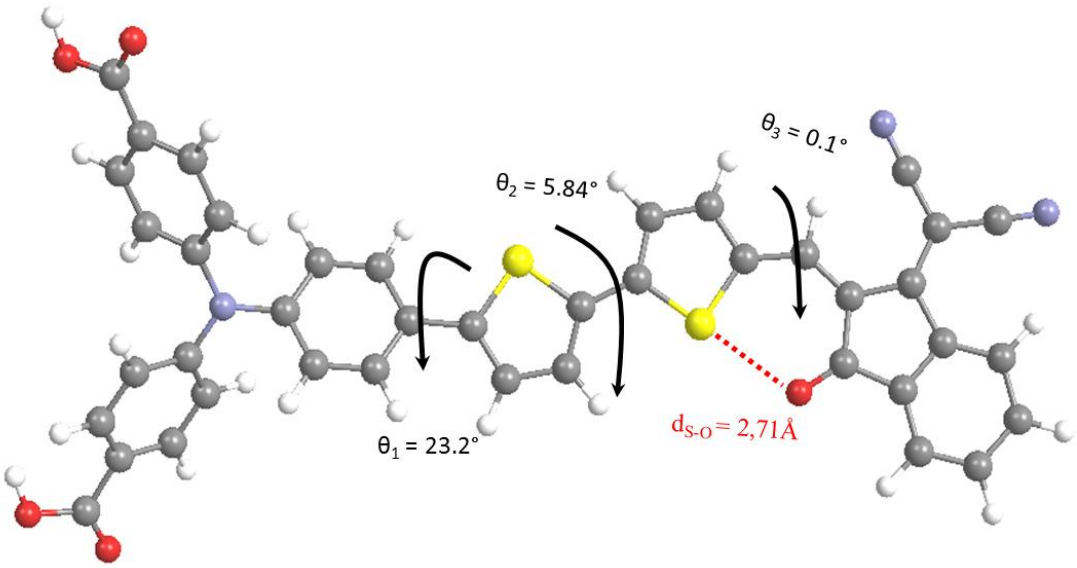


Fig. 124- Optimized geometry for (17) in vacuum

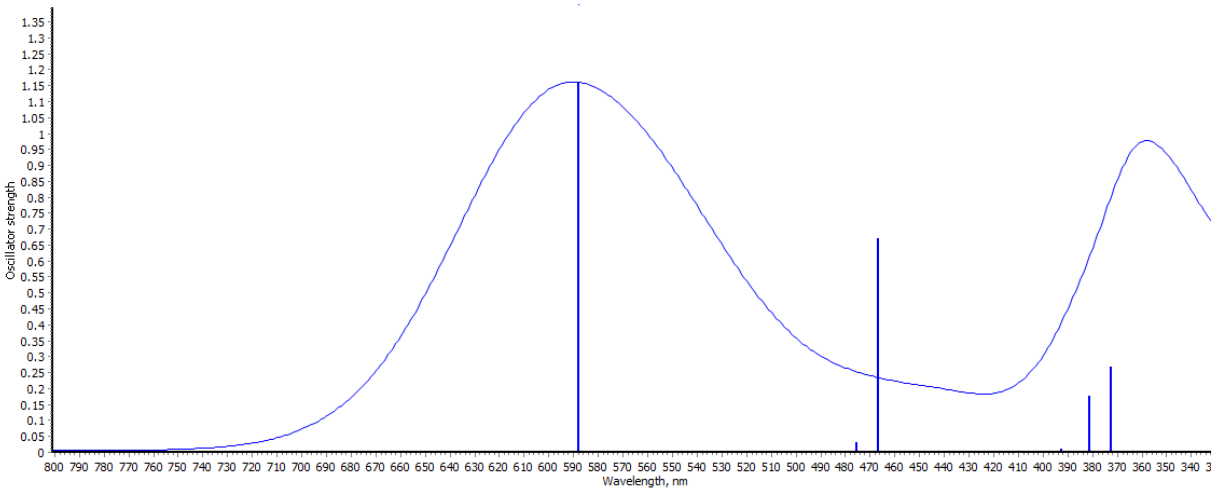


Fig. 125- Computed optical transitions for (17) in vacuum and the experimental spectrum in DCM for (16)

Tab. 27- Computed transition energies (λ_{max}), orbital contributions, associated oscillator strength and the calculated absorption molar extinction coefficient at λ_{max} (ε_{max}), in vacuum, for compound (17)

Computed λ_{max}	Orbitals contribution	Oscillator strength	Type of transition
587.83 nm/ 2.1092 eV	HOMO -> LUMO (85.76 %)	1.1619	CT
466.72 nm/ 2.6565 eV	HOMO-1 -> LUMO (71.35%) HOMO->LUMO+1 (15.75%)	0.6709	CT
381.02 nm / 3.2540 eV	HOMO-2 -> LUMO (13.71 %) HOMO-> LUMO+2 (69.19 %)	0.1761	The whole dye
372.41 nm/ 3.3293 eV	HOMO-> LUMO+3 (89.49 %)	0.2658	TPA centered

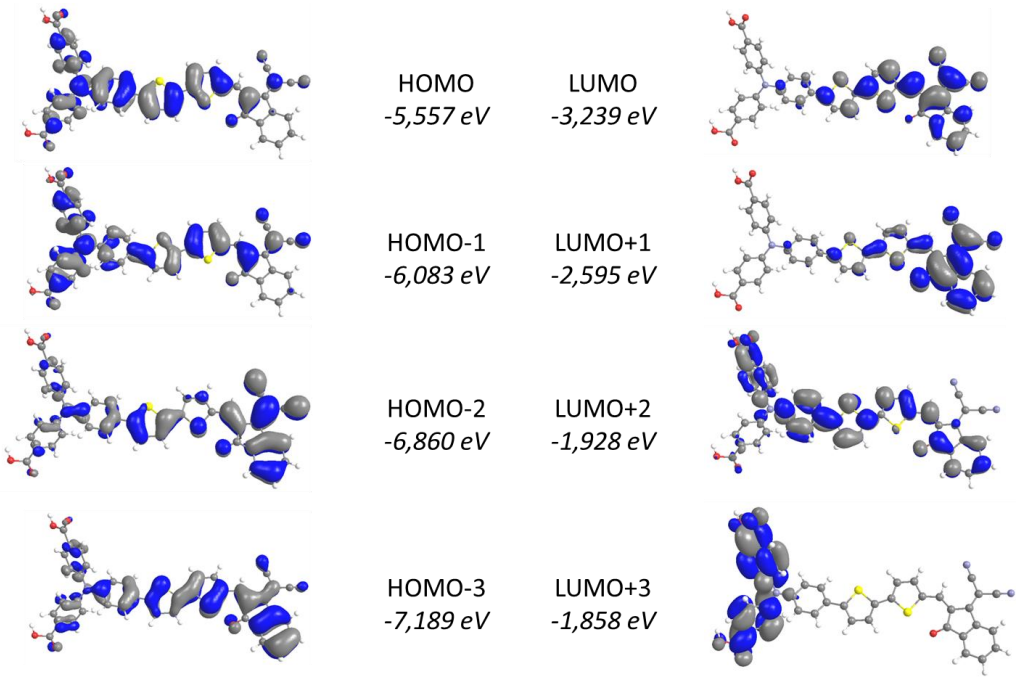


Fig. 126- Computed orbitals for compound (17) in vacuum. In blue, the positive lobes and in grey, the negative lobes. Isovalue was set to 0.02 a.u.

III.C. Various remarks

For dye **(11)**, **(14)** and **(17)**, the sulfur-oxygen distance ($d_{S\text{-}O}$, see Fig. 118, Fig. 121 and Fig. 124) was calculated, and this distance was shown to be always shorter than the sum of the Sulfur and

Oxygen Van-Der Walls radii. (R_S = 1.8 Å, R_O = 1.4 Å, $R_S + R_O$ = 3.2 Å). This indicates a Sulfur-Oxygen interaction at the ground state and then an intramolecular bond. The becoming to this interaction at the excited state could be studied more deeply.

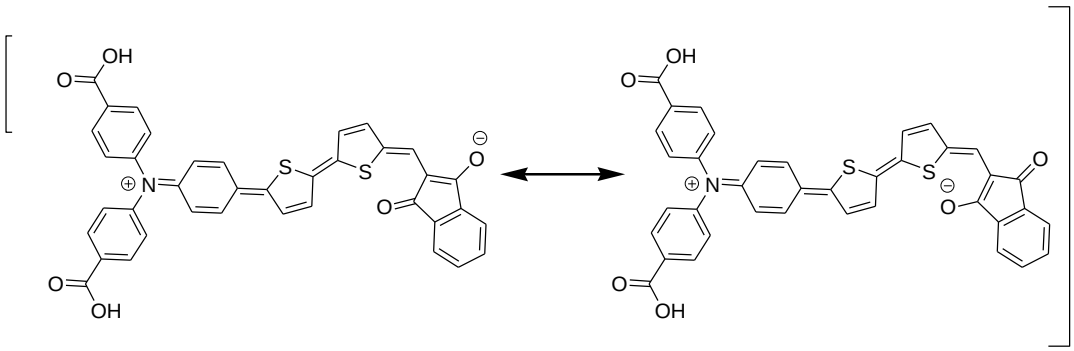


Fig. 127- Two possible mesomeric forms for the CT state of (11). What is the becoming of the S-O bond after charge separation ?

One should remark the nice correlation for dye **(11)**, **(14)** and **(17)**, between experimental and theory for transition energy. For **(11)**, the computed transitions are overestimated but this result is usual for push-pull dyes [1]. The orbitals involved in the optical transitions were also displayed, as well as the associated oscillating factor.

III.D. Modular analysis of the push-pull interaction

In order to better understand the reason for the HOMO / LUMO energy level position in the final organic dyes. A modular analysis was performed for the compounds, in the same ways as in Homnick et al [2,3]. This approach decomposes the different parts of the molecules into modules and describes the orbital interactions of the different modules in the final molecule. In the case of push-pull compounds, this approach permits to understand better the interactions between the donor and the acceptor part.

III.D.1. Modular gap tuning

As it can be seen on Fig. 128, the computed HOMO/LUMO energy values of the final dyes were close to the ones of the separate donor and acceptor "modules". From this, it can be concluded that the interactions between the donor and the acceptor group, at the ground state are limited. This explains why the strategy to tune the HOMO/LUMO gap of TPA-2T molecules by only

changing the acceptor strength has been efficient. Due the limited coupling between the TPA-2T donor module and the various acceptor modules, the strength of the acceptor (that is its LUMO level) is conserved after integration into the final dye entity.

III.D.2. Frontier orbitals coupling

Actually, this kind of modular behavior, for push-pull compounds, has already been reported by Homnick et al. [2,3]. Besides, this group pointed out that the nature of the orbital interactions between the donor and the acceptor modules was HOMO/HOMO and LUMO/LUMO interactions. These interactions correspond to the creation of a stabilized LUMO and destabilized HOMO for the final donor-acceptor compound (see Fig. 129). However, this kind of interaction mechanism seems to be only partly appropriate for the push-pull dyes presented in this thesis, especially for **(14)** and **(17)**. Judging by their stabilized HOMO and their non-stabilized LUMO, theses dyes probably show substantial HOMO/LUMO modular coupling. This coupling is due to the smaller difference of energy between the HOMO and LUMO of the donor and acceptor modules.

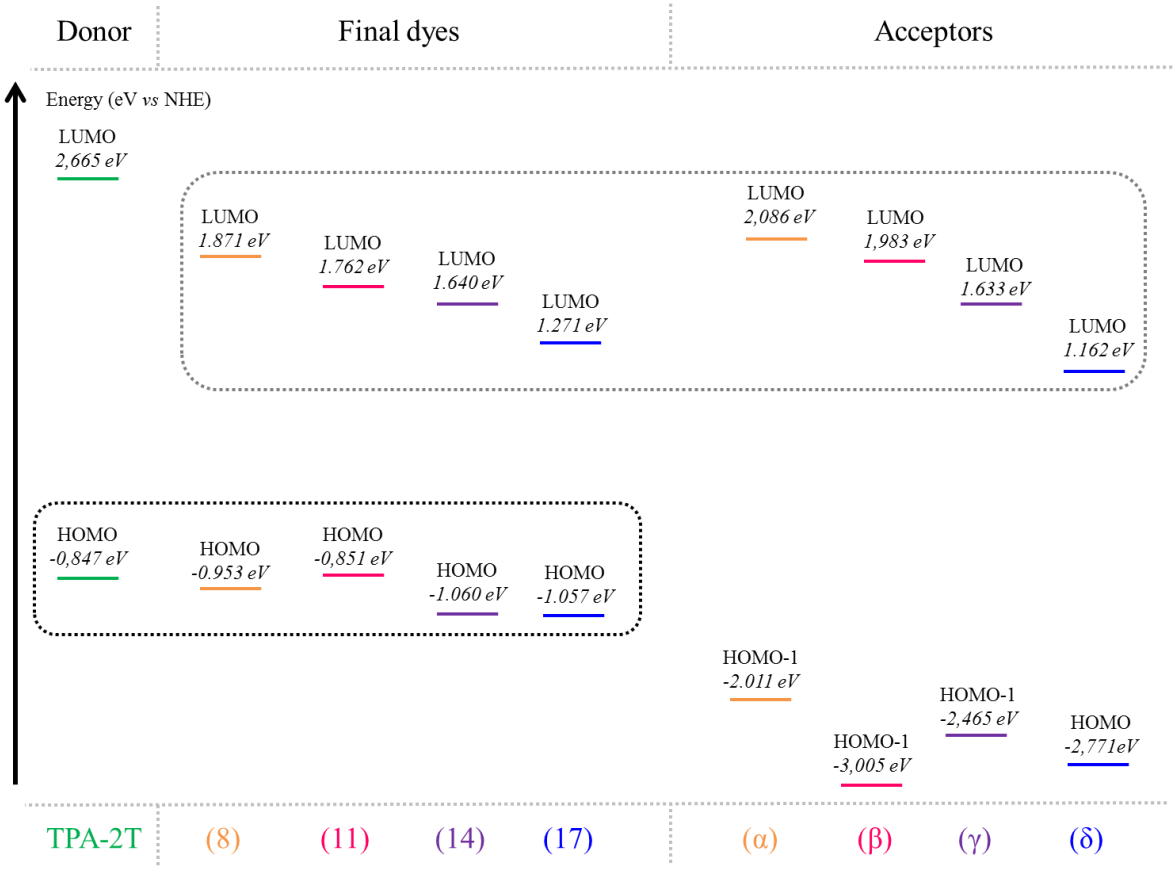


Fig. 128- Modular analysis for the final compounds, based on DFT calculations in vacuum for each module and the

As reported by the group of Oliva et al [4], HOMO/LUMO interaction between the donor and the acceptor module stabilizes the LUMO and destabilizes the HOMO of the final compound (see Fig. 130).

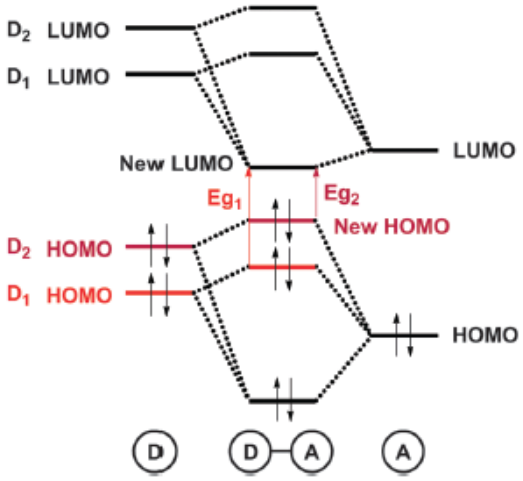


Fig. 129- Modular analysis proposed for push-pull compounds with no HOMO/LUMO coupling, proposed by Homnick et al. Reproduced Homnis et ak

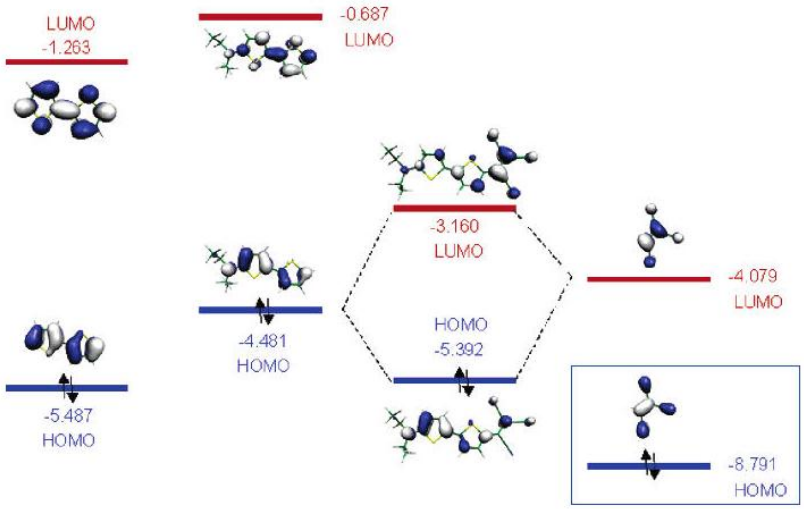


Fig. 130- Deconstruction diagram of a push-pull compound with strong HOMO/LUMO interactions, studied by Oliva et al. Reproduced from the publication by Oliva et al

From a physical point of view, this HOMO/LUMO modular coupling can be viewed as an enhanced partial electron transfer at the ground state, from the donor to the acceptor. This electron transfer is induced by the strength of the donor and the acceptor modules, and also the geometry of the dye. This effect can be seen on Fig. 132 which displays the variations of the bond lengths across the Pi-skeleton of the different dyes and compares to the situation were no acceptor is grafted, in the pristine "TPA-2T" donor group. For **(17)** and **(14)**, the electronic effect on the thiophen bridge is impressive and reaches the second thiophen ring in the Pi-bridge! This effect is

less important in the case of **(11)**, in accordance with a weaker HOMO/LUMO coupling. For **(8)**, the structural change is very low, which shows how important is the effect of the dihedral angle for the low coupling between the donor and the acceptor units.

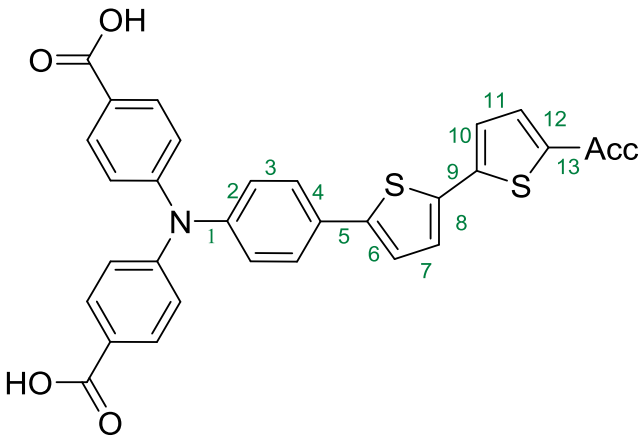


Fig. 131- Bond number across the Pi-conjugated skeleton

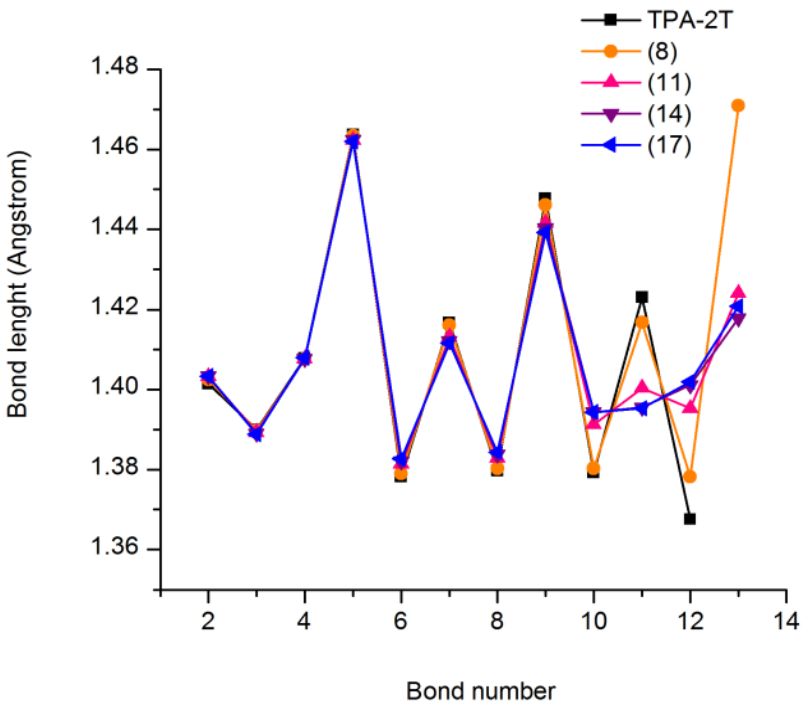
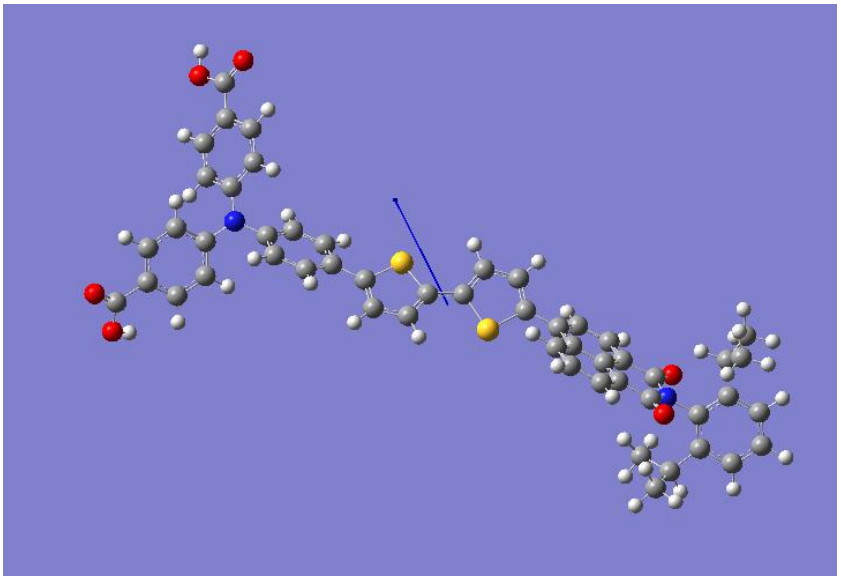


Fig. 132- Evolution of the bond length across the Pi-skeleton of the different dyes and comparison with the TPA-2T module (which has no accepting group).

III.E. **Dipolar moments of the dyes and orientation**

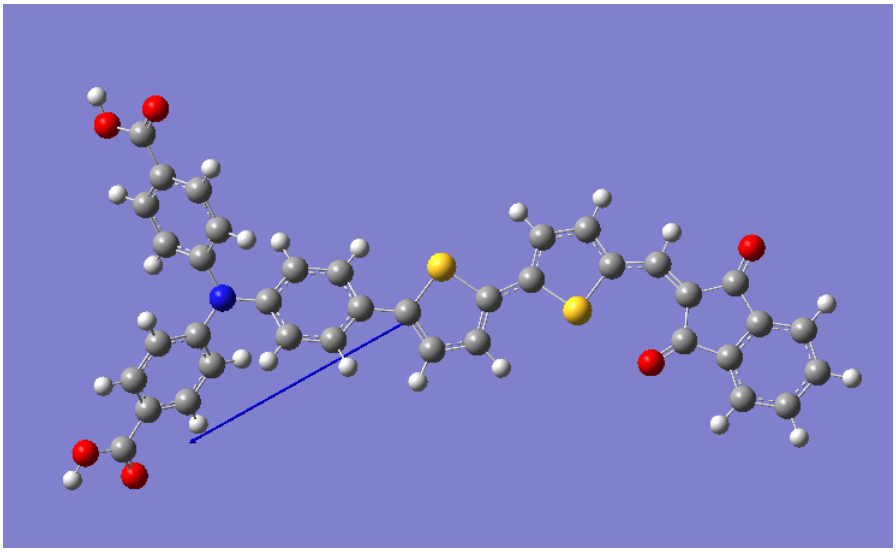
Thanks to Gaussian, we could calculate the dipolar moment of the dyes. Assuming that the dyes a grafted vertically on the NiO surface, thanks to the two carboxilic acids, we calculated the parallel and perpendicular component of the dipolar moment. It is interesting to remark that the compounds with the most important parallel dipolar moment perform the best (except for dye 17, but aggregation was supposed for this dye).

III.E.1. **Dye (8)**



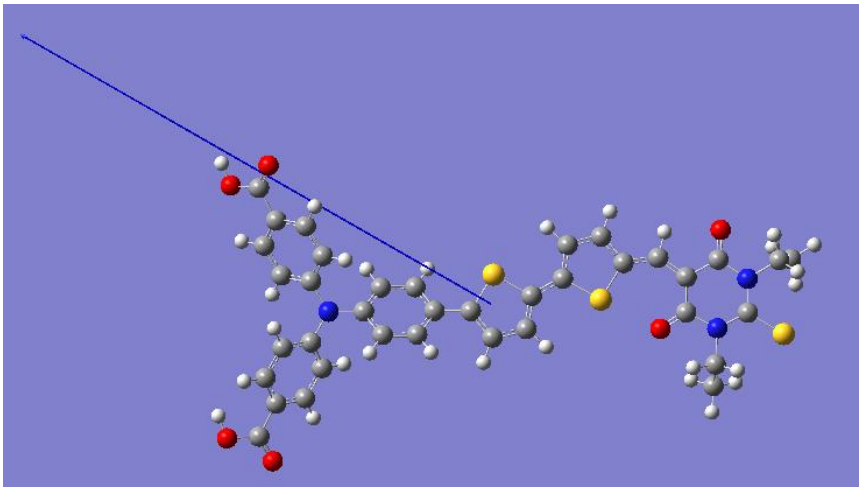
μ = 2.72 D, μ_{parr} = 2.26 D, μ_{perp} = 1.52 D

III.E.2. **Dye (11)**



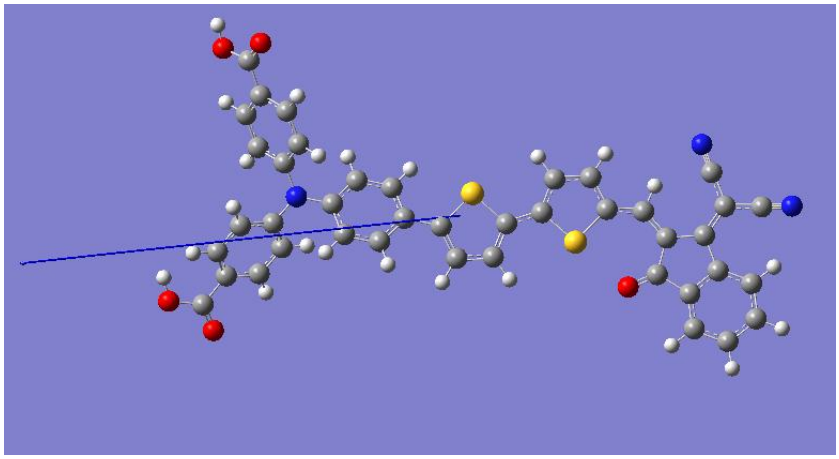
μ = 2.69 D, μ_{parr} = 1.48 D, μ_{perp} = 2.24D

III.E.3. **Dye (14)**



$\mu = 7.24$, $\mu_{parr} = 3.65$ D, $\mu_{perp} = 6.26$ D

III.E.4. **Dye (17)**



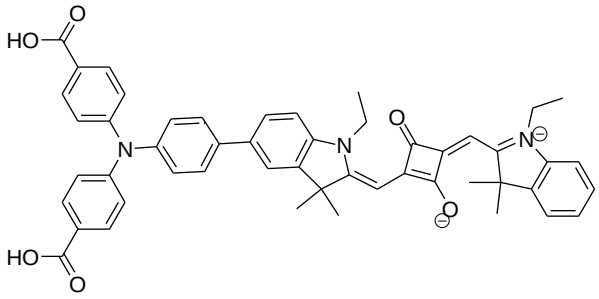
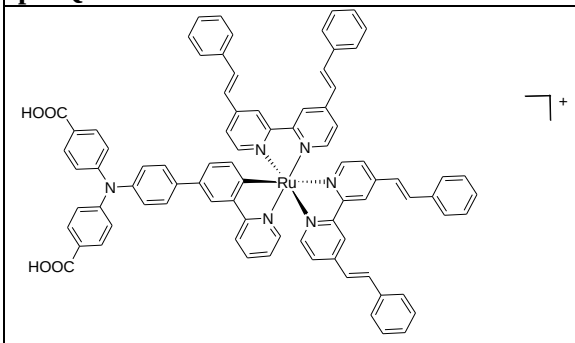
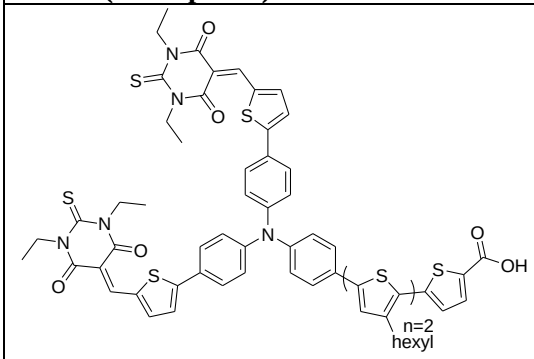
$\mu = 5.78$, $\mu_{parr} = 2.11$ D, $\mu_{perp} = 5.38$ D

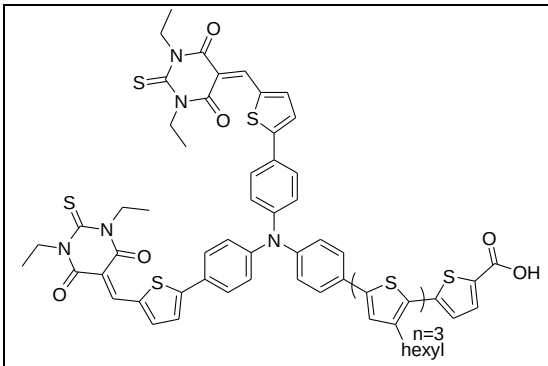
Reference

1. Wood, C. J. *et al.* Red-Absorbing Cationic Acceptor Dyes for Photocathodes in Tandem Solar Cells. *J. Phys. Chem. C* **118,** 16536–16546 (2014).
2. Homnick, P. J. & Lahti, P. M. Modular electron donor group tuning of frontier energy levels in diarylaminofluorenone push–pull molecules. *Phys. Chem. Chem. Phys.* **14,** 11961–11968 (2012).
3. Homnick, P. J., Tinkham, J. S., Devaughn, R. & Lahti, P. M. Engineering Frontier Energy Levels in Donor–Acceptor Fluoren-9-ylidene Malononitriles versus Fluorenones. *J. Phys. Chem. A* **118,** 475–486 (2014).
4. Oliva, M. M. *et al.* Structure−Property Relationships in Push−Pull Amino/Cyanovinyl End-Capped Oligothiophens: Quantum Chemical and Experimental Studies. *J. Org. Chem.* **71,** 7509–7520 (2006).

IV. Annex 4 – Red absorbing dyes review

Tab. 28- The up to date efficient red absorbing dyes in October 2015 (all used with iodine electrolyte)

Dye	Year of publication	Ref	λmax in solution (nm)	PCE (%)
 **p-SQ2**	2012	[1]	646	0.113
 **O-18**	2014	[2]	593	0.104
CAD3 (cf chapter 1)	2015	[3]	614	0.250
 **T3H**	2016	[4]	575	0.226

 **T4H**	2016	[4]	575	0.317

Reference

1. Chang, C.-H., Chen, Y.-C., Hsu, C.-Y., Chou, H.-H. & Lin, J. T. Squaraine-Arylamine Sensitizers for Highly Efficient p-Type Dye-Sensitized Solar Cells. *Org. Lett.* **14,** 4726–4729 (2012).
2. He, M., Ji, Z., Huang, Z. & Wu, Y. Molecular Orbital Engineering of a Panchromatic Cyclometalated Ru(II) Dye for p-Type Dye-Sensitized Solar Cells. *J. Phys. Chem. C* **118,** 16518–16525 (2014).
3. Wood, C. J., Summers, G. H. & Gibson, E. Increased photocurrent in a tandem dye-sensitized solar cell by modifications in push-pull dye-design. *Chem. Commun.* (2015).
4. Wu, F., Zhu, L., Zhao, S., Song, Q. & Yang, C. Engineering of organic dyes for highly efficient p-type dye-sensitized solar cells. *Dyes Pigments* **124,** 93–100 (2016).

V. Annex 5 – Light soaking effect

An important light soaking effect was noticed for the DSSC, with dye **(8)**. An example of this light soaking effect has been exemplified for a p-type DSSC made with two layers of NiO. The photocathode was continuously irradiated under one sun and the photovoltaic characteristics of the device was measured at different time of irradiation. As it can be seen on Tab. 29 and on Fig. 133, the performance of the DSSC change within time. An important J_{SC} soaring is to be noticed in the first minutes, this soaring then appears to stabilize and reach a plateau value (around 1.5 $mA.cm^{-2}$). On the contrary, the VOC tends to rapidly decrease with time. Its stabilization actually seems to be less rapid than J_{SC} stabilization. Then, if PCE remains stable in the first minutes (compensation of the evolution of J_{SC} and VOC), it finally decreases, due to the continuation of VOC decrease.

Tab. 29- Evolution of the photovoltaic performance of a two layers of NiO, sensitized with dye (8), photocathode, continuously irradiated under one sun.

Time of irradiation (min)	**0**	**1**	**2**	**3**	**10**
η (%)	0.046	0.047	0.047	0.046	0.038
Jsc ($mA.cm^{-2}$)	1.122	1.278	1.337	1.412	1.478
VOC (mV)	111	99	95	89	73
FF (%)	0.37	0.37	0.37	0.37	0.35

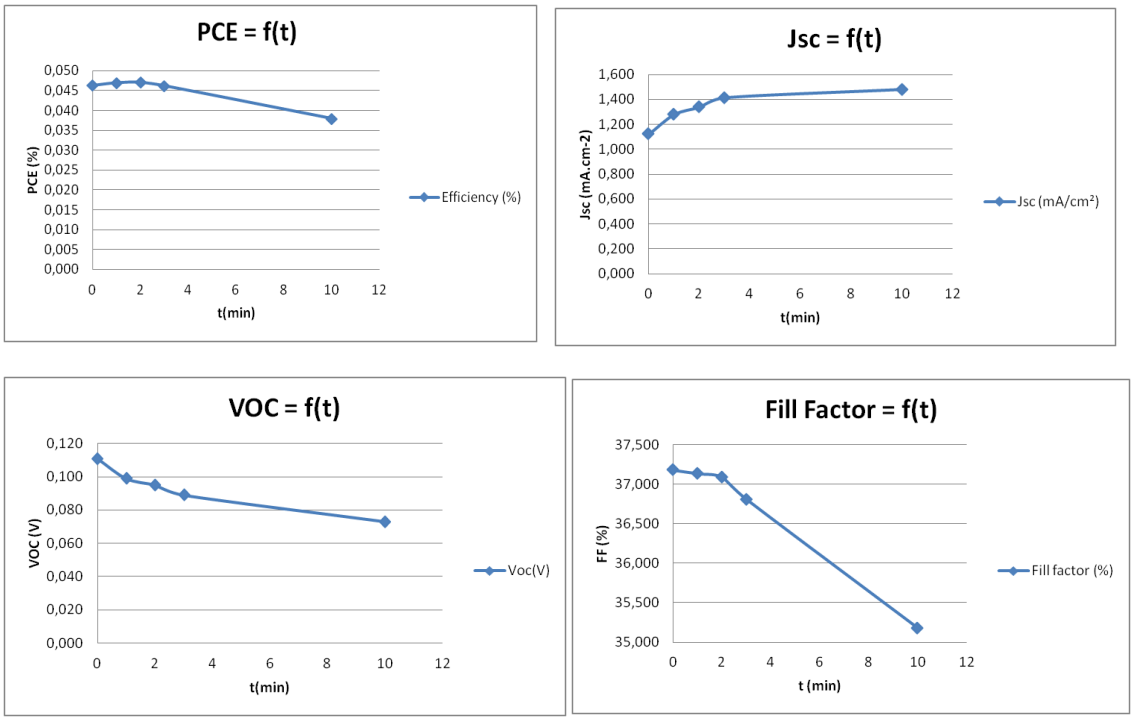


Fig. 133- Graphic representation of the performance evolution of a two layers of NiO, sensitized with dye (8), photocathode, continuously irradiated under one sun.

The physical reasons for this light soaking to happen are not fully understood and the purpose of this paragraph is just to point out that the performance of the device are strongly dependent on time of measurement. Then, in order to compare device between one each other, it is important not to irradiate the device prior to testing.

Abstract

Avec des rendements théoriques importants et un bas coût de fabrication, les cellules à colorants (DSSCs) « tandem » représentent une voix prometteuse pour la conversion de l'énergie solaire en électricité. Néanmoins, du fait d'un matériau de photocathode peu performant, et pourtant encore incontournable, le NiO, les rendements de ce type de cellule sont encore trop faibles (aux alentours des 2%). Des recombinaisons de charges géminées trop rapides sont notamment tenues pour responsables des faibles performances des photocathodes de NiO. Le colorant employé pour sensibiliser le NiO est un élément crucial pour lutter contre les recombinaisons de charges. Dans cette optique, quatre nouveaux colorants organiques de type « push-pull », ont été synthétisés et testés en DSSC de type p. Ces colorants sont à base de tri-arylamine (TPA) bithiophen pour la partie donneuse et possèdent des groupements accepteurs différents. Deux groupements acides carboxyliques permettent l'accroche des molécules, par la partie donneuse, sur le NiO. Une méthode efficace de synthèse de la TPA en une étape, par couplage de Buchwald-Hartwig, a d'abord été développée. Un couplage de Suzuki assisté par micro-ondes a ensuite permis de greffer, de façon versatile, les différents accepteurs à la partie donneuse. Les propriétés physiques (Electrochimie, UV/Visible) des colorants ont été analysées et corrélées de façon approfondie à des simulations par DFT/TDDFT. Les colorants ont l'avantage de posséder des coefficients d'absorption très élevés et des niveaux redox adaptés à une intégration en photocathode de NiO. Par ailleurs, ils possèdent une intense et large bande de transfert de charge, dont le maximum est décalé de façon graduelle vers les grandes longueurs d'onde, lorsque la force de l'accepteur augmente. Ceci permet d'obtenir une palette de longueur d'onde absorbée s'étendant du proche UV au rouge. Un des colorants, absorbant entre 450 et 700 nm, est notamment un très bon candidat en vue d'une future implémentation synergétique en cellule tandem. Par ailleurs, une nouvelle voie de synthèse de NiO, mettant en jeu l'impression jet d'encre d'un sol à base de $NiCl_2$ et d'un copolymère tribloc, le F127 est présentée. Cette famille d'encre est déjà employée et donne actuellement les meilleurs photo-courants pour des DSSCs de type p. Néanmoins, du fait du recours au doctor-blade pour le dépôt de l'encre, un grand manque de reproductibilité est souvent pointé du doigt. L'impression jet d'encre permet de pallier à ce problème. Dans un premier temps, les propriétés rhéologiques de l'encre ont été adaptées. Puis, après optimisation des paramètres d'impression, les dépôts de NiO ont été réalisés et caractérisés par MEB et XPS. De façon satisfaisante, les films obtenus sont d'épaisseur quasi uniforme, sans craquage et constitués de nanoparticules d'un diamètre entre 15 et 20 nm, densément arrangées. La maîtrise des conditions de séchage inter-couche a permis de former deux types de dépôts de NiO d'épaisseur significative. Introduire une étape de recuit à haute température permet d'avoir des dépôts de nanoparticules de NiO plus compacts et adaptés aux DSSCs de type p. Après un travail sur l'optimisation des conditions de sensibilisation du NiO, les photocathodes ont été testées en dispositif. Les performances obtenues sont compétitives par rapport aux meilleures photocathodes actuelles et ont l'avantage d'être reproductibles. Cela valide cette nouvelle méthode de formation du NiO pour l'application en DSSC. Cette nouvelle méthode permet également un bon degré de contrôle des conditions de dépôt et laisse donc envisager une étude approfondie de plusieurs paramètres de synthèse. Ceci offre des perspectives intéressantes pour la fabrication de cellules tandems performantes.

Abstract

Tandem Dye Sensitized Solar Cells (T-DSSCs) represent a promising, low cost, way for light conversion to electricity. Actually the theoretical yield of such device overstep the one of classical, one photo-electrode, DSSCs. However, due to a still irreplaceable, but not optimal, photocathode material: NiO, the yields of tandem DSSCs are still very limited (around 2%). This is due to the rapid geminate charge recombination that happens with NiO. In order to fight against charge recombination, the colorant employed is of paramount importance. For this, in this thesis, four new dyes, « push-pull » type, are presented. They have been synthesized and implemented into p-type DSSCs. These colorants are all triphenyl-amine (TPA) bithiophen based, for the electron rich part, and bear four different acceptors of different strenght. Two carboxylic acids permit dye anchoring at the NiO surface. An efficient synthetic method of TPA, in one step and through a Buchwald-Hartwig amination reaction, has first been developed. Then a microwave assisted Suzuki cross-coupling permitted to graft all the different acceptors to the donor TPA part. The dyes' physical properties (electrochemistry, UV/Visible) were assessed and precisely correlated to theoretical DFT/TDDFT results. The colorants possess very high molar extinction coefficients, and adapted redox levels for integration into NiO based device. Besides, they possess a wide and intense charge transfer band, which maximum is gradually shifted toward high wavelengths when the strength of the acceptor is increased. This allows the photocathode to absorb light from the near UV to the red part of the solar spectrum. Interestingly, one of the colorant absorbs between 450 and 700 nm and then represents a good candidate for a synergistic integration into tandem DSSC. In this work, a new way to synthesize NiO is also presented. It consists of ink-jet printing a sol-gel ink, containing $NiCl_2$ salt, as the NiO precursors and a triblock copolymer F_{127}. This family of ink has already been employed for NiO synthesis and has given the actual highest photo-currents. However, until now, doctor-blade is mandatory for the ink deposition. This doctor blade step is source of important irreproducibility. Indeed, ink-jet printing permits to solve this issue. Firstly, the rheological parameters of the ink were adapted for ink-jet printing. Then, after optimization of the printing parameters, NiO films were realized and analysed (MEB, XPS). The obtained films possess a quasi-uniform thickness, with no cracking and are constituted of 15 to 20 nm densely packed nanoparticles. Interlayer drying conditions' control permitted to form two types of NiO films, thicker than one micrometer. Sintering the printed film at high temperatures between each layer permitted to obtain compact films of NiO nanoparticles, more adapted to p-type DSSCs. After optimization of the sensitization conditions of NiO, the photocathodes were assembled into devices and tested. Their performance challenge the one of the most efficient photocathodes found in the literature, in a very reproducible way for the first time. Then ink-jet printing is an adapted way for NiO synthesis for p-type DSSCs. This new method allows a good level of control of the film formation conditions and then may a deeper study of the synthesis parameters is possible. This offers interesting prospects for future more performing tandem DSSCs.